University of Glamorgan

Accurate Prediction of Scintillation Degradation Applicable to Satellite Communication Systems Design

PhD Thesis

Ali Savvaris

October 2004

Certificate of Research

This is to certify that, except where specific reference is made, the work described in this Thesis is the result of the candidate. Neither this Thesis, nor any part of it, has been presented, or is currently submitted, in candidature for any degree at any other university.

Signed _____
Candidate

Signed _____
Director of Studies

Date 11 May 2005

Accurate Prediction of Scintillation Degradation Applicable to Satellite Communication Systems Design

By Ali Savvaris

The University of Glamorgan

A thesis submitted in partial fulfillment of the requirements for the degree of Doctor of Philosophy

October 2004

To my family for all their help and support

Abstract

Satellite communication was operated exclusively in C-band prior to 1970. Since then there has been an explosive growth in the demand for telecommunication services that are either only feasible via satellite or very cost effective by that means. This has prompted a steady growth in the utilization of higher frequencies in the Ku-band and above. The higher frequencies offer various advantages such as increased bandwidth, smaller antennas, and smaller satellite footprints that give higher EIRP permitting greater frequency reuse. The main drawback however is that they are subject to more severe propagation degradation. The small size antennas employed in VSAT and USAT systems significantly reduce the cost of earth station terminals and also eliminate tracking requirements, but they lose the mitigating effect of aperture averaging and hence experience stronger scintillation. The result is random fading and enhancement in the received signal amplitude, which will have a significant impact on the performance of low-margin communication systems operating at high frequencies (> ~10GHz) and low elevation angles, and utilising small antennas. Scintillation effects need to be considered in the design and link-budget calculations of these systems.

In this thesis, the results are shown of an extensive measurement analysis of tropospheric scintillation, using the ITALSAT satellite beacon signals at 18.7, 39.6 and 49.5 GHz, recorded at Sparsholt, U.K., at an elevation angle of 29.9^0. The analysis was carried out in order to study the effects of scintillation due to tropospheric turbulence and their impact on satellite digital communication systems.

The first part of the thesis deals with the preprocessing of raw propagation data and presents various statistical results relating to the stationary aspects of the scintillations, i.e. pdf of amplitude and intensity; long and short term statistics of amplitude scintillation distributions. The relationship of scintillation with link parameters and meteorological parameters are also studied.

The second part of the thesis investigates the dynamic characteristics of scintillation. It examines the observed effects of wind and cloud presence on the intensity and power spectrum of tropospheric scintillation and then moves on to present results relating to the analysis of the instantaneous frequency scaling of scintillation.

In the third part of the thesis scintillation fade and enhancement duration statistics are presented for various threshold signal levels, and their use in fade countermeasures is examined. Finally, a study of adaptive fade countermeasures (FCM) that could be used for systems operating at Ka-band and above for mitigating the effects of scintillations and rain attenuation is presented.

The last part, presents an improved global prediction model for both the long-term standard deviation and the signal level distribution of tropospheric scintillation. The model is validated using measurement results from satellite links in Europe, the United Sates and Japan at frequencies from 11 GHz to 50 GHz, and path elevation angles 5.8^0 to 40^0.

Table of Content

List of Tables

List of Figures

List of Symbols, Abbreviations & Acronyms

List of Symbols

α_a	The adiabatic rate of decrease of the temperature
C_n ( )	The structure constant of the index of refraction fluctuation.
D_u	Structure function of the velocity fluctuation.
$D_f(\tau)$	Structure function
$D_n(r)$	The structure function for the conservative passive additives.
D (m)	The physical diameter of the antenna
De (m)	Effective antenna diameter
e	The water vapour pressure in millibars.
E_k	Kinetic energy.
E_d	Energy dissipation.
E (V/m)	Electric field strength.
$F(\eta, \kappa, \rho)$	Filter function.
f (GHz) (Hz)	Frequency
gx ( )	Aperture averaging function of scintillation
h (m)	The height of turbulence
i ( )	Index
k_0	Free-space wave number
k (m^{-1})	Wave number
^0K	Kelvin
l	Length.
L_0	Outer scale of turbulence.
l_0	Inner scale of turbulence.
L	Distance
M	Rate of production of turbulent energy
n	The index of refraction.
Nwet (ppm)	Wet term of ground refractivity
P	The pressure in millibars.
p( )	Probability
q	Specific humidity.
Q ( )	Parameter for the long term scintillation standard deviation model (Van de Kamp model)
Re	Reynolds number.
Re_{cr}	Reynolds number critical value.
R_e (m)	The effective Earth radius (=8.5x10^6m).
RH (%)	Relative humidity
T (^0K)	The absolute temperature in degrees Kelvin.
u	Velocity of eddies in a pipe.
U_t	Wind velocity transverse to the direction of the wave propagation.
V	Velocity
V_f	Velocity fluctuations.
v_t (m/s)	Transverse wind speed

Whc (kg/m^2)	Average water content of heavy clouds
$W_x(\omega)$ ( )	Temporal frequency spectrum
$W_x^o(\omega)$	The low frequency asymptote of the power spectrum density of scintillation
$W_x^\infty(\omega)$	The high frequency asymptote of the power spectrum density of scintillation
W ( )	The new modified wet part of refractivity
X_{nor} ( )	Normalised cumulative distribution
y (dB)	Signal level deviation from the mean, due to scintillation

Greek Symbols

θ	Potential temperature
ε	Energy dissipation per unit mass per unit time
λ (m)	Wave length.
τ (s)	Time.
ψ	Complex phase
κ	Spatial wave number
ρ	The distance in the plane of observation transverse to the direction of propagation.
π ( )	3.141
η	The distance along the propagation path.
ν	Kinematic viscosity.
$\theta(^0)$	The path elevation angle
Γ	Gamma function
η ( )	Antenna aperture efficiency
σ (dB)	Standard deviation
σ_{pre} (dB)	Predicted standard deviation
σ^2 (dB^2)	Variance
$\Phi_n(k)$ ( )	Kolmogorov spectrum
Δ ( )	Generalised scaling factor

Abbreviations and Acronyms

ACTS	Advanced Communications Technology Satellite
APC	Adaptive Power Control
COST	COperation européenne dans le domaine de la recherche Scientifique et Technique
CDIAC	Carbon Dioxide Information Analysis Centre
CDMA	Code Division Multiple Access
Cdf	Cumulative distribution function
EIRP	Effective Isotropically Radiated Power
ESA	European Space Agency
FDMA	Frequency Division Multiple Access

ITU-R	International Telecommunication Union - Radiocommunication Sector
LEO	Low Earth Orbit Satellite
LPF	Low-Pass Filter
NASA	National Aeronautics and Space Administration
Pdf	Probability distribution function
Psd	Power spectrum density
TDMA	Time Division Multiple Access
ULPC	Up-Link Power Control
UTC	Coordinated Universal Time
USAT	Ultra Small Aperture Terminal
VSAT	Very Small Aperture Terminal

Acknowledgements

I would like to express my profound gratitude to my director of studies Dr. Ifiok E. Otung for his encouragement, support, patience and guidance through out this research work. His experience and feedback have been a continuous source of inspiration which has helped me enormously to complete this project. Thanks are also due to my second supervisor Professor Miqdad Al-Nuaimi.

I would like to thank Dr. Constantinos N. Kassianides for all his valuable help and support through my research. The author also wishes to thank Dr. Petros Panayi, Dr. Spiros Ventouras, Mr. Charles Wrench and Ms. Sarah Callaghan from Rutherford Appleton Laboratories, UK, for the satellite data and help in the preprocessing stage.

Finally I would like to thank my girlfriend Adaya and all my friends and family for all their help, motivation and support through the years. Especially my sisters Hanna and Alia for being there for me all these years. I really appreciate all what you did for me ... Thank you.

CHAPTER I

Introduction

1.1. INTRODUCTION

Since the launch of the world's first satellite, Sputnik, in 1957, satellite technology has come a long way. In 1965 the first geostationary commercial satellite (INTELSAT I) was launched and marked the beginning of global satellite communications. Today satellite communication networks are an indispensable part of most major communication systems. Satellite have the big advantage of providing cover over large geographical areas.

Communication satellite systems are classified in terms of their territorial coverage, for example global, regional, or national; or in terms of the type of services offered, e.g. fixed, mobile, maritime, aeronautical... etc; or point-to-point, broadcasting, commercial, experimental... etc. The first commercial satellite communication systems were designed with one primary application in mind: high capacity transcontinental trunk links for telephone traffic. The satellites were small and the Earth-stations large and provided a low capacity at a relatively high cost. However, recent technological advances have made possible the low-cost implementation of Very Small Aperture Terminal (VSAT) and Ultra Small Aperture Terminal (USAT) systems.

These capabilities have opened a new market for satellite communication – large distributed data networks. VSAT/USAT networks have provided cost effective wide-area coverage at performance levels that can be specified and optimised by a network user. Using innovative architectures, VSAT/USAT networks can be optimised to the specific topology, application, equipment characteristics, and management requirements of a variety of network users. The ease with which users are able to deploy them have a great influence on their success.

Most present VSAT networks operate at the Ku-band. However, the increasing demand in traffic capacity and the introduction of new services will necessitate a move to higher frequency bands.

The main future advanced applications will likely cover [1, 2]:

- Fixed multimedia communication for private business networks
- Mobile/Personal communications
- Digital high definition television (HDTV)
- Audio broadcasting to portable receivers
- Navigation and Air traffic Management

VSAT/USAT systems are finding increasing applications as an alternative to terrestrial networks for servicing areas with no, poor or sparse infrastructure, for example in India, China, Australia, Northern Canada and Alaska [3]. Services such as communications, television, weather forecast and distance learning are already being provided to remote communities in Canada via satellite.

A good example of the use of satellite communications for distance learning and corporate training is the Fordstar System. It is a system that the Ford Motor Company uses to connect their dealerships around the USA. The network connects thousands of dealerships throughout North America, and broadcasts some 450 different training programs every month using eight channels.

Operations at Ka-band and above has many attractive features. The most important of all is probably the greater bandwidth available and the high antenna gains which makes VSAT/USATs even smaller and more attractive for installation at user's premises. Smaller antennas and smaller satellite footprints give higher EIRP and permit greater frequency reuse, without generating extra interference, when compared to C- or Ku-band systems [4]. On the other hand, the use of these higher frequency bands is not as simple as the use of lower frequencies where high link availability can be achieved by introducing relatively small fixed link power budget margins. At Ka-band and above atmospheric degradation become so severe that adaptive methods or fade countermeasures (FCMs) are required to achieve high standards of availability [5].

An electromagnetic signal transmitted by a satellite passes through space and the atmosphere before reaching the Earth station. In so doing it incurs losses due to a number of propagation impairments. The main degradation factors are summarised in Table 1.1. Most tropospheric degradation effects become more severe at higher frequencies.

Table 1.1: Propagation concerns for satellite communication Systems.

Propagation impairment	Physical cause	Prime importance
Attenuation and sky noise	Atmospheric gases, cloud, rain	Frequencies above about 10 GHz
Signal cross-polarisation	Rain. Ice crystals	Dual-polarisation systems at C- and Ku bands (depends on system configuration)
Refraction, atmospheric multipath	Atmospheric gases	Communication and tracking at low elevation angles.
Reflection multipath blockage	Earth's surface, objects on surface	Mobile satellite services
Propagation delay variations	Troposphere, ionosphere	Precise timing and location systems; time-division multiple access (TDMA) systems
Inter-system interference	Ducting, scatter, diffraction	Mainly C- band at present; rain scatter may be significant at higher frequencies

1.2. Propagation Effects

Attenuation on radio propagation paths is generally caused by various atmospheric components: gases, water vapour, clouds, and rain [6]. Rain attenuation, caused by scattering and absorption by the water droplets, is one of the most fundamental limitations to the performance of satellite communication links in the Ka-band and above, causing large variations in the received signal power, with little predictability and many sudden changes. This kind of signal fading is also prevalent on earth-space links in the C- and Ku-bands, however, the depth of fades in those frequency bands is small enough to be compensated for by including a small fixed fade margin in the link budget in order to maintain the desired performance.

In the Ka- and V-bands, the attenuation caused by rain is too severe to be accounted for by a fixed margin in the link budget [7, 8]. In order to provide the same performance as in the lower frequency bands, an excessively large margin would be required. Considering that this power margin is needed only occasionally, this is clearly uneconomical. In addition, the power margin needed would result in prohibitive requirements for satellite power, and interference to other communication systems operating at the same frequency band during clear-sky conditions.

To avoid these problems, alternative methods to reduce communication outage due to rain fading have been developed. These 'fade countermeasures' compensate for rain attenuation adaptively, i.e. the quality of the link is improved when the signals are degraded. One of these countermeasures is Adaptive Power Control (APC), in which the transmitted power is increased to compensate for fading due to rain on the propagation path [9]. Other fade countermeasure techniques that could potentially be deployed will be discussed in more detail in section 7.5 of Chapter 7.

Rain attenuation, although an important signal impairment in the Ka- and V-bands, is not directly studied in this thesis. This is because this phenomenon is already widely being considered in many other studies and measurement campaigns, and the theoretical background of rain attenuation is already relatively well understood.

Furthermore, many of the emerging applications of satellite communications do not require the high availability specifications of public-switched telephony networks (PSTNs). The activity ratio (ratio of up time to total time) of some of these systems may be less than 10% [10]. Relatively low-availability will therefore be acceptable, and since the probability of rain is less than 5% in most regions of the world, scintillation will replace rain as the predominant degrading factor in such systems [11].

For low fade margin systems operating at high frequencies and low elevation angles, the impact of scintillation becomes an important factor that need to be considered [12]. In the Ka-band and above, and low elevation angles ($\leq\approx 15°$), scintillation may contribute as much as rain, or even more, to the total fade measured, especially for time percentages larger than 1%, and therefore for low fade margin systems. Some applications in the Ka- and V-band will be aimed at Very Small Aperture Terminal (VSAT) services with low fade margins, so there is a need to quantify propagation phenomena in the low fade margin range. Knowledge of the dynamic characteristics of scintillation is also important for the design of Adaptive Power Control (APC) and antenna tracking systems, because of the fast variations in signal level and phase it causes.

1.3. Objectives of Research

As already mentioned in section 1.2 in satellite communications at frequencies above 10 GHz, signal level attenuation by rain, together with signal level fluctuations caused by tropospheric scintillation are the major problems in radiowave transmission. In general the impact of rain attenuation on the communication signal is predominant. Scintillation however becomes important for low-fade margin systems operating at high frequencies along low-elevation paths, sometimes producing signal fading in excess of 10 dB [13].

Scintillations are rapid fluctuations in amplitude and phase of the received signal, arising from random fluctuation in the atmospheric refractive index due to turbulent irregularities in temperature, humidity and pressure. The result is random fading and enhancement in the signal amplitude and phase received on a Satellite-Earth link [14,

15]. Tropospheric amplitude scintillation can be observed during rain as well as under clear weather conditions. Clear-sky amplitude scintillation manifests itself as rapid random fluctuations around the mean signal level. If rain is present on the propagation path, the receiver will see fast amplitude fluctuations superimposed on the slow variations caused by rain attenuation. This type of amplitude scintillation is often referred to as "wet scintillation".

Amplitude scintillation occurring in the troposphere increases with signal frequency and depends on a number of other link and meteorological parameters. As a result, scintillation will have a significant impact on the performance of low-margin communications systems operating at frequencies above ≈10 GHz, low elevation angles and utilising small antennas (VSATs and USATs). Therefore, accurate estimates of signal degradation due to these effects must be included in the design of satellite communication systems. A thorough understanding, quantification and modelling of scintillation are imperative for the reliable design and operation of these increasingly popular telecommunication systems.

This thesis will investigate the effects of tropospheric scintillation on satellite communication systems operating at Ka-band frequencies and above. The aim of the project is to carry out a detailed and thorough scintillation analysis of the ITALSAT satellite beacon measurements by Rutherford Appleton Laboratory (RAL) at three frequencies (18.69, 39.59, and 49.49 GHz) in order to:

1. Extend the UK scintillation data base.
2. Make a detailed analysis of the scintillation data along with concurrent meteorological data.
3. Include the results of previous UK satellite link measurements (at frequencies 11, 12, 14, 20, and 30GHz, and path elevation angles 3^0, 10^0, and 30^0) by RAL and British Telecommunication plc using Olympus and INTELSAT satellites [16-18].
4. Develop accurate semi-empirical models that predict the occurrence and dynamics of scintillation in the UK and similar climates.

5. Validate the developed models by comparison with available non-UK based measurements and models.
6. Assess the impact of scintillation on emerging satellite communication systems.

1.4. Overview - Content of the Thesis

Following this introductory chapter, the content of Chapter 2 serves to introduce the cause of atmospheric turbulence, which is responsible for tropospheric scintillation. The Chapter begins with an overview of the atmosphere, followed by a summary of atmospheric turbulence. Attention is paid to the amplitude fluctuations of a radiowave travelling through a turbulent medium, referred to as amplitude scintillation. A summary of the parameters affecting amplitude scintillation and its characteristics is then presented, which helps the reader to gain a clearer insight into the phenomenon.

In Chapter 3 the satellite receiver system and the data preprocessing are described. Sparsholt data format, the calibration factors and the meteorological data format are also covered in this Chapter. The 20, 40 and 50 GHz raw propagation data were obtained from monitoring the ITALSAT F1 and F2 satellite beacon signals at Sparsholt, UK, for the period covering June 1996 to May 1999 for the 40 and 50 GHz beacons and for the period covering September 1999 to August 2000 for the 20 GHz beacon. Chapter 4 presents results relating to the stationary aspects of the scintillations, i.e. pdf of amplitude and intensity; long and short term statistics of amplitude scintillation distributions and comparisons are discussed. In the second part of Chapter 4, the dependence of scintillation on various meteorological parameters (wind speed, clouds, temperature and relative humidity) is investigated. The impact of period length over which those parameters are averaged is also investigated and an improved relationship between the wet-part of refractivity, N_{wet}, and the measured standard deviation is given.

Chapter 5 examines the observed effects of wind and cloud presence on the intensity and power spectrum of tropospheric scintillation at three respective beacon frequencies (20, 40 and 50GHz). The novelty of some aspects of this analysis comes

from the fact that it quantifies the amount by which the presence of cumulus clouds increases the observed scintillation levels. This is followed by a discussion in using the slant path spectrum as a tool for remote sensing applications.

Chapter 6 - This Chapter presents an analysis of instantaneous frequency scaling of scintillation. The frequency power exponent α forms an important parameter in the current prediction models. Results concerning the frequency exponent of scintillation from 22 sites around the world involving different frequencies and path elevation angles are investigated, in an attempt to explain the significant variation in the mean values of α from site to site.

Chapter 7 starts with some general definitions and equations related to satellite communication system design, followed by an overview of digital modulation techniques used in satellite communications. Scintillation fades and enhancements durations Statistics are also presented for various threshold signal levels, and their use in fade countermeasures is examined. Finally, a study of adaptive fade countermeasures (FCM) that could be used for systems operating at ka-band and above for mitigating the effects of scintillations and rain attenuation.

One of the objectives of this research project is to develop an accurate semi-empirical model that predict the occurrence and dynamics of scintillation. Chapter 8 presents an improved global prediction model for both the long-term scintillation intensity and the signal level distribution. The model is validated using measurements results from satellite links in Europe, the United Sates and Japan at frequencies from 11 GHz to 50 GHz, and path elevation angles 5.8^0 to 40^0.

Finally in Chapter 9 the conclusions of the research are summarised and recommendations made for areas of further research. To preserve the continuity of the main chapters some detailed information, publications and graphs have been placed in the appendices at the end of this thesis.

References

[1] E. R. Laase and M. d. l. Chapelle, "New Aviation and Maritime Applications for MObile VSATs," presented at AIAA 2004, Monterey, USA, 2004.

[2] B. Gremont, "Fade Countermeasure Modelling for Ka Band Digital Satellite Links." Coventry: Coventry University, 1997.

[3] A. K. Ghose, "VSAT Networks in India, Specifications and Applications," *Int. Journal of Satellite Communication*, vol. 11, pp. 211-216, 1993.

[4] D. V. Rogers, J. L. Ippolito, and F. Davarian, "System Requirements for Ka-band Earth-Satellite Propagation Data," *Proceedings of IEEE*, vol. 85, 1997.

[5] M. J. Willis and B. G. Evans, "Fade Countermeasures at Ka band for Olympus," *Int. Journal of Satellite Communication*, vol. 3, pp. 301-311, 1988.

[6] G. Brussaard and P. A. Watson, *Atmospheric Modelling and Millimetre Wave Propagation*. London: Chapman & Hall, 1995.

[7] R. Polonio and C. Riva, "ITALSAT Propagation Experiment at 18.7, 39.6, and 49.5 GHz at Spino D'Adda: Three Years of CPA Statistics," *IEEE Transactions on Antennas and Propagation*, vol. 46, pp. 631-635, 1998.

[8] Y. Karasawa and T. Matsudo, "Characteristics of Fading on Low-Elevation Angle Earth-Space Paths with Concurrent Rain Attenuation and Scintillation," *IEEE Transactions on Antennas and Propagation*, vol. 39, 1991.

[9] J. Hörle, "Up-Link Power Control of Satellite Earth Stations as a Fade Countermeasure of 20/30 GHz Communication Systems," *Int. Journal of Satellite Communication*, vol. 6, pp. 323-330, June 1988.

[10] J. E. Allnutt and D. V. Rogers, "Low-fade Margin Systems: Propagation considerations and Implementation Approaches," presented at International Conference on Antennas and Propagation (ICAP89), Coventry, UK, 1989.

[11] I. E. Otung, "Accurate prediction of scintillation degradation applicable to satellite communication system design," University of Glamorgan 1998.

[12] J. D. VANHOENACKER and H. VASSEUR, "Prediction of scintillation effects on satellite communications above 10 GHz," *IEE Proceedings on Microwave Antennas Propagation*, vol. 142, pp. 102-108, 1995.

[13] Y. Karasawa, M. Yamada, and J. E. Allnutt, "A New Prediction Method for Tropospheric Scintillation on Earth-Space Paths," *IEEE Transactions on Antennas and Propagation*, vol. 36, pp. 1608-1614, 1988.

[14] A. Ishimaru, *Wave Propagation and Scattering in Random Media*: IEEE Press, 1997.

[15] I. E. Otung, M. O. Al-Nuaimi, and B. G. Evans, "Extracting Scintillations from Satellite Beacon Propagation Data," *IEEE Transactions on Antennas and Propagation*, vol. 46, pp. 1580-1581, 1998.

[16] D. L. Bryant, "Low Elevation Angle 11GHz Beacon Measurements at Goonhilly Earth Station," *BT Technol. J.*, vol. 10, pp. 68-75, 1992.

[17] R. G. Howell, R. W. Thorn, M. T. Hewitt, J. Thirlwell, P. T. Thompson, and J. E. Allnutt, "Long-term Satellite and Radiowave Measurements on a Low-Angle Satellite Path at Frequencies in the Range 11.2 to 14.8 GHz," presented at International Conference on Antennas and Propagation (ICAP89), Coventry, 1989.

[18] R. G. Howell, J. W. Harris, and M. Mehler, "Satellite Co-polar Measurements at BT Laboratories," *BT Technol. J.*, vol. 10, pp. 34-51, 1992.

CHAPTER II

Theory of Tropospheric Scintillation

Summary – *This chapter will discuss the theoretical aspects of tropospheric scintillation of a wave propagating in a random medium. Starting with an overview of the Earth's atmosphere, followed by turbulence theory and the onset of turbulence. Attention is paid to amplitude scintillations – the amplitude fluctuations of the wave travelling through turbulent medium. A summary of the factors that affect amplitude scintillation and its characteristics are also discussed.*

2.1. INTRODUCTION

The study of band limiting atmospheric phenomena is essential to develop the future communications systems at millimeter waves. Among the atmospheric phenomena affecting Earth-Space communications above 10 GHz, turbulence cannot be neglected. By inducing time varying refractive index inhomogeneities, atmospheric turbulence yields random fluctuations of the amplitude, the phase and the angle-of-arrival of radiowaves, called tropospheric scintillation. Scintillations are produced by the small-scale inhomogeneities of the atmospheric refractive index induced by turbulence. Due to the random movement of fluid parcels, called turbulent eddies, turbulence effects an intensive mixing of the atmospheric medium. Hence, atmospheric turbulence yields both time and space small-scale fluctuations of various features such as wind speed, temperature, humidity and refractive index.

Atmospheric turbulence occurs from the surface of the earth up to heights of hundreds of kilometers. However the turbulent eddies that are significant in causing fluctuations in the radio refractive index are those occurring in the boundary layer of the troposphere, extending up to about 10 km above the earth's surface. These eddies range in size from the order of millimeters to several hundreds of meters. Above the boundary layer, in the 'free atmosphere' the eddies have sizes of several kilometers or larger and are responsible for the slow, longer term variations in the refractive index.

There are two main mechanisms responsible for the introduction of energy into the turbulence in the troposphere. These are wind shear, that is spatial variation in the average wind velocity, and buoyancy, which is related to the vertical temperature gradient [1].

The basis for the theory of scintillation is the fluid dynamics model for velocity fluctuations in a turbulent medium, proposed first by Kolmogorov in the 1940's. This theory linked the large-scale air motions that generate turbulence to the very small-scale motions where that energy is ultimately dissipated. Another key to understanding and applying turbulence information is Taylor's frozen turbulence hypothesis. This is the

assumption that the turbulent eddies do not change significantly as they move by at the mean wind velocity. This is discussed in more details in Section 2.7 of this chapter.

In order to better appreciate the various propagation effects that can occur on an earth-space path, we will start with a brief overview of the Earth's atmosphere. It is a complex structure with regions of widely differing composition and characteristics, affecting the propagation of radiowaves in a variety of ways.

2.2. The Atmosphere

The Earth's atmosphere contains several different layers that can be defined according to air temperature or chemical composition. Figure 2.1 displays some of these layers in an average atmosphere. Variations in the way temperature changes with height indicate the atmosphere is composed of a number of different layers (identified below). These variations are due to alterations in the chemical and physical nature of the atmosphere with altitude.

According to temperature, the atmosphere contains seven different layers. From the surface of the Earth to approximately 11 kilometers in altitude the layer called the *troposphere* exists. About 75 % of the total mass of the atmosphere is contained in this layer. It is also the layer where the majority of our weather occurs. Maximum air temperature also occurs near the Earth's surface in this layer. With increasing height, air temperature drops uniformly with altitude at a rate of approximately 6.5 degrees Celsius per 1000 meters. At an average temperature of -55 degrees Celsius, the top of the troposphere is reached.

The *tropopause*, extending from 11 to 20 kilometers, is an isothermal layer in the atmosphere where temperature remains constant over a distance of about 9 kilometers. It is also the layer in the atmosphere where the *jet streams* occur.

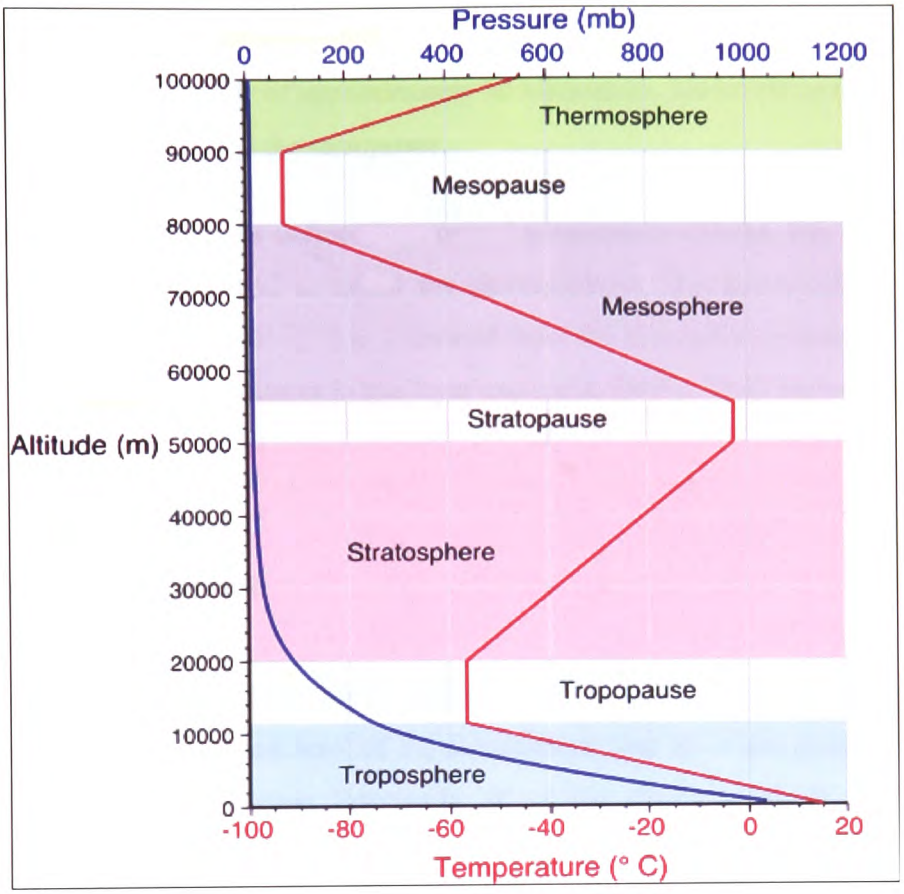

Figure 2.1. Vertical change in average global atmospheric temperature and pressure [2].

Above the *tropopause*, is the *stratosphere*. This layer extends from an average altitude of 20 to 48 kilometers above the Earth's surface. In the stratosphere, temperature increases with altitude because a localized concentration of *ozone* gas molecules absorbs ultraviolet sunlight creating heat energy. Ozone is primarily found in the atmosphere at varying concentrations between the altitudes of 10 to 50 kilometers. This layer of ozone is also called the *ozone layer*. The ozone layer is important to organisms at the Earth's surface as it protects them from the harmful effects of the sun's ultraviolet radiation. Without the ozone layer life could not exist on the Earth's surface.

Separating the *mesosphere* from the stratosphere is another isothermal layer called the *stratopause*. In the mesosphere, the atmosphere reaches its coldest temperatures (about -90 degrees Celsius) at a height of approximately 80 kilometers. Above the mesosphere is another isothermal layer called the *mesopause*.

The last atmospheric layer, as defined by vertical temperature change, has an altitude greater than 90 kilometers and is called the *thermosphere*. The thermosphere is the hottest layer in the atmosphere. Heat is generated from the absorption of solar radiation by oxygen molecules. Temperatures in this layer can reach 1300 to 1800 degrees Celsius.

2.1.1 The Troposphere

The troposphere will be of most importance to us in our study. It is this region and possibly also in the very lowest level of the stratosphere, that all of the phenomena we normally call the weather occur. Practically all of the clouds, certainly all of the precipitation, and the endless interplay between temperature, pressure, and atmospheric humidity contribute to the phenomena of the troposphere. It causes the most significant impairments of radiowave propagation.

The main propagation phenomena affecting Earth-space paths are:

A. Attenuation due to scattering and absorption by hydrometeors: Hydrometeor is the general name for condensed water vapour existing in the atmosphere. Rain attenuation falls in this category. It is the most important atmospheric phenomenon affecting Earth-space communications at frequencies above $\approx$ 10 GHz. Other hydrometeors such as fog, snow flakes and clouds can also cause attenuation.

B. Gaseous absorption: Oxygen and water vapour are the principal absorbers of radiowave energy. As well as causing an increasing background level of attenuation with an increase in frequency, there are a number of critical frequencies where resonant absorption take place. Water vapour has three resonant absorption lines at

22.4, 183.3 and 323.8 GHz. Oxygen has an isolated absorption line at 118.74 GHz and a host of absorption lines around approximately 60 GHz.

C. Tropospheric scintillation: Scintillations are rapid fluctuations in amplitude and phase of the received signal, arising from random fluctuation in the atmospheric refractive index due to turbulent irregularities in temperature, humidity and pressure. Amplitude scintillation occurring in the troposphere increases with signal frequency and depends on a number of other link and meteorological parameters [3]. There is a strong correlation with temperature and humidity. Evidence of a weak correlation with wind speed has been reported [4]. The presence of wind causes the atmosphere to become mixed rather than stratified, and this causes relatively rapid variations in refractive index to occur over small intervals, referred to as scale sizes, which in turn causes an increase in the Fourier components of the scintillation spectrum. The presence of cumulus clouds along the propagation path has also been associated with an increase in scintillation intensity. This is discussed in more details in Chapter 4.

D. Cross-depolarisation by hydrometeors: Hydrometeors, mainly rain but also snow and ice cause cross-polarisation of radiowaves. In the case of rain, cross-polarisation results from the non-spherical shape of the raindrops. The shape distorts owing to hydrodynamic forces. The drops, as well as becoming non-spherical in shape, may be tilted away from the local horizontal and vertical axes of symmetry in relation to the wave passing through owing to wind shear. This effect increases with increasing signal frequency and lower elevation angles.

This section is not meant to be a literature survey of various areas of propagation research but rather an illustration of the significance of tropospheric scintillation in relation to the other propagation impairments occurring on Earth-space paths. There are several other factors such as ray bending, scattering and absorption due to sand and dust particles that were not covered due to their weaker contribution at Ka- and V-band. The next section

will discuss atmospheric turbulence in more detail, with emphasis on tropospheric scintillation.

2.3. Atmospheric Turbulence

The problem of wave propagation through a turbulent medium has been quite well dealt with in the literature. The theory was first used in connection with optical propagation [5] but afterwards extended to micro- and millimetre-wave transmission [1].

Atmospheric turbulence affects the propagation of radio waves by creating random variations of the refractive index that yield amplitude, phase and angle-of-arrival fluctuations of the received signal. Due to the random movement of fluid parcels, called turbulent eddies, turbulence effects an intensive mixing of the atmospheric medium.

Turbulent media has the following characteristics [6]:

i) Turbulence consists of random velocity fluctuations.
ii) Turbulence causes rapid mixing at a much greater rate than molecular diffusion.
iii) Turbulent flow is characterised by large Reynolds numbers.
iv) Turbulence is rotational and three-dimensional.
v) Turbulent flows are dissipative.
vi) The smallest scale size is very much greater than molecular scales.
vii) The characteristics of the turbulent flow depend very much on the nature of the producing environment.

Reynolds deduced a non-dimensional number, Re, based on the flow of viscous fluid. If a viscous fluid is passed through a pipe of dimension l with velocity v, the motion of this fluid can be characterised as laminar, provided that the Reynolds number is less than some critical value.

Consider an initially laminar flow of a viscous fluid. This flow can be characterised by the values of the kinematic viscosity v, the characteristic velocity scale u and the

characteristic length l. The quantity l characterises the dimensions of the flow as a whole, and arises from the boundary conditions of the fluid dynamics problem. The laminar flow of the fluid is stable only in the case where the Reynolds number Re=ul/v does not exceed a certain critical value Re_{cr}. As the number Re is increased (e.g. by increasing the velocity of the flow) the motion becomes unstable (turbulent).

If a turbulence is created within a pipe of dimensions l and velocities of eddies are of the order of u, then the characteristic time associated with the eddy is of the order of $\tau = l / u$. The kinetic energy E_k of the turbulence per unit mass of the fluid per unit time is, therefore, on the order of

$$E_k = u^2 / \tau = u^3 / l \tag{2.1}$$

On the other hand, the energy of the turbulence is dissipated due to viscosity. If the turbulence is to be sustained, the kinetic energy must be much greater than the energy dissipation. The energy dissipation E_d per unit mass per unit time is on the order of

$$E_d = \frac{vu^2}{l^2} \tag{2.2}$$

The ratio of the kinetic energy and the energy dissipation is recognised as the Reynolds number.

$$\mathrm{Re} = \frac{E_k}{E_d} = \frac{ul}{v} \tag{2.3}$$

The critical Reynolds number Re_{cr} is not a universal constant. Its value depends not only on the geometry of the structure but on how the turbulence is introduced. Kolmogorov advanced an important theory of local structure of turbulence with a very large Reynolds number and postulated that energy is introduced into the turbulence as a result of variations in average velocity.

2.3.1 Developed Turbulence

The size of the eddies at which the energy enters the turbulence is called the outer scale of turbulence and is denoted by L_0, with typical values ranging between 50 and 100m. In general, the turbulence is anisotropic in this range, while eddies of smaller size are isotropic.

The kinetic energy per unit mass per unit time of eddies with size L_0 is given by V_0^3/L_0, where V_0 is the velocity. Since the Reynolds number is very large then the dissipation energy per unit mass, vV_0^2/L_0^2, is negligible, so all the kinetic energy is transferred to eddies with smaller sizes. As the size becomes smaller, the dissipation increases. The same will continue until the kinetic and dissipation energies are equalised and all the energy is dissipated into heat. There is therefore no energy to be transferred to eddies with smaller size, as shown in Equation (2.4).

The size of the eddies from where all the energy is dissipated into heat is denoted as l_0 and is called the inner scale of turbulence. Let V_1, V_2, V_3, ... , V_n be the respective velocities of eddies with sizes L_1, L_2, L_3, ... , L_n, where $L_0>L_1>\ldots>L_n$. Using these velocities and sizes the following expression can be written [1]:

$$\frac{V_0^3}{L_0} \approx \frac{V_1^3}{L_1} \approx \ldots \approx \frac{V_l^3}{l_0} \approx \frac{vV_l^2}{l_0^2} \approx \varepsilon \tag{2.4}$$

where ε is the energy dissipation per unit mass per unit time. It can be seen from Equation (2.4) that if the eddy size is between the inner and outer scales of turbulence then the velocity fluctuations V depend only on the size L and the energy dissipation rate ε, i.e. $V\sim(\varepsilon L)^{1/3}$, so the size of the fluctuational energy belonging to perturbations with sizes of the order L is proportional to $L^{1/3}$. If we take r to be large compared with the inner scale size and small compared with the outer scale size of the turbulence; then the velocity difference at two points r_1 and $r_1' = r_1 + r$ is characterised by the energy dissipation rate ε.

The structure function D_u (where, $D_u(r) = \left\langle [u(0) - u(r)]^2 \right\rangle$) of the velocity fluctuation can be deduced from this and must be a function of r and ε. The only combination of the quantities r and ε with the dimensions of velocity squared is $(\varepsilon r)^{2/3}$.

$$D_u(r) = C(\varepsilon r)^{2/3} \qquad \text{for } l_0 << r << L_0 \tag{2.5}$$

where C is a dimensionless constant and must be found experimentally. Equation (2.5) is known as the "two-thirds law". For $r << l_0$, the structure function of the velocity fluctuation is given by [5]:

$$D_u = \frac{1}{15}\left(\frac{\varepsilon}{\nu}\right) r^2 \qquad \text{for } r << l_0 \tag{2.6}$$

The scattering caused by this wide range of turbulent eddies results in fast variations of the signal around the mean signal level which are called clear sky amplitude scintillations. Scintillations consist of enhancement above and fades below the clear sky signal level. The duration of the fading or enhancement peak of a scintillation event is typically of a few seconds. These scintillation effects are non-absorptive and tend to occur "on axis".

2.4. Index of refraction structure function

The index of refraction n of the earth's atmosphere in the troposphere (height <17 km) is given by:

$$n - 1 = \frac{77.6}{T}(P + 4810\, e/T) \times 10^{-6} \tag{2.7}$$

Where, T is the absolute temperature in kelvin, P the pressure in millibars, and e the water vapour pressure in millibars. In turbulent atmospheres, P, T, and e vary randomly and do not necessarily follow the motions of the turbulence [1]. In order to establish the effect of the turbulence in producing refractive index fluctuations one can work in terms

of what is called *conservative passive additives*, i.e. parameters which do not exchange energy with the turbulence and which are conserved as a volume of turbulent air moves about in space. In general, there are two quantities which may be regarded as *conservative*: potential temperature and specific humidity.

Consider a mass of air at T and p at a height z. If we bring this air to the earth's surface ($P=P_0$ and $z=0$) adiabatically, then the temperature T becomes θ. This temperature θ is called the potential temperature and is given by

$$\theta = T + \alpha_a z \tag{2.8}$$

Where α_a is called the adiabatic rate of decrease of the temperature. The specific humidity q, which is the mass of water vapour per unit mass of air is given by

$$q = 0.622\, e / P \tag{2.9}$$

The expression for the refractive index n becomes

$$n-1 = \frac{77.6P}{\theta - \alpha_a z}\left(1 - \frac{7733q}{\theta - \alpha_a z}\right)\times 10^{-6} \tag{2.10}$$

The fluctuation characteristics of the index of refraction can thus be directly related to the variations in the conservative passive additives, θ and q [1].

Consider a random function of time *f(t)*, which may be wind velocity, humidity, temperature, pressure, or the refractive index in the turbulent atmosphere. *f(t)* is not strictly stationary, but the difference $f(t+\tau)-f(t)$ is considered stationary.

To describe random functions, which are more general than stationary random functions, in turbulence theory one can use instead of correlation functions the so-called *structure functions*. The structure function of the velocity variations is defined as:

$$D_f(\tau) = \overline{[f(t+\tau) - f(t)]^2} \tag{2.11}$$

The structure function is the basic characteristic of a random process with stationary increments. Roughly speaking the value of $D_f(\tau)$ characterises the intensity of those fluctuations of $f(t)$ with periods which are smaller than or comparable with τ.

The basic idea behind this method consists of the following:
In the case where $f(t)$ represents a non-stationary random function, i.e., where $f(t)$ changes in the course of time, we can consider instead of $f(t)$ the difference $f_\tau(t)=f(t+\tau) - f(t)$. For values of τ which are not too large, slow changes in the function $f(t)$ do not affect the value of this difference, and it can be a stationary random function of time, at least approximately.

It is generally easier to work in terms of the structure function rather than the correlation function. This is especially the case for locally homogenous and isotropic turbulence described by Kolmogorov spectrum. Since the fluctuation of the index of refraction is directly proportional to the fluctuation of the conservative additive, working in terms of the structure function for the conservative passive additives it can be shown [1] that the structure function for the refractive index $D_n(r)$ is given by:

$$D_n(r) = \begin{cases} C_n^2 r^{2/3} & \text{for} \quad l_0 << r << L_0 \\ C_n^2 l_0^{2/3} (r/l_0)^2 & \text{for} \quad r << l_0 \end{cases} \tag{2.12}$$

C_n is the structure constant of the index of refraction fluctuation, which is a measure of the energy in the fluctuations of the normalised refractive index. This is in turn directly related to the energy of the turbulence.

2.5. Kolmogorov Spectrum

Kolmogorov [1] obtained the spectrum of the fully developed turbulence based on the physical consideration of turbulence. According to the Kolmogorov theory, the turbulence eddies may be characterised by two sizes: the outer scale of turbulence L_0 and the inner scale of turbulence l_0. We therefore divide the turbulence characteristics according to the size of the eddy into three regions:

a) The region of the spectrum $\phi_n(\kappa)$ for which $\kappa < 2\pi/L_0$ is called the input range. In general, the turbulence is anisotropic in this range. The shape of the spectrum in this region depends on how the particular turbulence is being created, and therefore no universal spectrum can be assigned.

b) The region between $2\pi/L_0$ and $2\pi/l_0$ is called the inertial subrange. In this region, the kinetic energy of the eddies dominates over the energy dissipation and the spectrum should have the general slope $\phi_n(\kappa) \sim \kappa^{-11/3}$, where $\kappa = 2\pi /$ (eddy size). [See Appendix A]

c) The region for which $\kappa > 2\pi/l_0$ is called the dissipation range, where the energy dissipation dominates the kinetic energy, and consequently there is very little energy in this range and therefore the spectrum is extremely small, see Figure 2.2.

Considering these three ranges, mathematically we may write [1]:

$$\phi_n(\kappa) = \begin{cases} unknown & 0 \le \kappa \le 2\pi / L_0 \\ 0.033 C_n^{\,2} \kappa^{-11/3} & 2\pi / L_0 < \kappa < 2\pi / l_0 \\ 0 & 2\pi / l_0 < \kappa \end{cases} \qquad (2.13)$$

Or, we may combine the later two regions:

$$\phi_n(\kappa) = 0.033\, C_n^{\,2} \kappa^{-11/3} \exp(-\kappa^2 / \kappa_m^{\,2}) \qquad for\ 2\pi / L_0 < \kappa \qquad (2.14)$$

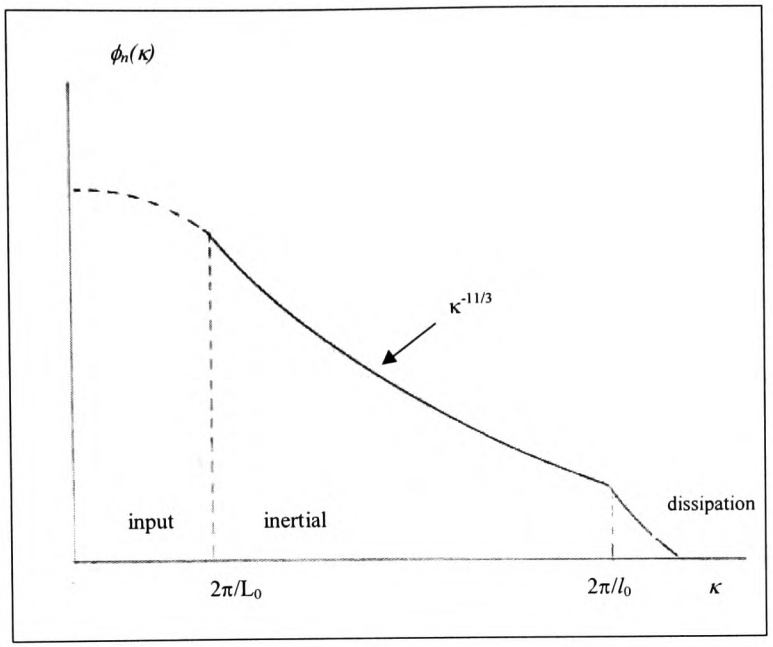

Figure 2.2. Kolmogorov Spectrum [1].

with $\kappa_m = 5.92/l_0$. For mathematical convenience,

$$\phi_n(\kappa) = 0.033\, C_n^{\,2}\, (\kappa_L^2 + \kappa^2)^{-11/6} \exp(-\kappa^2 / \kappa_m^{\,2}) \qquad (2.15)$$

with $\kappa_L = 1/L_0$, is often used to describe the entire range of κ, even though as we already indicated, the input range cannot be simply described in an isotropic form as in the foregoing. Equation (2.15) is also known as von Karman spectrum [1].

Let us consider the total spectrum which is the product of $f_x(\kappa)$ [or $f_s(\kappa)$] and $\phi_n(\kappa)$. It is clear that the product shows quite different characteristics, depending on whether $2\pi / \sqrt{\lambda L}$ is greater than $2\pi/l_0$, or between $2\pi/L_0$ and $2\pi/l_0$, or smaller than $2\pi/L_0$. These three cases represent the following ranges of distance L :

$L < (l_0^{\,2} / \lambda)$	(geometric optical region)
$(l_0^{\,2} / \lambda) < L < (L_0^{\,2} / \lambda)$	(diffraction region)
$(L_0^{\,2} / \lambda) < L$	

In the earth's atmosphere, the inner scale l_0 is of the order of millimeters and the outer scale L_0 is on the order of 10-100m.

The geometric optical region, $L << (l_0^2 / \lambda)$, will not be discussed in this thesis, however, reference to this topic can be found in [1], [5], [7]. Instead we will examine the condition where, $(l_0^2 / \lambda) << L << (L_0^2 / \lambda)$. This is the diffraction region, and therefore, in general, both l_0 and L_0 affect the fluctuations of the wave. For the amplitude fluctuation, the filter function $f_x \sim \kappa^2$ for κ small, and, therefore, the effect of the outer scale L_0 is negligibly small. If $L >> (l_0^2 / \lambda)$, then we can use

$$\phi_n(\kappa) = 0.033 C_n^2 \kappa^{-11/3} \tag{2.16}$$

for all ranges of κ, and we obtain the variance

$$\sigma_x^2 = 2\pi^2 \kappa^2 L \int_0^\infty \kappa \, d\kappa \, f_x(\kappa) \phi_n(\kappa) \tag{2.17}$$

$$= 0.033 C_n^2 \pi^2 \kappa^{7/6} L^{11/6} \left[-\Gamma\left(-\frac{5}{6}\right) \right] \frac{6}{11} \cos(5\pi/12) \tag{2.18}$$

$$= 0.307 C_n^2 \kappa^{7/6} L^{11/6} \tag{2.19}$$

In contrast to the geometric optical case, where σ_x^2 is independent of κ and proportional to L^3, σ_x^2 in the diffraction region is proportional to $\kappa^{7/6}$ and $L^{11/6}$. These powers (7/6 and 11/6) are directly related to the shape of the Kolmogorov spectrum $\kappa^{-11/3}$ and thus they are often used to verify the validity of the Kolmogorov representation.

2.6. Amplitude fluctuations of a wave

In line-of-sight propagation one deals with a mixture of the incident and scattered waves. The variation of the refractive index in the turbulent medium results in fluctuations of the amplitude and phase of the plane wave travelling through it. Solutions to this propagation problem must then include the coherent, time- averaged field, and the incoherent fluctuation component. Figure 2.3 is a 'flow-diagram' which illustrates electromagnetic propagation theories for line-of-sight propagation in random continuous medium [6]. The objective here is to relate these fluctuations to the properties of the turbulence (e.g. the spectrum of refractive index fluctuations) and other factors such as the path length, L.

If, within a given distance, the intensity of the turbulence is weaker than a certain level (see section 2.4), and consequently the refractive index fluctuations are small, relatively simple solutions to Maxwell's equations for the random medium may be obtained. This is known as the weak fluctuation or scintillation approximation and in the microwave region it is valid for most practical path lengths within the earth's atmosphere [1].

In terms of the refractive index n, the wave equation can be expressed in the form:

$$\nabla^2 E(r) + k_0{}^2 n^2 E(r) - 2\nabla(\frac{\nabla n}{n} \bullet E) = 0 \qquad (2.20)$$

Where, $E(r)$ is the electric field vector, $k_0=2\pi/\lambda$ the free-space wave number, and $n(r)$ the refractive index. The last term of equation (2.20) can be neglected as long as the wavelength λ is much smaller than the scale size l_0 of the random medium. We note that neglecting the last term in equation (2.20) will automatically neglect any cross-polarisation effects [8].

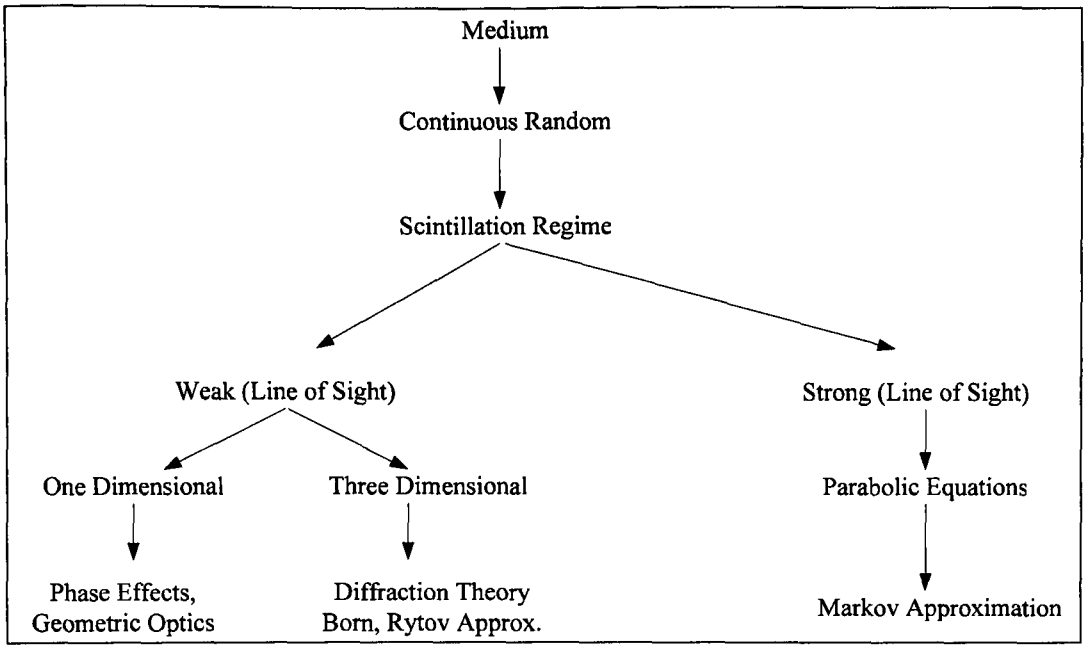

Figure 2.3. Electromagnetic propagation theories for line-of-sight propagation in random continuous medium.

Considering wave propagation in the direction of the x axis, the y component of the electric field $U(r) = E_r(r)$ satisfies:

$$(\nabla^2 + k_0^2 n^2)U(r) = 0 \tag{2.21}$$

The index of refraction n fluctuates about the average value $\langle n \rangle$, and thus using the wave number for the average $k^2 = k_0^2 \langle n \rangle^2$, we can write the wave scalar equation:

$$[\nabla^2 + k^2(1+n_1)^2]U(r) = 0 \tag{2.22}$$

Where n_1 represents the fluctuation of the index of refraction.

For weak fluctuation, it is necessary to obtain an approximate solution of equation (2.22) for small n_1. There are three methods used to solve equation (2.22),

a) Geometrical optics,
b) Born Approximation: In the scalar wave equation (2.22), U is expanded in a series $U = U_0 + U_1 + U_2 + \ldots$, and
c) Rytov Approximation: This time U is expanded in a series of the form $U = \exp(\psi_0 + \psi_1 + \psi_2 + \ldots)$.

They all have as a condition that the wavelength λ be much smaller than the inner scale of turbulence l_0.

If the width of the scattering cone $\lambda L / l_0$ is much larger than l_0, the receiver 'sees' many eddies, and diffraction effects become important. In this case geometric optics cannot be used. Instead, applying Born or Rytov approximations to the scalar wave equation can include these effects. However, the geometrical optics approach is still useful to describe phase fluctuations at microwave frequencies even though the restriction $L << l_0^2/\lambda$ may not be valid. This is because the spectral content of the refractive index fluctuations is small for large wave numbers i.e., small eddy sizes. Thus, diffraction effects from these eddies will be small.

Rytov first solution is extensively used in weak fluctuation theory and can be written as:

$$U(r) = \exp(\psi_0 + \psi_{10}) = U_0(r)\exp(\psi_{10}(r)) \tag{2.23}$$

where the complex phase ψ, has real and imaginary components, given by

$ln(A/A_0) = Re_{\psi}$ (log-amplitude fluctuations (χ))
$\phi = Im\ \psi$ (phase fluctuations)

However, for $|\chi| << 1$, χ is approximately equal to $(A-A_0)/A_0$.

Using Rytov approximation and assuming a homogeneous, isotropic turbulence, Tatarskii [5] obtained the variance of the log-amplitude and phase fluctuations in terms of the three-dimensional wave number spectrum.

Ishimaru [1] carried the work of Tatarskii further, and after lengthy calculations derived an expression for the correlation function $B(L,\rho)$ in terms of the spectral density $\phi_n(\kappa)$ of the refractive index fluctuations for a plane wave propagating through turbulent medium. This expression has the general form:

$$B(L,\rho) = \int_0^L d\eta \int_0^\infty \kappa \, d\kappa F(\eta,\kappa,\rho)\phi_n(\kappa) \tag{2.24}$$

Where κ is the spatial wave number, η is the distance along the propagation path, ρ is the distance in the plane of observation transverse to the direction of propagation, L is the extent of the turbulent medium in which the receiver is located, and the function $F(\eta,\kappa,\rho)$ is called a filter function as it plays the role of filtering a certain portion of the spectrum ϕ_n to produce the correlation function B. The spectral density of the index of refraction fluctuation $\phi_n(\kappa)$ in this expression is evaluated at the location η, and it may vary along the path of wave propagation.

However, if ϕ_n does not depend on the location η the filter function for the log-amplitude fluctuations is given by [1]:

$$f_x(\kappa) = 1 - \frac{\sin(\kappa^2 L/k)}{\kappa^2 L/k} \tag{2.25}$$

For the phase fluctuations,

$$f_s(\kappa) = 1 + \frac{\sin(\kappa^2 L/k)}{\kappa^2 L/k} \tag{2.26}$$

For the case of constant turbulence along the path, the amplitude fluctuations are affected mostly by eddies with dimensions smaller than or equal to the Fresnel zone radius $\sqrt{\lambda L}$. For locally homogenous turbulence, modelled by the Kolmogorov spectrum it can hence be shown that the variance of the log-amplitude fluctuation, σ_x^2 is given by [1]:

$$\sigma_x^2 = B_x(L,0) = 0.307 C_n^2 \kappa^{7/6} L^{11/6} \tag{2.27}$$

with the condition that $l_0 << \sqrt{\lambda L} << L_0$ (diffraction region).

2.7. Temporal Frequency Spectra of the log-amplitude Fluctuation

So far we have assumed that the refractive index fluctuation is a random function of position only and independent of time. However, atmospheric turbulence is in a constant motion and, therefore, a wave in the turbulence fluctuates with time. A statistical description of the temporal wave fluctuations in a moving random medium may be given in terms of the temporal correlation function.

In order to relate the temporal to the spatial variations one must apply Taylor's 'Frozen Turbulence' hypothesis [1], [9]. This considers the turbulent medium as being 'frozen' and is transported by the wind without changing its detailed variations. This hypothesis is valid in most atmospheric turbulence and mathematically we can write

$$n_1(r,t) = n_1(r - Vt, 0) \tag{2.28}$$

Where, V is the wind velocity, expressed as the sum of the average wind velocity U and the velocity fluctuations V_f. When the average wind velocity U_t is transverse to the direction of the wave propagation and the fluctuating component V_f is negligible compared with U_t, the correspondence between temporal and spatial correlation functions is obtained by simply replacing r by $(r - U_t t)$. The temporal correlation function is therefore given by:

$$B_x(L,\tau) = 2\pi^2 k^2 L \int_0^\infty \kappa \, d\kappa \, J_0(\kappa U_t \tau) f_x(\kappa) \phi_n(\kappa) \tag{2.29}$$

The temporal frequency spectrum $W_x(\omega)$ is the Fourier transform of the correlation function (2.29) and after carrying out some calculations and simplifications Ishimaru [1] derived the asymptotic form of the spectrum of amplitude fluctuations of a wave travelling in a random medium.

When $\omega < \omega_t$, $W_x(\omega)$ is practically constant, but when $\omega > \omega_t$, $W_x(\omega)$ decays as $\omega^{-8/3}$. The two asymptotic values are given by:

$$W_x^{\,0}(\omega) = 2.765\frac{\sigma_x^{\,2}}{\omega_t} \qquad (\text{as } \omega \to 0) \qquad (2.30)$$

$$W_x^{\,\infty}(\omega) = 7.13\frac{\sigma_x^{\,2}}{\omega_t}\left(\frac{\omega}{\omega_t}\right)^{-8/3} \qquad (\text{as } \omega \to \infty) \qquad (2.31)$$

Where σ_x^2 is the variance of the log-amplitude fluctuations and is given by equation (2.19). The two asymptotes meet at the corner frequency $\omega = 1.43\omega_t$, where ω_t is known as the Fresnel frequency and is given by $U_t\sqrt{k/L}$, where U_t is the transverse wind speed. The departure of the actual spectrum from the asymptotes indicates the effects of the outer and inner scales of turbulence.

2.8. Influence of Antenna Aperture

The intensity fluctuations (square root of the variance) discussed in the preceding section are those observed by a point receiver. If the receiver has a finite size, the fluctuations are averaged over the receiving aperture and the fluctuations will be reduced. This phenomenon is called aperture averaging.

An antenna with finite aperture applies a low-pass filtering to the amplitude fluctuations of a wave. This low-pass filtering or averaging effect becomes significant when the transverse correlation length of the amplitude fluctuations is smaller than the antenna diameter. Therefore, if the antenna diameter is large enough, the incident wave-front fluctuations become uncorrelated and the receiver output is a spatial average of the wave-front fluctuations over the aperture. The result of this is that the observed fluctuations are smaller than those expected for a point receiver. If the effective antenna diameter is less than the correlation length, the antenna acts as a point receiver. The effective antenna aperture is the product of the physical antenna aperture and the efficiency of the antenna.

Haddon and Vilar [10] normalising the scintillation variance for a receiving antenna with effective diameter D to the point receiver, for the special case of n=11/3, found that a finite antenna aperture reduces the intensity fluctuations from its point receiver value by a factor:

$$g_x = \left[\frac{\sigma_x^{\,2}(D)}{\sigma_x^{\,2}(O)}\right]^{1/2}$$

$$= \left[3.86(x^2+1)^{11/12}\sin\left(\left(\frac{11}{6}\right)\arctan\left(\frac{1}{x}\right)\right) - 7.08x^{5/6}\right]^{1/2} \qquad (2.32)$$

where

$$x = 0.0584\, k \frac{(D\eta)^2}{L} \tag{2.33}$$

D is the physical diameter of the antenna of illumination efficiency η, $k=2\pi/\lambda$ is the wave number, λ is the signal wavelength and $L = 2h/\left\{\sqrt{\left[\sin^2\theta + (2h/R_e)\right]} + \sin\theta\right\}$ is the turbulent path length, h is the height of turbulence, θ is the path elevation angle and R_e is the effective Earth radius (=8.5x10^{6}m).

2.9. Tropospheric Scintillation Characteristic

2.9.1 Propagation Research

In this section a short survey of previous research into tropospheric amplitude scintillation will be presented. Further details are discussed in the relevant sections of this thesis.

Propagation experiments are important in the design of satellite communication systems. Satellite systems rely on the transmission of radiowaves to and from the satellite and are dependent on the propagation characteristics of the transmission path, primarily the Earth's atmosphere. Radiowave propagation thus plays a very important part in the design and ultimate performance of these systems. Propagation experiments started as early as the first communications satellites were in orbit, to describe how these propagation phenomena affect the design and performance of those systems. Initially operations were at C-band (6/4 GHz) and no significant propagation induced outages were observed. In this frequency band ionospheric effects are the main degradation factors. In late 1969 severe amplitude scintillation activity at C-band induced by ionospheric effects was reported [11].

In recent years the rapid growth in capacity requirements led to the introduction of higher frequency bands. The higher frequencies offer various advantages such as, increased

bandwidth, smaller antennas, and smaller satellite footprint that give higher EIRP and permit frequency reuse. The main obstacle however is that they are subject to stronger propagation degradation. The small size antennas employed in VSAT and USAT systems significantly reduce the cost of earth station terminals and also eliminate tracking requirements, but they lose the mitigating effect of aperture averaging and hence experience stronger scintillation [12].

In general, the impact of rain attenuation on communication signals is predominant. Results obtained from the analysis of rain attenuation in the United Kingdom and Italy showed that at V-band the attenuation levels exceeds 20dB for 0.1% of the time [13], [14]. In typical European mid-latitude climates for links operating at >20GHz it is difficult to include fade margins of more than approximately 10dB in typical down-link budgets for broadcast systems. Based on these statistics, the implementation of fade countermeasure techniques is vital in order to compensate for the high levels of dynamic fading.

The need to improve the skills and knowledge in prediction of such propagation effects fostered the realisation of some important propagation experiments like OLYMPUS, ACTS and ITALSAT. These experiments have been conceived with the aim of assessing the effects of atmosphere in radio link at various frequencies, elevation angles, antenna diameters and meteorological conditions.

The effects of scintillation on low elevation angle, Ku-band links were measured in two long-term experiments by INTELSAT in the United Kingdom [15] and United States [16]. The data showed that on links with elevation angles below 10°, not only was tropospheric scintillation a significant limitation to performance but also when the link approached 5° in elevation angle, it would cause the signal to drop below the availability threshold.

Vilar and Larsen [15] analysed and compared the cumulative distribution, variance and spectral density of non-skewed amplitude scintillations measured at three sites during the four summers 1982-85 and combining elevations θ = 5°, 7.2°, 8.9° and 31°. They concluded that at low elevation, amplitude scintillations are slow but large in amplitude.

Their results show that the lower the elevation the higher the amplitude scintillations. In Japan Karasawa *et al.* [17] reported peak-to-peak signal level variations in excess of 10dB. The results were based on the analysis of satellite beacon data in the 14/11 GHz band, at a path elevation angle of 6.5^0 using Cassegrain antenna of diameter 7.6m.

Measurements of tropospheric scintillation on a 14-degree path at 12, 20 and 30 GHz are reported in [16]. The observed scintillation spectra were consistent with Tatarskis theory showing high frequency slopes between –8/3 and –11/3, with most of the power below 1 Hz. Measured probability densities and cumulative distributions of scintillation intensity agreed with the Moulsley-Vilar model [17]. It is also shown that as the season shifts from winter to summer, there is an increase of the monthly average of scintillation intensity. The spring and summer scintillation on the contrary show a strong diurnal trend with maximum scintillations occurring in the afternoon between local times 13:00 and 15:00. Scintillation intensity on a monthly basis is strongly correlated to the ground temperature and humidity. The authors reported correlation coefficients at 12, 20 and 30 GHz of 0.841, 0.835, 0.789 and –0.880, -0.870, -0.827 respectively. According to measurements reported in [18] and [19], scintillations show a marked seasonal dependence, reaching a maximum in August and minimum in February in northern middle latitude regions such as Japan.

In [17] the diurnal and seasonal variations, frequency dependence derived from a comparison of the 11 and 14 GHz signals, and elevation angle dependence of the scintillation data are presented. A comparison between the propagation data and ground-level meteorological measurements indicated a high correlation between the scintillation characteristics and the water vapour contribution to the radio refractive index inferred from local humidity and temperature data. The authors concluded that this suggests a method for predicting the severity of scintillation fading using local measurements of meteorological parameters. Their analysis on the distribution of scintillation shows that over short periods of about an hour, the probability density function of signal level variations in dB due to scintillation follows the normal distribution well. Over longer periods, such as one month, the standard deviations calculated every hour can be approximated by the gamma distribution.

Otung and Evans [18] found that during strong scintillations, the short-term distribution significantly departs from Gaussian. The mean probability that 1-min distribution of scintillation amplitude is Gaussian falls sharply as scintillation becomes more intense and for intensities greater than 0.5dB the probability is less than 5%, and there is a trend of increased negative skewness of the short-term pdf. Van de Kamp showed that the observed asymmetry follows directly from theory, if a different modeling approach is applied [19].

Banjo and Vilar [4] using experimental results measured on a 7.1° elevation, 11 GHz path and certain meteorological parameters measured at ground level, found a strong dependence of scintillation intensity on temperature but a weaker correlation with relative humidity and wind speed, and no correlation at all with barometric pressure.

Increase in attenuation caused by specific cloud types over the U.K. has been reported by Wrench *et. Al.* [20]. Their analysis of the 40 and 50GHz beacon signal measurements together with inputs from a suite of zenith pointing measurements at Chilbolton, U.K. (including, radiometers, lidar ceilometer, and a digital camera) found that in the absence of rain, the largest slant path 50GHz attenuation of up to 14 dB is caused by deep convective (Cb) cloud, which gives rise to attenuation greater than 6 dB for 1% of the time that it is present.

These results may be expected to be approximately valid for other locations, although slightly larger attenuation may occur in tropical latitudes because of greater liquid water content (LWC).

It appears that irregularities in temperature, humidity and pressure are not the only cause of scintillation. Low cumulus cloud is also associated with the turbulent activity that causes scintillations at millimeter wavelengths [21], and this is responsible for a part of the measured scintillation effects. The average diurnal variation of scintillation intensity is uncorrelated with N_{wet}, and strongly correlated with cumulus cloud cover [22].

The influence of antenna aperture was studied theoretically by Von Weert [22] and Haddon and Vilar [11]. In [11] an analytical solution to the problem is given. They

showed that because the scintillation intensity depends on the ratio between the antenna diameter and the diameter of the Fresnel zone in the turbulent region, low elevation paths counteract the tendency to smoothing by large earth station antennas and the scintillations observed remain large.

By combining theoretical relations and experimentally observed dependencies, several semi-empirical models have been developed for the prediction of tropospheric scintillation [23-26]. The ITU-R [27] presented a prediction method for the calculation of the standard deviation of signal fluctuations due to scintillation. This model is very similar to the Karasawa model [28], being based on formulation technique employed in the Karasawa model. Van de Kamp *et. al.* [29] compares the Karasawa and ITU-R model with measurements at 19.8 GHz on a 12.7° elevation path in Kirkkonummi, Finland. Both models predict higher scintillation variance than the measured. They then proposed a new prediction model that incorporates a new parameter representing the average water content of heavy clouds [30].

The general characteristics of tropospheric scintillation are summarised and presented here. These characteristics are identified in the turbulence theory and also from a world-wide data base of long-term measurements [31].

2.10. General characteristics of tropospheric scintillation

2.10.1 Meteorological Dependence

(a) High temperature and humidity give the greatest scintillation amplitudes for a given path. Scintillation amplitude fluctuations are about three times more severe in summer than in winter. Thus a fairly large seasonal variation exists [31, 32].

(b) Very weak correlation of scintillation intensity with wind reported in [4, 33]. Cross-path wind speed is correlated with the spectrum corner frequency.

(c) Presence of rain does not significantly affect the amplitude of the scintillation until the path attenuation exceeds about 5 dB. The low frequency end of the spectra is modified by rain but the corner frequency roll-off remains essentially unchanged [31].

2.10.2 Geographic Dependence

As there is a significant correlation of scintillation with temperature and humidity, there is therefore a dependence on latitude. The higher the latitude, the colder is the average temperature of the atmosphere and so the lower the amplitude of scintillation over a given path will be. For a given latitude, there does not appear to be a longitudinal dependence.

2.10.3 Frequency Dependence

(a) The frequency dependence of amplitude scintillation is approximately the ratio of the frequency raised to the power 7/12. This was derived from Kolmogorov spectrum.

(b) The rate of change of amplitude is slower than that for ionospheric scintillation, the corner frequency is lower, and the roll-off is less steep. The power spectra rolls off as $f^{-8/3}$, generally independent of the elevation angle and frequency. The corner frequency and the rate of change of amplitude vary with elevation angle [31].

2.10.4 Systematic Dependence

As the elevation angle goes down for a given location [31]:

(a) Scintillation amplitude increases on the average.

(b) Period of the scintillation increases.

(c) Corner frequency of the spectrum decreases.

(d) There is an increasing tendency for non-symmetrical scintillation distribution

As the antenna diameter decreases for a given path

(a) Scintillation amplitude increases, due to the reduced averaging effect of the spatial fluctuations of the wave.

(b) Probability of multipath increases.

In Chapter 3 analysis of scintillation data from a beacon is presented and the distribution of scintillation amplitude is investigated, along with other statistics to see the effects of meteorological and link parameters on scintillation amplitudes.

2.11. Conclusion

A brief presentation of turbulence theory has been given and it was noted that turbulence is well developed only in the inertial sub-range where the Kolmogorov spectrum holds. In this region the medium is assumed to be statistically homogeneous and isotropic. Tatarskii [5] obtained an expression for the variance of amplitude fluctuations while Ishimaru [1] expressed the generalised spectrum in asymptotic form using Taylor's frozen-in hypothesis. These two regions of the spectrum meet at a corner frequency that depends on the cross-path wind velocity. A brief summary of the dependence of scintillation on various link and meteorological parameters was also presented.

References

[1] A. Ishimaru, *Wave Propagation and Scattering in Random Media*: IEEE Press, 1997.

[2] M. Pidwirny, "The Layered Atmosphere," www.physicalgeography.net/fundementals, 2004.

[3] O. P. Banjo and E. Vilar, "Measurement and modelling of amplitude scintillations on low-elevation earth-space paths and impact on communication systems," *IEEE Transactions on Communications*, vol. COM-34, pp. 774-780, 1986.

[4] O. P. Banjo and E. Vilar, "The dependence of slant path amplitude scintillations on various meteorological parameters," presented at International Conference on ANtennas and Propagation (ICAP 87), 1987.

[5] V. I. Tatarskii, *Wave Propagation in a Turbulent Medium*: New York, Dover, 1961.

[6] J. Haddon, "A study of microwave scintillations on a satellite down-link at X-band," Portsmouth Polytechnic, 1982.

[7] R. L. Fante, "Electromagnetic beam propagation in turbulent media: an update," *Proceedings of IEEE*, vol. 68, pp. 1424-1443, 1980.

[8] J. W. Strohbehn, "Line-of-Sight Wave Propagation though the Turbulent Atmosphere," *Proceedings of IEEE*, vol. 56, 1968.

[9] G. Brussaard and P. A. Watson, *Atmospheric Modelling and Millimetre Wave Propagation*. London: Chapman & Hall, 1995.

[10] J. Haddon and E. Vilar, "Scattering induced microwave scintillations from clear air and rain on earth space paths and the influence of antenna aperture," *IEEE Transactions on Antennas and Propagation*, vol. 34, pp. 646-657, 1986.

[11] J. E. Allnut, "INTELSAT Propagation Experiments: The Focus and Results of Recent Campaigns," *Proceedings of the IEE*, vol. 81, pp. 856-864, 1993.

[12] I. E. Otung, "Accurate prediction of scintillation degradation applicable to satellite communication system design," University of Glamorgan 1998.

[13] S. A. C. a. C. L. W. S. Ventouras, "Results and Implications from ITALSAT Propagation Experiment Measurements at the CCLRC-Chilbolton Observatory," presented at Internation Conference on Antennas and Propagation (ICAP2003), UK, 2003.

[14] R. Polonio and C. Riva, "ITALSAT Propagation Experiment at 18.7, 39.6 and 49.5 GHz at Spino D'Adda: Three Years of CPA Statistics," *IEEE Transactions on Antennas and Propagation*, vol. 46, pp. 631-635, 1998.

[15] E. C. Johnston, "Results on low-elevation anle 11GHz Satellite Beacon Measurements at Goonhilly," ibidem 1993.

[16] W. J. Vogel, "Estimating Satellite Beacon Attenuation From Radiometer data: Error Statistics Based on Two years Low Elevation Angle Measurements at 11.2GHz," ibidim 1991.

[17] K. Y. a. M. Y. Y. Karasawa, "Tropospheric Scintillation in the 14/11-GHz Bands on Earth-Space Paths with Low Elevation Angles," *IEEE Transactions on Antennas and Propagation*, vol. 36, pp. 563-569, 1988.

[18] I. E. Otung and B. G. Evans, "Short-Term Distribution of Amplitude Scintillation on a Satellite Link," *Electronics Letters*, vol. 31, pp. 1328-1329, 1995.

[19] M. M. J. L. V. d. Kamp, "Asymmetric Signal Level Distribution due to Tropospheric Scintillation," *Electronics Letters*, vol. 34, pp. 1145-1146, 1998.

[20] P. M. S. C. L. Wrench, A. J. Gibson and O. T. Davies, "Statistics of liquid water path in cloud, and slant path propagation loss in cloud at V-Band, based on measurements at Chilbolton," presented at International Conference on Antennas and Propagation (ICAP 03), UK, 2003.

[21] H. W. A. D. C. Cox, and H. H. Hoffman, "Observations of cloud-produced amplitude scintillation on 19- and 28-GHz earth-space path," *Radio Science*, vol. 16, pp. 885-907, 1981.

[22] M. M. J. L. V. d. K. J. K. Tervonen, and E. T. Salonen, "Prediction Model for the Diurnal Behaviour of the Tropospheric Scintillation Variance," vol. 46, pp. 1372-1378, 1998.

[23] ITU-R, "P.618-7 Propagation data and prediction methods required for the design of Earth-space telecommunication systems," Recommendations and Reports of the ITU-R 1997.

[24] Y. Karasawa, M. Yamada, and J. E. Allnutt, "A New Prediction Method for Tropospheric Scintillation on Earth-Space Paths," *IEEE Transactions on Antennas and Propagation*, vol. 36, pp. 1608-1614, 1988.

[25] I. E. Otung, "Prediction of Tropospheric Amplitude Scintillation on a Satellite Link," *IEEE Transactions on Antennas and Propagation*, vol. 44, pp. 1600-1608, 1996.

[26] M. M. J. L. V. d. Kamp, J. K. Tervonen, E. T. Salonen, and J. P. V. Baptista, "Improved Models for Long-Term Prediction of Tropospheric Scintillation on Slant Paths," *IEEE Transactions on Antennas and Propagation*, vol. 47, pp. 249-260, 1999.

[27] I.-R. P.618-7, "Propagation data and prediction methods required for the design of Earth-space telecommunication systems," Recommendations and Reports of the ITU-R 2001.

[28] M. Y. Y. Karasawa, J. E. Allnutt, "A New Prediction Method for Tropospheric Scintillation on Earth-Space Paths," *IEEE Transactions on Antennas and Propagation*, vol. 36, pp. 1608-1614, 1988.

[29] J. K. T. M.M.J.L. Van de Kamp, E.T. Salonen and J.P.V. Baptista, "Scintillation Prediction Models Compared to Measurements on Time Base of Several Days," *Electronics Letters*, vol. 32, 1996.

[30] J. K. T. M.M.J.L. Van de Kamp, E.T. Salonen and J.P.V. Baptista, "Improved Models for Long-Term Prediction of Tropospheric Scintillation on Slant Paths," *IEEE Transactions on Antennas and Propagation*, vol. 47, pp. 249-260, 1999.

[31] J. E. Allnutt, *Satellite-to-Ground Radiowave Propagation*. London: Peregrinus Ltd., 1989.

[32] Y. Karasawa, K. Yasukawa, and M. Yamada, "Tropospheric Scintillation in the 14/11-GHz Bands on Earth-Space Paths with Low Elevation Angles," *IEEE Transactions on Antennas and Propagation*, vol. 36, pp. 563-569, 1988.

[33] A. Savvaris, C. N. Kassianides, and I. E. Otung, "Observed Effects of Wind on the Spectrum and Intensity of Scintillation," presented at International Conference on Antennas and Propagation (ICAP 2001), Manchester, UK, 2001.

CHAPTER III

Receiver System and Data Preprocessing

Summary – *This chapter will cover the receiver system located at Sparsholt were the satellite beacon data were recorded. The measurement setup is described, together with the measured data sets, and the additional information which is used in the project: local and global meteorological data. The data preprocessing procedures are described as well as the resulting data sets which were used in the analysis.*

3.1. Introduction

3.1.1 ITALSAT F1 Satellite

The scintillation analysis carried out in this project was performed using beacon measurements received from the ITALSAT satellite. An artist's impression of the ITALSAT satellite is shown in Figure 3.1. ITALSAT F1 is Italy's first operational communications satellite launched on the 16th of January 1991 by an Ariane booster and stationed in geostationary orbit at 13.2 degrees East and has been maintained at this position within $\pm 0.15^0$ box as seen from the Earth's centre.

Developed by a contractor team led by Alenia Spazio, ITALSAT carries ten active transponders plus five spares for 30/20 GHz and 50/40 GHz links with a capacity of 12,000 telephone circuits. The propagation package includes a telemetry-modulated 20 GHz beacon (also used for tracking), a 40 GHz beacon phase modulated by a 505 MHz coherent subcarrier, and a polarisation-switched (but otherwise unmodulated) 50 GHz beacon. It supports attenuation and cross-polarisation measurements at 20, 40, and 50 GHz, as well as new measurements of phase and amplitude dispersion. The availability of a polarisation-switched signal enables earth stations to fully characterise the cross-polarisation matrix of the 50 GHz channel [1].

The exact propagation beacon frequencies are 18.7, 39.6 and 49.49 GHz; they will hereafter be referred to in this thesis as the 20, 40 and 50 GHz beacons, respectively. The 50 GHz beacon signal is switched between vertical and horizontal polarisation at a rate of 933 Hz, had a specified EIRP of 26.8 dBW, after five years of operation.

The 40 GHz beacon, which is fully redundant, consists of an exciter and an impatt amplifier. The beacon is fed by a low-level S-band signal, provided by the L.O. The input signal, after being multiplied by 4 goes to the exciter. The later is fed also by 505 MHz tone coming from the L.O. and provides 1/4 radian peak phase modulation of the input signal. After modulation, this frequency is again multiplied by 4 giving rise to a 40 GHz signal with 1-rad peak phase modulation. This signal is fed to an injection locked impatt amplifier providing final amplification with minimum spectrum distortion of the composite signal.

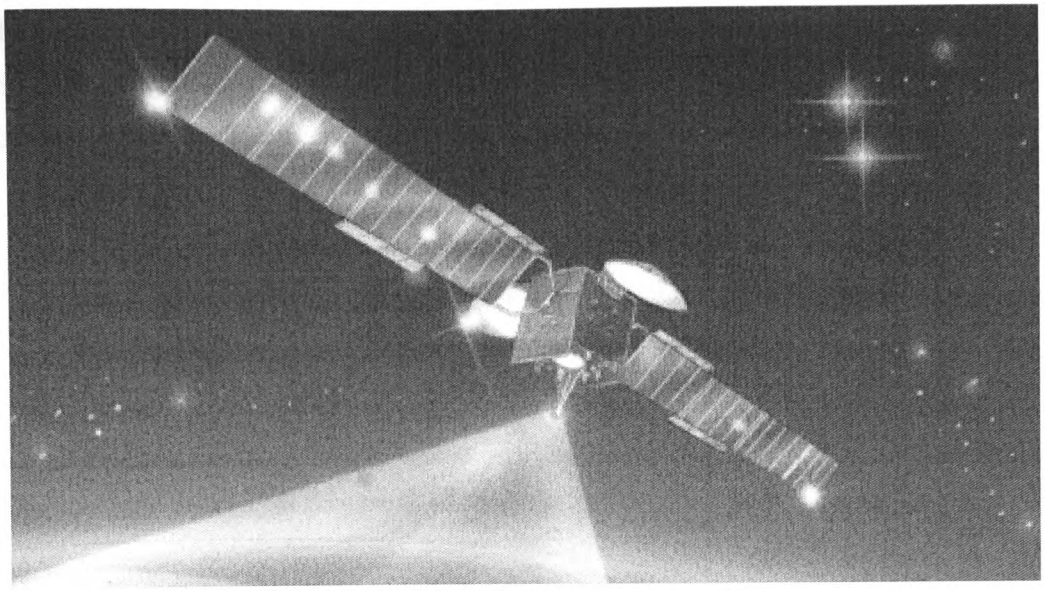

Figure 3.1 Artistic impression of the ITALSAT satellite

Figure 3.2 Sparsholt location

The modulated signal is radiated by a circular beam antenna with the required polarisation characteristics. The beacon is continuously transmitted with the exception of eclipse periods. The average EIRP values of the central 40 GHz beacon are:

30.0 dBW	Edge of coverage, no subcarrier modulation
28.0 dBW	Edge of coverage, with subcarrier modulation

The coverage area (3 dB footprint) of the three beacons includes most of the UK.

3.1.2 ITALSAT F2 Satellite

ITALSAT F2 is an experimental communications satellite also built by Alenia Spazio for ASI, the Italian Space Agency. It was launched in August 1996 by an Ariane IV booster and placed in a geostationary orbit at 16.4 degrees east (initially foreseen at 10.2 degrees east). ITALSAT F2 has an operational life expectancy of 7 years and is similar to the first model. Apart from the European Mobile Systems (EMS) package which replaces the 40/50GHz propagation package carried by ITALSAT F1, most of the other packages are duplicates of their counterparts on F1. ITALSAT F2 antenna provides a single, 46 dBW EIRP fixed beam that covers Europe, part of Russia, and North Africa.

The EMS is a high-performance communications payload for the provision of a variety of L-band satellite services principally to mobile users throughout Europe and northern Africa. It allows users with small portable terminals, as well as those with vehicle-mounted terminals, to have access to communications at very reasonable costs.

3.2. Receiver System

The receiver system shown in Figures 3.4 and 3.5, is located at Sparsholt (51.5850° N, 1.5033° W), U.K. The location of Sparsholt was shown on the map in Figure 3.2. The principal system parameters are summarised in Table 3.1, further details can be found in [2]. The system comprises of:

1) Three earth-station receiving Cassegrain antennas of diameter 1.22m for the 18.68 GHz and 0.61m for the 39.59 GHz and 49.49 GHz, from where ITALSAT was viewed at an elevation angle of 29.9°,
2) Meteorological instruments (temperature, pressure and humidity sensors. Rapid response rain gauge and an impact distrometer),
3) Data logging and storage equipment.

Regular sampling and recording of all the receivers and meteorological parameters is carried-out at a sampling rate of 1 Hz. However a number of enhancements were made to receiver system during 1997. A modification to the IF section of the 49.49 GHz beacon receiver has meant that it was possible to sample the output at up to 10 Hz; this procedure was performed for periods of 5 minutes every 30 minutes. These extra measurements were first collected in December 1997 [3].

The satellite beacon receiving system comprises a 0.61-metre Cassegrain antenna (1.22-metre for the 20GHz) feeding into a polarisation switch to allow selection of either vertical or horizontal polarisation (only in the 50GHz receiver). Then through single balanced mixer with a noise figure of 6 dB, in which the received signal is down-converted to a frequency of 70MHz. The local oscillator (LO) consists of a VHF crystal source which phase locks to an X-band generator (103MHz), which is then multiplied to 49.42 GHz by a times-four multiplier. The IF signal is then amplified and filtered, before final detection by a conventional phase-lock loop beacon receiver. The received signal level achieved with this simple system is 34 dB above the noise level in clear sky conditions and quite adequate for observing significant propagation effects. A block diagram of the 50GHz receiver is shown in

Figure 3.3. The 70MHz receiver output is a D.C. voltage proportional to the logarithm of the received signal level.

Table 3.1 Main System Parameters

Satellite			
Name	ITALSAT F2	ITALSAT F1	ITALSAT F1
Position	Geostationary, 13.2^0 East	Geostationary, 13.2^0 East	Geostationary, 13.2^0 East
Earth Station			
Location	Sparsholt, UK (51.585^0 N, 1.5033^0 W)	Sparsholt, UK (51.585^0 N, 1.5033^0 W)	Sparsholt, UK (51.585^0 N, 1.5033^0 W)
Frequency	18.69GHz	39.59GHz	49.49GHz
Intermediate Frequencies	70MHz, 10.7MHz	70MHz, 10.7MHz	70MHz, 10.7MHz
Antenna Diameter	1.22m	0.61m	0.61m
Antenna Gain	45.6932 dBi	46.1896 dBi	48.1261 dBi
Elevation Angle	29.9^0	29.9^0	29.9^0
EIRP	61 dBm	61 dBm	56.8 dBm
Free Space Loss	209.6133 dB	216.1303 dB	218.0668 dB
Gaseous absorption	0.8554 dB	1.5735 dB	4.2755 dB
Rain Rate for 0.01%	28 mm/h	28 mm/h	28 mm/h
Rain Attenuation for 0.01%	12.4 dB	34.7 dB	43.2 dB
System Noise Temperature	≈ -197.4 dBW/Hz	≈ -197.4 dBW/Hz	≈ -197.4 dBW/Hz
Detectors	Complex demodulator (I and Q outputs) and logarithmic amplifier	Complex demodulator (I and Q outputs) and logarithmic amplifier	Complex demodulator (I and Q outputs) and logarithmic amplifier

The 20 GHz dish is mounted outside, on top of the hut and then routed to the data-logging system inside the hut via a cable. The 40 and 50 GHz earth station receiver systems and the data logging units are housed inside the temperature-controlled hut, as shown in Figures 3.4 and 3.5. The system is temperature controlled to 20^0C; the gross weight of the 40 and 50GHz receiver systems is approximately 20 kg each. The accuracy of the measured attenuation is about ± 0.5 dB [4].

The design life for the ITALSAT vehicle originally was only five years, but ITALSAT F1 operated beyond its expected life and remained in orbit for an additional ~ 5 years. To extend the beacons transmission time, a propellant saving option had been adopted in which the North/South station keeping was abandoned. As a consequence a need for the beacon receivers to track the satellite position became apparent during the year and towards the end of 1997, the 50 GHz beacon receiver at Sparsholt was equipped with a tracking unit to counter the problem. The same goal was attained for the 40 GHz receiver in August 1998.

The next section will cover the data preprocessing and the problems encountered with the 20 GHz receiver.

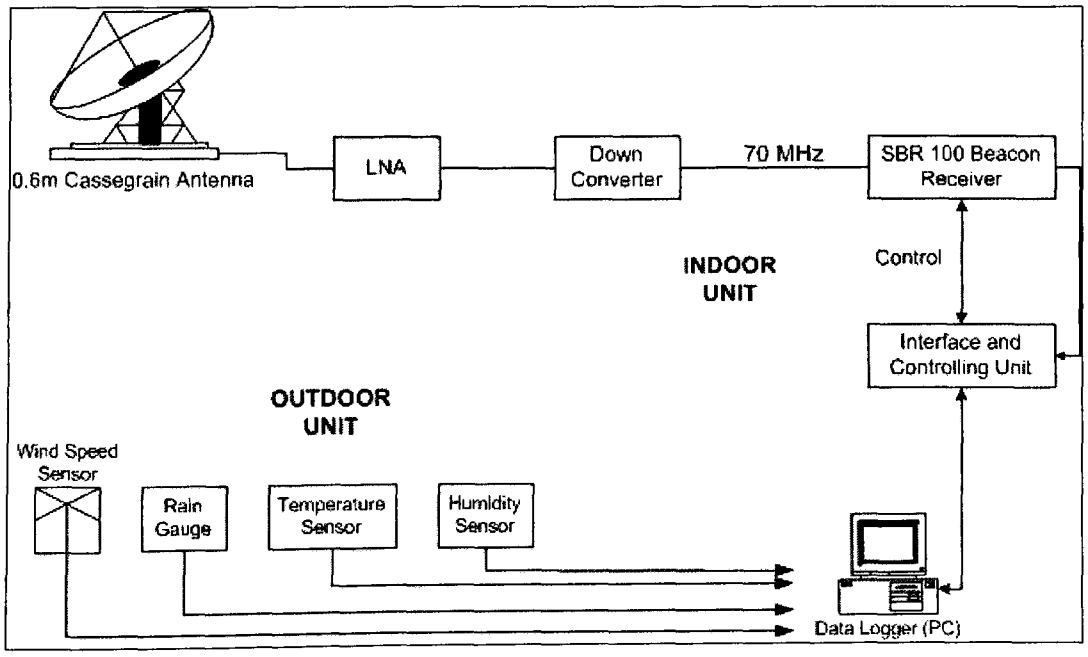

Figure 3.3 Block diagram of ITALSAT receiver at 50 GHz

Figure 3.4 The hut at Sparsholt were the receiving antennas have been installed along with the data logging system.

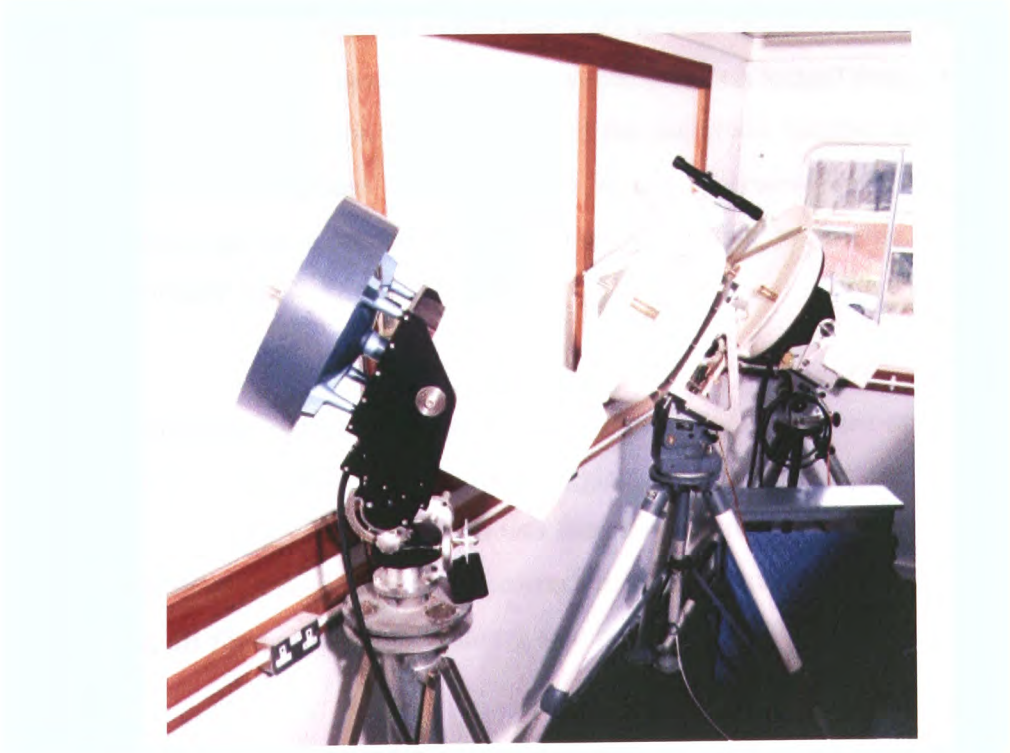

Figure 3.5 From left to right, the 51GHz radiometer, the 50GHz receiver and the 40GHz receiver.

3.3. Data Preprocessing

Before the scintillation data could be involved in any data analysis process, irrecoverably corrupted data had to be removed. Originally data preprocessing were to be performed for the period from June 1996 to May 1999, on the ITALSAT F1 satellite beacon at frequencies 18.68GHz, 39.59GHz and 49.49GHz recorded at Sparsholt. Unfortunately the 18.68GHz beacon data are not useful for the period after March 1998, due to satellite movements. Originally the satellite was designed to remain in orbit for five to six years. In order to extend its life, energy savings had to be made. As a result the satellite was not completely stationary anymore but had a north-south movement. In August 1999, the 18.7 GHz receiver was switched to monitor the beacon on ITALSAT F2. To account for this loss in data, preprocessing of ITALSAT F2 18.7 GHz beacon was also carried out, for the period from September 1999 to August 2000.

A painstaking visual inspection of plotted raw data at each frequency was crucial to identify and exclude clearly unrealistic sample values and data logged during receiver system downtime. This section covers details of the important features noted in the three-year data during visual inspection and shows representative plots of the scintillation time series extracted from the raw data using a filtering technique discussed elsewhere [5].

The raw propagation data along with relevant meteorological variables had been saved in daily binary files by the data logging system used at the Sparsholt measurement site. A MATLAB program was therefore written to read these files and calibrate each data channel to give the correct measured quantity, such as relative signal level in dB for a propagation channel, rain rate in mm/hr for a rain channel, and so on.

The resulting daily time series of the received signal level of each beacon frequency was plotted and subjected to a careful visual inspection in order to identify gaps and periods of non-genuine signal level, see Figure 3.6. The indices of these gaps (if any)

were stored in a separate file. Each propagation data sample within such invalid periods is replaced by the standard value –9999. In this way non-genuine samples are clearly marked so that they can be subsequently excluded from data analysis without losing the time reference inherent in the index of the vector variable containing the samples of each channel over a one-day period [6].

Finally the data were passed through a high-pass Butterworth filter with a cut-off frequency of 0.04 Hz [5] to extract scintillations, which were then saved in one file for each day. The choice of the high-pass filter cut-off frequency was made such that all non-scintillation effects were excluded and only legitimate scintillation contributions were included. Figure 3.6 illustrates the raw data before and in Figure 3.7 after being filtered to extract scintillation and invalid data being excluded. It can be seen that the observed scintillation has maximum peak-to-peak amplitude greater than 5dB on the day shown. Days containing less than 30- minutes of valid propagation data were excluded. Further details regarding problems encountered with the ITALSAT raw propagation data can be found in [2].

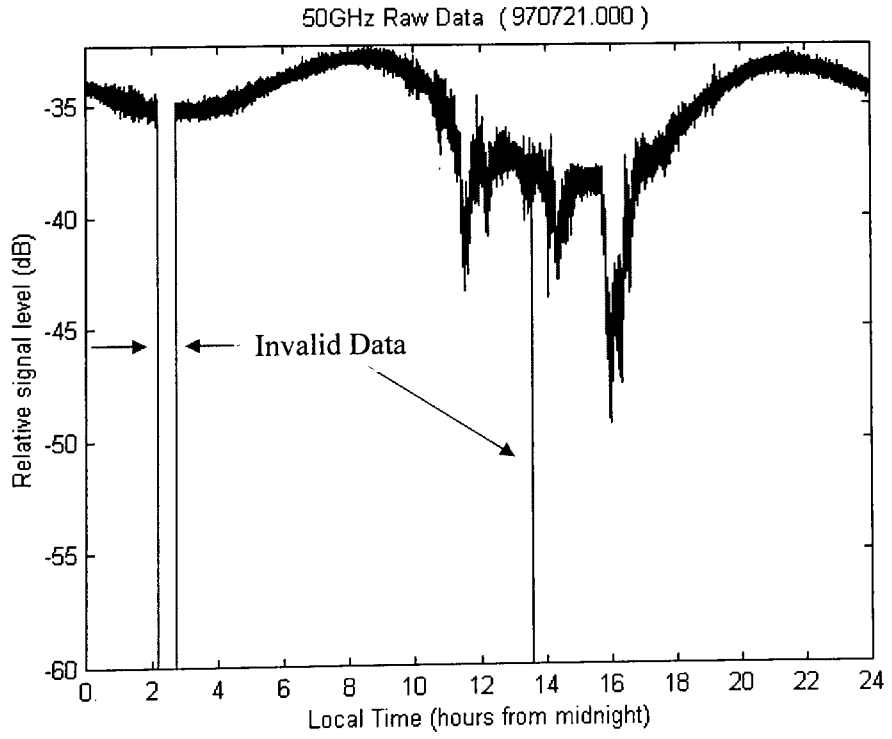

Figure 3.6 Plot of the received raw data for a period of one-day, where *INVALID* data are identified.

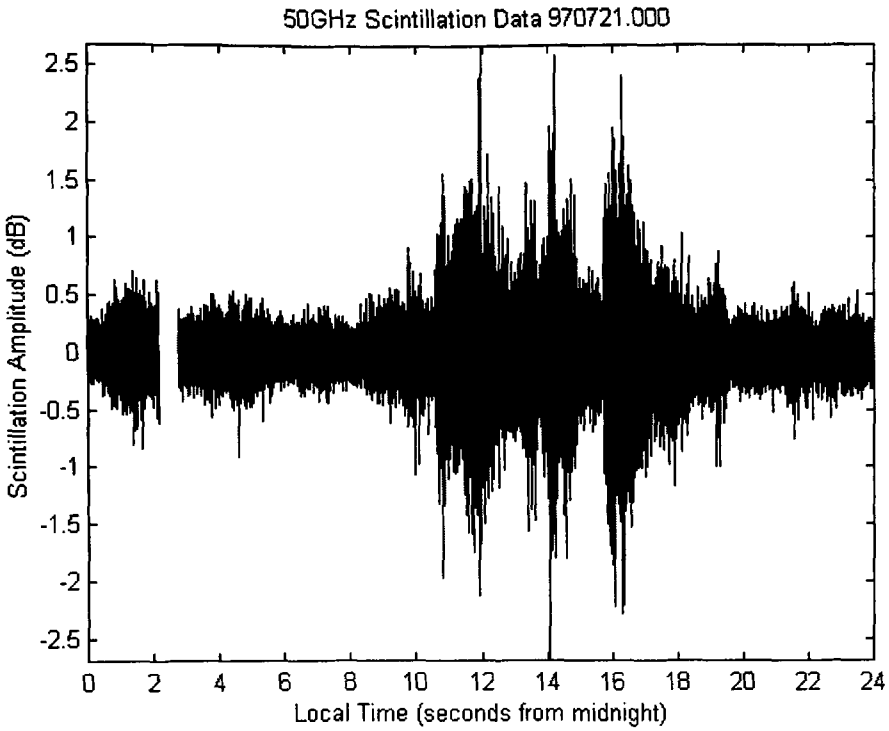

Figure 3.7 Scintillation time series plot for the same period of one-day as in Figure 3.6, note that *INVALID* data have been excluded.

3.4. Resulting Data Sets

As mentioned earlier the data preprocessing was carried out in order to exclude (as much as possible) any effects other than scintillation. Unfortunately, this resulted in:

1. All the data after August 1997 recorded from the ITALSAT F1 satellite had to be excluded completely from the analysis, due to the satellite North-South movement. Originally we were to analyse satellite beacon measurement from the ITALSAT F1 satellite for the period covering June 1996 to May 1999. Unfortunately the exclusion of all the data after August 1997 meant that we could not make any comments on the yearly variation of scintillation.

2. For the months June and August 1996, the data have had to be removed also from the analysis.

3. The 20GHz ITALSAT F1 beacon data were valid only for the period from May 1997 to July 1997. This can be explained by the fact that there is a strong correlation between scintillation intensity and temperature, during the hot summer months as will be shown in following sections of this thesis, observed tropospheric amplitude scintillation are at their highest levels. Since the received signal was weak and was contaminated with noise, it was only during those hot summer months that scintillation amplitude was sufficiently high to be valid and to be included in the analysis.

Therefore, in summary the valid data used in the analysis were:

a) For the ITALSAT F1 data

- 40GHz and 50GHz beacon data for the period from July 1996 to August 1997 (excluding August 96).

- 20GHz beacon data for the period from May 1997 to July 1997.

b) For the ITALSAT F2 data

- 20GHz beacon data for the period from September 1997 to August 2000.

Figures 3.8 to 3.10 illustrate for each month, the percentage of valid data of the total monthly measured data. The amount of rain events in the data was computed using the rain gauge rainfall data, recorded simultaneously as well at Sparsholt with other meteorological parameters. In Figures 3.11 and 3.12*, the percentage of 'rainy' data is shown for the different months of the period covering September 1999 to August 2000 for the 20GHz ITALSAT F2 data set, and for the period covering July 1996 to August 1997 (excluding August 1996) for the 40 and 50GHz ITALSAT F1 data set.

Note however that although this fraction (of rainy data) is largest for the winter months, this does not necessarily mean that the strongest attenuation was measured in those months of the year.

*In Figure 3.12, the "Theoretical Ideal Percentage Amount" is based on *the total monthly measured data at 'one beacon' frequency* (the 40GHz or the 50GHz). Since the total monthly measured data at any one of the two beacons were very similar, choosing either for comparison will not cause any significant errors.

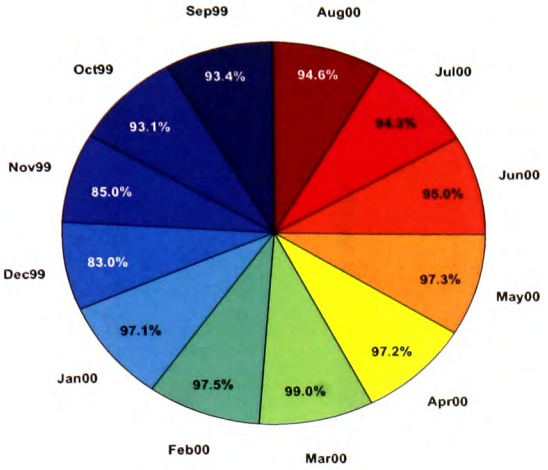

Figure 3.8
Amount of valid data, in percentage of the total monthly measured data of ITALSAT F2 20GHz data set, for each month, covering the period from Sep.99 to Aug.2000.

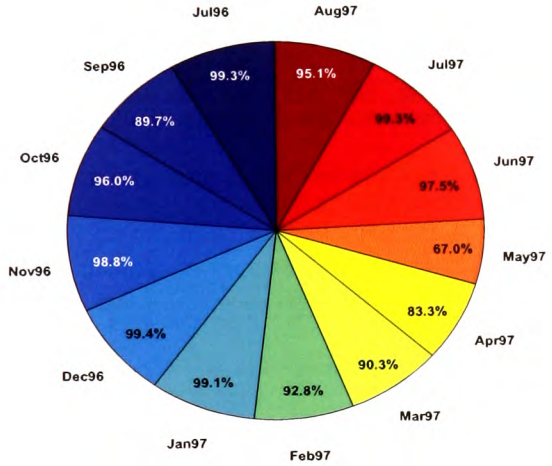

Figure 3.9
Amount of valid data, in percentage of the total monthly measured data of ITALSAT F1 40GHz data set, for each month, covering the period from July 96 to Aug. 97 (excluding Aug. 96).

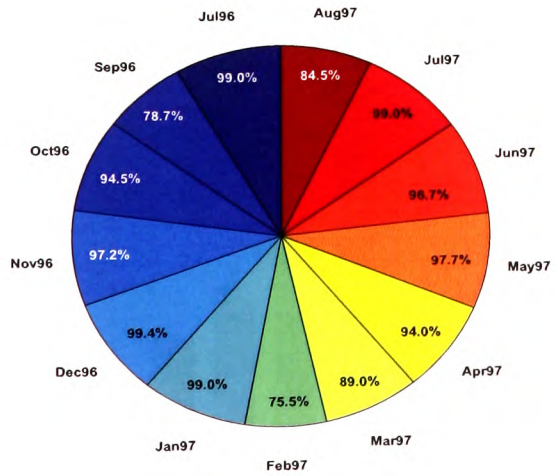

Figure 3.10
Amount of valid data, in percentage of the total monthly measured data of ITALSAT F1 50 GHz data set, for each month, covering the period from July 96 to Aug. 97 (excluding Aug. 96).

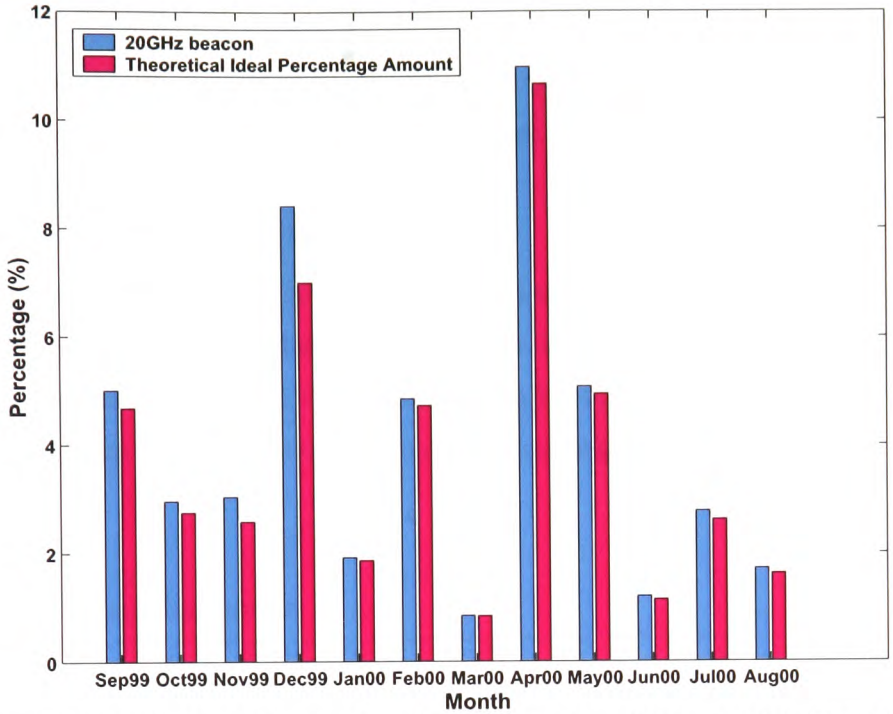

Figure 3.11 Amounts of rain event data, in percentage of total measured data (Theoretical Ideal Percentage Amount) and as percentage of total monthly valid data (20 GHz beacon).

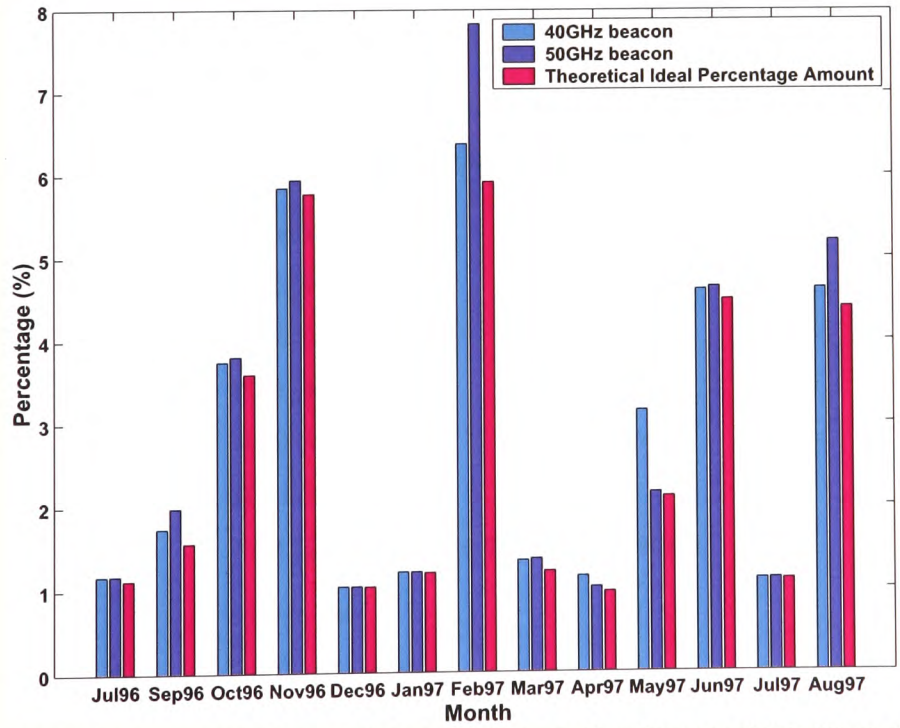

Figure 3.12 Amounts of rain event data, in percentage of total measured data (Theoretical Ideal Percentage Amount) and as percentage of total monthly valid data (40 and 50 GHz beacon).

3.5 Sparsholt Data Format

The data stored on the CD are in binary form and they are recorded in the following format, for every second the corresponding data are stored in a record containing 52 bytes, see Table 3.2.

The data received are stored as a voltage on a hard disk and are collected once every month. The system is connected via a modem to the Internet, where low quality signal figures of the received data are displayed and can be accessed. It is used mainly to monitor the system on a daily basis to ensure that everything is working fine.

Table 3.2 Sparsholt data format

Byte	Counter
0	**Year**
1	**Month**
2	**Day**
3	**Hours (GMT)**
4	**Minutes**
5	**Seconds**
6--7	F12 Beacon
8--9	**F20 Beacon**
10--11	R50 Radiometer V
12--13	Radiometer H
14--15	**F40 Beacon, Use this Frequency**
16--17	Don't use
18--19	39 GHz Beacon
20	Don't Use
21	Don't Use
22--23	41 GHz Beacon

24--25	Don't Use
26--27	Don't Use
28--29	**50 GHz Beacon**
30--31	Don't Use
32--33	Don't Use
34--35	Don't Use
36--37	**Air Temperature**
38--39	**Relative Humidity**
40--41	**Pressure**
42--43	Don't Use
44--45	Don't Use
46--47	Don't Use
48	(Rain Gauge)
49	Don't Use
50	Don't Use
51--52	Don't Use

3.6 Calibration

Since the data received are stored as a voltage, calibration factors are used to translate those values into dB for the signal level, degree Celsius for the temperature, millibars for the pressure and finally to obtain the humidity as a percentage.
It is a linear calibration and the formulae needed are given below:

Linear Calibration

$$Xv = [Xv(0), \quad Xv(1)] \tag{3.1}$$

$$Yv = [Yv(0), \quad Yv(1)] \tag{3.2}$$

$$A = \frac{Yv(0) - Yv(1)}{Xv(0) - Xv(1)} \tag{3.3}$$

$$B = \frac{Yv(1) * Xv(0) - Yv(0) * Xv(1)}{Xv(0) - Xv(1)} \tag{3.4}$$

$$Calibrated\ \ Data = (data \times A) + B \tag{3.5}$$

- **Calibration factors for the 20, 40 and 50 GHz beacons to obtain the signal level in dB**

  Xv = [-2048, 2048]
  Yv = [-60, -20]

- **Calibration factors for the temperature to obtain it in ^{0}C**

  Xv = [0, 1024]
  Yv = [-40, 60]

- **Calibration factors for the pressure to obtain it in millibars**

  Xv = [0, 2048]
  Yv = [900, 1050]

- **Calibration factors for the relative humidity to obtain it in %**

1. If the relative humidity is measured, then the calibration factors are

   Xv = [0, 1024]
   Yv = [0, 100]

2. If the dew point is measured then the calibration factors are

Xv = [0, 1024]
Yv = [-40, 60]

substituting those calibration factors in the general Equation (3.5) will yield a value say *'RR'*.

To estimate the relative humidity from dew point measurements, use the following equations:

Substitute the value of *'RR'* found from Equation 3.5 into Equation 3.6:

$$ww_1 = \frac{RR}{(RR + 238.3)} \tag{3.6}$$

$$ww_2 = \frac{Temperature\ (^oC)}{Temperature\ (^oC) + 238.3} \tag{3.7}$$

*Relative Humidity = 100 * exp [17.2694 * (ww_1-ww_2)]*

Starting from the 3rd of April 1997 relative humidity was measured using dew point. Therefore to obtain the relative humidity for any data obtained after the 3rd of April 1997, use the dew point formula.

3.7 Met Office Surface Data

The first set of data has been purchased from the UK Met Office. It contains the following hourly information:

Wind speed, Wind direction, Air temperature, and Relative humidity, covering the period from June 1996 to May 1999.

The second Met Office data set was obtained from the British Atmospheric Data Centre (BADC), [7]. It contains the hourly Met Office –Land Surface Observation Stations Data from stations in 110 UK counties for the period from 1983 to July 2000. But specifically, only the UK Hourly Weather Observations data covering the period from January 1997 to July 2000 recorded at Brize-Norton were used. The content and format of the data can be found in Appendix Four.

3.8 CDIAC Data

The cloud data used in the analysis were obtained from the Carbon Dioxide Information Analysis Center (CDIAC), [8]. Specifically the NDP-026C data archive, produced by Hahn, C.J., and S.G. Warren, 1999, which contain surface synoptic weather reports for the entire globe, gathered from various available data sets. The U.K. ground station Brize-Norton (51.75 Lat., 358.42 Lon.) chosen was the nearest to Sparsholt were the ITALSAT data were recorded. Approximately 20 km north of Sparsholt. The time resolution of this database is 3 hours, i.e., observations are performed at 0:00, 3:00, 6:00, 9:00, 12:00, 15:00, 18:00, and 21:00 UTC. The data were then processed and edited to extract only the low cloud type.

This database consists of extended edited synoptic cloud reports from ships and land stations around the globe from 1952-1995 for ship data and from 1971-1996 for land station data. In addition to the cloud portion of the synoptic report, each edited report also includes the associated pressure, present weather, wind, air temperature, and dew

point (and sea surface temperature over oceans). This data set is called the "Extended Edited Cloud Report Archive" (EECRA).

The EECRA contains 71 million cloud observations from ships and 311 million from land stations. Each report is 80 characters in length. The archive consists of 841 files of edited synoptic reports, one file for each month of data for land and ocean separately, and 4 ancillary files which provide important information about reporting characteristics of the land stations. The content and format of one 80-character extended edited cloud report are given in Table 3.3. Where values differ, L=Land, S=Ship.

The method for obtaining the average amount for a low cloud type is to compute the frequency of occurrence (*f*) of the type (the number of occurrences of the type divided by the number of contributing reports) and the amount-when-present (*awp* = sum of lower cloud amount divided by the number of occurrences of the type) separately. Then the average cloud amount is:

$$amt = f \times awp \tag{3.8}$$

This method is described because it is often of interest to know the frequency of occurrence of a type in addition to its amount, in this case Cumulus and Cumulonimbus type.

In this project, besides the time and space information, only the following synoptic codes were used: the 'low cloud type' gives the classification of low level clouds and the 'lower cloud amount' gives the amount of sky covered with low level clouds. This is because only low clouds are associated with microwave signal scintillation. The low cloud amount can have integer values from 0 to 8 indicating how many eighth parts of the sky are covered with low level clouds.

Table 3.3 Contents and format of the 80-character Extended Edited Cloud Report [9]

Item	Description	Abbreviation	Num Chars	Minimum Value	Maximum Value	Missing Value
1	year,month,day, hour	Yr,mn,dy,hr	8	51120100	96123021	None
2	Sky brightness indicator	IB	1	0	1	None
3	Latitude x100	LAT	5	-9000	9000	None
4	Longitude x100	LON	5	0	36000	None
5	Land: station number Ship: source deck,ship type	ID	5	01000 1100	98999 9999	None None,9
6	Land/ocean indicator	LO	1	1	2	None
7	Present weather	ww	2	0	99	-1
8	Total cloud cover	N	1	0	8	None
9	Lower cloud amount	Nh	2	0	8	-1
10	Lower cloud base height	h	2	0	9	-1
11	Low cloud type	CL	2	0	11	-1
12	Middle cloud type	CM	2	0	12	-1
13	High cloud type	CH	2	0	9	-1
14	Middle cloud amount x100	AM	3	0	800	900
15	High cloud amount x100	AH	3	0	800	900
	Non-overlapped amounts:					
16	Middle cloud amount	UM	1	0	8	9
17	High cloud amount	UH	1	0	8	9
18	Change code	IC	2	0	9	None
19	Solar altitude (deg. x10)	SA	4	-900	900	None
20	Relative lunar illuminance x100	RI	4	-110	117	None
21	Sea level pressure (mb x10)	SLP	5	9000,L 8700,S	10999,L 10746,S	-1
22	Wind speed (ms^{-1} x10)	WS	3	0	999	-1
23	Wind direction (degrees)	WD	3	0	361	-1
24	Air temperature (^{0}C x10)	AT	4	-949,L -880,S	599,L 580,S	900
25	Dew point depression (C x10)	DD	3	0	700	900
26	Land: station elevation (m) Ship: sea surface temp (C x10)	EL SST	4	-350 -50	4877 400	9000
27	Wind speed indicator	IW	1	0	1	9
28	Land: sea level pressure flag Ship: cloud height indicator	IP IH	1	0 0	2 1	9

References

[1] ESA, "ITALSAT Propagation Handbook," European Space Agency.

[2] A. Savvaris, "Transfer Report: Accurate Prediction of Scintillation Degradation Applicable to Satellite Communication Systems Design," University of Glamorgan, Pontypridd 2002.

[3] RCRU, "Report of the RCRU at RAL for the Year 1997, Annual report," Rutherford Appleton Laboratory (RAL) 1997.

[4] J. M. Woodroffe, R. C. H. Morgan, and J. R. Newbury, "Preliminary Results from an ITALSAT Propagation Experiment at 49.5GHz in the UK," presented at Olympus Utilisation Conference (WPP-60), Seville, Spain, 1993.

[5] I. E. Otung, M. O. Al-Nuaimi, and B. G. Evans, "Extracting Scintillations from Satellite Beacon Propagation Data," *IEEE Transactions on Antennas and Propagation*, vol. 46, pp. 1580-1581, 1998.

[6] A. Savvaris and I. E. Otung, "Preliminary Preprocessing of ITALSAT Data at 20, 40 and 50GHz," presented at URSI Symposium, 2000.

[7] BADC, "Detailed information regarding BADC can be found at the following address, www.badc.rl.ac.uk."

[8] CDIAC, "Detailed information regarding CDIAC can be found at the following address, ftp.cdiac.esd.orln.gov."

[9] CDIAC, "Extended Edited Synoptic Cloud Reports from Ships and Land Stations over the Globe 1952-1996."

CHAPTER IV

Statistical & Meteorological Analysis

Summary – *This chapter presents the results of the statistical and meteorological analysis. Monthly, annual and worst month cumulative distribution functions at three beacon frequencies are presented. The extensive study of the probability density function (pdf) of scintillation amplitude and standard deviation have shown that for short time intervals, scintillation amplitude fluctuations can be assumed to follow a Gaussian distribution, while the lognormal probability density function provides a better approximation to the distribution of scintillation standard deviation than the Gamma pdf.*

The second part of this Chapter investigates the relations of scintillation with meteorological parameters. The results show a strong correlation between scintillation intensity, temperature and the wet-part of refractivity. A weaker correlation with relative humidity and a negligible correlation between scintillation intensity and transverse wind speed. Furthermore, it was found that the presence of cumulus clouds led on average to increased scintillation levels. The parameter N_{wet} shows no significant diurnal variation that can relate to scintillation intensity. The diurnal variations of cumulus cloud and scintillation intensity however are very well correlated.

4.1. Distribution of Scintillation Amplitude

4.1.1 Short-term Scintillation Amplitude pdf

It is known from theoretical and experimental investigations that over a short-term period when meteorological conditions may be regarded as constant, signal level fluctuations due to turbulence follow a Gaussian distribution [1]. This is why they can be characterised by the variance or the standard deviation. Under this assumption, the probability density function (pdf) of signal deviation x from the mean signal level can be written as:

$$p(x) = \frac{1}{\sigma\sqrt{2\pi}} e^{-x^2/2\sigma^2} \tag{4.1}$$

where σ^2 is the variance and σ is the standard deviation.

Studies of short-term distributions of scintillation amplitude shows that this period must be well below one hour [2]. The period here for short-term is taken to be 30 minutes. Because of the sampling frequency of 1-Hz i.e. one sample per second, in this time period (30-min.) there are 1800 data samples. The data used for this analysis was that described in Sections 3.3 and 3.4. The short-term probability density function was computed only on blocks of 1800 samples containing more than 90% valid data. These 1800 samples are distributed in bins according to their amplitude. The bin size was chosen to be 0.05 dB. It should be noted that the parameters of the model distributions are determined from the measured data in every case.

Figure 4.1 shows a plot of the probability density function of scintillation amplitude for a 30-minute period that passed the Chi-squared goodness of fit test. The solid line represents the experimental probability density function (pdf) of scintillation amplitude, while the dotted line shows the theoretical Gaussian curve computed using measured mean amplitude and standard deviation. We can see that it follows reasonably well a Gaussian distribution and the only significant departures are in the low probability region for time percentage $p < 0.1\%$.

There are arguments for short-term pdf of scintillation amplitude, being of either Gaussian or Nakagami-m form. Van de Kamp [3], using measurements of three beacon signals from the ITALSAT satellite at 18.7, 39.6, and 49.5 GHz, which were received at Spino d'Adda using a 3.5m Cassegrain antenna in Italy at an elevation angle of 37.8^0, found that for large scintillation intensities, the short term distribution is not symmetrical like the Gaussian. The negative signal deviation, or 'fade', was on average larger than the positive, or 'enhancement', for large signal fluctuations.

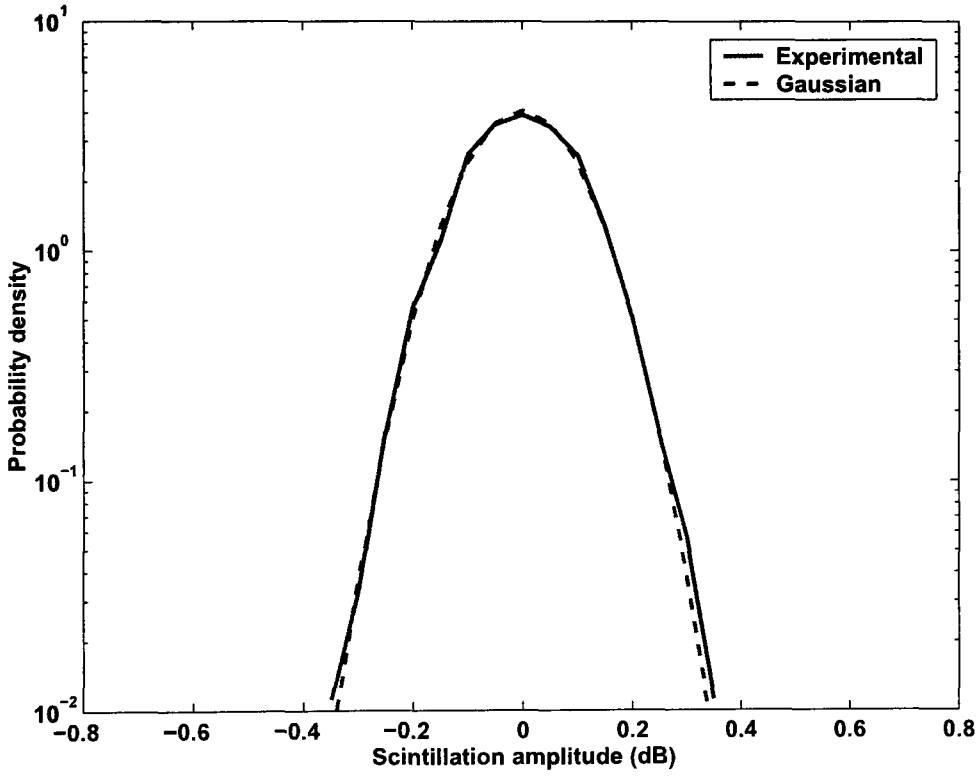

Figure 4.1. Distribution of scintillation amplitude over 30 minute period; 21 July 1997. (Solid line experimental, Dotted line Gaussian)

Otung and Evans [4], after the extensive study of experimentally observed short-term probability distributions, found that weak scintillation amplitude fluctuations are normal, but intense fluctuations (>0.5 dB) do not follow normal distribution. The mean probability is less than 5% for intensities greater than 0.5 dB. The threshold between weak and intense amplitude fluctuations was given to be a scintillation intensity of ~0.5 dB.

If turbulence is confined to a thin slab located far from the receiver, the amplitude of the received wave obeys a Nakagami-Rice distribution [5], which in the limiting case of a strongly scattering slab reduces to a Rayleigh distribution [6]. Banjo [7] have reported the following observations:

i) The Gaussian pdf is a closer fit to the large enhancements while the Nakagami-m is a closer fit to the large fades.
ii) For small to moderate fluctuations, there is litte difference between the Gaussian and Nakagami-m pdfs.

Results reported from the analysis of measurements conducted in Leeheim, Germany [8] using the OTS satellite at 11.8 GHz, also revealed that the 1-minute scintillation amplitude fluctuations were normally distributed. In this analysis a chi-square goodness-of-fit test was performed on 13855 30-min intervals (representing 79.1% of the annual period) at the 1% and 5% significance level to determine if they follow a normal distribution with statistical significance. At 50GHz the number of distributions that passed the test were 12499 and 11563, or 90.5% and 83.8% passed the test, respectively. For the 40GHz beacon, out of 14968 30-min intervals tested (representing 85.4% of the annual period) at the 1% and 5% significance level, 12759 and 11572 or 84.9% and 77.0% passed the test, respectively.

Finally, for the 20GHz beacon, out of 15761 30min intervals tested (representing 90.0% of the annual period) at the 1% and 5% significance level, 14771 and 13767 or 84.3% and 78.6% passed the test, respectively. All the results are summarised in Table 4.1, below.

Table 4.1: Short-term amplitude scintillation chi-square goodness-of-fit test results to determine if they follow a Normal distribution.

		1% Significance level	**5% Significance level**
	NO. OF TESTS	**PASS**	**PASS**
20GHz	15761	14771 (84.3%)	13767 (78.6%)
40GHz	14968	12759 (84.9%)	11572 (77.0%)
50GHz	13855	12499 (90.5%)	11563 (83.8%)

4.1.2 Long-term Scintillation Amplitude pdf

However, in the long term meteorological variables are not constant, the scintillation process ceases to be stationary and the variation of scintillation amplitude no longer follows a Gaussian distribution. The same procedure has been followed, to calculate the histograms and the pdfs for the long-term distributions. Figure 4.2 shows a typical summer day scintillation amplitude distribution for the 21st of July 1997, with standard deviation $\sigma_{day} = 0.2557\,\text{dB}$. It is evident that the distribution is non-Gaussian.

Whereas Figure 4.3 shows a plot of a daily scintillation amplitude distribution of a typical winter day with predominantly weak scintillations, for the 5th of January 1997. The standard deviation was $\sigma_{day} = 0.1074\,\text{dB}$. Although Figure 4.3 shows the daily distribution to fit a Gaussian shape very well, the departure from the theoretical distribution is significant in the tails. Both distributions failed the goodness-of-fit test.

We performed a Chi-square goodness-of-fit test on all measurement days with more than 90% valid samples at the 1% and 5% significance level, out of 917 distributions (representing 83.7% of the measurement period at 20, 40 and 50GHz) only 3 distributions passed the test at the 1% significance level and none of the distributions tested passed the test at the 5% significance level. The same test was also carried out on the monthly distributions, none passed the test at the two significance levels.

Therefore we can conclude that long term (≥ one day) scintillation amplitude distributions are non-Gaussian, although in the winter months when scintillations are predominantly weak the departure from the Gaussian shape may be significant only in the tails of the distribution.

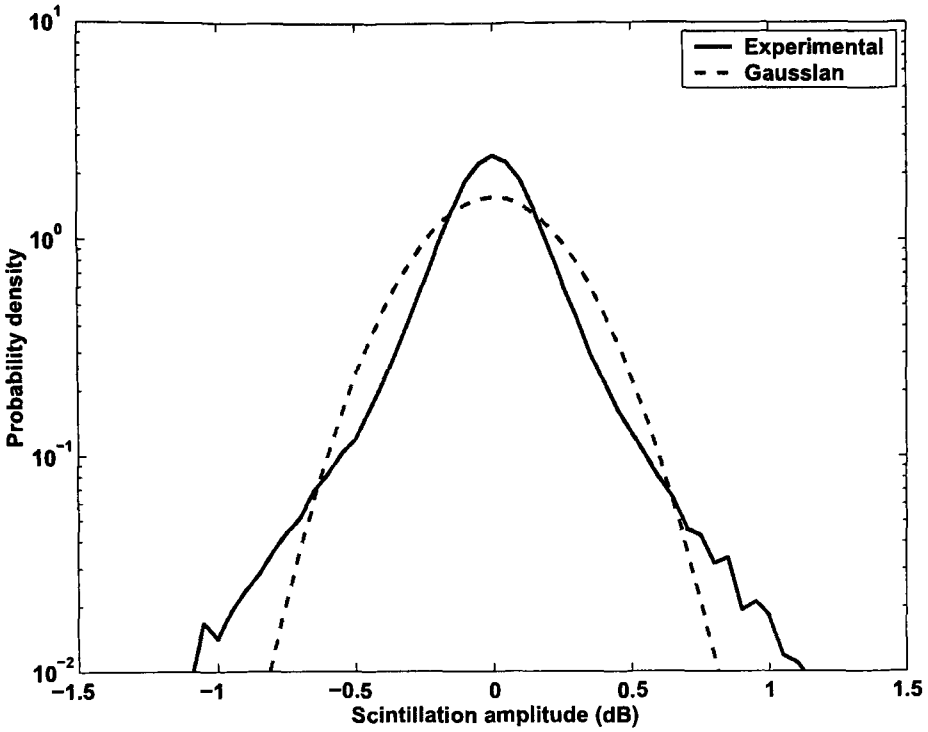

Figure 4.2. Distribution of scintillation amplitude over a 1-day period; 21 July 1997. (Solid line experimental, ... dotted-line Gaussian).

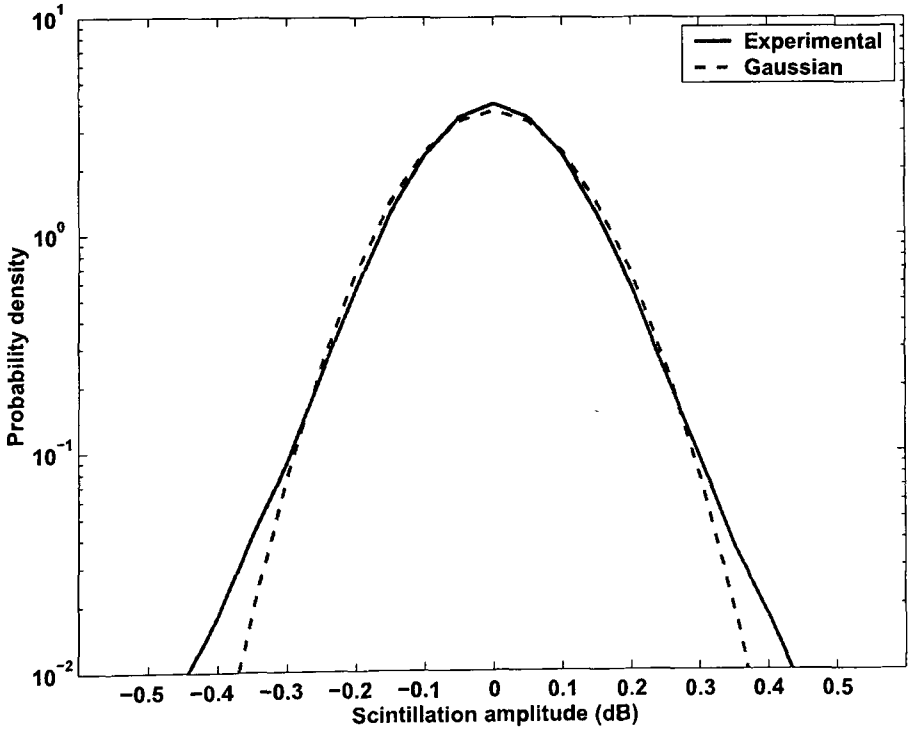

Figure 4.3. Distribution of scintillation amplitude over a 1-day period; 5 January 1997. (Solid line experimental, ... dotted-line Gaussian).

4.2. Scintillation Intensity pdf

As mentioned previously over long periods meteorological quantities at every point of space undergo irregular fluctuations due to the varying turbulent conditions. Under these conditions, the short-term standard deviation also referred to as scintillation intensity σ_x is also a random variable with a variation which may be approximated by a lognormal or a gamma distribution [9]. The probability density function (pdf) of x over such long periods is given by:

$$P(x) = \int_0^\infty P(\sigma_x) P(x \mid \sigma_x) d\sigma_x \tag{4.2}$$

where, $P(\sigma_x)$ is the long term pdf of σ_x and $P(x|\sigma_x)$ is the pdf of x conditional on σ_x.

Moulsley and Vilar [1] computed scintillation intensity σ_x over 10-minute intervals and found that its pdf over long periods has a lognormal distribution, and evaluated Equation (4.2) for $P(x)$ by assuming a Gaussian $P(x|\sigma_x)$ and a lognormal $P(\sigma_x)$. This distribution model is symmetrical, whereas the long-term pdf of scintillation amplitude x has been observed [10] to be larger in the negative tail of x. Ortgies [8] reported similar results and later suggested [11] that for higher elevation paths, it appears that the lognormal distribution is more adequate than the gamma distribution for fitting the measured pdf, especially for scintillation variance below about 1 dB^2.

The authors in [9], found that the scintillation intensity σ_x for a monthly period, calculated every hour can be approximated by the gamma pdf. Karasawa *et al* [12] later proposed a semi-empirical prediction model for tropospheric scintillation by assuming a Gaussian $P(x|\sigma_x)$ and a gamma pdf for $P(\sigma_x)$.

To examine the form of $P(\sigma_x)$ for a low elevation path, the daily and monthly experimental distributions of scintillation intensity σ_x were computed for the entire measurement period at the three respective beacon frequencies, by taking the 1-minute

standard deviation of the preprocessed beacon data in each block interval, which had more than 90% valid samples.

In Figure 4.4 and Figure 4.5 the daily and monthly probability density functions of the standard deviation are compared to the lognormal and gamma distributions. The input parameters for these theoretical distribution models are the mean and standard deviation of $\log(\sigma_x)$ for the lognormal distribution, and the mean and standard deviation of σ_x for the gamma distribution, which are all calculated from the measured distributions.

A visual inspection of these distributions would suggest that sometimes they follow reasonably well a lognormal or a gamma distribution. Also, sometimes both fit the data very well, and sometimes neither. A more quantitative method to decide whether a measured distribution is well represented by a certain theoretical distribution model, is the chi-square test. In our analysis a chi-square goodness-of-fit test was performed on 306 (at 20GHz), 455 (at 40GHz) and 430 (at 50GHz) daily distributions of 1-minute scintillation intensity tested at 1% and 5% significance level, respectively, the results of which are tabulated in Table 4.2, below.

Table 4.2: Long-term scintillation intensity chi-square goodness-of-fit test results

	20GHz	**40GHz**	**50GHz**
No. of Daily Distributions	306	455	430
Lognormal			
1% significance level	59 (19.3% pass)	39 (8.6%)	27 (6.3%)
5% significance level	47 (15.4% pass)	23 (5.1%)	21 (4.9%)
Gamma			
1% significance level	55 (18% pass)	13 (2.9%)	19 (4.4%)
5% significance level	40 (13.1% pass)	7 (1.5%)	14 (3.3%)

Of 306 daily one-minute scintillation intensity distributions tested at the 1% level at 20GHz, 59 (19.3%) were lognormal and 55 (18%) were gamma. At 40GHz out of 455 distributions tested, 39 (8.6%) were lognormal and 13 (2.9%) gamma, and finally at 50GHz out of 430 distributions tested, 27 (6.3%) passed as lognormal and 19 (4.4%) were gamma.

At the higher significance level of 5%, for the 20GHz beacon, the results were 47 (15.4%) lognormal and 40 (13.1%) gamma. At 40GHz, 23 (5.1%) distributions were lognormal and 7 (1.5%) were gamma. Finally at the higher frequency of 50GHz, the results yielded 21 (4.9%) and 14 (3.3%) as lognormal and gamma distributions, respectively.

The same test was also carried-out on all monthly distributions, but none of these passed the test. These results suggest that the likelihood of a distribution being a lognormal or a gamma is very small. Another conclusion, which may be drawn based on the results obtained in Table 4.2, is that out of the two distributions of the 1-min scintillation intensity, the lognormal distribution gives a slightly better approximation than the gamma distribution.

Another interesting aspect of the difference between the lognormal and the gamma distributions is found when the behaviour of the characterising parameters is compared. Figure 4.6 shows a scatter plot of the mean versus the standard deviation of scintillation intensity, σ_x. They are strongly correlated, with correlation coefficient R=0.8633, while the mean and standard deviation of $\log(\sigma_x^2)$ are not, having correlation coefficient R=0.3549. The high correlation value (R = 0.8633) observed, is in agreement with the theory of the gamma distribution. This gives the impression that this distribution represents the data well. However, this would be wrong in light of the goodness-of-fit results obtained from the analysis.

Marzano and G. d'Auria [13], based on their proposed statistical method to predict tropospheric amplitude scintillation have also concluded that the best-fitting long-term pdf is lognormal on month, season, and year time periods analysed on an hourly basis. However, neither of these theoretical pdf's give a very good fit. Various researchers are now trying a different modelling approach, such as using a Rice-Nakagami distribution instead of a lognormal distribution [3].

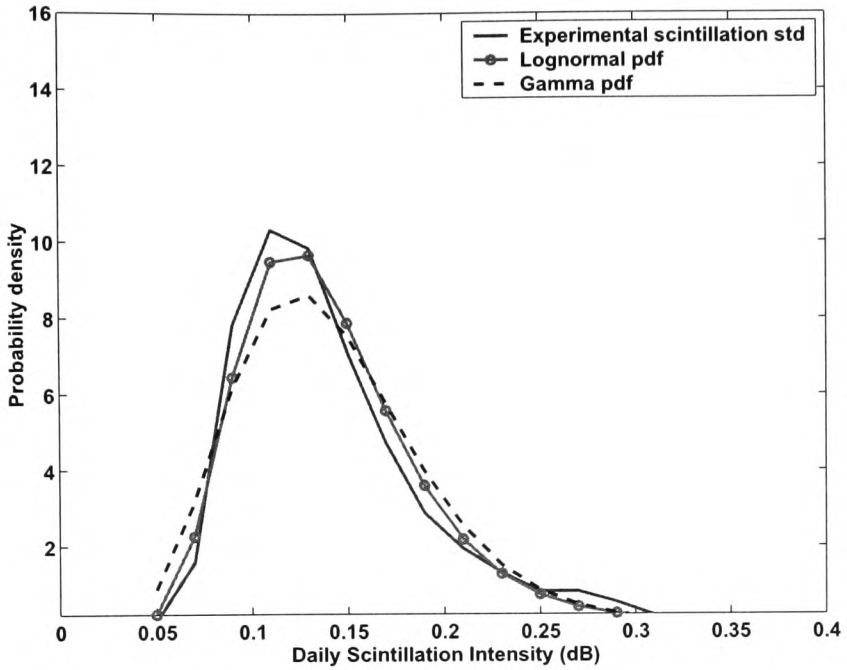

Figure 4.4. Comparison of lognormal (-o- line) and gamma distributions (dotted line) with daily experimental data 1-min scintillation intensity distribution (solid line), computed for the 24th of Sep. 1999 at 20GHz.

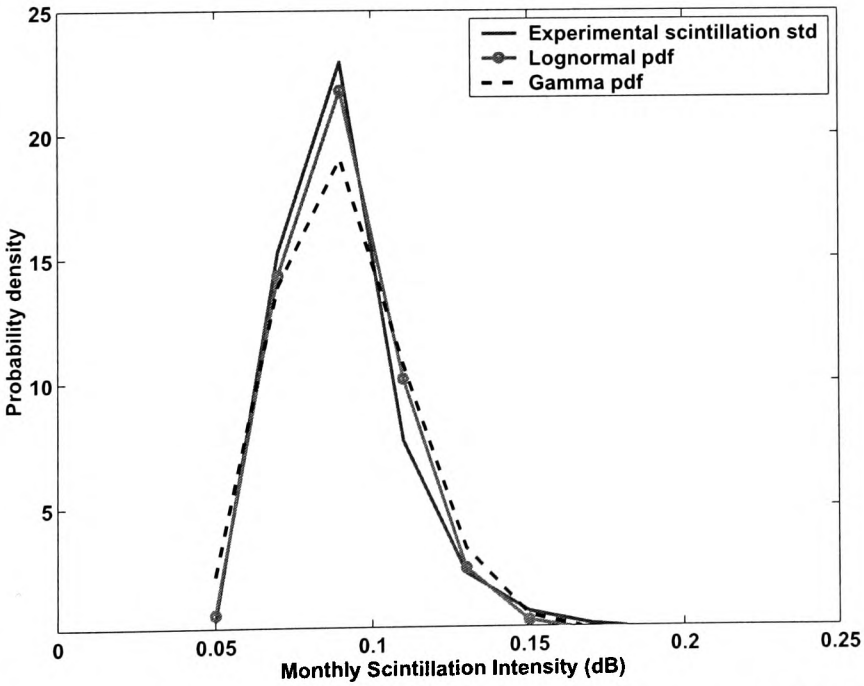

Figure 4.5. Comparison of lognormal (-o- line) and gamma distributions (dotted line) with monthly experimental data 1-min scintillation intensity distribution (solid line), computed for November 1996 at 40GHz.

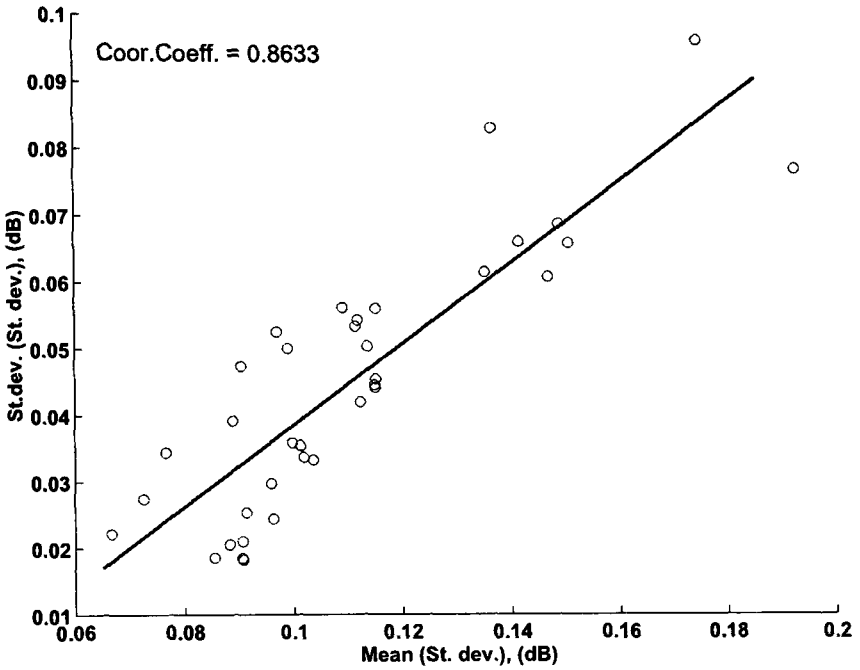

Figure 4.6. Scatter plot of the mean versus the standard deviation of σ_x.

4.3. Cumulative Distribution of Scintillation Intensity

The yearly cumulative distributions of scintillation intensity (standard deviation) for the 20, 40 and 50GHz beacon signals for the period covering September 1996 to August 1997 at 40 and 50GHz and for the period covering September 1999 to August 2000 for the 20GHz beacon are plotted in Figure 4.7. These are useful as a quick reference for seeing how often a particular value of scintillation intensity σ_x, is likely to be exceeded.

In Figure 4.8, the monthly cumulative distributions of scintillation intensity for the three beacon signals are plotted. As expected, scintillation intensity is significantly higher in the summer months. For example, in January at 40 and 50GHz, scintillation intensity values for 0.1% of the time are 0.2092 dB and 0.2668 dB, respectively. In July these values are 0.6953 dB and 0.8212 dB, respectively. This represents an increase of 232% and 208%, respectively.

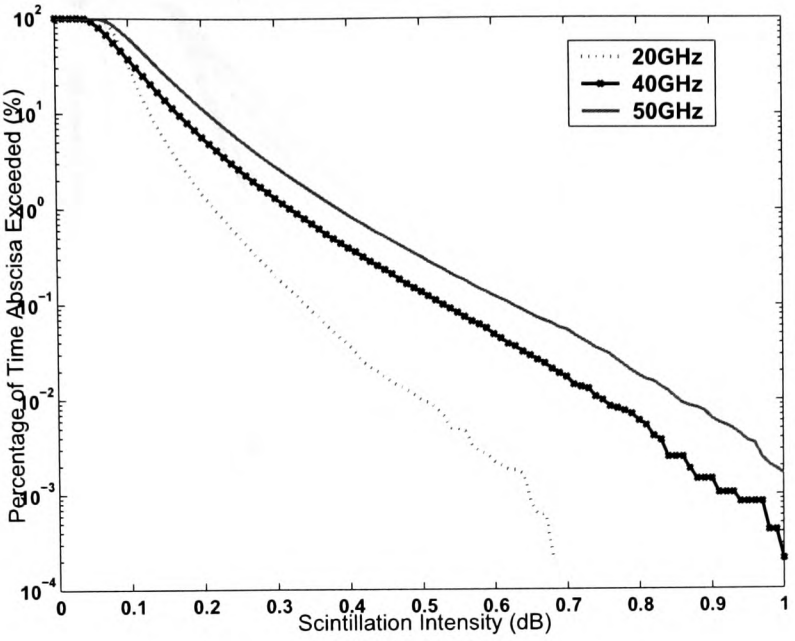

Figure 4.7. Yearly cumulative distributions of scintillation intensity at 20, 40 and 50GHz.

Some more numerical results can be found in Table 4.3 and Table 4.4: scintillation intensity (standard deviation), temperature, humidity, and the wet-part of refractivity (N_{wet}) averaged over every month and over the whole measurement period are shown for the three respective beacon signals. Here it appears that the wet-part of refractivity (N_{wet}) has a similar trend as scintillation intensity, as was predicted by the models of Karasawa et. al. and the ITU-R. The seasonal variability and correlation with meteorological parameters will be discussed in Section 4.5.

During August 1996 there was a problem in recording the meteorological data at Sparsholt, instead the data recorded at Brize-Norton were used in the analysis. Brize-Norton meteorological station is approximately 20 km north of Sparsholt.

Table 4.5 shows the temperature and humidity data recorded at Brize-Norton for the entire 14-month period, starting from July 1996 to August 1997. The averaged absolute error made by using this dataset is 3.44% for the temperature and 2.25% for the relative humidity. It is therefore expected that the data from Brize-Norton can be used to estimate the monthly averaged wet-part of refractivity (N_{wet}) without loss of accuracy.

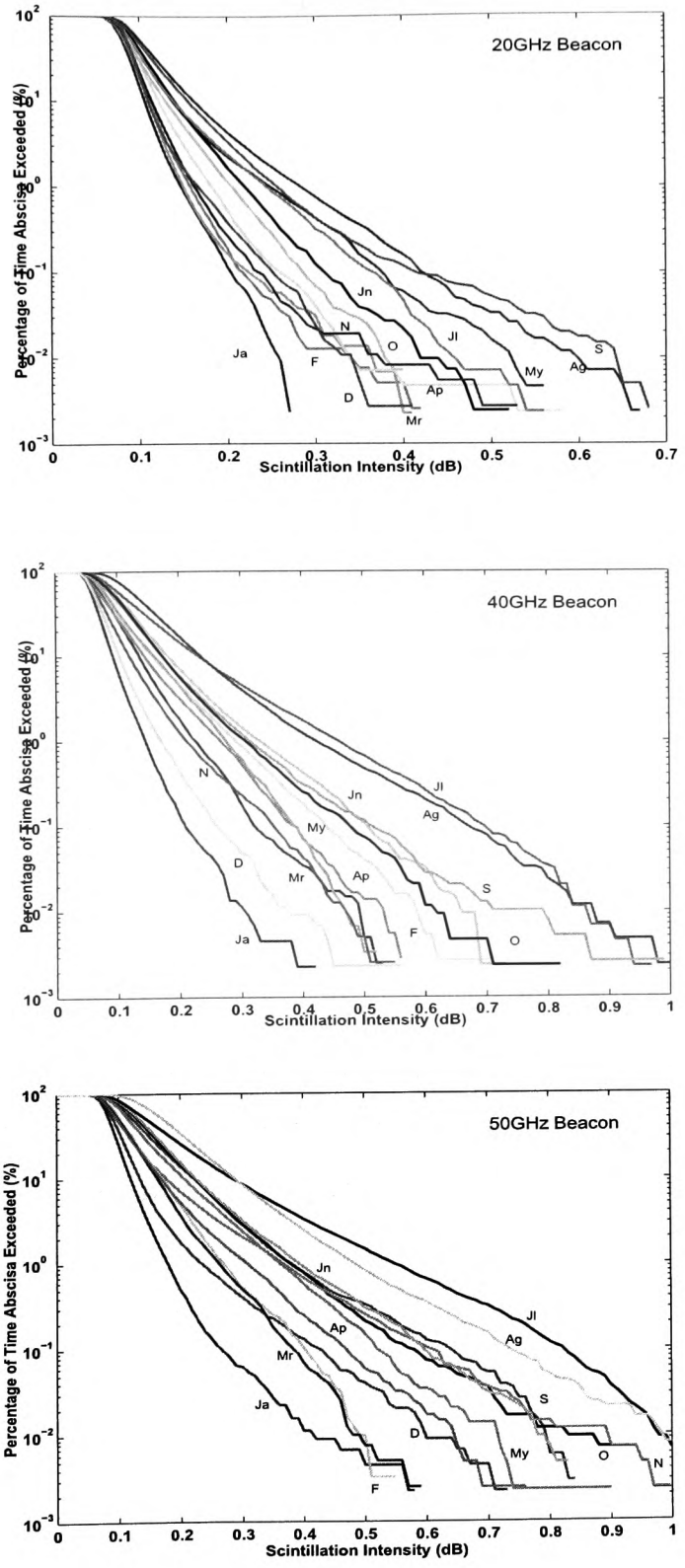

Figure 4.8. Cumulative distributions of scintillation intensity for each month of the year for the period covering September 1996 to August 1997 for the 40 and 50GHz beacons and for the period covering September 1999 to August 2000 for the 20GHz beacon.

Table 4.3: Mean meteorological data for every month and the whole year, from the meteorological data recorded at Sparsholt. For the ITALSAT F2 data recorded at 20GHz.

Month	Temperature (^{0}C)	Humidity (%)	N_{wet} (ppm)	Standard deviation, σ_x (dB)
September 99	15.3398	83.0829	64.9749	0.1163
October 99	9.4945	83.5912	46.3883	0.0995
November 99	7.5404	86.1870	42.4831	0.0925
December 99	4.7568	86.0151	35.6877	0.0926
January 00	4.4358	89.1483	36.2503	0.0865
February 00	6.1993	84.1538	38.1962	0.0903
March 00	6.9256	79.0317	37.5148	0.0917
April 00	7.0935	82.9057	39.7617	0.0980
May 00	11.6295	82.1084	51.7494	0.1085
June 00	13.6256	82.5122	58.4543	0.1068
July 00	16.0819	72.8276	59.4194	0.1073
August 00	16.4028	77.5116	64.4049	0.1218
Whole year	**9.9605**	**82.4230**	**47.9404**	**0.10098**

Table 4.4: Mean meteorological data for every month and the whole year, from the meteorological data recorded at Sparsholt. The values in brackets are for the data recorded at Brize-Norton.

Month	Temperature (^{0}C)	Humidity (%)	N_{wet} (ppm)	Standard deviation, σ_x 40GHz, 50GHz
June 96	Ignored	Ignored	Ignored	Ignored
July 96	16.1124	73.2152	59.8394	0.1574, 0.1876
August 96**	(16.3649)	(72.9180)	(60.4579)	0.1409, 0.1905
September 96	13.2223	75.8753	52.5058	0.1217, 0.1560
October 96	11.4883	81.9582	51.2254	0.1225, 0.1603
November 96	5.9945	84.9885	38.0889	0.1012, 0.1306
December 96	2.6720	85.8592	31.2243	0.0775, 0.1053
January 97	1.9961	80.8290	28.1509	0.0696, 0.0940
February 97	6.8580	85.4851	40.4097	0.1099, 0.1544
March 97	8.3516	79.3239	41.0820	0.0958, 0.1208
April 97	8.8700	69.1578	36.9600	0.0997, 0.1224
May 97	11.5225	75.9630	47.5744	0.1097, 0.1471
June 97	13.6067	81.0180	57.3328	0.1289, 0.1636
July 97	16.3711	75.8702	62.9278	0.1585, 0.1976
August 97	18.4265	81.3351	75.7353	0.1716, 0.2103
Average (over 14 months)	**10.8469**	**78.8426**	**48.8225**	**0.1189, 0.1529**

*** During August 1996 there was a problem in recording the meteorological data, in the analysis the data from Brize-Norton were used instead.*

Table 4.5: Mean temperature and humidity data for the 14-month period (July 96 to August 97) recorded at Brize-Norton.

Month	Temperature (^{0}C)	Humidity (%)
June 96	Ignored	Ignored
July 96	16.8940	69.2097
August 96	16.3649	72.9180
September 96	13.6354	72.3278
October 96	11.3730	81.8871
November 96	5.6192	84.3833
December 96	2.5195	87.2836
January 97	1.7747	87.6358
February 97	6.7524	81.6696
March 97	8.3516	79.3239
April 97	9.1668	67.8847
May 97	11.5417	75.7325
June 97	14.1718	77.6620
July 97	16.9522	71.7796
August 97	19.1456	76.3884
Average (over 14 months)	**11.0188**	**77.5776**

4.4. Cumulative distribution function of scintillation fades and enhancement

Link budget engineers use annual and worst month cumulative distribution functions to calculate the link budget for a new satellite communication system. These provide the system designer with information on the probability that a certain level of fading is exceeded in terms of the percentage of the time in a monthly or annual period that this level is exceeded. Based on these statistics and the required link availability, the system fade margin is calculated.

Karasawa *et al.* [12] presented some expressions for the long-term cumulative distribution of amplitude level, expressed in terms of the predicted long-term standard deviation. Assuming a Gaussian short-term probability density function (PDF) of scintillation amplitude and a Gamma PDF of scintillation intensity σ_x. The resulting amplitude level y, exceeded for a time percentage of P, is given by:

For signal enhancements

$$y = \left(-0.0597\log^3 P - 0.0835\log^2 P - 1.258\log P + 2.672\right)\sigma_{pre} \qquad (4.3)$$

for $(0.01\% \le P \le 50\%)$

For signal fades

$$y = \left(-0.061\log^3 P + 0.072\log^2 P - 1.71\log P + 3\right)\sigma_{pre} \qquad (4.4)$$

for $(0.01\% \le P \le 50\%)$

In Equations (4.3) and (4.4) σ_{pre} is the predicted long term standard deviation. The ITU-R [14] adopted only the signal fades cumulative distribution (Equation (4.4)) in the proposed prediction model.

The measured annual cumulative distribution function (cdf) of scintillation fades at 20GHz for the period September 1999 to August 2000, and for the period covering September 1996 to August 1997 at 40 and 50GHz, is shown in Figure 4.9. It can be seen

from this figure, that for 0.01% of the time the fade levels at 20 and 50GHz are 0.805 dB and 1.457 dB, respectively. This represents an increase in the scintillation fade level of 81%. Figure 4.10 illustrates the corresponding measured annual cdf of scintillation enhancements for the same period. In general measurement of scintillation fades are larger than enhancements, particularly in the low probability region. The differences in the data presented in Figures 4.9 and 4.10 are small however.

The monthly measured cumulative distribution functions were also computed for the entire measurement period at 20, 40 and 50GHz, and can be found in Appendix B. Once more it can be seen that in all distributions in the low probability range the curves spread out, and the distribution of signal fades for probabilities lower than 0.1%, exceed that of scintillation signal enhancements. All distributions are compared to the ITU-R Model for signal fades, given by Equation (4.4). Since in the ITU-R Report [14] only the distribution function for signal fade is mentioned, this is the only curve from ITU-R included in the graphs. The input parameters for this model are the surface temperature and relative humidity, which are given in Tables 4.3 - 4.5. In Chapter 7 of this thesis the current prediction models are discussed in more details.

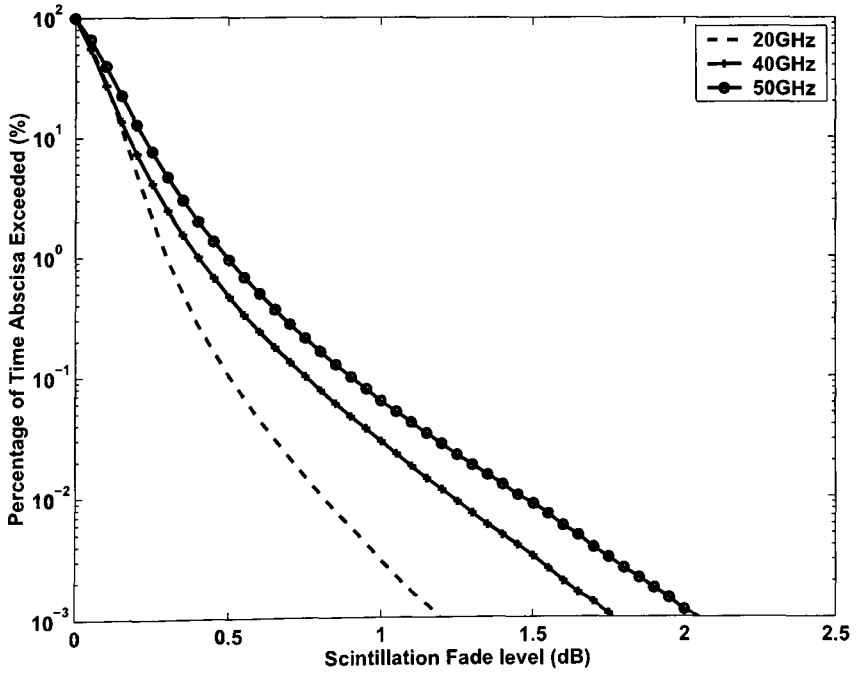

Figure 4.9. Yearly cumulative distribution function (cdf) of scintillation fades amplitude at 20, 40 and 50GHz.

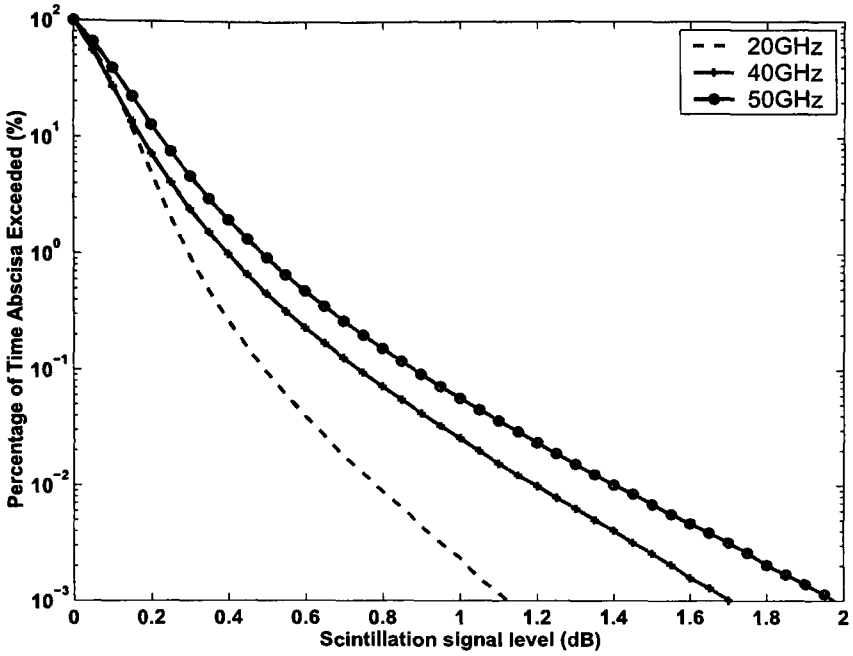

Figure 4.10. Yearly cumulative distribution function (cdf) of scintillation enhancements amplitude at 20, 40 and 50GHz.

Analysis of scintillation worst-month cumulative distribution function was also carried out. The distribution was computed from the monthly cumulative probability distributions over the 12-month period by taking the maximum value at each percent of time. Figure 4.11 shows the observed worst-month cumulative distribution of scintillation fade. As expected, worst-month values exceed annual values, for example for 0.01% of the time the fade levels at 20 and 50GHz are 1.023 dB and 1.869 dB, respectively. This represents an increase of 21.8% and 28.3%, respectively, in comparison with the annual values at the same percent of time.

Of course the values of both annual and worst month cumulative distribution functions would be different on other links. However, if we have a scenario in which an earth station is tracking more than one satellite, and if we assume that the link parameters and meteorological conditions remains the same and only the elevation angle varies, then by using the theoretical scaling factors (see Chapter 5) it is possible to calculate the ratio by which those values will change. For example, if the elevation angle is now 10^0 then

$F=[\sin(29.9^0)/\sin(10^0)]^{11/12} = 2.6292$. Where 29.9^0 is the Sparsholt-ITALSAT path elevation angle. In this case the annual and worst-month values will have to be multiplied by F (the scaling factor).

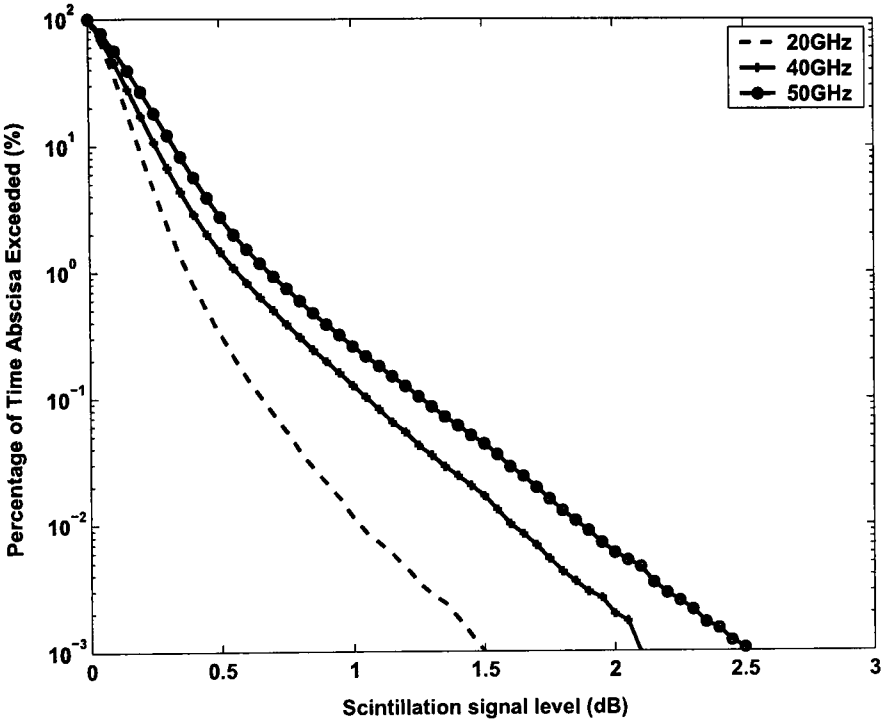

Figure 4.11. Worst month cumulative distribution function (cdf) of scintillation fades at 20, 40 and 50GHz.

The annual cumulative distribution function can allow the link margin for a service to be developed but it does not give any insight into potential variations in service quality due to propagation effects that exist over smaller intervals of time. The dependence of signal fading on the time of day is an important consideration in the provision of broadcast satellite services.

The next section will discuss the dependence of tropospheric scintillation on various meteorological parameters.

4.5. Meteorological Dependence

4.5.1 Introduction

Various experimental studies show that scintillation exhibits diurnal and seasonal variation. In this section we take a closer look at the correlation between tropospheric scintillation and various meteorological parameters. In addition to examining meteorological parameters directly, one can use them to derive dependent parameters such as the wet-part of refractivity (N_{wet}). One of the main objectives is to find the influence of the averaging period on the correlation between those parameters.

The data examined can be divided into two sets:

i) Data set 1: This contains data measurement from the ITALSAT F2 satellite, operating at 18.7 GHz and covering a 1-year period from September 1999 to August 2000.
ii) Data set 2: This contains data measurement from the ITALSAT F1 satellite, operating at 39.6 and 49.5 GHz and covering a 1-year period from September 1996 to August 1997.

The analysis can be split into two parts depending on the meteorological data used. The propagation data together with temperature and humidity measurements recorded at the same sampling rate were recorded at Sparsholt and archived to a compact disk once a month.

Wind speed, wind direction and cloud data used in the analysis were obtained from the Met Office - Land Surface Observation Stations Data. The database format is given in *Appendix C*. This database consists of synoptic (hourly) weather observations for the period covering 1983 to July 2000. The U.K. ground station Brize-Norton (51.75 Lat., 358.42 Lon.) chosen was the nearest to Sparsholt where the ITALSAT receivers were mounted, it was approximately 20 km North of Sparsholt. The time resolution of this database is 1-hour, i.e., observations are performed on the hour for every hour of the day starting from midnight local time. All the meteorological parameters were measured at the Earth's surface.

The intensity of scintillation σ_x is directly related to the refractive index structure constant C_n^2, which is a measure of the energy in the fluctuations of the normalised refractive index. This is in turn directly related to the energy of the turbulence. It is worth noting that there are two main mechanisms responsible for the introduction of energy into the turbulence, namely wind shear and buoyancy [6].

Wind shear results from a spatial variation in average wind speed. The rate at which it introduces turbulent energy into the flow is proportional to the rate of change with height of the wind velocity components in a plane parallel to the earth's surface. Buoyancy on the other hand arises from a convective heating of the atmosphere by the ground, which tends to lift the air mass upwards. Both mechanisms give rise to a turbulent mixing of air masses of different temperature and humidity. We can, therefore, expect an increase in wind shear or buoyancy to result in an increase in scintillation intensity.

The buoyancy term B depends on the vertical temperature distribution and is approximately given by [6]:

$$B = -K_h \frac{g}{\Theta} \frac{\partial \Theta}{\partial z} \tag{4.5}$$

Where, g is the gravitational acceleration, z is the height, and K_h is the eddy coefficient of heat conduction and Θ is the temperature (kelvin).

The results will show that by far the most influential meteorological factor in determining the intensity of scintillations is the temperature. The reader should note that all the correlation scattergrams to be shown in this section have linear regression lines fitted, and the correlation coefficients for each are given.

4.6. Correlation with Temperature and Humidity

To investigate the correlation between scintillation intensity σ_x, temperature and humidity, the hourly, six-hourly, twelve-hourly, daily, weekly and monthly temperature and humidity data were calculated for the entire period. The averaged scintillation intensities σ_x were computed by taking the mean of the standard deviations of the 1-minute blocks of the preprocessed scintillation data, with more than 90% valid samples. Therefore, hereafter when hourly, six-hourly, twelve-hourly, daily, weekly and monthly scintillation intensities are mentioned, we will mean the 1-minute value averaged for that particular period.

Figure 4.12 shows a scatter plot of the monthly averaged temperature versus standard deviation for the period covering September 1999 to August 2000 for the 20GHz beacon and September 1996 to August 1997 for the 40 and 50GHz beacons. One can see that there is a strong correlation between those two parameters, the correlation coefficients were 0.931, 0.945 and 0.956 at 20, 40 and 50GHz, respectively.

The relation between scintillation and ground temperature is further investigated in Figure 4.13, in which the scatter plot of the daily scintillation intensity (std) as a function of ground temperature is shown together with the best curve fit. This dependence was best approximated by using an exponential formula of the type $\sigma_x = ae^{bT}$; this is consistent with results found by Pratt and Haidara [15]. By observing the correlation of scintillation intensity and temperature for the various periods, from Table 4.6, it can be seen that the correlation increases as the averaging period increases. These results clearly show the importance of solar heating in the production of atmospheric turbulence. The scintillation intensity however is well represented by a linear function of the surface relative humidity and the surface wet-part of refractivity N_{wet}. Further discussion of the results will be made in the conclusions of this section.

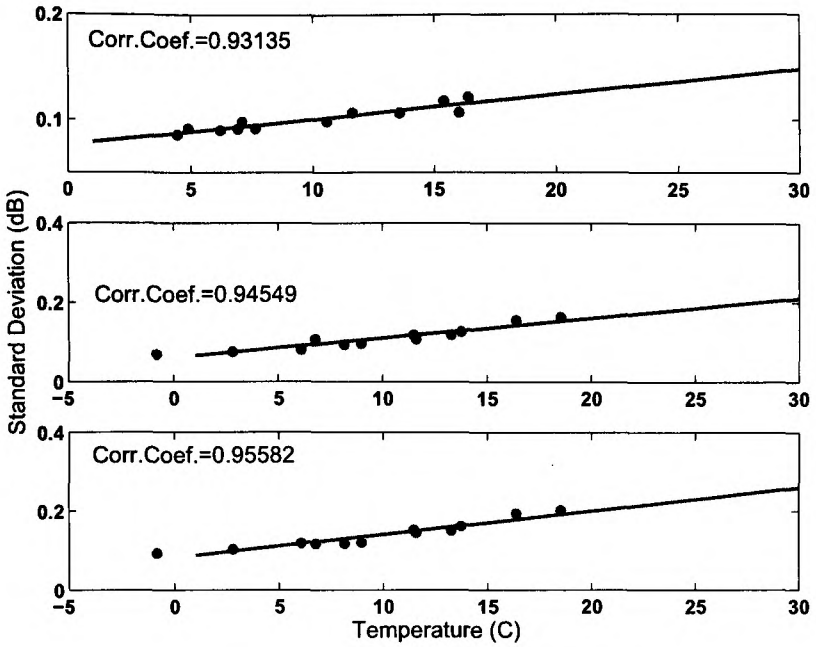

Figure 4.12. Starting from the top, monthly average temperature versus measured standard deviation at 20, 40 and 50GHz.

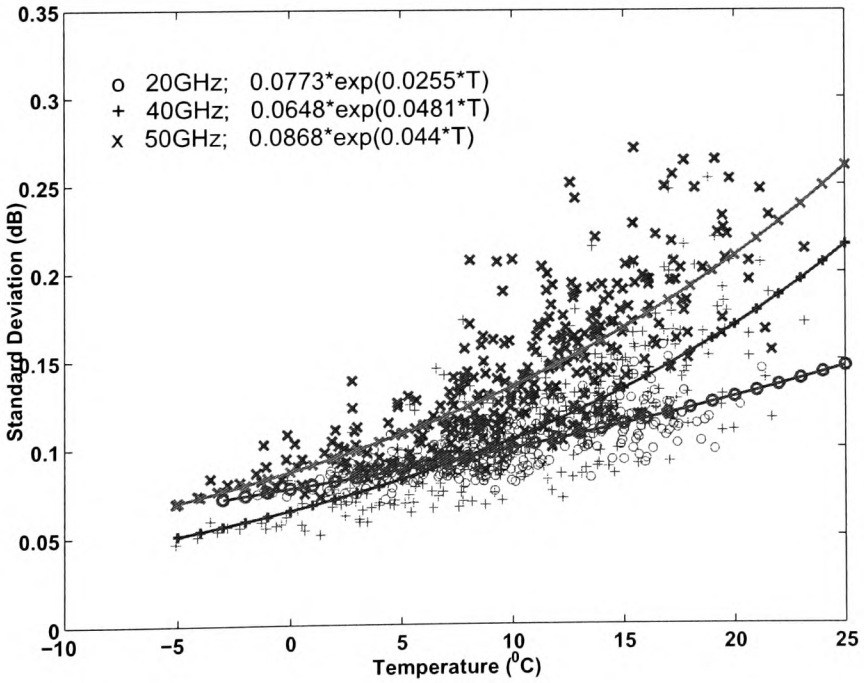

Figure 4.13. Scatter plot of daily average ground temperature as a function of the daily average scintillation intensity (std) at 20, 40 and 50GHz. The best-fit curves and their equations are also shown.

The correlation of monthly scintillation intensity with relative humidity at 20GHz is shown in Figure 4.14. The monthly correlation is found to be -0.549. However, it can be seen from Table 4.7 that there is no clear trend like the one observed with the averaged temperature. The correlations for other time periods are very low and negative. For example for an averaging period of one-day, the correlation is practically nonexistent, having values of -0.04 and -0.02 at 40 and 50GHz, respectively.

These findings agree with the results reported by Banjo and Vilar [16] based on their analysis of satellite beacon data at 11GHz, recorded in Southern England. They found a nearly zero correlation for the daily averages and a correlation of -0.31 for the hourly averaging period. Monthly averages were not reported.

Scintillation intensity increases directly with temperature and inversely with relative humidity. This can be explained by the fact that an increase in temperature which will result in warmer air, means that there will be a decrease in relative humidity due to the fact that warmer air being able to hold more moisture. This opposite behaviour can be seen in Figure 4.15. The highest temperatures occur during mid-day, where relative humidity is at its lowest value. The highest values of relative humidity occur during the nights. In terms of a diurnal cycle of period 24-hours, a phase difference of 180^0 (i.e. 12-hours) between temperature and relative humidity is observed.

Table 4.6: **Correlation coefficients between the measured standard deviation and temperature at 20, 40 and 50GHz, respectively, for different averaging periods.**

	20GHz	40GHz	50GHz
1-Hour	0.53142	0.58954	0.60207
6-Hour	0.61714	0.67707	0.67995
12-Hour	0.67467	0.72353	0.72477
1-Day	0.74198	0.75686	0.7719
1-Week	0.89023	0.90197	0.90762
1-Month	0.93135	0.94549	0.95582

Table 4.7: **Correlation coefficients between the measured standard deviation and relative humidity at 20, 40 and 50GHz, respectively, for different averaging periods.**

	20GHz	40GHz	50GHz
1-Hour	-0.23165	-0.23361	-0.22189
6-Hour	-0.1939	-0.256	-0.21229
12-Hour	-0.15908	-0.13988	-0.10253
1-Day	-0.12888	-0.04065	-0.019258
1-Week	-0.2509	-0.083394	-0.092938
1-Month	-0.54937	-0.20259	-0.22076

Table 4.8: **Correlation coefficients between the measured standard deviation and wet part of refractivity at 20, 40 and 50GHz, respectively, for different averaging periods.**

	20GHz	40GHz	50GHz
1-Hour	0.3897	0.47027	0.49889
6-Hour	0.50098	0.54755	0.5858
12-Hour	0.59259	0.66266	0.68355
1-Day	0.70653	0.74685	0.7667
1-Week	0.9047	0.9146	0.9216
1-Month	0.9425	0.9573	0.9708

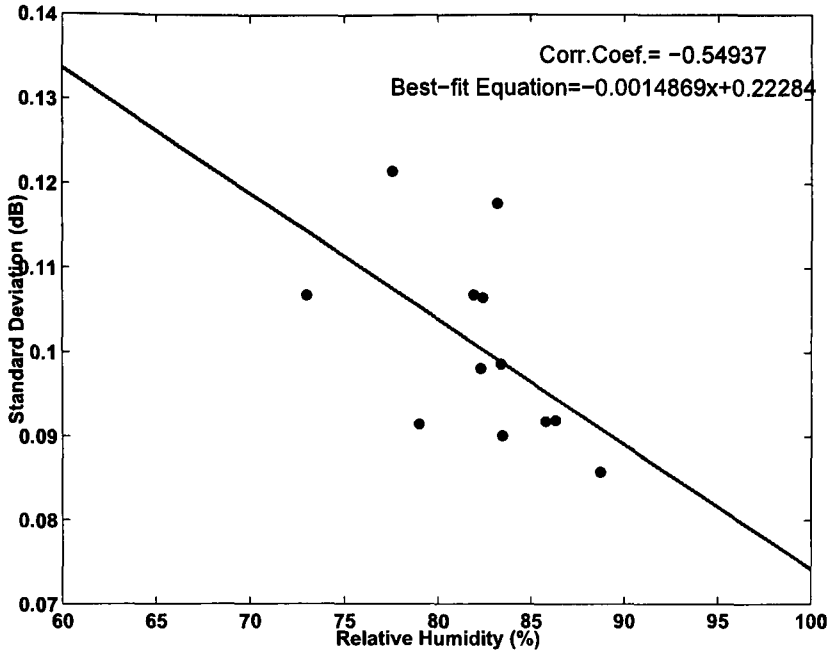

Figure 4.14. Monthly average relative humidity versus measured standard deviation for the period covering September 1999 to August 2000 at 20GHz.

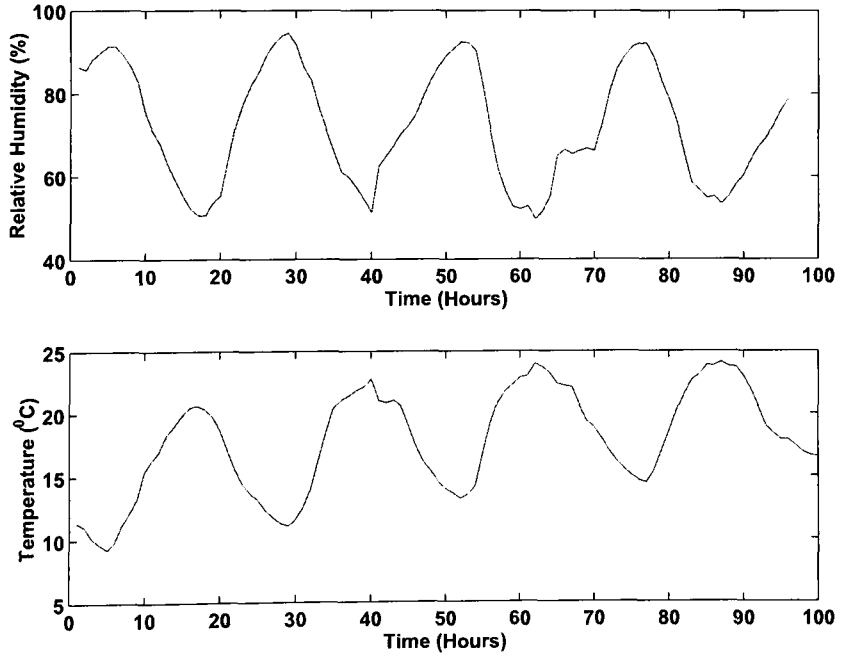

Figure 4.15. Variations of temperature and relative humidity.

The current prediction models (ITU-R, Karasawa and Otung) relate scintillation intensity to the wet-part of refractivity, N_{wet}, which is a function of ground temperature and humidity. In all three models those two meteorological parameters (temperature and humidity) should be averaged over a period of at least one month.

According to the ITU-R model, the relationship between temperature, humidity and the wet-part of refractivity N_{wet} is [17]

$$N_{wet} = 3730 He_s / (273 + t)^2 \quad \text{(ppm)} \tag{4.6}$$

where $e_s = 6.11\exp(19.7t / (t + 273))$ is the saturated water vapour pressure.
H is the mean-surface relative humidity in percent (%) and t is the mean-surface temperature in degrees centigrade (^{0}C).

Karasawa [12] found the average value σ_x for each month shows a high correlation to the wet-part of refractivity, N_{wet}, due to water vapour in the atmosphere, averaged over one month.

Figure 4.16 shows a scatter plot of the monthly averaged scintillation intensity (std) as a function of the averaged monthly wet-part of refractivity N_{wet}, for the period covering September 1999 to August 2000 at 20GHz and for the period covering September 1996 to August 1997 at 40 and 50GHz. The correlation coefficients obtained at 20, 40 and 50GHz are 0.943, 0.957 and 0.971, respectively. This very high correlation confirms the results obtained by Karasawa et al. [12] on which the current ITU-R model is based.

Figure 4.17 shows a scatter plot of the daily scintillation intensity σ_x versus N_{wet} for the period covering September 1996 to August 1997 at 50GHz. The observed significant correlation suggests that the accuracy of these prediction models is still significant for this relatively short time base. The correlation between scintillation intensity and the wet-part of refractivity at the three respective beacon frequencies, for different averaging periods is tabulated in Table 4.8. It can be seen that the same trend as the one followed by temperature is followed also by N_{wet}. As the period of observation increases so does the correlation, with the highest one observed in monthly averages.

4.7. Influence of the Averaging Period

We will now take a closer look at the influence of the length of the averaging period on the correlation between scintillation intensity and temperature, humidity and the wet-part of refractivity.

Tables 4.6-4.8 illustrated the observed correlation between the measured standard deviation, temperature, humidity and N_{wet} at the three frequencies. The correlation with temperature and N_{wet} was already >0.7, for averaging periods longer than 1-day at the three respective frequencies.

As we know the wet part of refractivity, N_{wet}, forms an important input into the current prediction models. Though for averaging periods of less than 1-day its correlation with the standard deviation drops significantly, making the prediction models less accurate in predicting scintillation for such short time scales. A modification to N_{wet}, was therefore necessary to improve its accuracy for such time periods. Below we introduce a new parameter, denoted W:

$$W = 3.732 \times 10^5 \times ((H^{1/5} \times e_s / 100) / T^{1/5}) \tag{4.7}$$

where e_s=6.1121 exp(17.502×t / t+240.97)

As can be seen from Table 4.9 to Table 4.11, the results obtained from the analysis of our data indicates that when W is plotted as a function of the standard deviation σ_x raised to the power of 1/5, an improvement of up to 40% can be achieved using this new relation, having values of 0.548, 0.635 and 0.659 at 20, 40 and 50 GHz, respectively, for an averaging period of 1-hour.

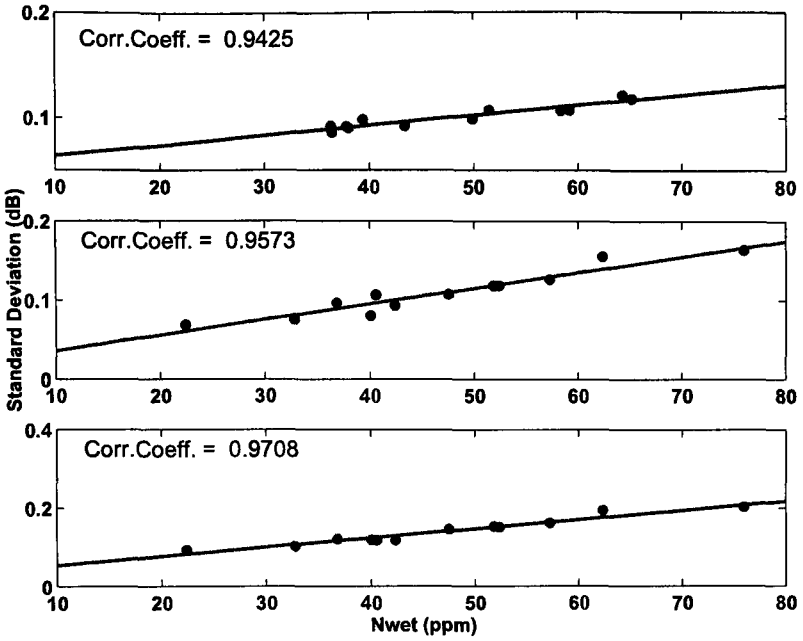

Figure 4.16. Starting from the top, monthly measured wet-part of refractivity (*Nwet*) versus measured standard deviation at 20, 40 and 50GHz.

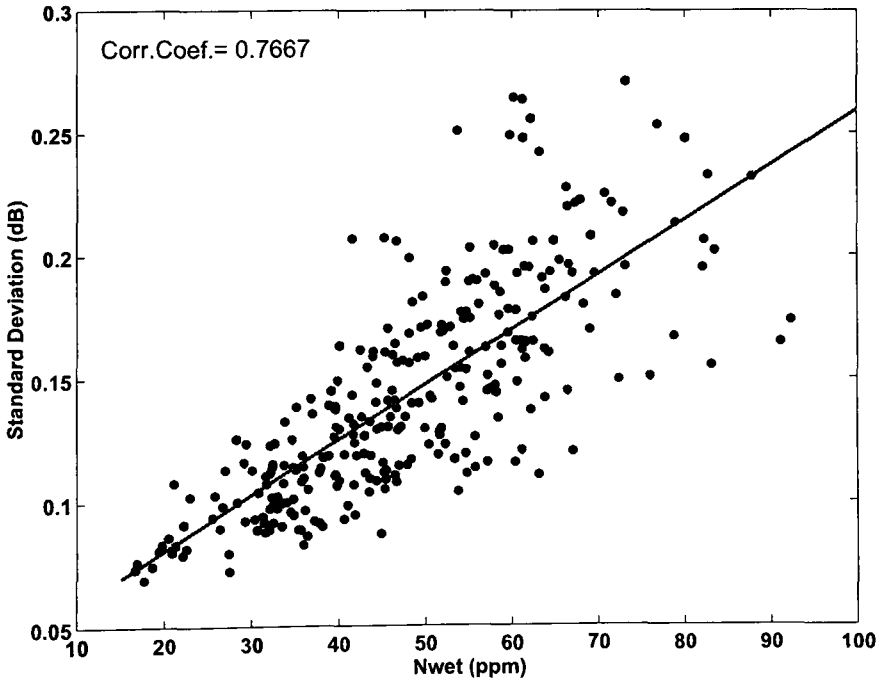

Figure 4.17. Daily wet-part of refractivity versus measured standard deviation for the period covering September 1996 to August 1997 at 50GHz.

Table 4.9: **Correlation coefficients between the measured standard deviation and modified wet-part of refractivity *W* at 20GHz, respectively, for different averaging periods.**

	20GHz	*W*	% improvement	*W* vs $(Std)^{1/5}$	% improvement
1-Hour	0.3897	0.53444	37.1	0.54828	40.7
6-Hour	0.50098	0.61980	23.7	0.63204	26.2
12-Hour	0.59259	0.67199	13.4	0.68175	15.0
1-Day	0.70653	0.73941	4.7	0.74743	5.8
1-Week	0.9047	0.89837	-0.7	0.89726	-0.8
1-Month	0.9425	0.93764	-0.5	0.93976	-0.3

Table 4.10: **Correlation coefficients between the measured standard deviation and modified wet-part of refractivity *W* at 40GHz, respectively, for different averaging periods.**

	40GHz	*W*	% improvement	*W* vs $(Std)^{1/5}$	% improvement
1-Hour	0.47027	0.59621	26.8	0.63519	35.1
6-Hour	0.54755	0.68072	24.3	0.70794	29.3
12-Hour	0.66266	0.72746	9.8	0.75118	13.4
1-Day	0.74685	0.76743	2.8	0.78476	5.1
1-Week	0.9146	0.92339	1.0	0.92197	0.8
1-Month	0.9573	0.97281	1.6	0.97030	1.4

Table 4.11: **Correlation coefficients between the measured standard deviation and modified wet-part of refractivity *W* at 50GHz, respectively, for different averaging periods.**

	50GHz	*W*	% improvement	*W* vs $(Std)^{1/5}$	% improvement
1-Hour	0.49064	0.61842	26.0	0.65887	34.3
6-Hour	0.57214	0.69600	21.6	0.72515	26.7
12-Hour	0.68355	0.74116	8.4	0.76435	11.8
1-Day	0.7667	0.78645	2.6	0.80204	4.6
1-Week	0.9216	0.93104	1.0	0.92891	0.8
1-Month	0.9708	0.98522	1.5	0.98742	1.7

4.8. Diurnal and Seasonal Variations of Scintillation Intensity

Scintillation is strongly dependent on temperature and water vapour densities. High temperature and water vapour densities give the greatest scintillation amplitude for a given path. As a consequence of this dependence we expect scintillation to exhibit geographical, seasonal and diurnal patterns of variations. Figure 4.18 and Figure 4.19 illustrate the seasonal variations of scintillation intensity and temperature. There is reasonable correlation between the two parameters, with scintillation reaching its peak in August which was the warmest month of the period.

It appears that irregularities in temperature, humidity and pressure are not the only cause of scintillation, but turbulence in clouds also contributes to the rapid fluctuations of the received signal and are responsible for a part of the measured scintillation effects. At millimetric wavelengths low cloud type (mainly cumulus clouds) are associated with the turbulent activity causing scintillations [18].

The hourly wet-part of refractivity N_{wet}, averaged over a period of one month, for each month of the year, covering the period from July 1996 to July 1997, was calculated using the meteorological data obtained from Brize-Norton meteorological station ($\approx$ 20km North of Sparsholt). The same scale was used for all seasons, in order to make the comparison clearer. The average diurnal variation of scintillation intensity is uncorrelated with N_{wet}, and strongly correlated with cumulus cloud cover as is evident in Figure 4.20, which shows plots of scintillation intensity, N_{wet}, and frequency of cumulus cloud occurrence versus time of day during the summer months. It can be seen that the diurnal variation of scintillation intensity corresponds very well with that of cumulus cloud cover. Scintillation intensity is larger in the day when cumulus cloud cover is also more frequent. N_{wet} on the other hand exhibits little or no diurnal variation, as illustrated in Figure 4.21.

The diurnal behaviour of Cumulus cloud and scintillation intensity are very well correlated, except in the winter months, when there is hardly any diurnal variation of scintillation at all. Whereas the seasonal behaviour is clearly correlated with N_{wet}, varying

from around 28 ppm in the cold winter months to about 64 ppm for the hot summer months. The seasons have been defined as: winter = December + January + February; spring = March + April + May; summer = June + July + August; autumn = September + October + November. These observations agree with the findings of Tervonen et al [19], based on the analysis of Olympus satellite measurements at 20 and 30 GHz in Southern Finland at a path elevation of 12.7°.

Significant fluctuations in the refractive index are most likely to occur in regions where weather fronts of warm moist air meet colder, drier air. Such circumstances are typically accompanied by the production of heavy cumulus cloud and precipitation. Mohd Yusoff *et al.* [20] suggested that the significant difference in the scintillation intensities observed for their wet databases from Goonhilly, U.K. (for the period covering February 1988 to August 1990) may be caused by what they called "turbulent attenuation". It is an effect caused by turbulent mixing of air masses with different water contents in and around clouds and precipitation.

Our analysis also showed that greater intensities were observed during the presence of cumulus clouds. Table 4.12 shows the mean, median and maximum scintillation intensities observed during periods with and without cumulus cloud cover. It can be seen that there is a significant increase in the scintillation levels observed, the mean value of the calculated scintillation intensity during cumulus cloud presence was ~ 74% higher in comparison with periods during which there were no cumulus clouds present. The median and maximum values were 64% and 45% higher, respectively.

These results are consistent with the thinking that physical processes occurring in clouds give rise to some of the atmospheric turbulence activities responsible for scintillation. Thus our observations appear to confirm that scintillation levels are increased when an earth-space path is crossed by clouds, which (due to their temperature as well as content of water and water vapour) have nonhomogenous refractive index values that are significantly different from those of the surrounding clear air.

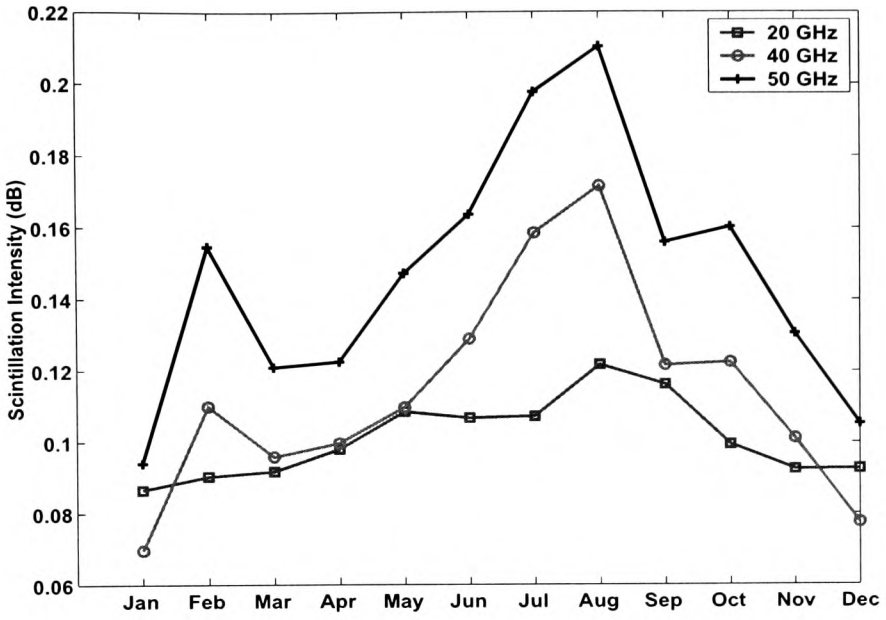

Figure 4.18. Monthly variations of scintillation intensity (std) at 20, 40 and 50GHz over a period of one-year.

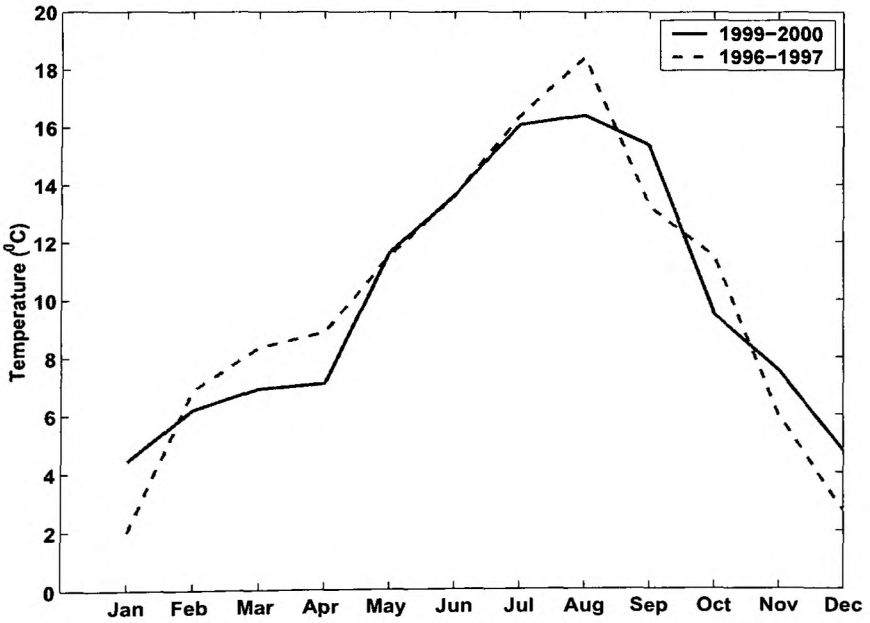

Figure 4.19. Monthly variations of temperature for the period covering Sep.1996 to Aug.1997 and Sep.1999 to Aug.2000.

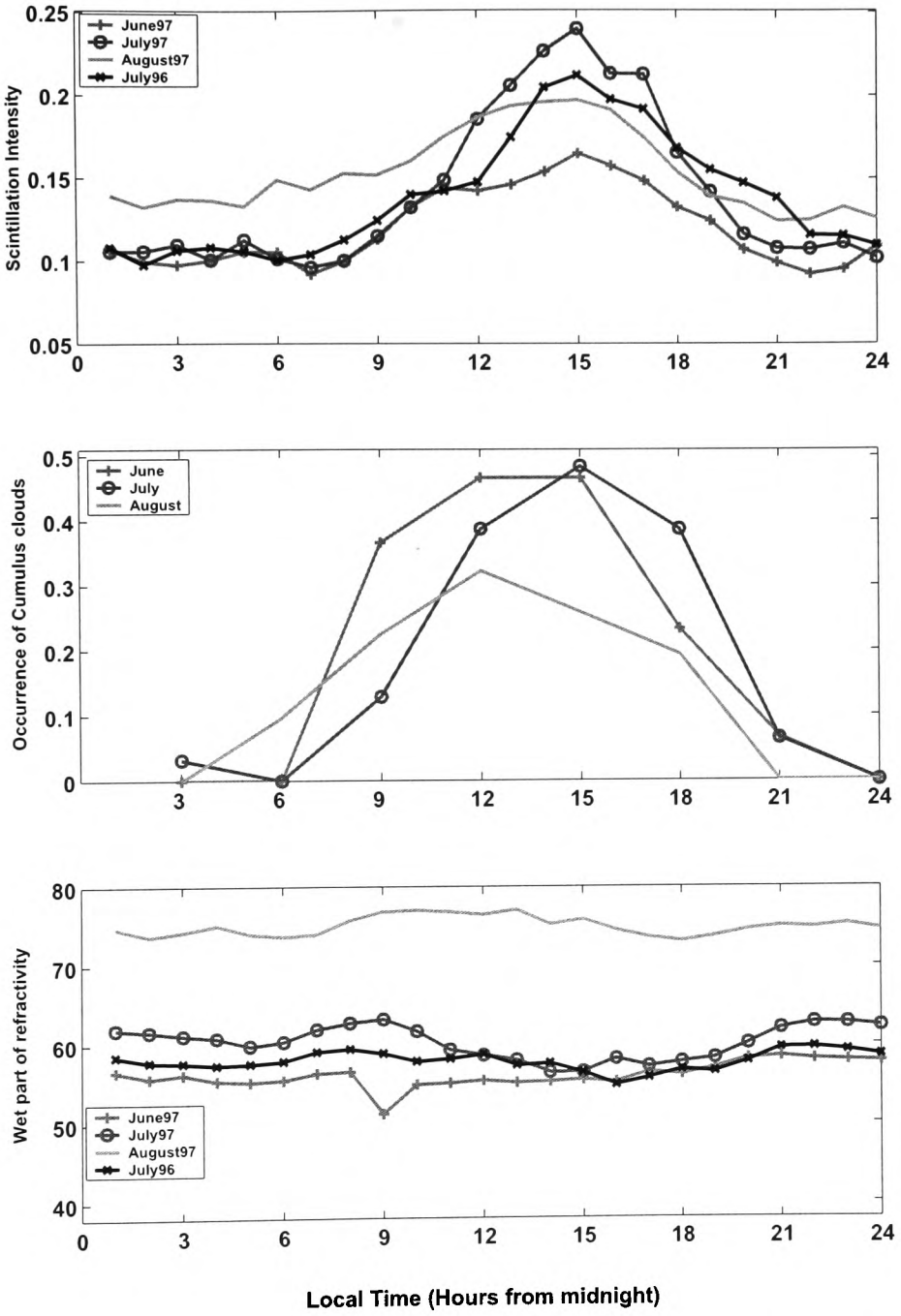

Figure 4.20. Diurnal variation of scintillation intensity, frequency of occurrence of cumulus clouds, and wet-part of refractivity (N_{wet}).

Table 4.12: Variations of scintillation intensity with cumulus cloud cover.

	Cumulus Cloud Present	No Cumulus Present	Difference (%)
Mean (dB)	0.2103	0.1211	73.658 %
Median (dB)	0.1852	0.1132	63.604 %
Maximum (dB)	0.5814	0.3999	45.386 %

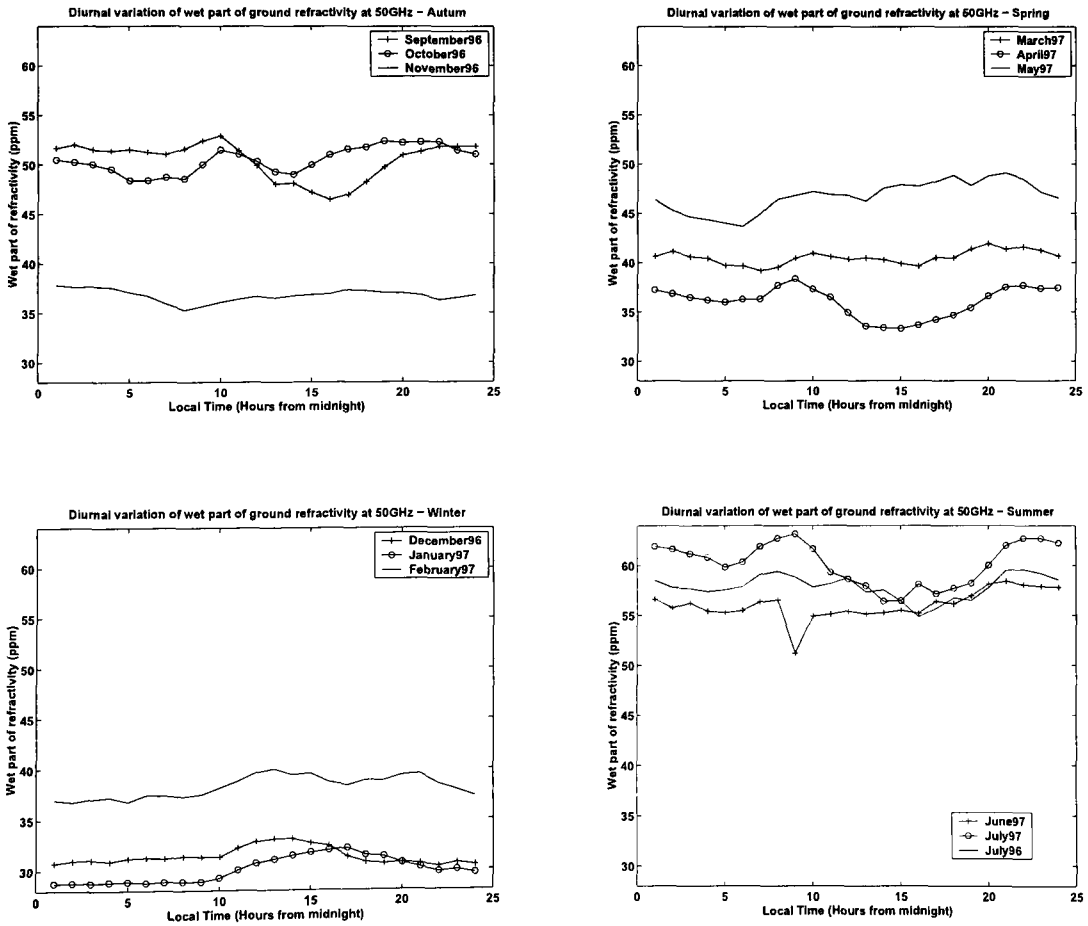

Figure 4.21. The diurnal and seasonal variation of wet part of ground refractivity, covering the period from July96 to July97, based on measurement data from Brize-Norton meteorological station.

4.9. Correlation with Wind Speed

In Section 4.5.1 we saw that there are two mechanisms by which atmospheric turbulence is produced, namely wind shear and buoyancy. The rate of production of turbulent energy M by wind shear is caused by the rate of change of wind velocity with height and is given by [6]:

$$M = K_m[(\partial v_x / \partial z)^2 + (\partial v_y / \partial z)^2] \tag{4.8}$$

Where, K_m is the coefficient of eddy viscosity, v_x and v_y are two orthogonal horizontal components of the wind velocity.

From the geometry shown in Figure 4.22, the expression for the transverse wind speed for a given azimuth (A) and elevation (α), the magnitude of the transverse wind component (v_t) due to a wind of speed (v) and wind direction (ϕ) relative to True North is given by [16]:

$$v_t = v[1 - \cos^2(\alpha)\cos^2(A - \phi)]^{1/2} \tag{4.9}$$

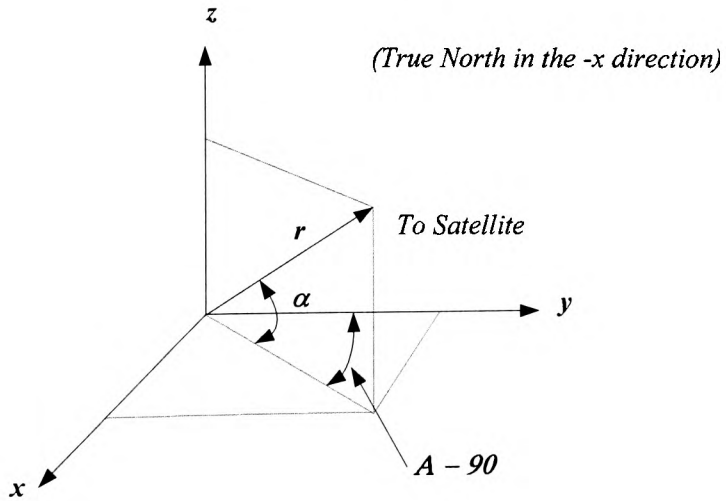

Figure 4.22. Geometry used for calculating the transverse wind speed

The correlation between hourly scintillation intensity (σ_x) and transverse wind speed (v_t) at 40 and 50GHz was found to be practically nonexistent, having values of 0.098 and 0.054, respectively, as shown in the scatter plots of Figure 4.23. This observed lack of correlation between scintillation intensity and transverse wind speed appears to be consistent with the assumption of a floating frozen turbulence structure in a largely horizontally homogeneous atmosphere. In this scenario, the effect of a strong wind presence is primarily to increase the rapidity with which eddies of roughly the same temperature, humidity and pressure are transported across the link. This would not be expected to contribute to an increase in the energy of the turbulence and hence of scintillation intensity, since the average features are maintained during the horizontal movement of the eddies [21, 22]. An increase in the energy of turbulence requires an exchange of features between mixing eddies, a situation created by buoyancy, wind shear and cloud activities, but not by strong winds acting alone in say a perfectly homogeneous atmosphere.

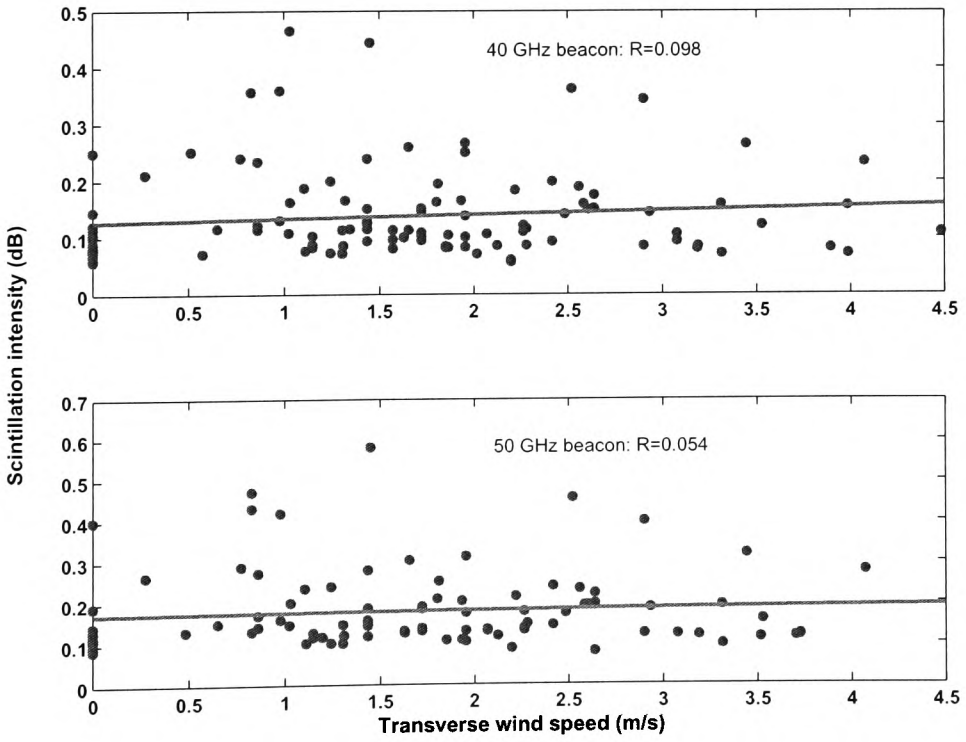

Figure 4.23. Scatter plot of scintillation intensity versus transverse wind speed.

4.10. Conclusions

The analysis carried out in this Chapter can be split into two parts; i) statistical analysis and ii) meteorological analysis.

The extensive study of the probability density function (pdf) of scintillation amplitude and standard deviation have shown that for short time intervals, scintillation amplitude fluctuations can be assumed to follow a Gaussian distribution, whereas the long-term amplitude fluctuations are definitely not Gaussian.

A visual inspection of the long-term scintillation intensity distribution would suggest that it follows reasonably well a Lognormal or a Gamma distribution, however this would be wrong in light of the Chi-square goodness-of-fit test. The results suggest that the likelihood of a distribution being a Lognormal or a Gamma is very small. Another conclusion, which may be drawn based on the results obtained from the analysis is that out of the two distributions of the 1-min scintillation intensity, the Lognormal distribution gives a slightly better approximation than the Gamma distribution.

The second part of the analysis in this chapter investigates the relation of scintillation with various meteorological parameters. Scintillation intensity was found to exhibit a clear diurnal and seasonal pattern of variations, which are due to the strong dependence of scintillation intensity on temperature.

In Section 4.5.1 we saw that there are two mechanisms by which atmospheric turbulence is produced, namely wind shear and buoyancy. The results show that by far the most influential factor is the (surface) temperature, and that the correlation with humidity is an indirect effect of this. Cumulus clouds appear to be responsible for at least part of the increase in the scintillation levels observed.

During hot weather solar heating of the ground results in a layer of warm air at the Earth's surface. The amount of solar heating of the ground will be related to the surface air

temperature. Based on Equation (4.5) this would result in an increase in turbulence due to the increase in buoyancy. Therefore the largest temperatures would produce the most turbulence and on this basis one would expect a correlation between temperature and scintillation intensity. In addition the correlation between scintillation intensity, temperature and the wet-part of refractivity increases as the averaging period increases.

Based on Equation (4.8) we would also expect an increase in wind shear to result in an increase in scintillation intensity. The experimental results however suggest that the increase in turbulence due to wind shear is very small. This appears to be consistent with the assumption of a floating frozen turbulence structure in a largely horizontally homogeneous atmosphere. In a perfectly homogeneous atmosphere the effect of a strong wind presence is primarily to increase the rapidity with which eddies of roughly the same features (temperature, humidity and pressure) are transported across the link. This would not be expected to contribute to an increase in the energy of the turbulence and hence of scintillation intensity, since the average features are maintained during the horizontal movement of the eddies.

This might also explain why in the cooler months of the year there is little or no observed diurnal variations in scintillation intensity. The effects of buoyancy dominate those of wind shear, and thus in cooler months when turbulence due to buoyancy is low, the observed scintillation levels are also low.

The hot weather as well causes a decrease in relative humidity due to the warmer air being able to hold more moisture, which explains the negative correlation observed between scintillation intensity and relative humidity.

Finally, the seasonal behaviour of scintillation intensity is clearly correlated with the wet-part of refractivity N_{wet}, whereas the diurnal behaviour appears to be due to contributions from cumulus cloud. Scintillation intensity and cumulus cloud presence are very well correlated except in the winter months when there is hardly any diurnal variation of scintillation. Furthermore, our analysis showed that greater intensities were observed during the presence of cumulus clouds. The mean value of the calculated scintillation

intensity during cumulus cloud presence was ~ 74% higher in comparison with periods during which there were no cumulus clouds present. These results are consistent with the thinking that physical processes occurring in clouds give rise to some of the atmospheric turbulence activities responsible for scintillation.

References

[1] T. J. Moulsley and E. VILAR, "Experimental and Theoretical Statistics of Microwave Amplitude Scintillations on Satellite Down-Links," *IEEE Transactions on Antennas and Propagation*, vol. 30, pp. 1099-1106, 1982.

[2] I. E. Otung, M. S. Mahmoud, and B. G. Evans, "Dual Frequency Scintillation Measurement for Remore Sensing," *Electronics Letters*, vol. 31, pp. 1972-1973, 1995.

[3] M. M. J. L. V. d. Kamp, "Asymmetric Signal Level Distribution due to Tropospheric Scintillation," *Electronics Letters*, vol. 34, pp. 1145-1146, 1998.

[4] I. E. Otung and B. G. Evans, "Short-Term Distribution of Amplitude Scintillation on a Satellite Link," *Electronics Letters*, vol. 31, pp. 1328-1329, 1995.

[5] K. A. Norton, L. E. Vogler, W. V. Mansfield, and P. J. Short, "The Probability Distribution of the Amplitude of a Constant Vector Plus a Rayleigh-Distributed Vector," *Proceedings of IRE*, vol. 43, pp. 1354-1361, 1995.

[6] A. Ishimaru, *Wave Propagation and Scattering in Random Media*: IEEE Press, 1997.

[7] O. P. Banjo, "An Investigation of Microwave Scintillations on Low-Elevation Satellite Link, with Application to Communication Systems." Portsmouth: Portsmouth University, 1986.

[8] G. Ortgies, "Probability Density Function of Amplitude Scintillations," *Electronics Letters*, vol. 21, pp. 141-142, 1985.

[9] T. J. Moulsley, J. Haddon, P. Lo, and E. Vilar, "Measurement and Modelling of the Probability Density Function of Amplitude Scintillations on an X-Band Satellite Down-Link," *Electronics Letters*, vol. 17, 1981.

[10] O. P. Banjo and E. Vilar, "Measurement and modelling of amplitude scintillations on low-elevation earth-space paths and impact on communication systems," *IEEE Transactions on Communications*, vol. COM-34, pp. 774-780, 1986.

[11] G. Ortgies, "Prediction of Slant-Path Amplitude Scintillations from Meteorological Parameters," presented at Proc. Int. Symp. on Radio Propagation, Beijing, 1993.

[12] Y. Karasawa, M. Yamada, and J. E. Allnutt, "A New Prediction Method for Tropospheric Scintillation on Earth-Space Paths," *IEEE Transactions on Antennas and Propagation*, vol. 36, pp. 1608-1614, 1988.

[13] F. Marzano and G. D'Auria, "Model-Based Prediction of Amplitude Scintillation Variance Due to Clear-air Tropospheric Turbulence on Earth-Satellite Microwave Links," *IEEE Transactions on Antennas and Propagation*, vol. 46, pp. 1506-1518, 1998.

[14] ITU-R, "P.618-7 Propagation data and prediction methods required for the design of Earth-space telecommunication systems," Recommendations and Reports of the ITU-R 1997.

[15] T. Pratt and F. M. Haidara, "Results from a Study of Scintillation Behavior at 12, 20 and 30 GHz Using the Results from the Virginia Tech Olympus Receivers," presented at International Communications Satellite Systems Conference (AIAA 1994), 1994.

[16] O. P. Banjo and E. Vilar, "The dependence of slant path amplitude scintillations on various meteorological parameters," presented at International Conference on ANtennas and Propagation (ICAP 87), 1987.

[17] ITU-R, "P.453-8: The Radio Refractive Index: Its Formula and Refractivity Data," Recommendations and Reports of the ITU-R 2001.

[18] D. C. Cox, H. W. Arnold, and H. H. Hoffman, "Observations of cloud-produced amplitude scintillation on 19- and 28-GHz earth-space path," *Radio Science*, vol. 16, pp. 885-907, 1981.

[19] J. K. Tervonen, M. M. J. L. V. d. Kamp, and E. T. Salonen, "Prediction Model for the Diurnal Behaviour of the Tropospheric Scintillation Variance," vol. 46, pp. 1372-1378, 1998.

[20] M. M. B. M. Yusoff, N. Sengupta, C. Alder, I. A. Glover, P. A. Watson, R. G. Howell, and D. L. Bryant, "Evidence for the Presence of Turbulent Attenuation on Low-Elevation Angle Earth-Space Paths - Part 1: Comparison of CCIR recommendation and Scintillation Observations on a 3.3^0 Path," *IEEE Transactions on Antennas and Propagation*, vol. 45, pp. 73-84, 1997.

[21] H. Vasseur and D. Vanhoenacker, "Characterization and Modelling of Turbulence-Induced Scintillation on Millimetre-Wave Line-of-Sight Links," presented at Internation Conference on Antennas and Propagation (ICAP95), 1995.

[22] A. Savvaris, C. N. Kassianides, and I. E. Otung, "Observed Effects of Cloud and Wind on the Intensity and Spectrum of Scintillation," *IEEE Transactions on Antennas and Propagation*, vol. 52, pp. 1492-1498, 2004.

CHAPTER V

Spectral Analysis

Summary – *This Chapter examines the observed effects of wind and cloud presence on the intensity and power spectrum of tropospheric scintillation, using the ITALSAT propagation data recorded at 20, 40 and 50GHz. The results show strong correlation between corner frequency and transverse wind speed, a weaker correlation with overall wind speed and a dependence on beacon frequency. Furthermore, a weak correlation exists between wind speed, scintillation intensity and the slopes of weak-to-moderate scintillation spectra. Finally, it was found that the presence of cumulus clouds led, on average, to increased scintillation levels and a reduced correlation of the corner frequency with wind speed, this is followed by a discussion in using the slant path spectrum as a tool for remote sensing applications.*

5.1. Introduction

This Chapter presents the results from the analysis of scintillation power spectral density (psd). The power spectral density of amplitude scintillation is an indication of the contribution to the scintillation variance σ_x^2 of a particular fluctuation frequency (Fourier component). The spectrum is thus of use in determining how fast the received signal level can be expected to change. The spectrum is also of use as a tool for remotely sensing parameters of the turbulence as we will see in Section 5.6. Most of the results presented in this Chapter have been published in the *IEEE* paper [1] titled "Observed Effects of Clouds and Wind on the Intensity and Spectrum of Scintillation".

5.2. Theoretical Considerations

Assuming a floating frozen turbulence structure, the power spectrum of amplitude scintillations in a point receiver antenna has a shape similar to that of a 'low pass filter' frequency response with a defined flat region followed by a single-slope high frequency roll-off of $f^{-8/3}$, which is derived from the assumption that spatial irregularities of the atmospheric refractive index follow Kolmogorov's turbulence spectrum. Ishimaru [2] derived the following expressions for the two regions:

$$W_x{}^0(\omega) = 2.765\frac{\sigma_x{}^2}{\omega_t} \qquad (\text{as } \omega \to 0) \tag{5.1}$$

$$W_x{}^\infty(\omega) = 7.13\frac{\sigma_x{}^2}{\omega_t}\left(\frac{\omega}{\omega_t}\right)^{-8/3} \qquad (\text{as } \omega \to \infty) \tag{5.2}$$

where,

$W_x^o(\omega)$ denotes the low frequency asymptote of the power spectrum density (psd) of scintillation.

$W_x^{\infty}(\omega)$ denotes the high frequency asymptote of the power spectrum density (psd) of scintillation.

$\omega = 2\pi f$ represents the Fourier frequency in the scintillation spectrum,

σ_x^2 is the variance of the log-amplitude fluctuations given by:

$$\sigma_x^2 = 23.16 C_n^2 k^{7/6} L^{11/6} \qquad (dB^2) \tag{5.3}$$

C_n^2 is the refractive index structure constant of the atmosphere, with a value of the order 10^{-9} for weak turbulence, and

$\omega_t = v_t\,[k/L]^{1/2}$, where $k=2\pi/\lambda$ is the wave number, v_t is the wind velocity component transverse to the propagation path, and L is the effective turbulent path length.

The point where the two regions intersect is referred to as the corner frequency ($\omega_c = 2\pi f_c$), which is related to the transverse wind velocity component by the equation [2]:

$$\omega_c = 1.43 v_t (k/L)^{1/2} \tag{5.4}$$

where,

$L = 2h/\{\sqrt{\sin^2\theta + (2h/R_e)} + \sin\theta\}$ is the effective turbulent path, h is the height of turbulence taken as h = 2000m (according to Karasawa *et al.* [3]), R_e is the effective earth radius = 8.5×10^6 m, θ is the elevation angle.

It follows from Equation (5.4) that if wind velocity v_t increases, then the scintillation fluctuations will be distributed over a wider frequency band.

As we mentioned previously in Section 4.9, Equation (5.3) directly relates scintillation intensity σ_x to the refractive index structure constant C_n^2, which is a measure of the energy in the fluctuations of the normalised refractive index. This is in turn directly related to the energy of the turbulence [2].

5.3. Calculating the Power Spectral Density (Psd)

Following the pre-processing of the raw propagation data [4], the hourly averaged scintillation intensities σ_x were computed by taking the mean of the standard deviations of sixty 1-minute blocks of the scintillation data centred around the instant of wind speed measurement. The power spectral density (psd in dB^2/Hz) of each signal was computed on a block of 2048 samples by breaking the block into seven half-overlapping segments of 512 samples, removing the mean from each segment before multiplying by a Hanning window and finally averaging the periodograms of the modified segments. The power spectral density was then smoothed using a third-order median filtering [5]. Note that for this analysis the dataset was not divided into rainy ('wet') and nonrainy ('dry') subsets. Figure 5.1 shows the power spectrum of signal fluctuations for a period of 34.13 min, with an identified slope of –1.1717 and an estimated corner frequency of 0.167 Hz. The shape is very similar to that theoretically predicted by assuming a Kolmogorov spectrum of atmospheric refractivity fluctuations [6]. However, a significant number of observed scintillation spectra did not follow this predicted shape.

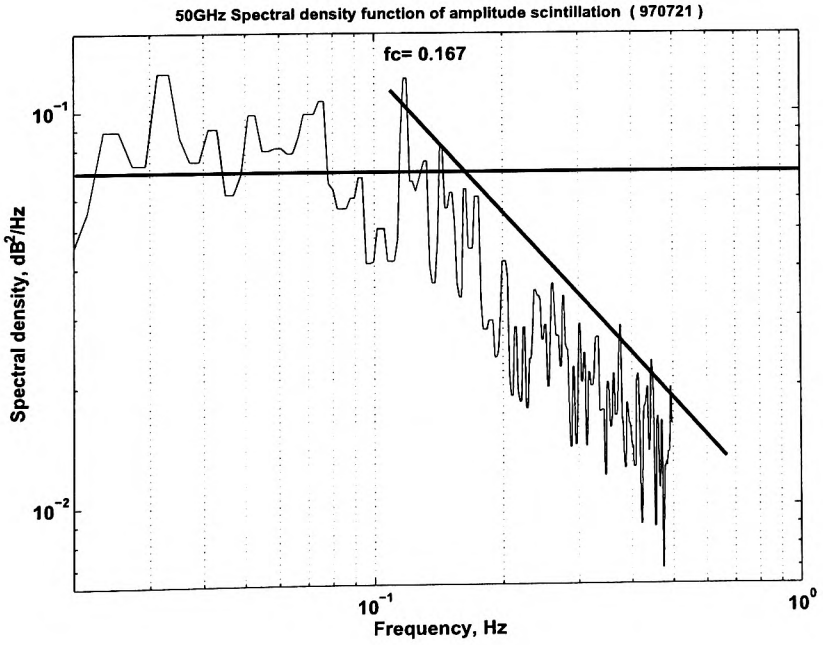

Figure 5.1. Power spectral density (psd), with an identifiable slope of -1.1717 and corner frequency f_c=0.167.

5.4. Effect of Wind

Power spectral densities (psd) at the respective beacon frequencies for the same period were computed in order to investigate the degree of correlation of corner frequency and scintillation intensity with various meteorological parameters. The spectral corner frequency f_c was obtained from the smoothed psd (an example of which is shown in Figure 5.1) using an algorithm that computed f_c as the first Fourier component in the spectrum beyond which all subsequent components had values at least 3 dB below the maximum value of the "flat" region. Spectra without an identifiable sloping region were excluded from the analysis. Figure 5.2, shows the cumulative distributions of the estimated corner frequencies at 20, 40 and 50GHz for the period covering May 1997 to July 1997.

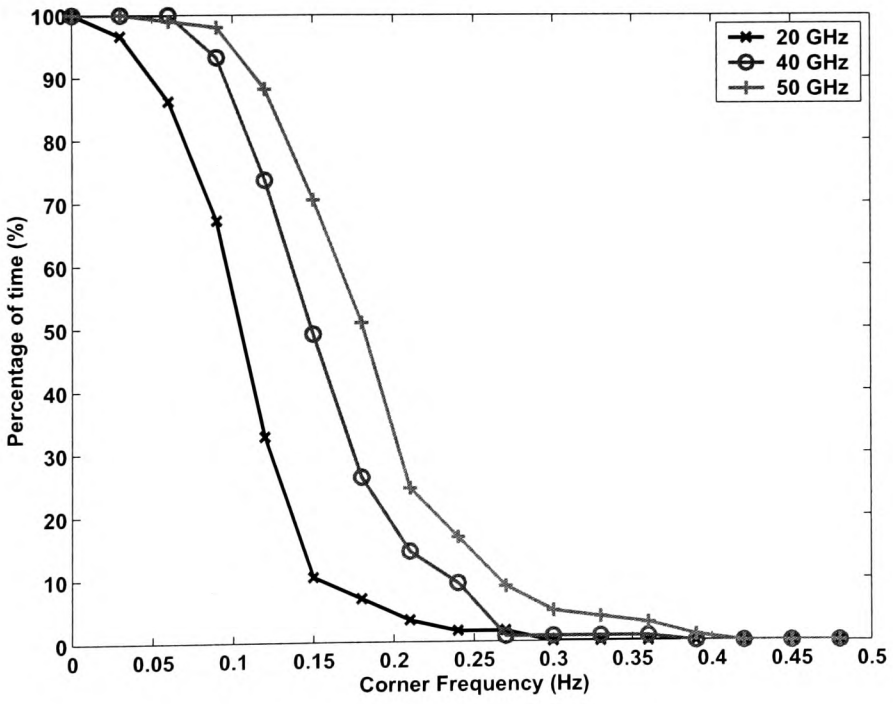

Figure 5.2. Cumulative distributions of scintillaion power spectral density (psd), at 20, 40 and 50GHz for the period covering May 1997 to July 1997.

It is worth noting that in this figure the corner frequency shows a dependence on frequency. The corner frequency f_c has been calculated using the assumption of the

Kolmogorov spectrum (see Chapter 2), that implies n=11/3 for the slope of the intermediate spectral region, which give the theoretical roll-off slope of $f^{-8/3}$. This theory assumes a uniform atmosphere along the propagation path, i.e. between the ground and the top of the turbulent layer, which is clearly not valid in the case of an Earth-space path. Van de Kamp [7], Vilar and Haddon [8] reported similar observations regarding the spectral slope. The latter reported that the power spectrum slope varies between 1.7 and 3.7, and is correlated to the scintillation variance. Banjo [9] reported that on a low-elevation link there are some differences between the spectra during weak and strong scintillations, with the stronger scintillations corresponding to a higher value of corner frequency and also a steeper spectral slope.

The findings illustrated in Figure 5.3 and Figure 5.4 are consistent with these observations. Both spectra were calculated for a period of 34.13 minutes. Because of the sampling frequency of 1 Hz i.e. one sample per second, in this time period (34.13 min.) there are 2048 samples of the data. The main features of those two power spectral densities are tabulated in Table 5.1 below. The spectral slope and estimated corner frequency calculated on the 28th and 16th of June 1997 at 40GHz are respectively 0.074, -1.986 and 0.23, -2.555. We can see that as scintillation intensity increases, the slope becomes steeper and the estimated value for the corner frequency is higher. As we mentioned previously for this analysis the dataset was not divided into rainy ('wet') and nonrainy ('dry') subsets. The choice of filter cut-off frequency ensured that all non-scintillation effects were excluded from the data fluctuations as further described and justified in [5].

Table 5.1: Main features of the power spectral densities calculated on 28th and 16th of June 1997 at 40GHz.

Date	**970628**	**970616**
Corner freq. (f_c)	0.0742 (Hz)	0.23 (Hz)
Slope	-1.9862	-2.5550
Measured transverse wind Speed	0.8611 (m/s)	2.2219 (m/s)
Calculated wind speed	0.92 (m/s)	2.2110 (m/s)
1-min. standard deviation (std)	0.1243 (dB)	0.1836 (dB)
Average Temperature	11.56 ^{0}C	13.53 ^{0}C

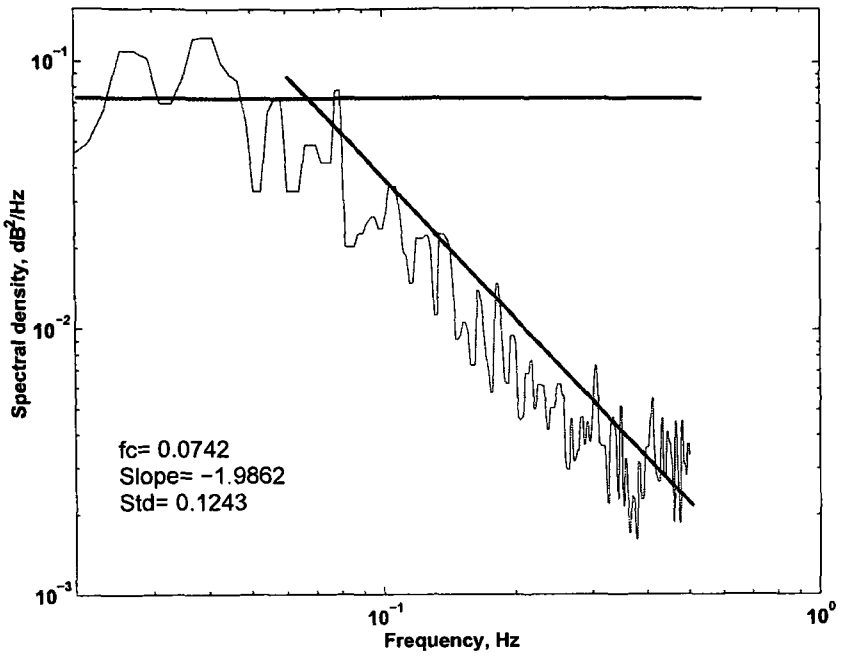

Figure 5.3. Power spectral density of amplitude scintillation calculated for a period of 34.13 minutes (2048 samples) on the 28th June 1997 at 3 pm, with an identifiable slope of -1.9862 and standard deviation of 0.1243 dB.

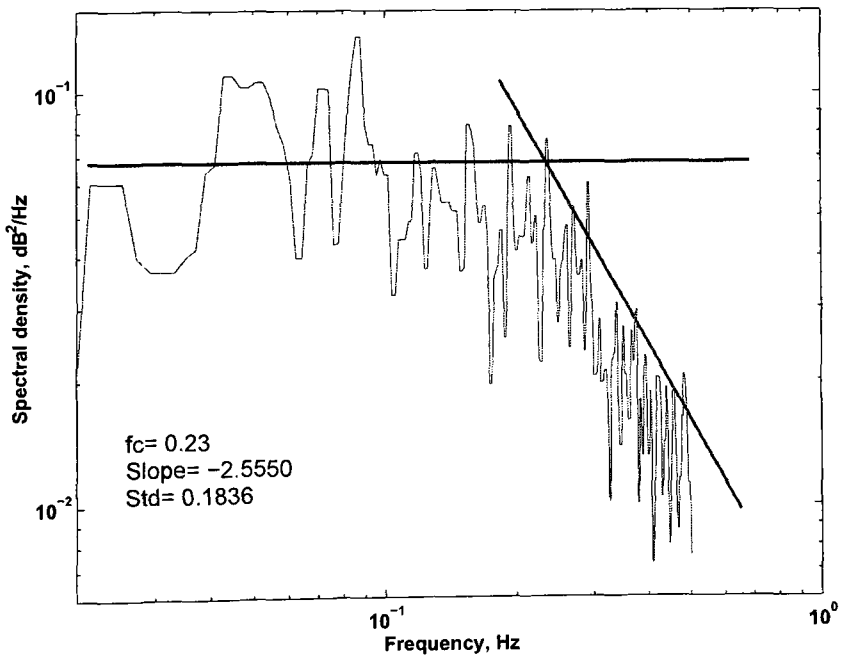

Figure 5.4. Power spectral density of amplitude scintillation calculated for a period of 34.13 minutes (2048 samples) on the 16th June 1997 at 10 am, with an identifiable slope of -2.555 and standard deviation of 0.1836 dB.

A brief analysis of the effects of meteorological parameters on the power spectrum slope of amplitude scintillation have already been published in the paper [10] in Appendix E. The power spectrum slope during weak-to-moderate scintillations obtained from the experimental spectra for the period covering April 1997 and July 1997 at 40 and 50GHz, was found to vary from -0.6092 to -2.272, which is significantly lower than the theoretical -2.667 slope, for fully developed turbulence. This variability in the power spectra shape could be caused by the variable nature of propagation conditions along the Satellite-Earth link. Furthermore, the results show a weak correlation between the spectrum slope, transverse wind speed and scintillation intensity, having correlation coefficients of 0.304 and 0.379, respectively.

The power spectral density (psd) under cold and rainy weather conditions were also investigated. Figure 5.5, shows the psd of the signal recorded during a rain event on the 21st of February 1997 at 40GHz. The rain rate at the measurement site reached values up to 14mm/hr. As for the cold clear-air conditions (Figure 5.6), the data records were obtained in clear cold days in January 1997, the daily average temperature was -1.1^{0}C. Both graphs have a similar shape to that theoretically predicted by assuming a Kolmogorov spectrum of atmospheric refractivity fluctuations. Furthermore, the only difference between the spectra observed during the summer from those observed during the winter period is that the flat-region of the scintillation spectrum in winter was about 1×10^{-2} dB^2/Hz, whereas for the summer samples it climbed to the higher level of 8×10^{-2} dB^2/Hz. The stronger turbulence in summer accounts for this observed rise in the flat-region of the spectrum.

The corner frequency is further investigated in Figure 5.7, the experimental results obtained show there is a significant correlation between the estimated corner frequency and transverse wind speed, with correlation coefficients of 0.629 and 0.544 at 39.59 GHz and 49.49 GHz, respectively. Correlation with over-all wind speed was found to be somewhat smaller, with values of 0.5411 and 0.4343 at the respective beacon frequencies. This reduced correlation is expected since the longitudinal component of the wind velocity has a negligible effect on the observed scintillation process.

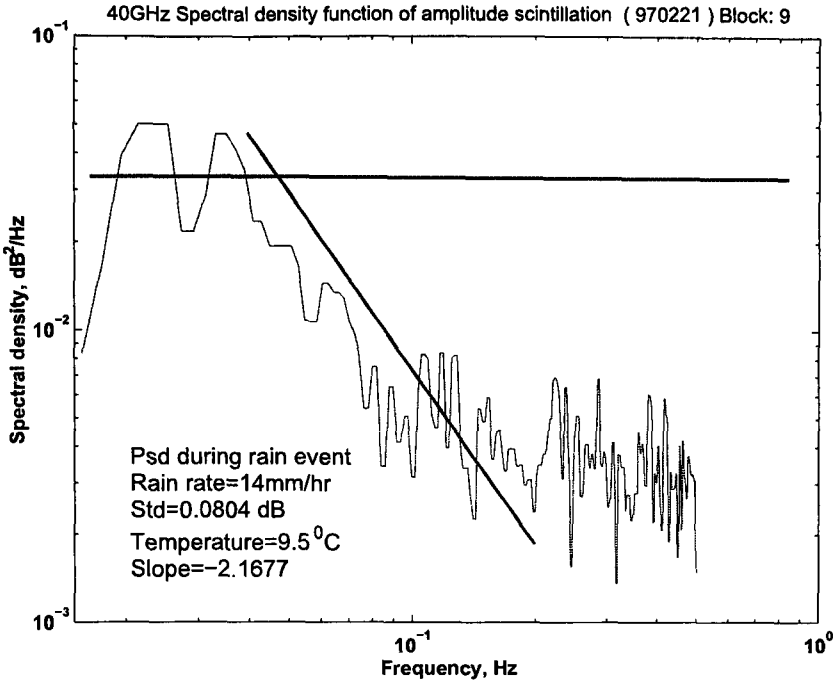

Figure 5.5. Power spectral density of amplitude scintillation calculated during a rain event on the 21st of February 1997 at 9 am, with an identifiable slope of -2.1677 and standard deviation of 0.0804 dB.

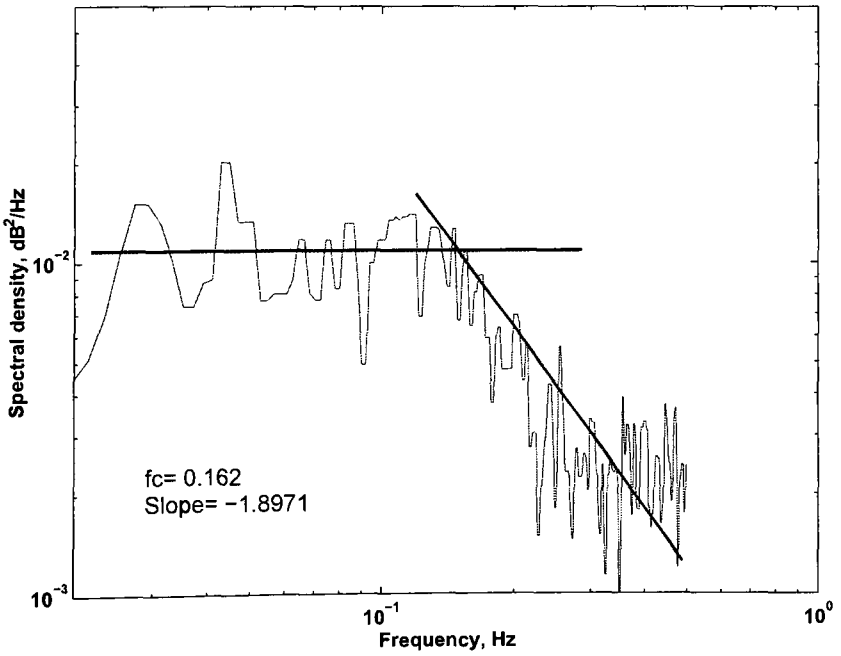

Figure 5.6. Power spectral density of amplitude scintillation calculated on a cold clear-sky day on the 10th of January 1997 at 9 am, with an identifiable slope of -1.8971 and corner frequency of 0.162 Hz.

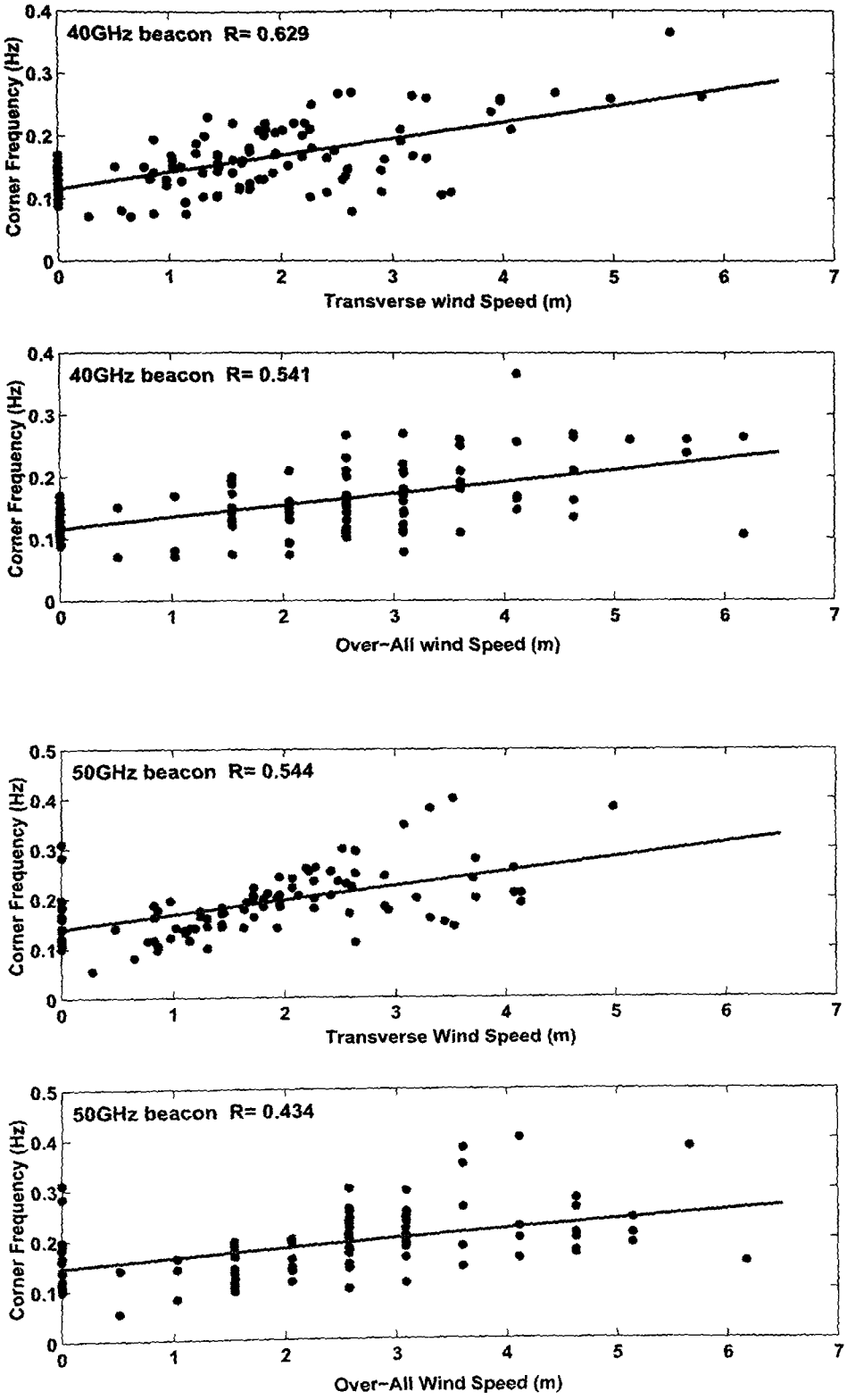

Figure 5.7. Corner frequency versus transverse wind speed and over-all wind speed at 40 and 50GHz.

5.5. Effects of Cloud

Figure 5.8 shows a very interesting observation that the correlation between spectral corner frequency and transverse wind speed is lower during periods of cumulus cloud cover than during intervals of no cumulus cloud, with respective values 0.4719 and 0.6357. This not only further strengthens the case for cloud contribution to observed scintillations, but is an indication that the influence of wind on cloud turbulence might be different than on clear air turbulence.

It should be noted that the meteorological station where the wind data were recorded is about 20km away from the receiver station. Thus taking into account the topography between the two sites might be necessary. Mechanical contributions from obstructions such as trees and buildings could cause the wind to change direction abruptly, upward and to the sides. In addition the motion of air particles across the prevailing flow causes local turbulent mixing to set in. Since this work is mainly focused on radiowave propagation, the study of meteorology is beyond our scope.

However, it is worth pointing out that vertical air movement is extremely important in weather processes, particularly with respect to clouds and precipitation. Ascending air currents represent a movement up the 'precipitation ladder' until there is cloud formation and possibly rainfall, depending on other meteorological parameters. Descending air currents on the other hand lead down the ladder with processes reversing until we are finally left with water vapour and dust in an air mass. This vertical air movement will always be present in regions where cloud formation is taking place and may reduce the significance of wind effects on the rapidity of turbulent mixing. If this is the case, then we would expect a reduced correlation between spectral corner frequency and transverse wind speed in the presence of cumulus clouds [1].

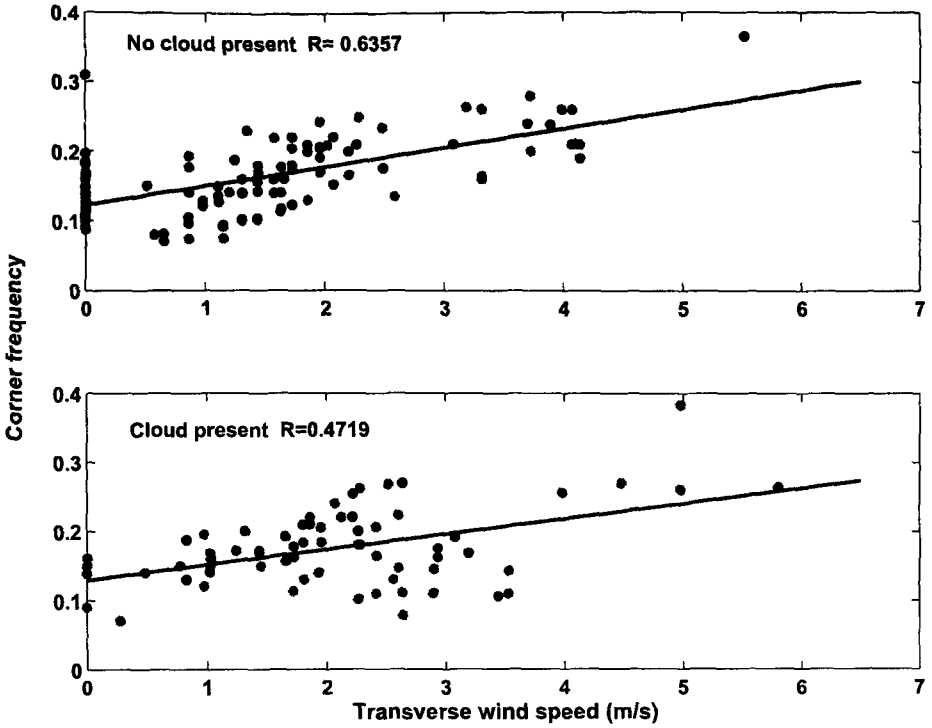

Figure 5.8. Scatter diagram of spectrum corner frequency versus transverse wind speed of the combined data at 39.59 and 49.49GHz, for periods with and without cumulus cloud cover.

5.6. Remote Sensing Applications

For completeness, in this section a brief discussion will be made in using the slant path spectrum as a tool for remote sensing and some of the problems associated with this approach.

The analysis of these turbulence-induced signal scintillations is important for both the remote sensing of the propagation medium and the design of radio communication systems [11]. Atmospheric turbulence parameters and wind speed can be obtained if scintillation variance is measured at two frequencies f_1 and f_2 transmitted with the

same polarisation. Otung *et al.* [12], based on the analysis of Olympus satellite scintillation measurements at 19.77GHz and a path elevation angle of 29.2^0, presented a dual frequency scintillation measurement scheme which exploits for remote sensing the relationships of temporal scintillation spectra to transverse wind speed and atmospheric turbulence parameters.

The expression for the spectral corner frequency f_c was given in Equation (5.4), thus by experimentally measuring the scintillation variance σ_x^2 and the corner frequency f_c it is possible to derive information about the structure constant parameter C_n^2, transverse wind speed v_t, and the height of turbulence h along the path. However, it is important to remember that these expressions apply to a uniform atmosphere, and the following assumptions were made:

i) The turbulent structure is a 'floating frozen structure'.

ii) Fluctuation of the refractive index n has a Kolmogorov spectrum $\Phi_n(k) = 0.033C_n^2 k^{-11/3}$ for $2\pi / L_0 \le k < 2\pi / l_0$, where l_0 and L_0 are the inner and outer scales of turbulence, of the order 1 to 10mm and 50 to 100m, respectively.

iii) The refractive index structure constant C_n is constant along the propagation path.

iv) $l_0 < \sqrt{\lambda L} \ll L_0$ and $L_0^2 k_m^2 \gg 1$, where λ is the signal wavelength and $k_m = 5.91/l_0$.

Using Equation (5.5) below and by making the following two assumptions $v_t > 0$ and $500 < h < 5000$, we used the experimentally estimated corner frequencies to calculate the height of turbulence.

$$h = k \sin\theta / (2\pi f_0 / v_t)^2 \tag{5.5}$$

where, the Fresnel frequency $f_0 = f_c / 1.43$.

Out of the hundreds of spectra inspected, 180 spectra in total at the three respective frequencies with an identifiable sloping region were selected. The mean value of the height of turbulence using the three beacon frequencies were h=1927m, h=2457m and h=2273m, giving an average value of 2219 meters, which is very close to the value suggested by Karasawa *et al* [3]. For a path elevation of 29.9^0 (as in Sparsholt) this gives a turbulent slant path L = 4449.1m. Despite the small variations observed in h, the mean value for the height of turbulence obtained is independent of the beacon frequency, as expected.

The refractive index structure constant C_n is a highly variable quantity, ranging from $\approx 10^{-7}$ $m^{-1/3}$ for a highly turbulent atmosphere to 10^{-9} $m^{-1/3}$ for weak turbulence [13]. The results tabulated in Table 5.2, below, are of the same order of magnitude as values in the range 1.04×10^{-7} to 3.29×10^{-9} $m^{-1/3}$, derived from meteorological and radiosonde data that have been published in the literature [12, 14].

Attempts were also made to compare our results to proposed models in the literature [15], [16]. Unfortunately the data required for those models were unavailable at the time of the analysis.

Table 5.2: Using spectral analysis results and theoretical expressions to derive atmospheric turbulence parameters.

Beacon Frequency	**20GHz**	**40GHz**	**50GHz**
Average yearly standard deviation (std)	0.10098 (dB)	0.11388 dB	0.14687 dB
Height of turbulence (h)	1927 (m)	2457 (m)	2273 (m)
Turbulent path length (L)	3863.9 (m)	4926.0 (m)	4557.3 (m)
Refractive index structure constant (C_n)	3.42×10^{-7} ($m^{-1/3}$)	1.96×10^{-7} ($m^{-1/3}$)	2.40×10^{-7} ($m^{-1/3}$)

5.7. Conclusions

In this Chapter we examined the effects of wind speed, cumulus cloud and scintillation intensity on the spectral corner frequency of amplitude scintillations. There was a strong correlation between transverse wind speed and estimated corner frequency, and a weaker correlation with over-all wind speed. The corner frequency shows some dependence on frequency. Furthermore, the analysis showed that the presence of cumulus clouds along the propagation path led to a drop in the observed correlation of the spectrum corner frequency with transverse wind speed. This might be due to the extra contribution to scintillation from physical processes that take place in the presence of clouds.

The shape of the power spectral density (psd) under cold and rainy weather conditions is similar to that theoretically predicted by assuming a Kolmogorov spectrum of atmospheric refractivity fluctuations, for clear sky conditions. The only difference is that the 'flat' part of the scintillation spectrum (observed during winter/summer 1997 in Sparsholt) for the summer months is higher due to stronger turbulence. In addition, the slopes of weak-to-moderate scintillation spectra revealed a weak correlation with transverse wind speed and scintillation intensity.

Finally, using measurements of amplitude scintillation for remote sensing application of transverse wind speed and turbulent parameters is feasible, however, they would not be very accurate. Over long periods meteorological conditions could not be regarded as constant, and in addition there is the practical difficulty in establishing an accurate value of the corner frequency by fitting linear regression lines to the flat and sloping portions of the spectrum.

References

[1] A. Savvaris, C. N. Kassianides, and I. E. Otung, "Observed Effects of Cloud and Wind on the Intensity and Spectrum of Scintillation," *IEEE Transactions on Antennas and Propagation*, vol. 52, pp. 1492-1498, 2004.

[2] A. Ishimaru, *Wave Propagation and Scattering in Random Media*: IEEE Press, 1997.

[3] Y. Karasawa, M. Yamada, and J. E. Allnutt, "A New Prediction Method for Tropospheric Scintillation on Earth-Space Paths," *IEEE Transactions on Antennas and Propagation*, vol. 36, pp. 1608-1614, 1988.

[4] A. Savvaris and I. E. Otung, "Preliminary Preprocessing of ITALSAT Data at 20, 40 and 50GHz," presented at URSI Symposium, 2000.

[5] I. E. Otung, M. O. Al-Nuaimi, and B. G. Evans, "Extracting Scintillations from Satellite Beacon Propagation Data," *IEEE Transactions on Antennas and Propagation*, vol. 46, pp. 1580-1581, 1998.

[6] V. I. Tatarskii, *Wave Propagation in a Turbulent Medium*: New York, Dover, 1961.

[7] M. M. J. L. V. d. Kamp, J. K. Tervonen, E. T. Salonen, and K. Kalliola, "Study of Low Elevation Angle Scintillation Modelling," Helsinki University of Technology, Espoo 1997.

[8] E. VILAR and J. HADDON, "Measurements and modeling of scintillation intensity to estimate turbulence parameters in an earth-space path," *IEEE Transactions on Antennas and Propagation*, vol. 32, pp. 340-346, 1984.

[9] O. P. Banjo, "An Investigation of Microwave Scintillations on Low-Elevation Satellite Link, with Application to Communication Systems." Portsmouth: Portsmouth University, 1986.

[10] A. Savvaris and I. E. Otung, "Spectral Analysis of Amplitude Scintillation on a V-band Satellite Link," presented at PREP2002, University of Nottingham, April 2002.

[11] G. D'Auria, U. Merlou, and D. Solimini, "Use of Scintillation Measurements for Remote Sensing of Meteorological Parameters," presented at International Conference on Antennas and Propagation (ICAP1987), 1987.

[12] I. E. Otung, M. S. Mahmoud, and B. G. Evans, "Dual Frequency Scintillation Measurement for Remore Sensing," *Electronics Letters*, vol. 31, pp. 1972-1973, 1995.

[13] V. I. Tatarskii, "The Effects of the Turbulent Atmosphere on Wave Propagation," Israel Program for Scientific Translations, Jerusalem 1971.

[14] H. Vasseur and D. Vanhoenacker, "Characterisation of Tropospheric Turbulent Layers from Radiosonde data," *Electronics Letters*, vol. 34, pp. 318-319, 1998.

[15] F. Rücker and F. Dintelmann, "Effect of Antenna Size on OTS Signal Scintillations and their Seasonal Dependence," *Electronics Letters*, vol. 19, pp. 1032-1033, 1983.

[16] E. Salonen, S. Karhu, P. Jokela, W. Zang, S. Upppala, H. Aulamo, and S. Sarkkula, "Final Report for ESA/ESTEC; Study of Propagation Phenomena for Low Availabilities," Helsinki University of Technology, Espoo 1990.

CHAPTER VI

Frequency Scaling of Amplitude Scintillation

Summary – *This Chapter presents an analysis of instantaneous frequency scaling of scintillation using propagation data recorded during a 3-month period (May–July 1997) at Sparsholt UK from the ITALSAT satellite beacons at frequencies 18.7, 39.6 and 49.5GHz. Variations in the height of turbulence within reasonable limits were found to have a negligible effect on the scaling ratios. Furthermore, the exponent in the power law dependence of scintillation intensity on signal frequency was found to be on average 27% smaller than the theoretical value of 7/12 and to exhibit a slight diurnal effect. It is shown that this behaviour can be partly accounted for by receiver thermal noise contribution to the measured signal variance. Ascribing the minimum observed short-term variance in each beacon to thermal noise and excluding this contribution yielded a higher exponent, which was nevertheless 15% below the theoretical value. Finally, results concerning the frequency exponent of scintillation from 22 sites around the world show a moderate correlation of about 0.72 with elevation angle.*

6.1. INTRODUCTION

This Chapter presents results relating to the instantaneous frequency scaling of tropospheric amplitude scintillation. As we have seen in Chapters 2 and 4, amplitude scintillation occurring in the troposphere increases with signal frequency and depends on a number of other link and meteorological parameters [1, 2]. As a result, scintillation will have a significant impact on the performance of low-margin communications systems operating at high frequencies (>~ 10 GHz), low elevation angles and utilising small antennas (VSATs and USATs). Scintillation effects need to be considered in the design and link-budget calculations of these systems. In particular, knowledge of the frequency scaling of scintillation is important to the operation of fade countermeasure systems such as uplink power control (ULPC).

In the design of an uplink power control (ULPC) system that can compensate for different types of fading, the short-term frequency scaling factor of both rain attenuation and amplitude scintillation is required [1, 3]. These factors differ from the long-term frequency scaling factor, which are intended to scale the statistics of a propagation effect. An ULPC system adjusts the power transmitted from Earth station to the satellite adaptively, according to the actual propagation conditions. The amount of extra power needed to compensate for the attenuation experienced on the uplink is obtained from measurement of the attenuation at the down-link frequency, which is generally lower than the up-link frequency, and applying a frequency scaling algorithm.

The performance of an ULPC system with respect to compensation of amplitude scintillation depends on the degree of correlation between amplitude scintillation measured on the two carrier frequencies in question: If they are highly correlated, it is possible to predict the behaviour of the amplitude scintillation at one frequency from measurement at the other so that the transmit power can be adjusted accordingly. Amplitude scintillation measured on two different carrier frequencies is however not

perfectly correlated. The degree of correlation depends on the frequencies under consideration and varies from one event to another.

6.2. Data Preprocessing

This Chapter discusses the instantaneous frequency scaling of scintillation using propagation data from the ITALSAT satellite beacons operating at 18.7, 39.6 and 49.5GHz. The data examined for this part of the analysis were recorded at Sparsholt over a 3-month period from May 1997 to July 1997. The propagation data together with a range of meteorological measurements recorded at the same sampling rate were archived to a compact disk once a month. Further description of the data preprocessing can be found in Chapter 2.

Scintillation is quantified here in terms of two commonly used measures, namely scintillation intensity and scintillation variance, which are respectively the standard deviation and variance of the pre-processed received beacon signal levels (in dB) within short time intervals of 1-min, 10-min and 30-minutes. Preprocessing is an essential step to extract a scintillation time series from the raw beacon data by excluding those fluctuations originating from sources other than scintillation, for example, gaseous absorption, rain attenuation, satellite movement and loss-of-lock. The preprocessing of the raw propagation data was discussed in Chapter 2. Further description and justification of the data preprocessing process are given in [4, 5].

During the satellite beacon measurements at Sparsholt, a status flag was logged for each recorded data sample in each of the three beacon channels. The 6 possible values of the status flag are listed in Table 6.1. In this part of the analysis data samples corresponding to status flag values other than simultaneous ones in all three channels were excluded. Furthermore, to counter an occasional receiving system problem with the 20GHz beacon signal that caused the onset of significant receiver phase noise, intervals in which observed scintillation variance on the 20GHz beacon exceeded the variance on either the 40 or 50 GHz beacon were excluded. These steps resulted in the

exclusion of 35.2% of the total data samples from the analysis, but this should not have a significant impact on the frequency scaling results since the excluded data were random and mainly from entire days.

Table 6.1: Status Flag

Value	Description
0	Gap or invalid data
1	Valid data
2	Attenuation not genuine but the data is valid
3	Loss of lock, valid data at other frequencies
4	Window error
5	Loss of lock, no valid data at other frequencies

Rain-gauge data recorded on-site were used to group the data into rainy and non-rainy scintillation data, for the purpose of examining the scaling of wet and dry scintillations respectively. Note however that on a slant path of elevation 30° and assuming a rain height of 2km, it is possible for the path to intercept a rain volume not registered by the gauge if a rain cell that does not extend to the site occurs within 3.5km of the site in the azimuth direction of the earth-space path. Although the probability of occurrence of such an event is low in Southern England, it is necessary nevertheless to caution that the terms dry and wet scintillations here refer to the condition of the lowest portion of the slant path.

The cloud data used in the analysis were obtained from the Met Office - Land Surface Observation Stations Data. Further description of this dataset can be found in Chapter 2.

6.3. Theoretical Considerations

The generalised scaling factor Δ of the variance of scintillation, assuming that the radio signal is received by a hypothetical point receiver [6], is expressed as a power law. The predicted ratio of the variances σ_1^2 at frequency f_1 and σ_2^2 at another frequency f_2, measured at the same site and with a common elevation angle during a time interval within which turbulence can be modelled as a stationary random process, can be written as

$$\Delta = \frac{\sigma_x^2(k_1)}{\sigma_x^2(k_2)} = \left(\frac{k_1}{k_2}\right)^{(6-n)/2} \tag{6.1}$$

where n has a value of 11/3 in the ITU-R model [6, 7]. When antenna aperture averaging is taken into account by including the factor $g(x)$ derived by Haddon and Vilar [8], the ratio between scintillation intensities σ_1 and σ_2 is therefore

$$\frac{\sigma_1}{\sigma_2} = \left(\frac{f_1}{f_2}\right)^{7/12} \left(\frac{g(x_1)}{g(x_2)}\right) \tag{6.2}$$

under the condition $l_o < \sqrt{\lambda L} << L_o$; where λ is the signal wavelength, L is the turbulent path length, and l_o and L_o are the inner and outer scales of turbulence — of the order 1-10 mm and 50-100 m, respectively. Note that this condition is valid for the link under consideration where λ = 15, 7.5 and 6mm respectively for the three beacons and L ~ 2000m. In equation (6.2),

$$\begin{aligned} g(x_i) &= \sqrt{3.8637\left(x_i^2+1\right)^{11/12} \sin\left[\frac{11}{6}\arctan\left(\frac{1}{x_i}\right)\right] - 7.0835x_i^{5/6}} \\ x_i &= \frac{0.0584\pi\eta D^2\left[\sqrt{\sin^2\theta + (2h/R_e)} + \sin\theta\right]}{h\lambda_i} \end{aligned} \tag{6.3}$$

$D \equiv$ physical diameter of antenna; $\eta \equiv$ illumination efficiency of antenna; $\theta \equiv$ path elevation angle; $R_e \equiv$ effective radius of Earth ($\approx 8.5 \times 10^6$ m); $h \equiv$ height of turbulent layer; and $\lambda_i \equiv$ signal wavelength.

In Equation (6.3) the height of turbulence h is an unknown parameter, which is assigned values of 1000 m and 2000 m respectively in the ITU-R [7] and Karasawa [9] models. However, by taking values of h in the range 500 m to 5000 m, it is shown in Table 6.2 (for $\theta = 29.9^0$ and $\eta = 0.64$ and $D = 1.22$m at 20GHz and 0.61m at 40 and 50GHz) that the variation of h has a negligible effect on the ratio of scintillation intensities observed using small antennas (as in this experiment). This agrees with the results reported by Van de Kamp et al. [3] based on the analysis of satellite beacon data at frequencies 19.77GHz and 29.66GHz. Their data were recorded at Kirkkonummi Finland (60.22 N; 24.40 E.) at a path elevation angle of 12.7^0 using a Cassegrain antenna of diameter 1.8 m. We note that only for h below about 500m is there a significant change in the scintillation intensity ratio. Because of these observations, we may assume a fixed value of h = 1000m without loss of accuracy. Note, however, that the effect of variations in h cannot be ignored for large antennas at moderate-to-high path elevations. For example, at D = 12 m, other parameters remaining unchanged, the ratio $g(x_{40})/g(x_{20})$ increases by ~ 24% as h is increased from 500 m to 5000 m..

Table 6.2: Variation of antenna aperture averaging ratio with the height of turbulence *h*

Frequency pair	Ratio for h =		Mean Ratio	Variation in ratio
	500 m	5000 m		
$g(x_{40})/g(x_{20})$	1.0288	1.0054	1.0101	2.271%
$g(x_{50})/g(x_{20})$	1.0200	1.0038	1.0070	1.590%
$g(x_{50})/g(x_{40})$	0.9915	0.9984	0.9970	0.697%

6.4. Data Analysis and Results

Scintillation intensities in 1-, 10- and 30-min data blocks were computed for the entire period covering the three months (May 1997 – July 1997), by taking the standard deviation of the preprocessed beacon data in each block interval. To maintain concurrent data sets across the measured frequencies, corresponding data blocks from all three beacon-channels were removed if one of the channels had invalid data. The scaling ratio was computed from the slope of the best-fit line passing through a scatter plot of scintillation intensities at two beacon frequencies. Figure 6.1-Figure 6.3 demonstrate this procedure for the ratios between 1-minute scintillation intensities at 50/20 GHz, 40/20 GHz and 50/40 GHz.

Table 6.3 shows the measured instantaneous (1–, 10– and 30–min) scintillation ratios at the three pairs of frequencies 50/40, 50/20 and 40/20 GHz, with comparisons to the theoretical prediction of Equation (6.2). It can be seen that the three scaling ratios are very close to the theoretical values predicted using Equation (6.2), thus confirming the validity of this relation. The small disparity of the 50/20 and 40/20 GHz ratios may be due to the increased significance of receiver noise contribution to the observed signal fluctuations at 20 GHz. The correlation coefficient between scintillation intensities at two different frequencies is also given in the Table. The high correlation values mean that scintillation intensity at one frequency can be predicted with some confidence from measurement at some other frequency, provided the two frequencies are not too far apart. For example, for the 1-minute scintillation intensities, the correlation between the 40 and 50 GHz measurements is ~0.95 whereas that between the 20 and 50 GHz measurements has fallen to ~0.86.

No significant variations in these ratios were observed when considering periods with rain/no-rain, and cloud/no-cloud. The most significant impact was on the frequency-dependence exponent α, when considering rainy periods only, which is discussed in the following section.

Table 6.3: Theoretical and measured scintillation intensity ratios

Scintillation Interval	$\sigma_{x50}/\sigma_{x40}$		$\sigma_{x50}/\sigma_{x20}$		$\sigma_{x40}/\sigma_{x20}$	
	Ratio	Correlation	Ratio	Correlation	Ratio	Correlation
1-min	1.159	0.954	1.718	0.861	1.487	0.906
10-min	1.151	0.969	1.854	0.893	1.641	0.938
30-min	1.128	0.969	1.865	0.902	1.682	0.946
Theoretical Ratio	1.133		1.786		1.576	

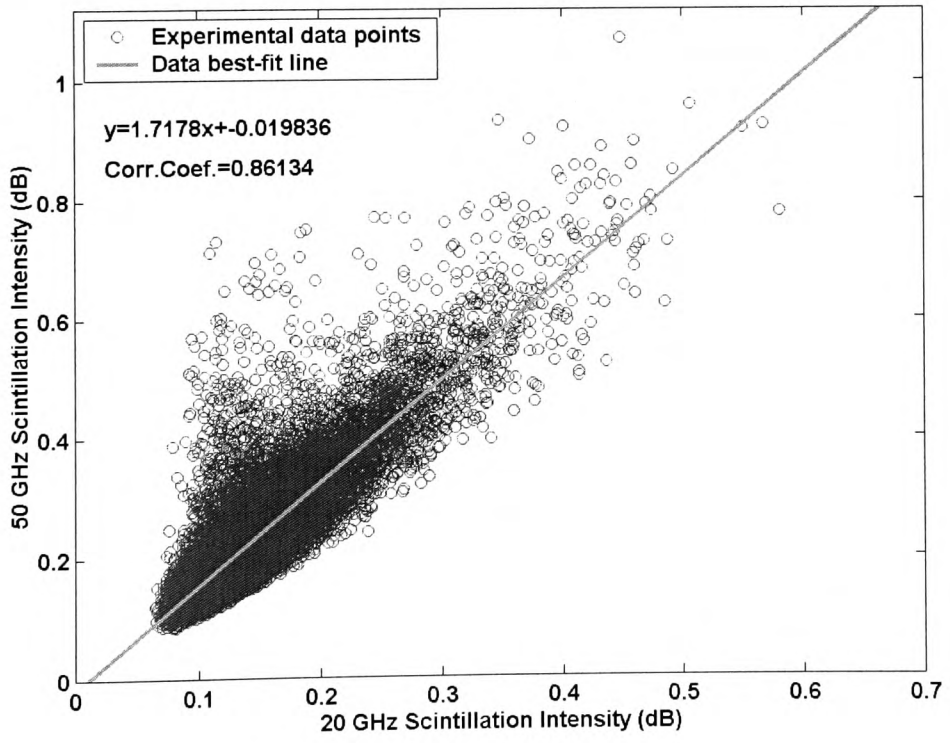

Figure 6.1. Scatter plot of scintillation intensity at 50GHz versus 20GHz.

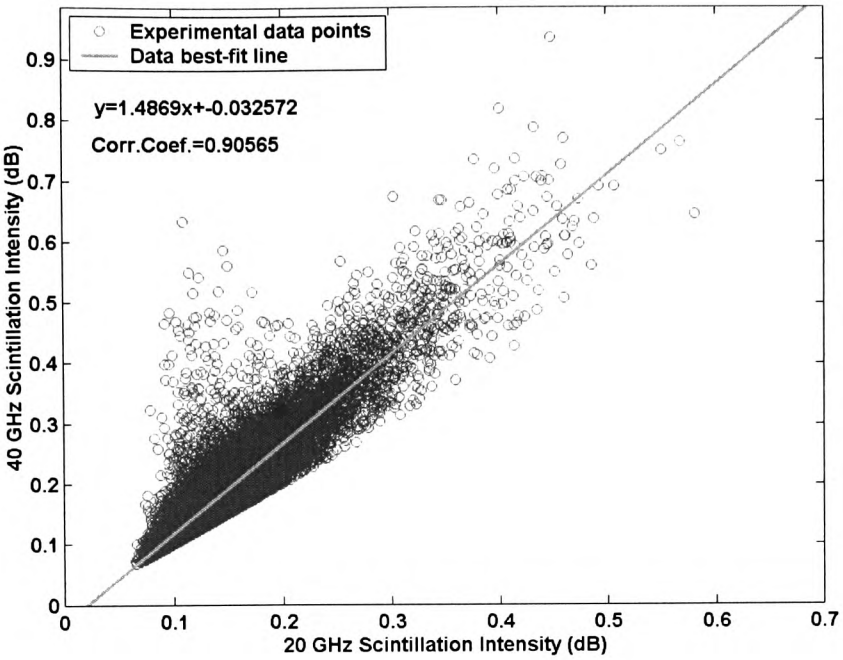

Figure 6.2. Scatter plot of scintillation intensity at 40GHz versus 20GHz.

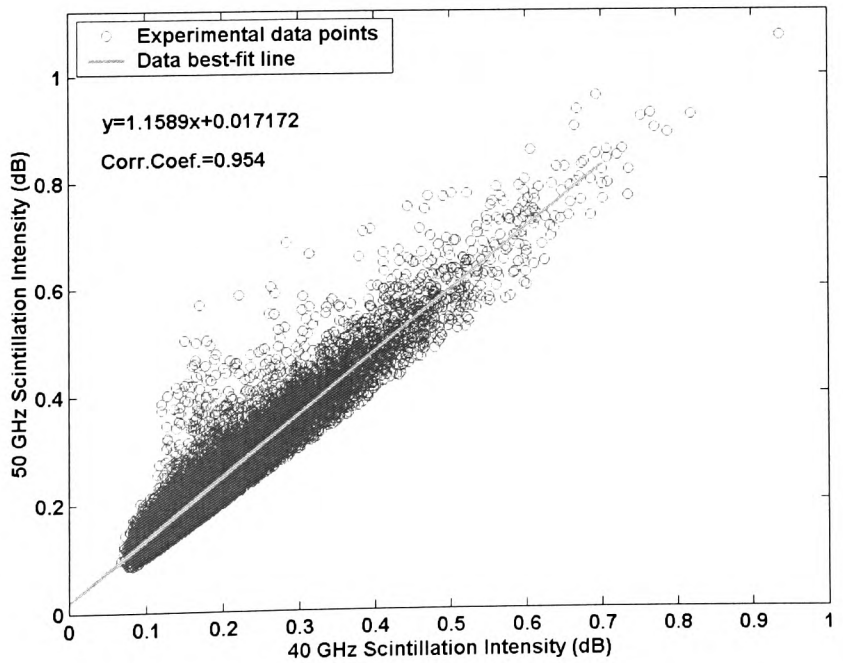

Figure 6.3. Scatter plot of scintillation intensity at 50GHz versus 40GHz.

6.5. Frequency-Dependence

6.5.1. Measurement Results

A number of simplifying assumptions [2] lead to the theoretical result that the scintillation intensity σ observed using a point receiver antenna increases with signal frequency as f^{α}, where the frequency-dependence exponent $\alpha = 7/12$. Karasawa et al. [6] reported a lower value of $\alpha = 0.45$ based on measurement in Japan at frequencies 11.5 and 14.2 GHz. Table 6.4 shows the values of α computed from our measurements by analysing the distribution (for mean, median, etc.) of the slope of the straight line that best fits a plot of $\log(\sigma)$ versus $\log(f)$ during each of the valid scintillation intervals in the 3-month period. Note that Equation (6.3) was first employed to scale the observed scintillation intensities to point receiver values. It can be seen that the observed frequency exponent α varies significantly, judging by the range from the 10^{th} to the 90^{th} percentile.

Table 6.4: Frequency Dependence f^{α}

Scintillation Intensity Interval	Mean α	Median α	10^{th} Percentile α	90^{th} Percentile α
1 minute	0.423	0.397	0.215	0.651
10 minutes	0.393	0.373	0.233	0.548
30 minutes	0.385	0.372	0.241	0.538
Measurement in Japan by Karasawa et al [6]: $\alpha = 0.45$				
Theoretical prediction: $\alpha = 0.58$				

Furthermore, both α and its variability decrease with the interval over which scintillation intensity is observed. Choosing a one-minute interval to ensure that the random scintillation process can be regarded as stationary, we obtain a mean value α

= 0.42, which is less than the theoretical value (7/12 = 0.58) but very close to the value earlier reported by Karasawa. By separating the data into daytime (0600 – 1800 hours local time) and night-time blocks, respective mean values of α = 0.44 and 0.37 were obtained. This represents a 16% drop in the measured night-time value of α.

As earlier indicated rain and cloud data were incorporated in the analysis to investigate the degree of their impact on the results.

Table 6.5 shows the variation in the frequency-dependence exponent α, calculated using the 1-min standard deviation (std) for periods with and without rain, and periods with and without clouds. It was found that the mean value of α for wet scintillation was 0.55, which is ~30% higher than the value for dry scintillation. This may be due to the rain-induced scintillation component [10] having a stronger dependence on signal frequency. Observation of a higher value of α for wet scintillation than for dry on a 10°-elevation satellite link at Ku-band was also reported by Jones et al [11]. The authors interpreted this as evidence for the presence of turbulent attenuation — a rapidly fluctuating attenuation mechanism — which cannot be spectrally separated from classical clear-air-turbulence-induced scintillation.

There was a less significant 9% difference between the observed frequency exponents during cloud-covered intervals (α = 0.44) and those intervals with no cloud cover (α = 0.40).

Table 6.5: Variation of the frequency exponent α (calculated using 1-min Std)

	All Data	Non-Rainy Intervals Only	Rainy Intervals Only	Non-Cloudy Intervals Only	Cloudy Intervals Only
Mean	0.4232	0.4150	0.5521	0.3984	0.4361
Median	0.3975	0.3914	0.5095	0.3655	0.4138
10%	0.2149	0.2128	0.2602	0.1904	0.2304
90%	0.6510	0.6364	0.9042	0.6281	0.6608

6.5.2. Comparison with Other Sites

Table 6.6 presents a summary of frequency exponent results gleaned from reported scintillation measurements at various sites involving different frequencies and path elevation angles. The sites featured in Table 6.6 include Kirkkonummi (Finland) [3], Martlesham (UK) [11], Spino d'Adda (Italy) [12, 13], Eindhoven (Netherlands), Darmstadt (Germany), Blacksburg (Virginia, USA) [14], Reston (Virginia, USA) [15, 16], Fairbanks (Alaska, USA) [15, 16], White Sands (New Mexico, USA) [15, 16], Norman (Oklahoma, USA) [15, 16], Tampa (Florida, USA) [15, 16], Vancouver (Canada) [15, 16], Yamaguchi (Japan) [9], as well as our site at Sparsholt (UK). The site parameters and the mean value of the frequency exponent α for each site are given. A value of 0.65 was assumed for the antenna aperture efficiency η, when it is missing in Table 6.6, not having been provided in the source publication.

There is a significant and unexplained variation in the mean values of α from site to site, which does not appear to be related simply to meteorological or link parameters. For example, the Martlesham measurement shares the same climate with Sparsholt, a similar low path elevation with Kirkkonummi, and a similar frequency and path

elevation with Yamaguchi, yet its reported frequency exponent is about 3 times larger than the rather well-matched values from these three sites. This significant disparity does not appear to be explained by the presence of contributions from turbulent attenuation since our measurements indicated a more modest increase of ~30% in α (rather than ~200%) due to this factor. It can also be seen that the mean frequency exponent at Vancouver is ~70% larger than Sparsholt's even though both sites have roughly the same path elevation. However, apart from Vancouver and the atypical Martlesham, the other large values of α come from the remaining two sites which have higher path elevation angles.

An interesting result is obtained when the frequency exponent α is plotted versus the elevation angle (excluding Martlesham) as shown in Figure 6.4. The results suggest that the frequency exponent α may be dependent on the elevation angle, having a correlation coefficient of 0.723.

In order to draw a more quantitative conclusion the antenna aperture efficiency was also investigated. Touw and Herben [1] concluded that it is very important to know the exact aperture illumination efficiency for the calculation of short-term frequency scaling factors. In our analysis we varied the antenna efficiency η, for all sites from 10% to 90%, which are extreme values to assess the impact on the results obtained [17]. As expected it had a significant impact on the frequency power exponent values obtained for sites utilising large antennas and low elevation angles, such as Eindhoven in the Netherlands and Yamaguchi in Japan (see Figure 6.5). However it did not significantly change the trend observed in Figure 6.4. But it can be considered as one of the major factors which might be responsible for the observed trend.

The following section will discuss receiver thermal noise contribution, which is another factor that might be responsible for the observed variations in the frequency exponent.

Table 6.6: Frequency exponent (α) measured at various sites. Site parameters include station name, satellite name, sampling rate, elevation angle (θ), antenna diameter (D), and antenna aperture efficiency (η).

Ground Station	Satellite	f (GHz)	Sampling rate	θ (^{0})	D (m)	η	α (mean)
Blacksburg (Virginia Tech.)	Olympus	12.50, 19.77, 29.66	10 Hz	14	4, 1.5, 1.2	0.65 (assumed)	0.50
Darmstadt	Olympus	12.50, 19.77, 29.66	Averaged online to 1 Hz	27	1.8, 3.7, 3.7	0.5, 0.5, 0.5	0.76
Eindhoven	Olympus	12.50, 19.77, 29.66	3 Hz	26.8	5.5	0.92, 0.78, 0.44	0.62
Fairbanks	ACTS	20.19, 27.51	20 Hz	8.1	1.22	0.56	0.33
Kirkkonummi	Olympus	19.77, 29.66	20 Hz	12.7	1.8	0.63, 0.38	0.42
Martlesham	Intelsat-V	11.45, 14.27	2 Hz	≈10	6.1	0.61	1.30
Norman	ACTS	20.19, 27.51	20 Hz	49.1	1.22	0.56	0.86
Reston	ACTS	20.19, 27.51	20 Hz	39.2	1.22	0.56	0.77
Sparsholt	Italsat	18.69, 39.59, 49.49	1 Hz	29.9	1.22, 0.61	0.64	0.42

Spino d'Adda	Italsat	18.69, 39.59, 49.49	1 Hz	37.8	3.5	0.64	0.88
Spino d'Adda	Olympus	12.50, 19.77	1 Hz	30.6	3.5	0.64	0.63
Tampa	ACTS	20.19, 27.51	20 Hz	52	1.22	0.56	0.63
Vancouver	ACTS	20.19, 27.51	20 Hz	29.3	1.22	0.56	0.72
White Sands	ACTS	20.19, 27.51	20 Hz	51.5	1.22	0.56	0.69
Yamaguchi	Intelsat-V	11.45, 14.27	1 Hz	6.5	7.6	0.65 (assumed)	0.45

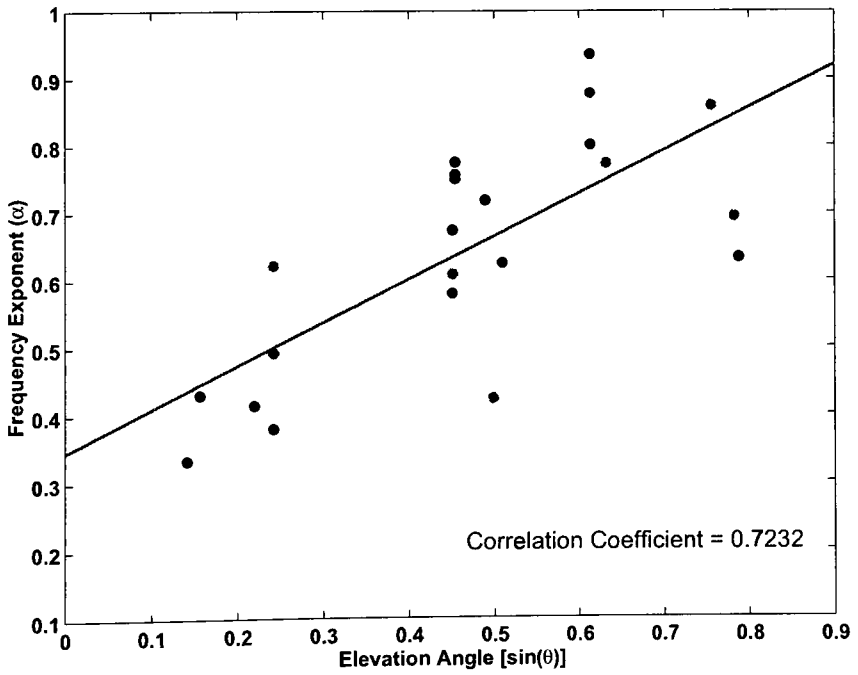

Figure 6.4. Global frequency exponent (α) versus elevation angle (sin(θ).

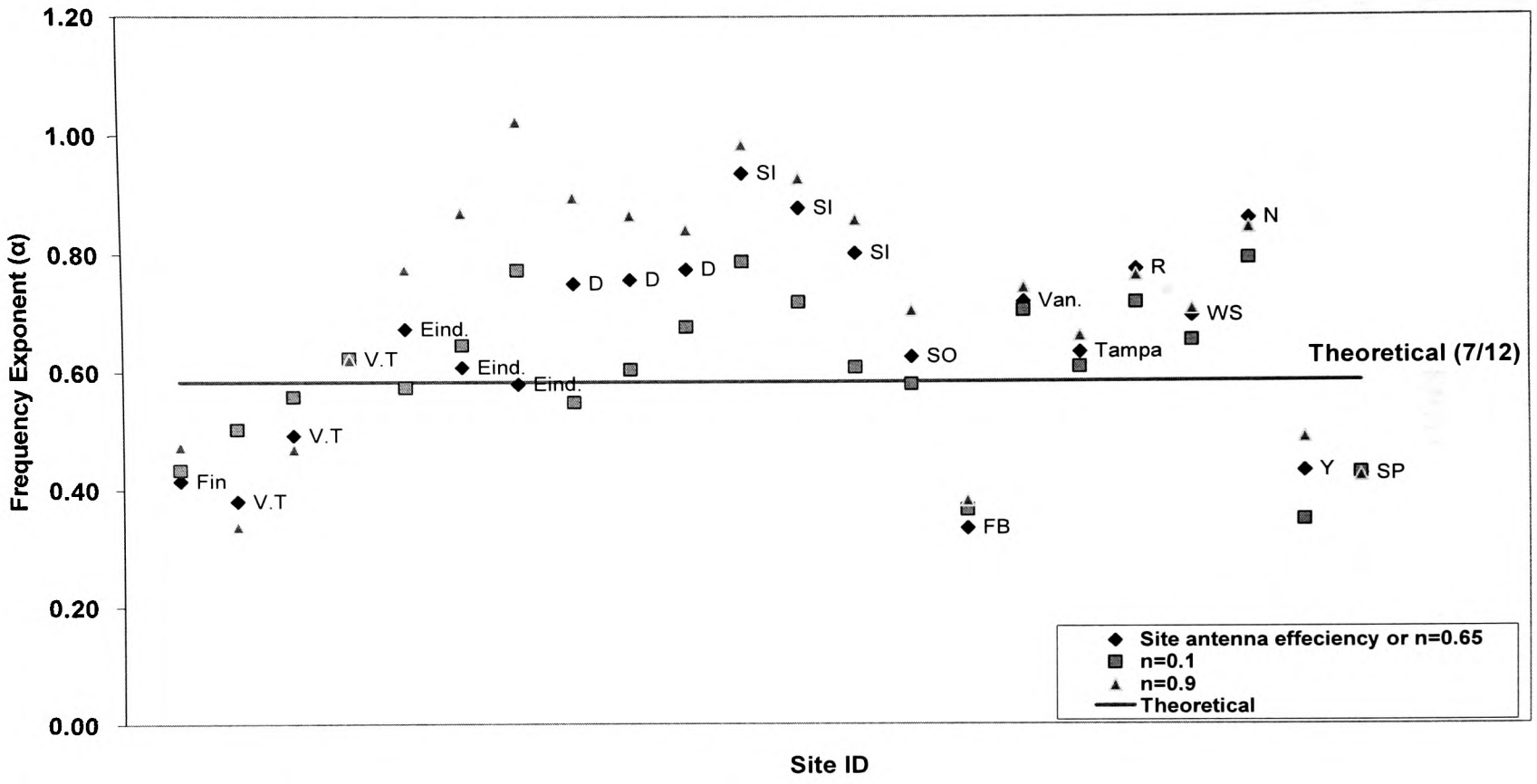

Figure 6.5. The frequency exponent α reported by various measurements sites.

Fin=Kirkkonummi; V.T= Virginia Tech.; Eind= Eindhoven; D=Darmstadt; SI=Spino d'Adda-Italsat; SO= Spino d'Adda-Olympus; FB=Fairbanks; Van=Vancouver;; Tampa=Tampa; R=Reston; WS=White Sands; N=Norman; Y=Yamaguchi; SP=Sparsholt.

6.6. Thermal Noise Effects

6.6.1. Receiver Thermal Noise Effect

Scintillation intensity was found to vary with frequency as f^{α}. However α was significantly variable with an average value of 0.423, which is 27% lower than the predicted theoretical value of 7/12 and to exhibit a slight diurnal effect. We can envisage as follows a situation where the lower-than-predicted value of α and its diurnal variation observed in our scintillation measurements at Sparsholt UK arise mainly from the effect of receiver thermal noise. The observed variance σ^2 in the high-pass-filtered data contains contributions from atmospheric scintillation and an uncorrelated receiver thermal noise. Thus we may write

$$\begin{aligned} \sigma_x^2 &= \sigma_s^2 + \sigma_n^2 = Kf^{7/6} + \sigma_n^2 \\ &\approx K'f^{2\alpha} \end{aligned} \tag{6.4}$$

where α is the exponent yielded by the data analysis earlier described, and K — a constant with respect to frequency f — varies with temperature and humidity and accounts for a higher daytime scintillation [18, 19]. In fact, the diurnal values of α reported in Table 6.7 can be produced entirely by thermal noise effects according to Equation (6.4) when (i) the value of K at night is 56% of a daytime value of 5.21×10^{-4}; and (ii) thermal noise variance σ_n^2 is 19.2% of the daytime scintillation variance σ_s^2 at 50 GHz. Note however that for a more typical noise variance σ_n^2 = 0.0034 dB^2 [20] and the day- and night-time values of K as above, the noise-induced drop in α is ~14% (compared to the observed ~27%) and the diurnal variation is ~7.5% (compared to the observed 16%). Further details and results from this analysis are given in reference [21].

6.6.2. Removing the minimum variance

To minimise the effect of receiver thermal noise contribution on the measured frequency exponent α, one may consider the smallest 1-minute variance $\sigma_{\min}^2$ in the

measured scintillation data of each beacon to be due entirely to thermal noise, and deduct this from the measured variance array. Note that this approach does overestimate thermal noise since it assumes the absence of scintillation during the interval of minimum fluctuations. Turbulence-induced scattering is however always present to varying degrees in a practical tropospheric path.

Nevertheless, estimating and excluding thermal noise contribution in the manner described above led to the results summarised in Table 6.7. Note that the mean frequency exponent α = 0.493, which is still 15.5% lower than the theoretical 7/12 value, and there remains a diurnal variation in α of 13%.

Table 6.7: Frequency exponent α (calculated using 1-min Std) after subtracting minimum variance.

	All-Day	Day-time	Night-time
Mean	0.4930	0.5075	0.4399
Median	0.4652	0.4790	0.4051
10%	0.2356	0.2532	0.1923
90%	0.7627	0.7729	0.7248

6.7. Conclusions

Observed frequency scaling of amplitude scintillation at 20, 40 and 50 GHz has been presented. There was a strong correlation between scintillations at different pairs of frequencies, which means that for uplink power control applications, scintillation intensity at one frequency can be predicted with some confidence from measurements at a different but close frequency. Scintillation intensity was found to vary with frequency as f^{α}. However α was significantly variable with an average value of 0.423, which is 27% lower than the predicted theoretical value of 7/12. It was shown that the observed shortfall and diurnal variation in α could be accounted for only partly by receiver thermal noise contribution. By ascribing the minimum observed 1-minute variance in each beacon to thermal noise and excluding this contribution from the measured scintillation variance, a higher average frequency exponent $\alpha = 0.493$ was obtained, which is still 15.5% below the theoretical value.

Finally, the exponent in the power law dependence of scintillation intensity on signal frequency α, as observed from measurement results at various sites around the globe, shows remarkable differences. A moderate correlation of about 0.72 was found between α and elevation angle. Hence, a possible explanation of these results would be that the frequency exponent α can be considered dependent on the elevation angle.

References

[1] S. I. E. Touw and M. H. A. J. Herben, "Short-term Frequency Scaling of Clear-sky and Wet Amplitude Scintillation," *IEE Proceedings on Microwave Antennas Propagation*, vol. 143, pp. 521-526, 1996.

[2] I. E. Otung, M. S. Mahmoud, and B. G. Evans, "Dual Frequency Scintillation Measurement for Remore Sensing," *Electronics Letters*, vol. 31, pp. 1972-1973, 1995.

[3] M. M. J. L. V. d. Kamp, C. Riva, J. K. Tervonen, and E. Salonen, "Frequency Dependence of Amplitude Scintillation," *IEEE Transactions on Antennas and Propagation*, vol. 47, pp. 77-85, 1999.

[4] A. Savvaris and I. E. Otung, "Preliminary Preprocessing of ITALSAT Data at 20, 40 and 50GHz," presented at URSI Symposium, 2000.

[5] I. E. Otung, M. O. Al-Nuaimi, and B. G. Evans, "Extracting Scintillations from Satellite Beacon Propagation Data," *IEEE Transactions on Antennas and Propagation*, vol. 46, pp. 1580-1581, 1998.

[6] V. I. Tatarskii, *Wave Propagation in a Turbulent Medium*: New York, Dover, 1961.

[7] ITU-R, "P.618-7 Propagation data and prediction methods required for the design of Earth-space telecommunication systems," Recommendations and Reports of the ITU-R 1997.

[8] J. Haddon and E. Vilar, "Scattering induced microwave scintillations from clear air and rain on earth space paths and the influence of antenna aperture," *IEEE Transactions on Antennas and Propagation*, vol. 34, pp. 646-657, 1986.

[9] Y. Karasawa, M. Yamada, and J. E. Allnutt, "A New Prediction Method for Tropospheric Scintillation on Earth-Space Paths," *IEEE Transactions on Antennas and Propagation*, vol. 36, pp. 1608-1614, 1988.

[10] I. E. Otung and M. S. Mahmoud, "Rain-induced Scintillation on Satellite Downlinks," *Electronics Letters*, vol. 32, pp. 65-67, 1996.

[11] S. M. R. Jones, I. A. Glover, P. A. Watson, and R. G. Howell, "Evidence for the Presence of Turbulent Attenuation on Low-Elevation Angle Earth-Space Paths - Part 2: Frequency Scaling of Scintillation Intensity on a 10^0 Path," *IEEE Transactions on Antennas and Propagation*, vol. 45, pp. 85-92, 1997.

[12] R. Polonio and C. Riva, "ITALSAT Propagation Experiment at 18.7, 39.6, and 49.5 GHz at Spino D'Adda: Three Years of CPA Statistics," *IEEE Transactions on Antennas and Propagation*, vol. 46, pp. 631-635, 1998.

[13] C. Riva. Milano, 2004.

[14] W. L. Stutzman, T. Pratt, A. Safaai-Jazi, P. W. Remaklus, J. Laster, B. Nelson, and H. Ajaz, "Results fron the Virginia Tech Propagation Experiment Using the Olympus Satellite 12, 20 and 30 GHZ Beacons," *IEEE Transactions on Antennas and Propagation*, vol. 43, pp. 54-62, 1995.

[15] NASA, "ACTS Propagation Experiment Handbook," NASA.

[16] C. E. Mayer, "Personal Communication," 2003.

[17] A. Savvaris and I. E. Otung, "Observed Correlation Between Frequency Exponent and Elevation Angle of Tropospheric Scintillation," presented at International Conference on Antenna and Propagation (ICAP2003), University of Plymouth, UK, 2003.

[18] I. E. Otung, M. S. Mahmoud, and J. R. Norbury, "Radiowave Amplitude Scintillation Intensity: Olympus Satellite Measurements and Empirical Model," *Electronics Letters*, vol. 31, pp. 1873-1875, 1995.

[19] J. K. Tervonen, M. M. J. L. V. d. Kamp, and E. T. Salonen, "Prediction Model for the Diurnal Behaviour of the Tropospheric Scintillation Variance," vol. 46, pp. 1372-1378, 1998.

[20] M. M. J. L. V. d. Kamp, "Climatic Radiowave Propagation Models for the Design of Satellite Communication Systems." Eindhoven: Technical University Eindhoven, 1999.

[21] I. E. Otung and A. Savvaris, "Observed Frequency Scaling of Amplitude Scintillation at 20, 40 and 50GHz," *IEEE Transactions on Antennas and Propagation*, vol. 51, pp. 3259-3267, Dec. 2003.

CHAPTER VII

Scintillation Fade and Enhancement Statistics – Effects on Satellite Communication Systems

Summary – *This Chapter starts with some general definitions and equations related to satellite communication system design, followed by an overview of digital modulation techniques used in satellite communications. Statistics of observed durations of scintillation fades and enhancements of the ITALSAT satellites at 20, 40 and 50GHz are also presented for various threshold signal levels, and their use in fade countermeasures is examined. Finally, a study of adaptive fade countermeasures (FCM) that could be used for systems operating a Ka-band and above showed that the implementation of adaptive up-link power control combined with adaptive signal processing techniques such as adaptive coding or modulation are the prime FCM candidates for mitigating the effects of scintillations and rain attenuation.*

7.1. INTRODUCTION

New services such as video conferencing and high-speed internet services via satellite for multimedia applications require greater bandwidth. This in conjunction with the saturation of C-band and the rapidly filling-up Ku-band has led to the exploitation of higher frequencies to provide new services.

The higher frequencies offer various advantages such as, increased bandwidth, smaller antennas, and smaller satellite footprint that give higher EIRP and permit frequency reuse. The main obstacle however is that they are subject to stronger propagation degradation. The small size antennas employed in VSAT and USAT systems significantly reduces the cost of earth station terminals and also eliminates tracking requirements, but they lose the mitigating effect of aperture averaging and hence experience stronger scintillation [1].

In general, the impact of rain attenuation on communication signals is predominant. Figure 7.1 illustrates the comparative levels of total attenuation at 20, 40 and 50GHz during a showery rain event recorded on the 5th of June 1997. The rain rate at the measurement site reached values up to 17mm/hr. During this event the attenuation at 20GHz reached $\approx$ 6dB, while at 40 and 50GHz the attenuation levels exceeded 20dB.

For completeness we calculated the cumulative distribution function of total attenuation at the respective frequencies (20, 40 and 50GHz) for the period covering August 1999 to July 2000. For 0.01% of the time the total attenuation at 20, 40 and 50GHz are 11.5, 19 and 21.1 dB, respectively. Assigning a fixed fade margin at these frequencies is not a feasible solution. The general approach for handling the large attenuation at those frequencies is to use adaptive methods or fade countermeasures (FCM).

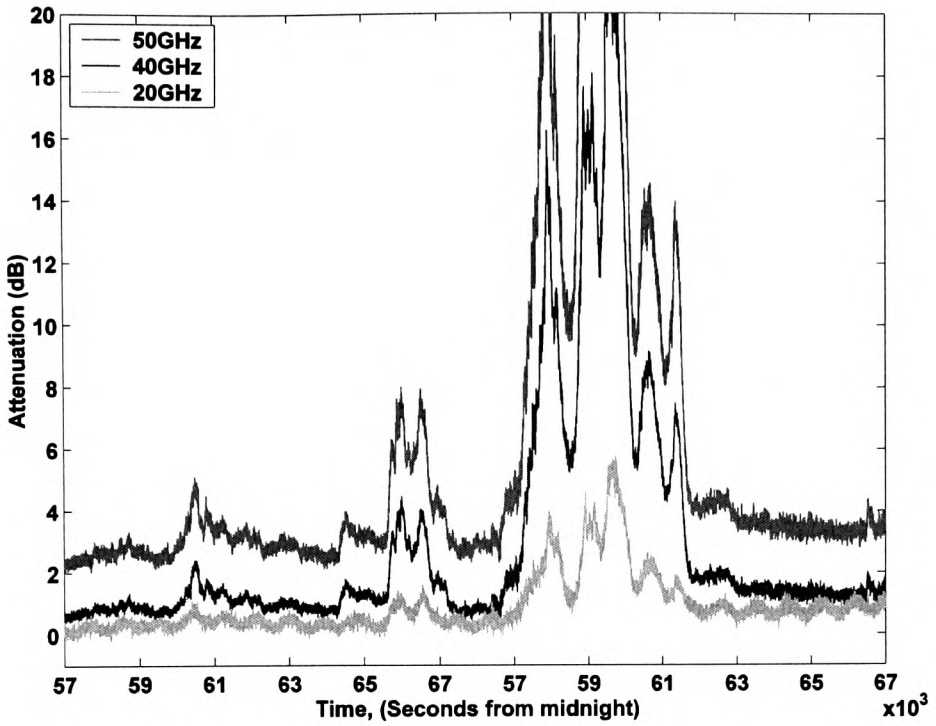

Figure 7.1. Comparative levels of total attenuation at 20, 40 and 50GHz during a showery rain event recorded on the 5th of June 1997.

In this Chapter we will start with some general definitions and equations related to satellite communication system design, followed by an overview of fade countermeasures that can be applied to mitigate the severe degradation due to the atmospheric propagation fading. Followed by results from the analysis of scintillation fade and enhancement duration statistics.

A critical parameter for a VSAT/USAT network is the availability of its link, that is, the percentage of time that information can be transmitted and received with acceptable quality. For digital signals, the information quality is objectively described in terms of the bit error rate (BER) and carrier-to-equivalent noise spectral density ratio (C/N_0 or CNR) at the demodulator/decoder input.

7.2. General Definitions

7.2.1 Bit-Error_rate (BER)

In digital satellite systems phase\amplitude errors under the influence of noise lead to errors in identification of the received symbols and hence the received bits. Bit-error-rate (BER) measures the performance of the system by counting the number of bits in error, in a stream of received bits.

Bit error rate is the primary performance criterion for digital data communication systems. In practice, the transmitted symbol is corrupted by noise before it reaches the detection point at the receiver. At the receiver a bank of correlators is used to extract the received vector. Then using this received data vector, the receiver has to make a decision on which message point in the signal constellation is most likely to have been transmitted. On the assumption that all M message points are transmitted with equal probability, the maximum likelihood detector will decide which message point has been transmitted in favour of the message point that is closest to the received signal point.

If the noise that the signal encountered is higher than half the distance between two neighbouring message points, the received symbol will be mistaken for the one next to it. Thus a symbol error will occur whenever noise effects shift the received point across the decision boundary between two points in the symbol space. As the space between the signal points decreases, the likelihood of error increases. A probability of symbol error equal to 0.001 means that, on average, there is one symbol error per 1000 received symbols. This is referred to as the symbol error rate (SER).

For a binary system, bit and symbol errors are identical as each symbol error corresponds to a single bit error. For M-ary systems ($M > 2$), however, this does not hold true. For example, a 64-ary scheme conveying six bits per symbol may incur anything from one bit error to six bit errors for each incorrectly decoded symbol,

depending on which symbol was mistakenly identified. So BER depends on the modulation method and of course the SER.

In practice, some symbols are more likely to be detected in error than others. It is more likely for one symbol to be mistaken to its neighbour and to minimise the number of bit errors occurring for every symbol error, it would be good to use Gray encoding.

Gray coding is the name given to a bit assignment where the bit patterns in adjacent message points only differ in one bit position. If an assumption is made that the detection process will only mistake symbols for those adjacent to the correct symbol, then the bit error probability will be given approximately by the symbol error probability divided by the number of bits in each symbol. Thus for an M-ary modulation scheme,

$$BER = \frac{Symbol \quad Error \quad Rate}{\log_2 M}$$

An example of a two dimensional symbol space using Gray coding for QPSK is given in Figure 7.2.

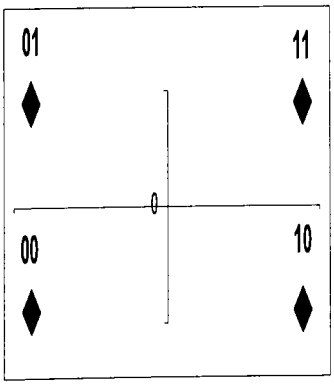

Figure 7.2. QPSK signal space diagram with Gray coding

7.2.2 Shannon's Capacity Expression

Channel capacity as defined by Shannon is a good measure of merit of any communication system since it gives the maximum rate of transmission of signals over the channel. If the channel is subject to fading, its capacity varies with the changes in the propagation medium. By increasing the level of modulation, i.e. the number of symbol states, the bit rate of a system can be increased. But the ability of the receiver to distinguish between the symbol states in the presence of noise becomes more difficult resulting in an increase in error rate. The Shannon capacity limit for error-free communication is given by:

$$C = B\log_2\left(1+\frac{S}{N}\right) \quad \text{bits/second} \tag{7.1}$$

where C is the channel capacity, B the channel bandwidth in Hz and S/N is the signal to noise ratio in the channel. It is theoretically possible to transmit at the above rate with the error rate made to approach zero as closely as desired. Note however that Shannon failed to specify a method to achieve this rate, showing only that complex coding and large delays in transmission would be needed. A good overview of Shannon's theorem can be found in [2], [3].

7.2.3 Outage and Availability

According to the ITU-R recommendations an outage event is said to occur in a digital receiver if its BER exceeds a specified threshold (typically 10^{-3} depending on the service required) for not more than 10 consecutive seconds. Outage time is the accumulated seconds for all outage events in a given time period, say a year. If the events last more than ten seconds, the link is said to be unavailable. This distinction between outage time and unavailability arises from the fact that digital trunks often lose framing when high BERs persist over a long period of time.

7.3. Modulation Techniques in Satellite Communications

This section will start with an overview of a number of digital modulation techniques that have found applications in digital communication systems, not all of which are suitable for satellite communications as will be shown below.

Most of the operational satellites are power limited i.e. the available ratio of energy per bit to noise density, E_b/N_0, is insufficient to enable the utilisation of modems which have spectral efficiency of more than 2 b/s/Hz and require a higher E_b/N_0 ratio. Because of their power efficiency, Binary Phase Shift Keying (BPSK) and Quadrature Phase Shift Keying (QPSK) are the more frequently employed modulation techniques. The spectral efficiency of such systems, employing BPSK and QPSK is less than 2b/s/Hz [4].

The spectral or bandwidth efficiency of a communication link is a measure of how well a particular modulation format makes use of the available bandwidth. It equals to the ratio between transmission bit rate and the system bandwidth, and is a measure in units of bits per second per hertz (b/s/Hz).

Amplitude, phase and frequency modulation are all applicable to digital modulation. The digital equivalent of these modulation schemes are known as Amplitude Shift Keying (ASK), Frequency Shift Keying (FSK) and Phase Shift Keying (PSK). Additionally, some modulation schemes have been developed specifically to optimise digital modulation. These are hybrid phase/amplitude schemes called Quadrature Amplitude Modulation (QAM).

7.3.1. ASK and FSK Modulation

Amplitude Shift Keying (ASK) is the simplest form of bandpass data modulation. Extending binary ASK to multilevel ASK (M-ASK) is simple. But the bit error rate (BER) of M-ASK is very poor caused by the use of strongly correlated sinusoidal

pulses. There is no opportunity to exploit orthogonality with M-ASK and this is an immediate penalty in BER performance. Its poor BER performance means that there are very few practical applications of ASK other than its binary form, despite its excellent bandwidth efficiency. Poor BER and its inherent characteristics of a non-constant envelope makes ASK unsuitable for applications in satellite communications.

M-ary FSK on the other hand gives us the ability to trade bandwidth for an improved noise performance in a way that is not possible with M-ary ASK and M-ary PSK. An M-ary FSK signal consists of one of the following M orthogonal sinusoidal pulses in each symbol interval of duration T_s. The pulses differ only in frequency, which are spaced at half the symbol rate to achieve mutual orthogonality of the transmitted symbols with minimum required bandwidth [2].

$$g_i(t) = A_c \cos[2\pi(f_0 + i\Delta f)t] \qquad \text{i = 0,1,2,...,M-1} \qquad (7.2)$$

$$\Delta f = 1/2T_s = R_s/2 \qquad (7.3)$$

The frequency f_0 is chosen to place the transmission in the desired or allocated frequency band.

As the number of symbol states employed increases, the symbol averaging time becomes very large, reducing the effect of noise. So M-ary FSK can be used in systems where noise immunity is the primary aim. On the other hand increasing the number of symbol states causes a rapid reduction in bandwidth efficiency. This low bandwidth efficiency of FSK schemes makes it inappropriate for satellite applications.

7.3.2. PSK Modulation

In a phase shift keying (PSK) system the phase of the carrier is changed in accordance with the baseband digital stream. A general form of expression of a PSK scheme is

$$v(t) = A\cos(\omega_0 t + \phi_m) \qquad (7.4)$$

where ϕ_m is the phase angle varied in accordance with the information signal. The signal space diagram of M-ary PSK consists of message points uniformly spaced, with constant phase shift, along a circle that is centred at the origin. In the simplest form of phase modulation, the binary phase shift keying, BPSK, the data is taken one bit at a time and the carrier phase is changed by 0 or π radians, according to whether the data is 1 or 0. The orthogonality between the sine and cosine function imply that if BPSK was to be used to transmit on a cosine carrier, and simultaneously a second BPSK signal is sent using a sine carrier of the same frequency, then it would be possible to detect each one independently of the other. This is called quadrature phase shift keying, QPSK. By applying Gray encoding to the symbols the BER of BPSK and the Gray encoded QPSK is the same. The advantage of using QPSK though is that it has twice the bandwidth efficiency of BPSK. The bandwidth efficiency of QPSK = 2 b/s/Hz in theory.

Increasing the number of symbol states for M-ary PSK beyond four allows further improvements in bandwidth efficiency. The bandwidth efficiency for M-ary PSK is equal to $\log_2 M$ b/s/Hz. The additional symbol states, though, are no longer orthogonal, they do not lie on the sine or cosine axis of the constellation diagram. The result is that the performance in noise for M > 4 degrades rapidly as M increases. The BER performance for M-ary PSK for M > 2 is given by [2]:

$$BER = \frac{1}{\log_2 M} erfc\left(\sqrt{\frac{E_b[1-\cos(2\pi/M)]\log_2 M}{2N_0}}\right) \tag{7.5}$$

PSK, because of its constant envelope, is generally preferred for satellite communications, which employs non-linear amplification in the travelling wave tube amplifier (TWTA).

7.3.3. QAM Modulation

Quadrature amplitude modulation is a combination of amplitude and phase signalling. BER performance improvement can be achieved, compared to that of PSK, if the

message states are spaced more freely and widely in the two-dimensional signal space. This requires combining two quadrature (sine and cosine) carriers that are modulated in both amplitude and phase. This combination gives us the quadrature amplitude modulation. There are different implementations of QAM, such as square QAM, circular QAM and star QAM.

Considering a square QAM that carries equal number of bits in the quadrature and in-phase channels, the BER is given by [2]:

$$BER = \frac{2}{\log_2 M}\left(1 - \frac{1}{\sqrt{M}}\right) erfc\left(\sqrt{\frac{3E_b \log_2 M}{2(M-1)N_0}}\right) \tag{7.6}$$

The bandwidth efficiency for M-ary QAM is the same as that of M-ary PSK and is equal to $\log_2$M b/s/Hz, but M-ary QAM yields a better BER performance. This is an important advantage of the M-ary QAM. QAM however has a non-constant envelope and has therefore not been widely implemented in satellite communication systems. However, their excellent bandwidth efficiency and their good BER performance make them worthy of consideration for satellite communications. Even high M-arity QAM could be considered for satellite applications where extremely high bandwidth efficiency is required [5]. In this case, however, back-off in the Travelling Wave Tube Amplifier (TWTA) input and output power must be provided to ensure the linearity of the power amplifier. The main drawback of using QAM techniques is their non-constant envelope. Such a modulation format greatly increases data throughput and hence the revenue produced by a transponder.

7.4. Fade and Enhancement Duration Statistics

The use of digital signal processing requires the knowledge of the dynamics of tropospheric scintillation, including the distribution of scintillation fade duration and inter-fade interval. Fade duration statistics are particularly important for the design of high frequency satellite systems. In such high frequency systems, operating at a fixed

small fade margin, the best way to mitigate propagation impairments is by introducing adaptive techniques, adaptive fade countermeasure strategies. Fade and interfade duration statistics provide the system designer with useful information for evaluating various mitigation techniques that will be employed to ensure a given system availability and quality of service.

Statistics of observed durations of scintillation fades and enhancements of the ITALSAT satellites at 20, 40 and 50GHz are presented for various threshold signal levels, and their use in fade countermeasures is examined. The analysis shows that most signal amplitude deviations from the mean level are of short duration and do not depend on the threshold level. Distribution of fade durations at thresholds 0.1 and 0.5dB were reasonably well approximated by the lognormal function.

7.4.1. Fade Duration

Fade duration D_- at threshold level χ_T below the mean level (= 0dB) of χ (scintillation amplitude) was taken as the time interval over which the signal level continuously fell below χ_T. Similarly, enhancement duration D_+ at threshold level χ_T above 0dB was obtained as the time interval over which the signal level continuously exceeded χ_T.

Inter-fade duration or non-fade duration is the complement of the fade duration. It is defined as the continuous time over which the attenuation is lower than a given threshold value. Figure 7.3 gives the graphical representation of this definition. A small hysteresis of 0.005 dB was used in the detection of the signal levels in order to mask the effects of system noise.

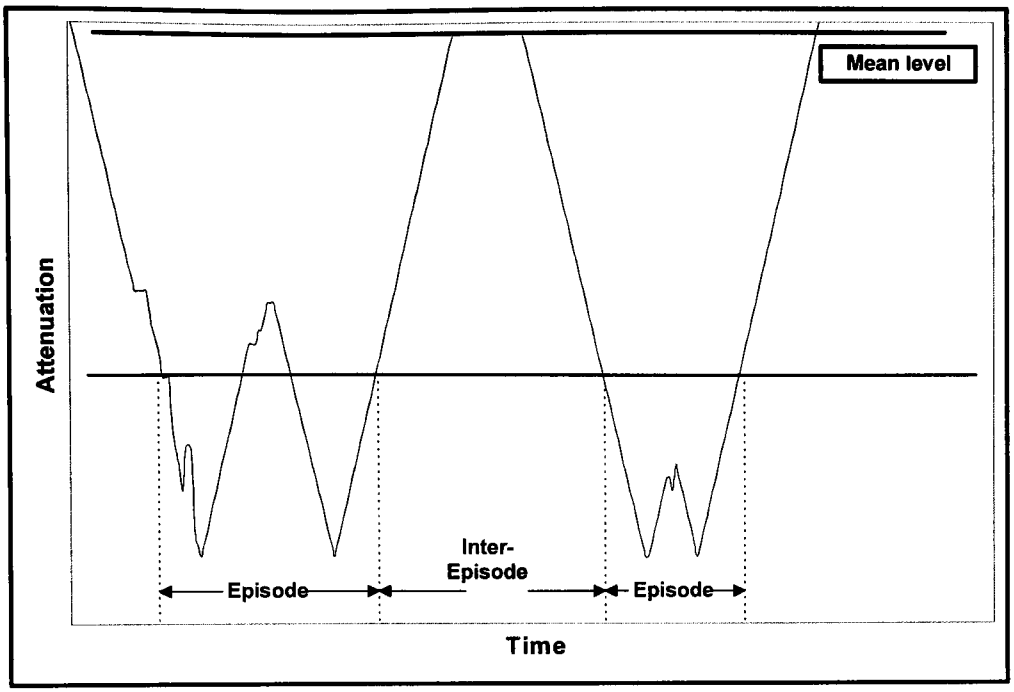

Figure 7.3. Definition of episode and inter-episode

The cumulative distribution function (cdf) at 20, 40 and 50GHz of fade duration at selected threshold levels is shown Figure 7.4. Use has been made of a logarithmic scale for the durations, and for the probabilities, a scale such that a lognormal distribution is represented by a straight line. It was observed that that the distribution of scintillation fade duration at threshold levels of 0.1dB and 0.5dB follows adequately a lognormal distribution. However, at threshold levels above 0.8dB the small number of sample points did not allow an accurate determination, e.g. the number of sample points corresponding to fades greater than 1dB at 20GHz were only 389, during the entire 1-year period.

We note that the fade duration statistics from SIRO measurements campaign indicated a lognormal distribution [6] whereas the OLYMPUS campaign has suggested a power-law dependence for short fades (< 20sec) which are generally the result of scintillation or noise and a lognormal distribution for longer fades. Based on the results obtained from Figure 7.4 it would appear that short fades tend also to follow a lognormal distribution. Similar conclusions were obtained from the analysis of enhancement duration statistics, which were on average of equal magnitude.

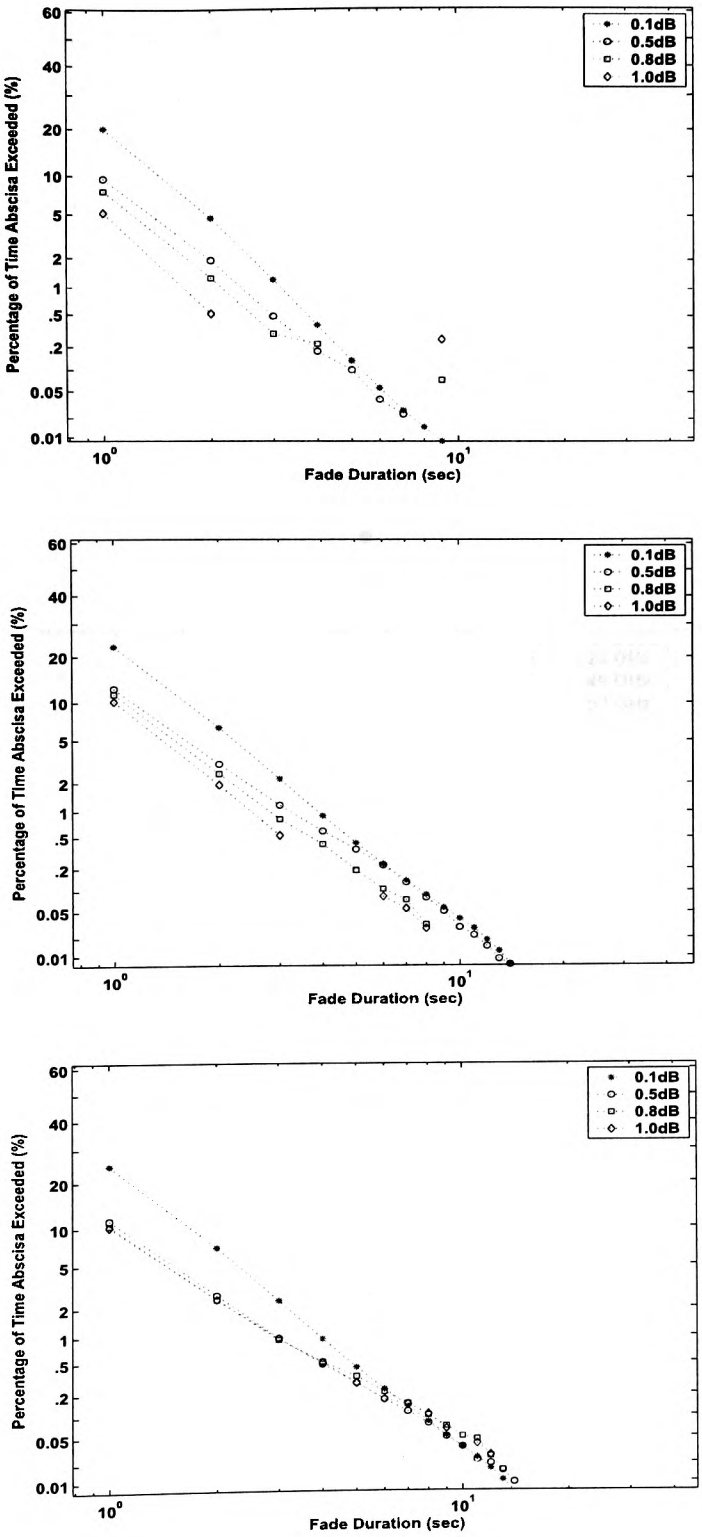

Figure 7.4. Starting from top to bottom the measured cumulative distribution of fade duration at various signal threshold levels at 20, 40 and 50GHz, respectively.

Furthermore, as illustrated in Figure 7.5 and Figure 7.6 the measured annual mean fade and enhancement duration displays no dependence on threshold level. The mean duration of both fades and enhancement are on average equal, lasting no longer than 1.4 seconds. For example, at 1dB threshold level at 40GHz the mean fade duration is ~1.125 seconds and at 2dB threshold level the mean duration is ~1.05 seconds.

However, at higher frequencies the observed percentage of long-fade duration exceeding a specific threshold is greater than that observed at a lower frequency. For example at 20GHz the percentage of 0.5dB fades lasting up to 8 seconds is ~ 0.01%, whereas at 50GHz the percentage is ~ 0.07%.

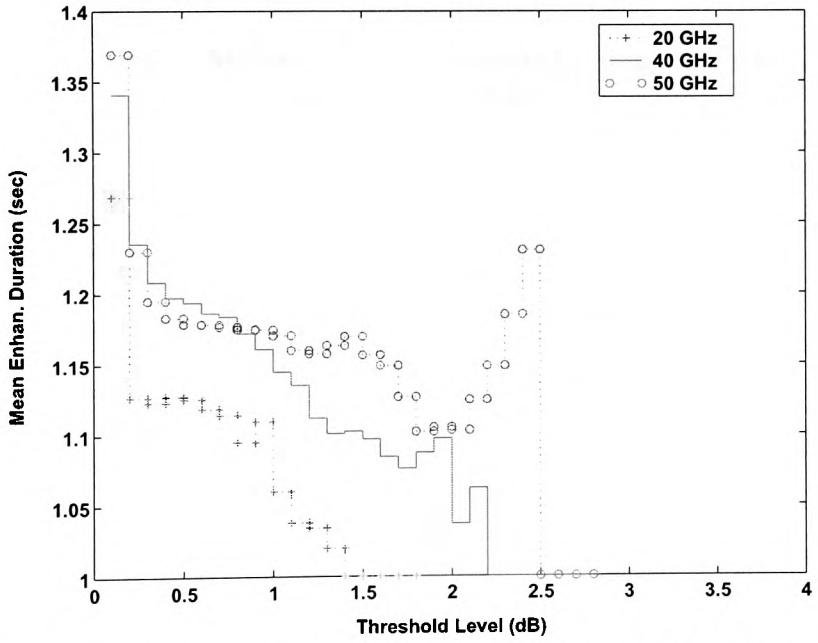

Figure 7.5. Measured annual mean enhancement duration for various signal threshold levels.

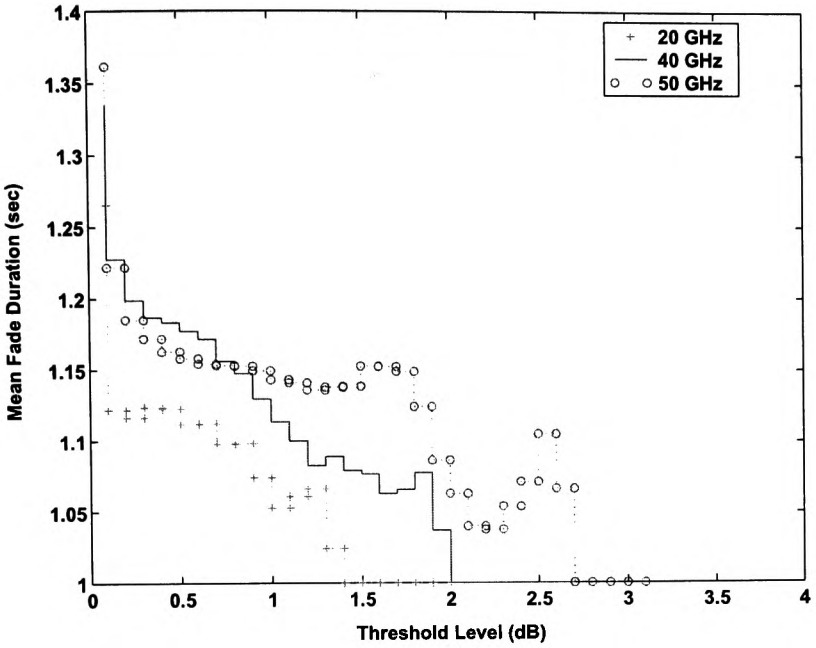

Figure 7.6. Measured annual mean fade duration for various signal threshold levels.

7.5. Fade Countermeasures

As we have seen in the previous sections assigning a fixed fade margin at frequencies above Ka-band is not a feasible solution. Designers are forced to design systems with only a low fixed excess margin of the order of a few dB. The general approach for handling the large attenuation at those frequencies is to use adaptive methods or fade countermeasures (FCM). Fade countermeasure action is effectively a time varying margin, which has to be added in real-time on top of this low fixed excess margin, so as to cover for propagation impairments and maintain a certain grade of service.

To be efficient, the FCM controller has to determine accurately when and how much time-varying effort must be provided by the FCM technique based on current measured channel conditions. The design of fade countermeasure systems should be seen as an optimisation problem once the link availability requirement have been met. FCMs are adaptive systems whereby the transmission is adapted to the channel fading conditions. In the case of adaptive transmission systems like adaptive rate, coding or modulation FCMs, the objective is to maximise the user data throughput while meeting BER requirements. This criterion can be used to compare and select the most appropriate countermeasure technique for any particular system based on adaptive transmission. This section gives an overview of all those techniques relevant to satellite communication systems, in particularly those relevant to VSAT/USAT applications.

7.5.1. Site Diversity

Site diversity is based on the concept of switching the Earth-Space communication from the station affected by fading to another connected ground terminal located at a distant site. Provided that the distance between the Earth station and its back-up(s) is larger than the expected extent of the raincells ($\approx$ 10 km to 15 km), so that the probability of joint fade occurring at the two sites simultaneously is low. The concept of this is shown in Figure 7.7.

Site diversity (SD) is one of the fade mitigation methods that take advantage of the finite size of rain cells. The high level of fading at high frequencies is due primarily to the passage of convective rainstorms through the satellite link. Meteorological data showed that such events are generally limited in geographical extent and that the stronger the rainstorm the smaller the rain cell is, therefore if two ground stations are separated by a distance greater than that covered by each rain cell, they will experience statistically independent fading. This technique is usually suited for rain fading; by monitoring the performance of the two stations and choosing the better of the two, a site diversity system can be implemented.

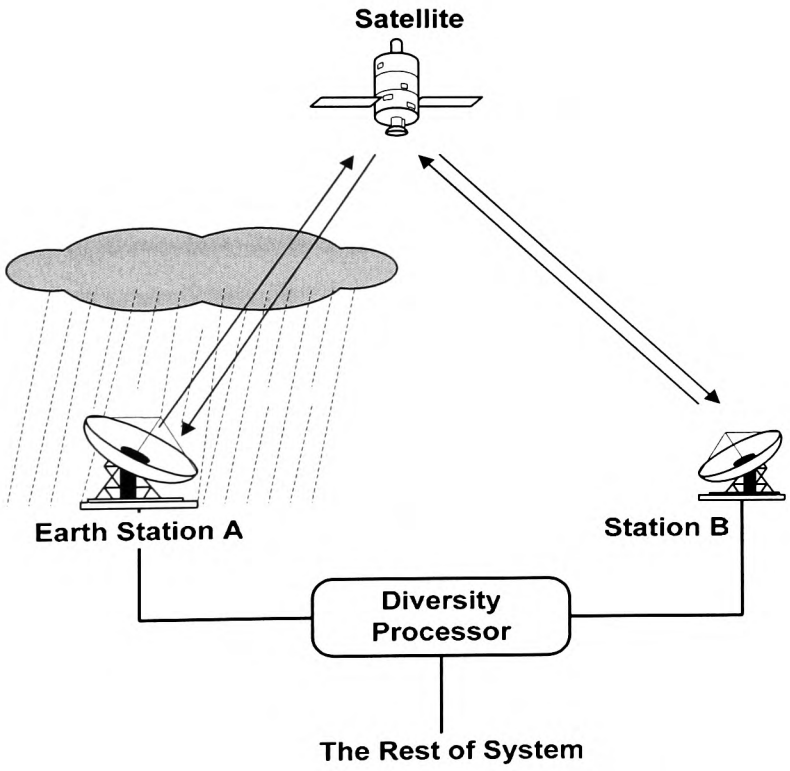

Figure 7.7. Concept of site diversity – if rain fade covers limited area as shown, station A suffers fading but not station B.

The evaluation of the performance of site diversity (SD) systems requires the knowledge of the joint distribution of attenuation amongst the stations. Diversity models derived from empirical data have been proposed in the literature [7, 8]. They

predict a sharp increase of diversity gain for site distances up to 15 km while the improvement stabilises for greater distances. In order to give an example for the effectiveness of site diversity, let us consider a case example of Sparsholt-ITALSAT link. Table 7.1 summarises the rain attenuation statistics for the link.

Table 7.1: Statistics of rain attenuation on a down-link exceeded for various percentages of an average year at 20, 40 and 50GHz.

f(GHz)	1%	0.1%	0.01%	0.001%
20	1.493 (dB)	4.728 (dB)	12.441 (dB)	26.624 (dB)
40	4.167 (dB)	13.196 (dB)	34.727 (dB)	74.316 (dB)
50	5.184 (dB)	16.415 (dB)	43.198 (dB)	93.308 (dB)

Let us find out what would be the diversity gain of a dual site diversity link, as shown in Figure 7.7, for down-link fades and outage time of 0.01% of an average year, which corresponds to availability of 99.99%.

For a conventional fixed link budget margin system operating at 40GHz, a down-link power margin of 34.7 dB would be required. For a two site diversity system, the diversity gain G according to the ITU-R Recommendations [9] is given by Equation 7.7.

$$G = G_d \times G_f \times G_\theta \times G_\psi \quad \text{(dB)} \tag{7.7}$$

The gain contributed by the spatial separation

$$G_d = a(1 - e^{-bd}) \tag{7.8}$$

Where a=0.78A-1.94(1-e$^{-0.11}A$) and

b=0.59(1-e$^{-0.1}A$).

The frequency-dependent gain

$$G_f = e^{-0.025f} \tag{7.9}$$

The elevation angle dependent gain term

$$G_\theta = 1 + 0.006\theta \tag{7.10}$$

The baseline-dependent term

$$G_\psi = 1 + 0.002\psi \tag{7.11}$$

Assuming separation distance between the two site d=15 km, path rain attenuation A=34.7 dB, satellite beacon frequency f=39.59 GHz, path elevation angle θ=29.9^0, the angle made by the azimuth of the propagation path with respect to the baseline between the two sites ψ=15^0. We obtain a net diversity gain G of about 11.4 dB. Note however, that this method has been validated only for frequencies between 10 GHz and 30 GHz.

Site diversity (SD) is one of the most powerful fade countermeasures techniques, because it is able to counteract deep rain fading occurring at high frequencies and is particularly suited to high availability communication systems. However, various problems arise in the implementation of the site diversity of an operational satellite communication system. Firstly, a suitably located additional site has to be available and the cost of it must be met. Earth station hardware has to be almost duplicated, a dedicated high reliability terrestrial link of a suitable capacity provided and a monitoring synchronisation and switching system implemented. SD is therefore more suitable for systems where quality prevails over price.

Site or space diversity can generally be implemented on a large scale, as the case discussed above, sometimes referred to as macrodiversity, and conversely, on a smaller scale called microdiversity. Macrodiversity is usually applied with the intent to mitigate large-scale fading (rain). In contrast, the aim of applying microdiversity is

to mitigate small-scale fading, which involves fades on the order of signal wavelengths. Site diversity could also prove effective for mitigating the degrading effects of scintillation over baseline distances much shorter than that for rain fade mitigation.

Other diversity FCMs systems are Orbital diversity and Frequency diversity. Orbital diversity consists in setting up two separated spacecraft so as to provide two separate converging paths to a single ground terminal. However, measured data [10, 11] indicate an improvement factor of the order of 20%, making orbital diversity quite unsuitable for systems operating at frequencies above Ka-band. In the case of satellites operating in two frequency bands, for example a high frequency band such as V-band and a lower frequency band such as Ku- or C-band, cross-band frequency diversity is possible. Most of the traffic is routed through the high frequency band, where a large bandwidth is available, and some capacity at the lower frequency band, that is less affected by rain acts as a back-up. If the power margin available to the higher frequency band is not sufficient to overcome the attenuation then the system switches to the lower frequency band [12, 13]. The only drawback is that it is probably the least economical of all FCM.

7.5.2. Power Control FCM

Power control as fade countermeasure is the most direct fade countermeasure and mitigates the fading effects by adapting the transmitted power to the attenuation of the affected link, in order to optimise the overall C/N_0. Power control can be carried out in two locations, first on the ground segment where the output power of a transmitting Earth station is adapted to up-link (Up-Link Power Control, ULPC), and secondly on-board the satellite for down-link adaptation, DLPC. To demonstrate the interest in ULPC, it is necessary to distinguish the cases for transparent and regenerative repeaters [14].

In the case of a transparent repeater, the adaptation of the carrier power level by the transmitting Earth station aims to control both up-link and downlink budgets [15]. It

can be implemented relatively easily provided that there is enough power available, i.e. if the satellite power amplifier is not operated at full power. This can, however, not always be the case due to the required dynamic range of fades. Power control on an Earth station attempts to maintain a constant power flux density at the satellite irrespective of fading conditions along the path, by either decreasing the power in clear sky conditions or by increasing the power to compensate fades under fading conditions. ULPC can be seen on the one hand as a way to keep a constant level of all the carriers at the input of the repeater, and on the other hand as a way to maintain the overall link budget of the links in order to optimise the satellite capacity.

With a regenerative repeater carriers are demodulated onboard the satellite, which makes the baseband signals available for specific processing prior to the modulation of the downlink carriers. On-Board Processing (OBP) can be used to optimise the overall link budget of the system. In principle, this technique allows to match the waveform (data rate, coding rate, modulation scheme) to the propagation conditions.

However, it is necessary to pay attention to the sensitivity of on-board demodulation to signal dynamic range at the input of the repeater. As Frequency Division Multiple Access (FDMA) is a typical choice on the uplink, if on-board processing is sensitive to strong variations between carriers, then even for high margin systems, it is recommended to use ULPC in order to avoid capture effects of carriers faded by severe propagation conditions. In this case, the monitoring of all carrier levels has to be carried out on-board the spacecraft, before the spacecraft indicates to the appropriate Earth station the necessary adjustments of up-link transmit power [14, 16]. This is particularly the case for systems operating at or above Ka-band, where there is a strong relative difference between up- and down-link frequencies, and for which a strong protection against uplink fading is important.

Most satellites carry beacon sources in the downlink frequency band. When using a downlink beacon for power control, the estimated downlink fade must be frequency scaled to the up-link frequency. A disadvantage of up-link power control is that, under unfaded conditions, the quality of the up-link will be worse than that of the fixed

power scheme for the same maximum power output required by the dynamic range of the power control scheme. The downlink is unaffected as a new transponder operating point may be chosen to compensate for reduced up-link power. The reduction in up-link quality in turn reduces the total link quality, and thereby decreases the system's tolerance to downlink fading [17].

In conclusion, Up-Link Power Control makes use only of transmitted Earth station power; without constraints on the sharing of the system resources and without a need for specific delay before mitigation. Furthermore, cost considerations and the flexibility of this technique make ULPC a good candidate as an additional technique to be coupled with another FCM.

7.5.3. Down-link Power Control

Down-link Power Control (DLPC) aims to allocate a relatively weak extra power on-board, in order to compensate a possible degradation in terms of down-link C/N_0 due to propagation conditions in the particular region [18]. In this case, all Earth stations in the same beam coverage benefits from the improvement of EIRP. However, it is necessary to verify that the ground power flux density specification is not exceeded, in order to abide by radio regulations and to avoid interference problems, and ensure that no service outage occurs during changes in power level. If the area covered by the satellite antenna beam stretches over several hundreds of kilometres, there may very well be several earth stations operating in it. At these other stations, this will sometimes result in under- or overcompensation. Fukuchi [19] studied the correlation of measured rain intensities at 23 locations in the UK. He found that the correlation decreases rapidly with increasing distance, and that instantaneous rainfall rates at two locations more than about 100 km apart can be regarded as independent. In fact, he found that the benefit of DLPC is confined to the areas less than about 10 km from the monitor station.

In addition, the satellite transponders must be designed in such a way that very little adjacent channel interference and intermodulation noise are produced by the increased

transmitted power. Adaptive DLPC therefore complicates the design and operation of the satellite transponder and is constrained by the limited available on-board power.

7.5.4. Signal Processing Techniques as FCM

These techniques can also be considered as Adaptive Resource Sharing because the available resources on the satellite depend on the number of users requesting a part of these resources at the same time. These techniques are adaptive, meaning that they can adapt to the channel characteristics in order to compensate deep fading when it is needed. As far as signal processing FCM is concerned, two classes of methods can be identified which lead to a modification of the sharing of the satellite resources by acting on the information data rate or on the bandwidth. The objective of the first class is to introduce extra coding in order to compensate additional attenuation on the link by maintaining the nominal BER or to change modulation schemes to implement more robust modulations requiring less symbol energy. A second class of techniques aims to reduce the information data rate at constant transmission data rate, which also leads to maintaining the BER.

Fading degrades the quality of the link by reducing the signal to noise ratio (C/N_0) at the receiver input. In digital communication systems, this signal to noise ratio is related to the bit energy to noise spectral density (E_b/N_0). Figure 7.8 shows the BER of various modulation techniques plotted against the bit energy per noise spectral density ratio (E_b/N_0) [20]. The lower the ratio, the higher the bit error rate (BER).

ITU regulations specify that the BER for data transmission in a system should be 10^{-7}. Thus by maintaining (E_b/N_0) constant at the value that is required for a service, one can ensure that the link quality is at a certain level. Unlike up-link power control (ULPC), which aims to restore the carrier to noise ratio (C/N_0) through an increase of the Earth station transmitted power, the signal processing techniques allows a decrease in the required C/N_0 while maintaining the link performance in terms of the BER. In the following sections these adaptive methods are presented.

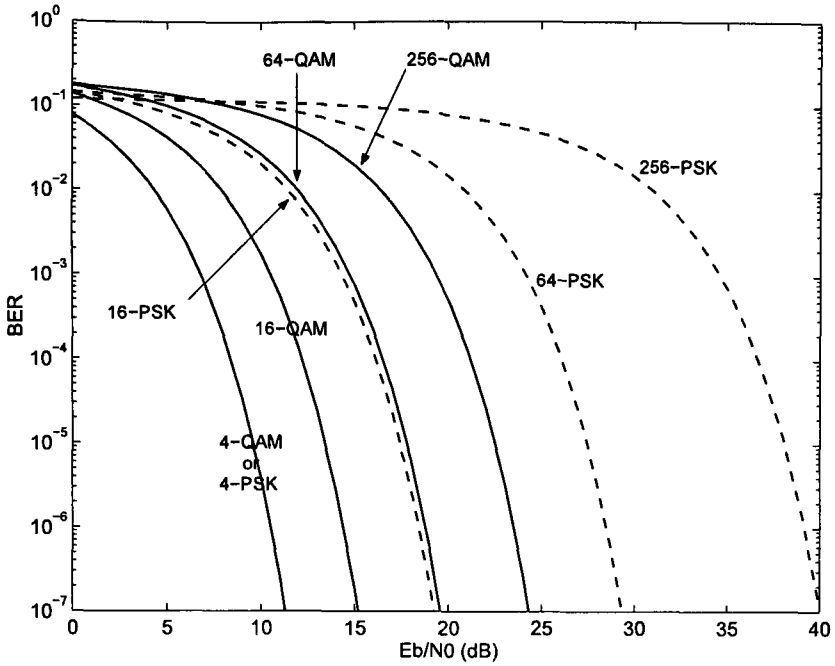

Figure 7.8. BER VS E_b/N_0 for M-ary QAM and M-ary PSK [20].

7.5.5. Adaptive Transmission Rate FCM

Adaptive transmission rate is aimed at maintaining the energy per symbol to noise spectral density ratio (E_s/N_0) at a given level by simply slowing or speeding up the channel symbol rate depending on the propagation conditions. This implies, of course, that the current symbol rate is known to both receiver and transmitter at any one time. High symbol rates are used under unfaded conditions when the signal to noise ratio is high, and the rate would be gradually reduced as fading occurs. For example, to obtain a protection margin of 3 dB, the data rate of the system must be reduced by a factor of 2. This is valid provided that the equivalent noise bandwidth is also reduced by 2 (since bandwidth=symbol rate/spectral efficiency).

For systems operating at or above Ka-band, to compensate for a moderate fade of 10 dB requires a reduction of the data rate by a factor of 10. Such dramatic reduction of the information rate may prove to be unacceptable to a majority of VSAT\USAT

applications. Furthermore, if the transmission rate is reduced, it will be necessary to reduce the bandwidth of the receiver to that of the data signal to obtain maximum gain by rejecting out-of-band noise. Variable bandwidth filter and the cost associated with a variable rate demodulator, are the major disadvantages of this type of fade countermeasure and will inevitably increase the system's cost. Therefore an adaptive transmission rate FCM may be a candidate as an additional strategy to be associated with another main FCM system.

7.5.6. Adaptive Fade Spreading FCM

Another technique which works on a similar principle as adaptive transmission rate is the Adaptive Fade Spreading. It increases the symbol energy at the receiver to compensate for deeper fades by reducing the information data rate. But, the very important difference is that it maintains the channel data rate at a constant level thus avoiding interference problems and the need for a variable receiver filter. In such a system, the user data is multiplied by a pseudo-random code (the spreading function) with fixed chip rate matched to the available spread spectrum bandwidth. This has the effect of spreading the data signal to the bandwidth of the pseudo-random code [21]. The spreading factor is the ratio between the bandwidth of the spread spectrum signal and the bandwidth of the original data stream; the higher the spreading factor, the higher the gain margin.

This fade mitigation technique can be applied only for specific services which can tolerate extra delay and significant reduction of the information rate, such as video download or data transmission (through an increase of transfer duration), but seems to be difficult to use with voice transmission for instance. In summary, adaptive fade spreading is certainly better and more practical than the simplistic adaptive transmission rate systems but is less attractive than other techniques in its class.

7.5.7. Adaptive Coding

Forward Error Correction (FEC) encoding is a technique used in many communication systems to counteract noisy channels. When the satellite

telecommunication link is experiencing fading, the introduction of coding allows to add redundant bits to the information bits, in order to detect and to correct errors caused by propagation impairments and leads to a reduction in the required energy per information bit. Each code is characterised by its rate. Code rate is the ratio between information bit rate and the channel bit rate as a result of the encoding, and its gain which is the reduction in the required energy per channel bit to noise density ratio for the same information bit error rate.

Adaptive coding consists in implementing a variable coding rate in order to match impairments due to propagation conditions. An adaptive FEC system would transmit its data with no encoding during clear-sky conditions, during fades the system would introduce a level of FEC but would at the same time keep the channel rate (and thus bandwidth) constant. Due to the introduced forward error correction encoding and decoding, the information rate will be reduced in accordance with the rate of the applied code. If adaptive coding is used in a communication link it is important that both ends of the link are aware of the code rate in use, i.e. before switching code rate the transmitter must notify the receiver.

The fading satellite communications channel does not produce independent errors but blocks of errors. Since most forward error correction codes are designed to improve system performances by correcting errors which are supposed to be independent, they are not very efficient in counteracting fading. The performance of the mitigation technique can be improved by using block codes (such as Reed-Solomon codes) which are more robust to bursts of errors, and with interleaving, which scrambles the coded data in such a way that, after descrambling, errors can be considered independent [22]. Interleaving is efficient for very short fades and especially for scintillation. Higher performances can be obtained by the concatenation of a convolutional code (Viterbi algorithm) with a block code (such as a Reed-Solomon code), the convolutional code being efficient at correcting random errors, whereas the block code is a good solution to correct error bursts [14].

Systems that employ encoding better utilise the channel. An adaptive FEC system should not be very expensive and difficult to implement, making it an attractive solution for VSAT applications. The main drawbacks of using this fade countermeasure technique are the complex decoding algorithms that have to be implemented in the receiver in order to decode the signal and extract the information, and the additional bandwidth requirements for Frequency Division Multiple Access (FDMA) and larger bursts in the same frame for Time Division Multiple Access (TDMA), due to transmission of redundant bytes.

7.5.8. Adaptive Modulation

In this section we will focus on using adaptive modulation as a fade countermeasure. An adaptive modulation system would transmit at its most complex modulation during fine propagation conditions and would reduce the complexity of the scheme when fades occur. Higher system capacity for a specified bandwidth can be achieved by using modulation schemes with high spectral efficiency.

Adaptive modulation is a powerful technique to improve the energy efficiency and increase the data rate over a fading channel. As with adaptive coding, the aim of the adaptive modulation technique is to decrease the required bit energy per noise energy ratio(E_b/N_0) corresponding to a given BER, by reducing the spectral efficiency as the C/N decreases. The reduction of the spectral efficiency can be obtained by introducing lower level modulation schemes. For instance, if very efficient modulations such as 16-PSK, 16-QAM, 64-PSK, 64-QAM or 256-QAM can be used in clear-sky conditions, in bad propagation conditions, adaptive modulation fade mitigation technique makes use of more robust modulations such as QPSK or BPSK [23].

Another way of reducing the required E_b/N_0 is to introduce coding into the modulation. Gremont *et al.* [24] proposed such a system based on adaptive pragmatic trellis coded modulation, suitable for services which can accept a variable user data rate (i.e. the satellite bandwidth occupancy is fixed on a channel basis). The authors showed that

such a multiple fade mitigation technique modem could very significantly outperform systems relying on single FCMs such as adaptive coding or adaptive (uncoded) modulation.

The use of adaptive modulation as a fade countermeasure technique is dealt with in more detail in the PhD thesis of Dr. C.N. Kassianides, using simulations implemented in COSSAP simulation platform [4]. Other fade countermeasure techniques such as reserve capacity (adaptive TDMA – FDMA) will not be discussed in this thesis. Reserve capacity can be extremely effective but are suited more to services such as trunk telephony rather than data applications.

7.6. Fade Countermeasures that can be Applied to Scintillation Fading

In the previous sections, an overview of the various fade countermeasure techniques was presented. Most of these techniques and most of the cases in the literature are concerned with rain attenuation. Not all of these techniques can be applied to mitigate scintillation. An effective FCM has to take into consideration also the effects of scintillation. Results obtained from the statistical analysis in Chapter 5 of this thesis showed that considering only scintillations in climates similar to the UK and moderate elevation angles to obtain 99.99% availability, a 2 dB fade margin is adequate at 50GHz. However, as shown in Figure 7.9, at low elevation angles in hot humid climates such as Japan at the same frequency to achieve the same availability, a fade margin of about 9.5 dB is required (based on predictions using the ITU-R model [9]). In this section we will look at some of the FCM techniques that could be applied to scintillation fading.

Power control is the most direct fade countermeasure and is relatively easy to implement. For low margin VSAT/USAT systems operating at or above Ka-band, power control can prove to be useful countermeasure technique to counteract fading and can be used to mitigate scintillations [25]. This technique can be used as a stand alone or combined with some other fade countermeasure and can be implemented as either Up-Link Power Control (ULPC) or as combined Up- and Down-Link Power Control system.

At these high frequency bands there is a strong relative difference between up and down frequencies, for which a strong protection against uplink fading is important. During small fades, which are mainly due to scintillation events or passing clouds the Earth station can adjust the transmitted power to compensate for propagation impairments to maintain the uplink budget.

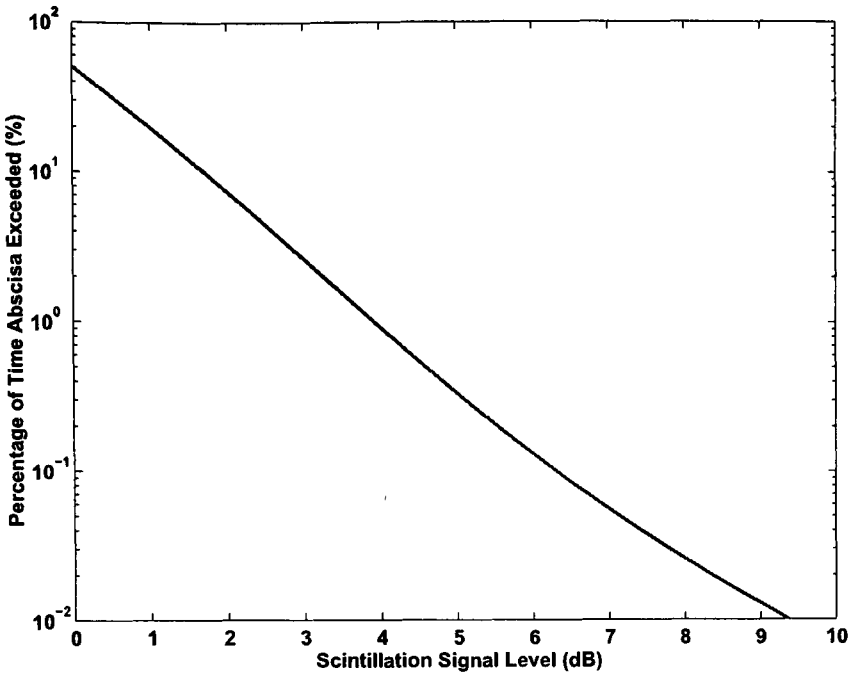

Figure 7.9. Predicted cdf of scintillation fade amplitude at 50GHz using the ITU-R model. Assuming: temperature=16^{0}C, humidity=77%, antenna diameter=0.61m, antenna efficiency=0.65 and elevation angle=6.5^0.

In actual fact, for the first generation Ka-band systems (30GHz uplink – 20GHz downlink) uplink power control (ULPC) is one of the basic FCMs which will be implemented with the objective of improving system availability (availability > 99%). More sophisticated techniques such as adaptive coding and modulation will be implemented in a second step, in particular for V-band (50/40 GHz) systems where propagation impairments at both the uplink and downlink are severe, and it is not possible to consider that the uplink is more critical than the downlink.

All signal-processing techniques can be applicable for mitigating scintillation. The need for adaptive filters makes adaptive rate transmission less attractive. Adaptive modulation schemes, like adaptive PSK or adaptive QAM allow the design of a link to maximise the information rate over a channel while maintaining a specified E_b/N_0 value. This technique assumes that sufficient resources like power are provided during clear air conditions. A review of adaptive modulation and coding has already been

presented. The question is which one of these two techniques will be more appropriate in satellite communication to counteract scintillation?

Table 7.2 shows the required E_b/N_0 for various QAM and PSK modulation techniques. It can be seen that 16-PSK requires E_b/N_0 =19.24 dB for BER of 10^{-7}. 16-QAM on the other hand, that has the same spectral efficiency (4 b/s/Hz), requires 15.18 dB, i.e. 4.06 dB less. That fade protection margin can be used to compensate for the propagation degradation caused by the atmosphere. In the case of a bandwidth efficiency of 6 b/s/Hz offered by both 64-QAM and 64-PSK, the QAM method needs 9.77 dB less E_b/N_0. Thus to transmit with 64-PSK instead of 64-QAM an increase of nearly 10 dB in power is needed, which ultimately represents a significant increase in cost to the end user. When propagation conditions become more severe, the system can switch for example from 64-QAM to QPSK, introducing a fade protection margin of 8.26 dB. The downside is the temporarily reduced data rate, however, when the conditions become more favourable the system can switch back to the higher modulation schemes.

Adaptive modulation assumes that sufficient resources are available in order to use the various modulation methods with the required E_b/N_0 for a specific BER. It is therefore appropriate for medium to high power applications, while adaptive coding or Adaptive Forward Error Correction (AFEC) countermeasure is more appropriate for more power-limited links. For the same power characteristics, AFEC would have a better availability than adaptive modulation, but the latter would have a greater throughput. These two approaches are in contention, and the basic selection can be made by asking which constraint, throughput or availability, is paramount to the system design and thus should be maximised. For a system with severely limited power resources where high order modulation methods can not be supported, AFEC is a better solution.

Table 7.2: Theoretical values of E_b/N_0 for BER 10^{-7} for M-QAM and M-PSK (see Figure 7.8)

	QPSK	16-QAM	64-QAM	8-PSK	16-PSK	64-PSK
E_b/N_0 (dB)	11.3	15.18	19.56	14.73	19.24	29.33

Site diversity as fade countermeasure, usually applies to rain attenuation. As mentioned earlier, it is a method that takes advantage of the finite size of rain cells. It can not be applied to mitigate scintillation fading because scintillation and rain do not have the same characteristics. Scintillation can be present in clear sky as well as cloud and is a fast fading process unlike rain attenuation. The time needed to switch from one station to another will often be greater than the duration of the scintillation on the communication link. Furthermore, there is no guarantee that the other earth station will not encounter scintillation fading at the same time. The level of scintillation fades, as it can be seen for the data analysis in Chapter 5, does not justify the high cost of site diversity. Therefore site diversity is excluded as fade countermeasure for mitigating scintillation.

Microdiversity or microscale diversity is a good technique to mitigate scintillation. Work on fade countermeasure [26-28], showed that scintillation effects can be alleviated by the use of two antennas separated laterally by several hundreds of meters or vertically by about 150 meters. In the Goonhilly experiment [29], it was shown that substantial improvement could be obtained with antennas separated vertically by an order of magnitude less – a much more practical spacing. In that experiment the authors used antenna spacing of 16.5 m. Their results show no correlation between the two signals.

Since the signal from the two antennas appear to be totally uncorrelated, it is unlikely that an increased separation would be of additional benefit. This would suggest that only a small vertical stratification of the atmosphere exists [30]. In [31] results from an investigation into a microscale diversity scheme for the purpose of mitigating scintillation are presented. It is shown that the optimum spacing of the two antennas at

an elevation angle of 14° is about 48m horizontally. At this spacing the two signals are completely decorelated.

A microscale system could be applied in situations where scintillations contribute significantly to propagation impairments such as in very low elevation angle terminals or in climates where scintillation events are frequent. Low-power-margin VSAT systems are a good example where microscale diversity could be useful.

Up/Down-Link Power Control (U/D-LPC) is another good and simple FCM technique that could be applied to mitigate both scintillation and rain attenuation. The delay in the control loop is at worst 2 satellite round trips ≈ 0.52 seconds, plus processing and switching times.

Several theoretical and experimental campaigns of Up/Down-Link Power Control have been reported [32-34]. Hörle [35, 36] showed that for excess up-link fades of more than 4 dB, the user data rate of a combined ULPC with Direct Sequence Spread Spectrum (DSSS) FCM system is always a factor of 2 higher than without ULPC.

It might be expected that a ULPC network will not be able to follow fast signal fluctuations due to scintillation. However, Touw and Herben [37] showed from a spectral analysis, that signal fluctuations due to scintillation at 12.5, 20 and 30 GHz on the same propagation path are quite well correlated for frequencies up to a few tenths of a Hz. This means that the lower part of the fluctuation spectrum, which contains the main portion of the power, can be compensated by open-loop ULPC using frequency scaling. The small faster signal fluctuations will not be followed. As a result, for an open-loop ULPC system operating at 20/30 GHz, the variance of the up-link amplitude scintillation (in dB^2) can be reduced to about 20% of its value.

Karasawa and Maekawa [38] found that at the 10 dB fade threshold level the improvement in link availability using DLPC was fairly close to the theoretical limit ignoring simultaneous rain in different areas. Therefore in climates similar to the UK, power control could be used as a stand alone technique to mitigate for small fades due

to scintillation events or passing clouds. However, at very low elevation angles (e.g. Japan) and frequencies above Ka-band, this technique alone is not sufficient and must be combined with some other adaptive fade countermeasure (for example Adaptive Coding or Modulation).

7.7. Conclusions

This Chapter started with some general definitions and equations related to satellite communication system design, followed by an overview of digital modulation techniques used in satellite communications. Phase Shift keying (PSK) and Quadrature Amplitude Modulation (QAM) were selected as the two most appropriate candidates. The PSK scheme, because of its constant envelope is generally preferred. QAM's excellent bandwidth efficiency and good BER performance, however, make them both possible choices for future high data-rate satellite communication systems.

Statistics of observed durations of scintillation fades and enhancements of the ITALSAT satellites at 20, 40 and 50GHz are presented for various threshold signal levels, and their use in fade countermeasures were examined. The analysis showed that most signal amplitude deviations from the mean level are of short duration and do not depend on the threshold level. Distribution of fade durations at thresholds 0.1 and 0.5dB were reasonably well approximated by the lognormal function.

As we have seen in the previous sections assigning a fixed fade margin at frequencies above Ka-band is not a feasible solution. At those frequencies the effects of atmospheric impairments are very severe. However, due to the considerable advantages of operating satellite communication systems in these frequency ranges, mitigating techniques have been developed to overcome the impairments associated with these frequency bands.

In general, the impact of rain attenuation on communication signals is predominant. But in order to develop effective fade countermeasures the impact of scintillation

needs also to be taken into consideration, especially at low elevation angles in hot and humid climates. In this Chapter we examined some adaptive fade countermeasure techniques that can be applied to mitigate the severe degradation due to the atmospheric propagation fading. Depending on the priorities of the system to be designed, adaptive power control and adaptive signal processing are the prime candidates.

Up-link power control (ULPC) makes use only of transmitted Earth station power; therefore it can be implemented for any percentage of time, which makes this technique a very flexible one and can be used as a fade countermeasure (FCM) for both scintillation and rain attenuation. Most first generation fade FCM techniques for Ka-band satellite systems will use ULPC with the objective of improving system availability. In addition, the flexibility of ULPC makes it easy to combine it with another FCM such as adaptive coding or modulation to improve system performance even more.

Up-link power control combined with adaptive coding are the prime fade countermeasure candidates for mitigating against rain attenuation and scintillation effects at Ka-band. At V-band, however, which will be used for multimedia systems, adaptive modulation is more likely to be implemented because of the higher throughput. An adaptive modulation system would transmit at its most complex modulation during good propagation conditions and would reduce the complexity of the scheme (i.e. introducing fade protection margin) when fades occur.

References

[1] I. E. Otung, "Accurate prediction of scintillation degradation applicable to satellite communication system design," University of Glamorgan 1998.

[2] I. Otung, *Communication Engineering Principles*: Palgrave, 2001.

[3] A. Bateman, *Digital Communications - Design for the Real World*: Addision Wesley, 1999.

[4] C. K. Kassianides, "A Study of the Effects of Scintillation on Digital Satellite Communication Systems," in *School of Electronics*. Pontypridd: University of Glamorgan, 2002.

[5] F. Xiong, "Modem Techniques in Satellite Communications," *IEEE Communications Magazine*, pp. 84-98, August 1994.

[6] F. Dintelmann, "Analysis of 11GHz Slant Path Fade Duration and Fade Slope," *Electronics Letters*, vol. 17, pp. 267-268, 1981.

[7] E. Matricciani, "Prediction of Site Diversity Performance in Communications Systems Affected by Rain Attenuation: Extension of Two Layer Rain Model," *Euro. Trans. on Telecomms and Related Technologies*, vol. 5, pp. 327-336, May-June 1994.

[8] D. B. Hodge, "An Improved Model for Diversity Gain on Earth-Space Propagation Paths," *Radio Science*, vol. 17, pp. 1393-1399.

[9] ITU-R, "P.618-7 Propagation data and prediction methods required for the design of Earth-space telecommunication systems," Recommendations and Reports of the ITU-R 1997.

[10] E. Matricciani and M. Mauri, "Italsat-Olympus Orbital Diversity Experiment at Spino d'Adda," *IEEE Transactions on Antennas and Propagation*, vol. 43, pp. 105-108, 1995.

[11] C. Capsoni, E. Matricciani, and M. Mauri, "Sirio-OTS Orbital Diversity Experiment at Fucino," *IEEE Transactions on Antennas and Propagation*, vol. 38, pp. 777-782, 1990.

[12] F. Carassa, G. Tartara, and E. Marticciani, "Frequency Diversity and its Applications," *Int. Journal of Satellite Communication*, vol. 6, pp. 313-322, 1988.

[13] G. Tartara, "Fade Countermeasures in Millimeter-wave Satellite Communications: A Survey of Methods and Problems," presented at Proc. Olympus Utilisation Conference, Vienna, 12-14 April 1989.

[14] COST255, "Cost Action 255: Final Report," European Space Agency (ESA) 2002.

[15] J. Horle, "Up-Link Power Control of Satellite Earth Stations as a Fade Countermeasure of 20/30 GHz Communication Systems," *Int. Journal of Satellite Communication*, vol. 6, pp. 323-330, June 1988.

[16] R. J. Acosta, "Rain Fade Compensation Alternatives for Ka-band Communication Satellite," presented at 3rd Ka-Band Ultilization Conference, Sorrento, Italy, 15-18 Sep. 1997.

[17] M. J. Willis and B. G. Evans, "Fade Countermeasures at Ka band for Olympus," *Int. Journal of Satellite Communication*, vol. 3, pp. 301-311, 1988.

[18] L. Castanet, J. Lemonton, and M. Bousquet, "Fade Mitigation Techniques for New SatCom Services at Ku-band and Above: a Review," presented at 5th International Workshop on Radiowave Propagation Modelling for SatCom Services at Ku-band and Above, Netherlands, 28-29 Oct. 1998.

[19] H. Fukuchi, "Quantitative Analysis of the Effect of Adaptive Satellite Power Control as a Rain Attenuation Countermeasure," presented at IEEE International Symposium on Antennas and Propagation, 1994.

[20] I. E. Otung, *Communication Engineering Principles*: Palgrave, 2001.

[21] C. D. Hughes and M. Tomlinson, "The Use of Spread-Spectrum Coding as a Fading Countermeasure at 20/30 GHz," *ESA Journal*, vol. 11, pp. 73-81, 1988.

[22] J. G. Proakis, *Digital Communications*, Third Edition ed: Mc Graw-Hill Int. Ed., 1995.

[23] M. Filip and E. Vilar, "Implementation of Adaptive Modulation as a Fade Countermeasure," *Int. Journal of Satellite Communication*, vol. 8, pp. 33-41, June 1990.

[24] B. C. Gremont, M. Filip, and E. Vilar, "Simulation of a High Frequency Satellite Link with a Fade Countermeasure," presented at International Conference on Antennas and Propagation (ICAP 1999), York, UK, 1999.

[25] M. J. Willis and B. G. Evans, "An Adaptive Coding/Up-Path Power Control Fade Counter Measure Experiment via Olympus," presented at OLYMPUS Utilization Conference Proceedings, Vienna, 1989.

[26] O. Gutteberg, "Measurements of Atmospheric Effects on Satellite Links at Very Low Elevation Angle," presented at AGARD EPP Symposium on Characteristics of the Lower Atmosphere Influencing Radiowave Propagation, Norway, 1983.

[27] J. I. Strickland, "Site Diversity Measurements of Low Angle Fading and Comparison with Theoretical Model," *Ann. Telecomm.*, vol. 36, pp. 457-463, 1981.

[28] V. Mimis and A. Smalley, "Low Elevation Angle Site Diversity Satellite Communications for the Canadian Arctic," presented at IEEE International Conf. on Communications (ICC82), Philadelphia, 1982.

[29] D. L. Bryant, "Low Elevation Angle 11GHz Beacon Measurements at Goonhilly Earth Station," *BT Technol. J.*, Oct.1992.

[30] D. L. Bryant and J. E. Allnutt, "Use of Closely-Spaced Height Diversity Antennnas to Alleviate the Effects of Low Elevation Angle Non-Absorptive Fading on satellite Slant Paths," *Electronics Letters*, vol. 26, pp. 479-480, 1990.

[31] J. C. Cardoso, A. Safaai-Jazi, and W. L. Stutzman, "Microscale Diversity in Satellite Communications," *IEEE Transactions on Antennas and Propagation*, vol. 41, June 1993.

[32] S. Tirro, *Satellite Communication Systems Design*. New York: Plenum Press, 1993.

[33] A. Dissanayake, "Application of Open-Loop Uplink Power Control in Ka-Band Satellite Links," *Proceedings of IEEE*, vol. 85, pp. 959-969, 1997.

[34] M. M. J. L. V. d. Kamp, "Climatic Radiowave Propagation Models for the Design of Satellite Communication Systems." Eindhoven: Technical University Eindhoven, 1999.

[35] J. Hörle, "Up-Link Power Control of Earth Stations as a Fade Countermeasure of a 20/30 GHz Satellite Communications Experiment," presented at Proceedings Olympus Utilisation Conference, Vienna, 1989.

[36] J. Hörle, "Up-Link Power Control of Satellite Earth-Stations as a Fade Countermeasure of 20/30 GHz Communication Systems," *Int. Journal of Satellite Communication*, vol. 6, pp. 323-330, June 1988.

[37] S. I. E. Touw and M. H. A. J. Herben, "Short-term Frequency Scaling of Clear-sky and Wet Amplitude Scintillation," *IEE Proceedings on Microwave Antennas Propagation*, vol. 143, pp. 521-526, 1996.

[38] Y. Karasawa and Y. Maekawa, "Ka-Band Earth-Space Propagation Research in Japan," *Proceedings of IEEE*, vol. 85, pp. 821-842, 1997.

- The refractive index structure constant C_n is constant along the turbulent path length L.
- The atmospheric turbulence lies in the inertial subrange $l_o < \sqrt{\lambda L} << L_o$; where l_o and L_o are the inner and outer scales of turbulence — of the order 1-10 mm and 50-100 m, respectively.
- $L_o^2 \kappa_m^2 >> 1$

and introduce the factor $(20\log e)^2$ to convert from Neper^2 to dB^2, then the variance of scintillation amplitude σ_x^2 is given by:

$$\sigma_x^2 = 23.162 C_n^2 \kappa^{7/6} L^{11/6} \qquad (\mathrm{dB}^2) \tag{8.2}$$

where

$$L = 2h/\{\sqrt{\sin^2\theta + (2h/R_e)} + \sin\theta\} \tag{8.3}$$

and

C_n^2 : is the refractive index structure constant

L : is the effective turbulent path length;

k : is the wave number ($k=2\pi/\lambda$);

θ : is the elevation angle;

h : is the height of turbulence;

R_e : is the effective earth radius (= 8.5 × 10^6 m);

Equation (8.2) is valid for point receivers only. A finite antenna aperture reduces σ_x from its point receiver value by a factor $g(x_i)$ given by Haddon and Vilar [2]

$$g(x_i) = \sqrt{3.8637\left(x_i^2+1\right)^{11/12}\sin\left[\frac{11}{6}\arctan\left(\frac{1}{x_i}\right)\right] - 7.0835x_i^{5/6}}$$
$$x_i = \frac{0.0584\pi\eta D^2\left[\sqrt{\sin^2\theta + (2h/R_e)} + \sin\theta\right]}{h\lambda_i} \tag{8.4}$$

where

D : is the physical diameter of antenna;

η : is the illumination efficiency of the antenna (= 0.64);

λ_i : is the signal wavelength;

In equation (8.2), the structure constant C_n^2, which is the main characterising parameter of the models derived from Tatarskii's theory, is a measure of the spatial variance of the refractive index fluctuations. It is dependent on height, which is important for elevated propagation paths. The derivation of a prediction model of long term scintillation variance directly using equation (8.2) would impose a difficulty; the structure parameter of the refractive index variations is an essential atmospheric parameter in equation (8.2), but this parameter can not directly be measured. Thus, some quantification must be obtained from scintillation measurements, and the model can be further developed semi-empirically, using the various other dependencies derived from theory.

Early work towards modelling scintillation has been done by various researchers [3, 4]. The predicted variance of scintillation amplitude fluctuations, depends upon frequency, elevation angle and antenna size, as:

$$\sigma^2 \propto G(D_e) f^{7/6} / (\sin\theta)^{11/6} \tag{8.5}$$

Where $G(D_e)$ is the antenna averaging function given by Crane and Blood [5]. In Equation (8.5) the elevation angle dependency exponent in Crane's model was slightly lower having a value of 1.7. However, those models do not incorporate meteorological parameters and are therefore insensitive to climatic variations. Karasawa, Yamada and Allnutt [6] presented a new prediction model for the calculation of the standard deviation of signal fluctuations due to scintillation, based on research done at KDN, Japan.

8.2. CURRENT PREDICTION MODELS

8.2.1. Karasawa Model

Karasawa, Yamada and Allnutt presented a prediction method for the calculation of the standard deviation σ_x of the signal fluctuations due to scintillation, based on measurement made during the year 1983 at Yamaguchi, Japan, at frequencies of 11.5 and 14.23 GHz [6]. The satellite was viewed from an elevation angle of 6.5^0, using Cassegrain antenna of diameter 7.6m. For the elevation angle dependence, they used more long term data from the same site, at elevation angles of 4^0 and 9^0. The model is based on the assumption that the short-term pdf of the log-amplitude is Gaussian, which leads to a symmetrical distribution of signal level; and a Gamma distribution for the long-term pdf of scintillation variance.

They derived the following prediction formula for calculating the standard deviation, σ_{pre} of signal level fluctuations, also referred to as scintillation intensity.

$$\sigma_{pre} = 0.0228(0.15 + 5.2\times10^{-3} N_{wet})\, f^{0.45} \sqrt{G(D_e)} / \sin^{1.3}\theta \qquad \text{(dB)} \qquad (8.6)$$

where

$$N_{wet} = \frac{22790 U\, e^{19.7t/\,(t+273)}}{(t+273)^2} \qquad (8.7)$$

f = frequency in GHz

θ = Elevation angle (degrees)

$G(D_e)$ = Antenna aperture averaging function given by Crane and Blood.

N_{wet} = Wet-part of refractivity (ppm)

t = temperature (^{0}C)

U = Relative humidity (%)

In order for the model not to predict the short-term scintillation variations with daily weather changes, the meteorological parameters (temperature and relative humidity) should be averaged at least for a period in the order of a month. The height of turbulence h in Karasawa model is assumed to be 2000m. If the elevation angle is below 5^0, then the term $\sin\theta$ in equation (8.6), should be replaced by $\left(\sin\theta+\sqrt{\sin^2\theta+2h/R_e}\right)/2$ taking into account the curvature of the earth, where R_e is the effective Earth radius (8.5×10^6 m).

The Karasawa model has been validated by comparison to measurements from four different sites in Western Japan, and from Haystack (USA) and Chilbolton (UK). These measurements were made at elevation angles from 4^0 to 30^0, frequencies from 7.3 to 14.2 GHz, and antenna diameters from 3 to 36.6m. The average wet-part of refractivity, N_{wet} in these different databases varied from 20 to 130 ppm.

Some expressions for the long-term cumulative distribution of amplitude level, expressed in terms of the predicted long-term standard deviation were also developed. The resulting amplitude level y, exceeded for a time percentage of P, is given by:

Enhancements

$$y=\left(-0.0597\log_{10}{}^3 P-0.0835\log_{10}{}^2 P-1.258\log_{10} P+2.672\right)\sigma_{pre} \tag{8.8}$$

for $(0.01\% \le P \le 50\%)$

Fades

$$y=\left(-0.061\log_{10}{}^3 P+0.072\log_{10}{}^2 P-1.71\log_{10} P+3\right)\sigma_{pre} \tag{8.9}$$

for $(0.01\% \le P \le 50\%)$

8.2.2. ITU-R Model

The ITU-R [7] prediction model is based on similar formulation technique as that used in the Karasawa model. It has been recommended for use between 4 and 20 GHz, and for elevation angles greater than 4^0. This model has also been compared to satellite measurements for frequencies up to about 30 GHz in the frameworks of the Olympus and ACTS propagation experiments.

$$\sigma_{pre} = \left(3.6\times10^{-3} + 10^{-4} N_{wet}\right) f^{7/12} g(x_i) / \sin^{1.2}\theta \tag{8.10}$$

where $g(x_i)$ is the aperture averaging function from Haddon and Vilar [2], given by Equation (8.4). A turbulent height of h=1000m is suggested by the ITU-R. Similar to the Karasawa model, the input meteorological parameters in the ITU-R model should be averaged over a period in the order of one month.

The ITU-R adopted only the signal fades cdf distribution (Equation (8.9)) in the proposed prediction model.

8.2.3. Otung Model

Another classical scintillation model is the Otung model [8]. Validated using measurements from the Olympus satellite, recorded at Sparsholt, U.K, this recent model (1996), is based on assumptions very similar to those used for the ITU-R and Karasawa models. The main difference is the elevation angle dependence of the predicted scintillation intensity and the time percentage dependence. In this model instead of using $sin^{1.2}\theta$ as in the ITU-R model, it uses the theoretical elevation angle dependence factor which is $sin^{11/12}\theta$.

$$\sigma_{pre} = \left(3.6\times10^{-3} + 10^{-4} N_{wet}\right) f^{7/12} g(x_i) / \sin^{11/12}\theta \tag{8.11}$$

Similar to the Karasawa model, in this model both fades and enhancements cumulative distributions are given.

Signal Enhancements

$$y = 3.1782\sigma_{pre}\exp\left\{-0.0359654p - \left[0.272113 - 0.00438p\right]\ln(p)\right\} \tag{8.12}$$

for $(0.01\% \le P \le 50\%)$

Signal Fades

$$y = 3.6191\sigma_{pre}\exp\left\{-\frac{9.50142\times10^{-4}}{p} - \left[0.40454 + 0.00285p\right]\ln(p)\right\} \tag{8.13}$$

for $(0.01\% \le P \le 50\%)$

8.2.4. Van de Kamp Model

Significant correlation as was shown in chapter 4, has been found between the occurrence of scintillation and the presence of Cumulus clouds along the propagation path [9, 10]. A new parameter, indicating the average water content W_{hc} of "turbulent clouds" occurring on the propagation path could be used to improve the prediction models of scintillation. Using the Salonen/Uppala cloud model [11], [12], the average water content of heavy clouds W_{hc} was calculated for the whole Earth from an ECMWF database. "Heavy clouds" are clouds with an integrated water content larger than 0.70 kg/m^2. Van de Kamp *et al.* [13] incorporated W_{hc} in a new empirical prediction model for σ_{pre} in the following way:

$$\sigma_{pre} = \frac{\sqrt{g^2(x_i)}f^{0.45}}{\sin^{1.3}\theta}0.98\times10^{-4}(N_{wet} + Q) \tag{8.14}$$

$$Q = -39.2 + 56\langle W_{hc}\rangle \tag{8.15}$$

where

$\langle x \rangle$ = long-term (at least annual) average of parameter x

W_{hc} = Average water content of heavy clouds (kg/m^2).

Q = Long-term average parameter and therefore constant for each site, so that all seasonal dependence of σ_{pre} is still represented by N_{wet}.

8.3. Comparison with Measurements

In this section, the results from the prediction models are compared to those obtained from the measurements site at Sparsholt. The comparison between measurements and predictions is achieved either using a graphical representation of the distributions along with the corresponding experimental data or through the calculation of the relative error (in percent, %) between the model and the measured values.

The averaged values for temperature, humidity and standard deviation used in testing the models (ITU-R, Karasawa and Otung) were given in Tables 4.3 - 4.5, in Chapter 4. These three input parameters have been averaged over every month and over the entire measurement period for the period covering September 1999 to August 2000 for the 20GHz ITALSAT F2 beacon, and from July 1996 to August 1997 (excluding August 1996), for the 40 and 50GHz ITALSAT F1 beacons.

Comparison of the performance of the three models (ITU-R, Karasawa and Otung) is shown in Table 8.1-Table 8.3. The performance of Van de Kamp model will be discussed separately under Table 8.4. As can be seen from these tables the performances of these models vary considerably depending on the month of the year and the beacon frequency under consideration. For example, at 20GHz the ITU-R model performs quite well with absolute errors of less than 8%, which is as expected since this model have been validated for frequencies up to 20GHz. However, at higher frequencies the ITU-R model greatly overestimates the standard deviation, with values varying by up to 76%.

Table 8.1: Comparison between measurement results of scintillation standard deviation (scintillation intensity) for the 20GHz beacon and those obtained using the prediction models. The error in percent is also shown for each model.

Month	**Measured**	**ITU-R Model**		**Karasawa Model**		**Otung Model**	
20GHz	Std (dB)	Std (dB)	Error (%)	Std (dB)	Error (%)	Std (dB)	Error (%)
Sep 99	0.1163	0.1225	5.3181	0.0972	-16.4051	0.1006	-13.5354
Oct 99	0.0995	0.0999	0.4412	0.078	-21.637	0.082	-17.5393
Nov 99	0.0925	0.0952	2.9209	0.0739	-20.0812	0.0782	-15.5034
Dec 99	0.0926	0.087	-6.092	0.0669	-27.7593	0.0714	-22.9029
Jan 00	0.0865	0.0876	1.3194	0.0675	-21.997	0.072	-16.8183
Feb 00	0.0903	0.09	-0.3304	0.0695	-23.0428	0.0739	-18.1727
Mar 00	0.0917	0.0892	-2.7534	0.0688	-24.9781	0.0732	-20.162
Apr 00	0.098	0.0919	-6.2237	0.0711	-27.4346	0.0754	-23.011
May 00	0.1085	0.1064	-1.8967	0.0835	-23.0188	0.0874	-19.4586
Jun 00	0.1068	0.1146	7.2802	0.0905	-15.2924	0.0941	-11.9245
July 00	0.1073	0.1157	7.8713	0.0915	-14.7351	0.095	-11.4392
Aug 00	0.1218	0.1218	-0.0053	0.0966	-20.654	0.1	-17.9058
Average 1-year T=9.9605, H=82.423	**0.10098**	**0.1007**	**-0.2539**	**0.0787**	**-22.12**	**0.0827**	**-18.11**

Table 8.2: Comparison between measurement results of scintillation standard deviation (scintillation intensity) for the 40GHz beacon and those obtained using the prediction models. The error in percent is also shown for each model.

Month	Measured	ITU-R Model		Karasawa Model		Otung Model	
40GHz	Std (dB)	Std (dB)	Error (%)	Std (dB)	Error (%)	Std (dB)	Error (%)
Jul 96	0.1574	0.1833	16.47	0.1312	-16.6772	0.1505	-4.3799
Sep 96	0.1217	0.1693	39.1092	0.1203	-1.1478	0.139	14.2067
Oct 96	0.1225	0.1668	36.2015	0.1184	-3.3522	0.137	11.8195
Nov 96	0.1012	0.1417	40.0385	0.099	-2.187	0.1163	14.9696
Dec 96	0.0775	0.1286	65.9204	0.0889	14.6538	0.1056	36.2182
Jan 97	0.0696	0.1227	76.3066	0.0843	21.167	0.1007	44.7451
Feb 97	0.1099	0.1462	32.9921	0.1024	-6.8139	0.12	9.1845
Mar 97	0.0958	0.1474	53.9083	0.1034	7.9522	0.121	26.3565
Apr 97	0.0997	0.1396	39.9796	0.0974	-2.3508	0.1146	14.9212
May 97	0.1097	0.1599	45.7276	0.113	3.0233	0.1312	19.6402
Jun 97	0.1289	0.1785	38.502	0.1274	-1.1479	0.1466	13.7081
July 97	0.1585	0.1892	19.3888	0.1357	-14.3809	0.1554	-1.9835
Aug 97	0.1716	0.2137	24.5512	0.1546	-9.8951	0.1755	2.2548
Average 13-Month T=10.4225, H=79.2984	**0.1172**	**0.1579**	**34.65**	**0.1115**	**-4.9281**	**0.1296**	**10.5457**

Table 8.3: Comparison between measurement results of scintillation standard deviation (scintillation intensity) for the 50GHz beacon and those obtained using the prediction models. The error in percent is also shown for each model.

Month	Measured	ITU-R Model		Karasawa Model		Otung Model	
50GHz	Std (dB)	Std (dB)	Error (%)	Std (dB)	Error (%)	Std (dB)	Error (%)
Jul 96	0.1876	0.2077	10.7202	0.1442	-23.1131	0.1705	-9.1003
Sep 96	0.156	0.1918	22.9598	0.1323	-15.1857	0.1575	0.9482
Oct 96	0.1603	0.189	17.9303	0.1302	-18.771	0.1552	-3.1809
Nov 96	0.1306	0.1606	22.9492	0.1089	-16.6413	0.1318	0.9395
Dec 96	0.1053	0.1457	38.3611	0.0977	-7.1934	0.1196	13.5925
Jan 97	0.094	0.139	47.9078	0.0927	-1.3306	0.1141	21.4301
Feb 97	0.1544	0.1656	7.2549	0.1126	-27.0512	0.136	-11.9453
Mar 97	0.1208	0.1671	38.2935	0.1137	-5.8442	0.1372	13.5369
Apr 97	0.1224	0.1581	29.1872	0.1071	-12.522	0.1298	6.0608
May 97	0.1471	0.1811	23.1336	0.1243	-15.502	0.1487	1.0909
Jun 97	0.1636	0.2023	23.6422	0.1401	-14.3412	0.1661	1.5084
July 97	0.1976	0.2144	8.5043	0.1493	-24.4683	0.176	-10.9195
Aug 97	0.2103	0.2422	15.1508	0.1701	-19.1383	0.1988	-5.4628
Average 13-Month T=10.4225, H=79.2984	**0.1500**	**0.1788**	**19.2325**	**0.1226**	**-18.2822**	**0.1468**	**-2.1118**

The predicted standard deviation (std) of the Karasawa model and Otung model vary from month to month, with the Karasawa model having slightly better performance at 40 GHz while the Otung model performs better at 50GHz. The absolute error between measured and predicted standard deviation (std) for the entire 13-month measurement period at 40 GHz were 4.9% and 10.5%, respectively. Whereas at 50 GHz they were 18.3% and 2.1%, respectively.

The effect of meteorological variables (temperature and humidity) on scintillation are included in the three models mentioned above only through the wet-term of refractivity, N_{wet}. Hence, these models fail to predict the dependence of scintillation on temperature in a dry atmosphere when N_{wet} is negligible. Van de Kamp incorporated a new parameter in the prediction model. It is the average water content of heavy clouds, W_{hc}. The value derived for W_{hc} from the global map of annual average W_{hc} [13] was in the range 1.0 to 1.2 kg/m^2. The predicted σ_{pre} calculated using equations (8.14) and (8.15) are tabulated in Table 8.4 below. As it can be seen from the results, at the three respective beacon frequencies Van de Kamp model always underestimate the standard deviation in comparison with the measured results. In actual fact when considering the entire measurement period at each beacon frequency, out of the four models, it gave the highest absolute percentage error.

Table 8.4: Measured and predicted standard deviation at 20, 40 and 50 GHz according to Van de Kamp model, W_{hc} is the annual average water content of heavy clouds.

	Measured std	Predicted (W_{hc} = 1.0)	Predicted (W_{hc} = 1.2)
20 GHz	0.10098 dB	0.0561 dB, (-44.4%)	0.0660 dB, (-34.7%)
40 GHz	0.1172 dB	0.0789 dB, (-32.7%)	0.0928 dB, (-20.8%)
50 GHz	0.1500 dB	0.0869 dB, (-42.1%)	0.1023 dB, (-31.8%)

All distributions are compared to the models by ITU-R, Karasawa and Otung for signal fades and enhancements. Since in the ITU-R recommendations [7] only the cumulative distribution function for signal fades is cited, this is the only curve from the ITU-R included in the graphs. From the Karasawa and Otung models, the curves for both signal fades and enhancements are included.

The annual distributions for the period covering September 1999 to August 2000 for the 20GHz ITALSAT F2 beacon, and from September 1996 to August 1997 for the 40 and 50GHz ITALSAT F1 beacons, are presented in Figure 8.1-Figure 8.3. The measured fades and enhancements are very close to each other. This is in agreement with the assumption that short-term signal level fluctuations follow a Gaussian distribution around the mean. The shapes of the measured curves at the three respective frequencies for both fades and enhancement are very similar to the ITU-R empirical fades curve. Whereas for probabilities smaller than 1% it appears that the Karasawa model always underestimates the signal deviation for both fades and enhancements, at all three frequencies. The Otung predicted enhancement curves are very close to the measured ones, however, the predicted fade curves deviates significantly from the measured curves in the low probability region.

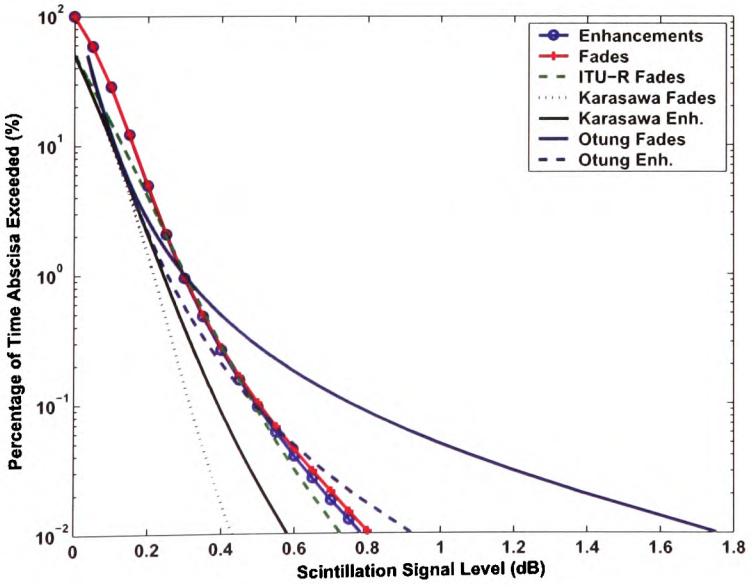

Figure 8.1. Annual cdf of scintillation signal fades and enhancements at 20GHz, and comparison with the ITU-R, Karasawa and Otung models.

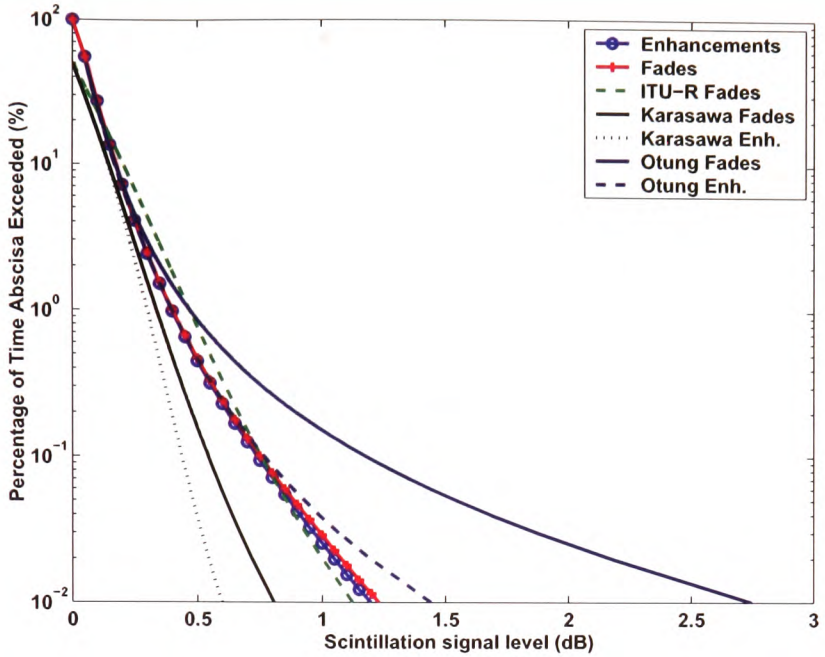

Figure 8.2. Annual cdf of scintillation signal fades and enhancements at 40GHz, and comparison with the ITU-R, Karasawa and Otung models.

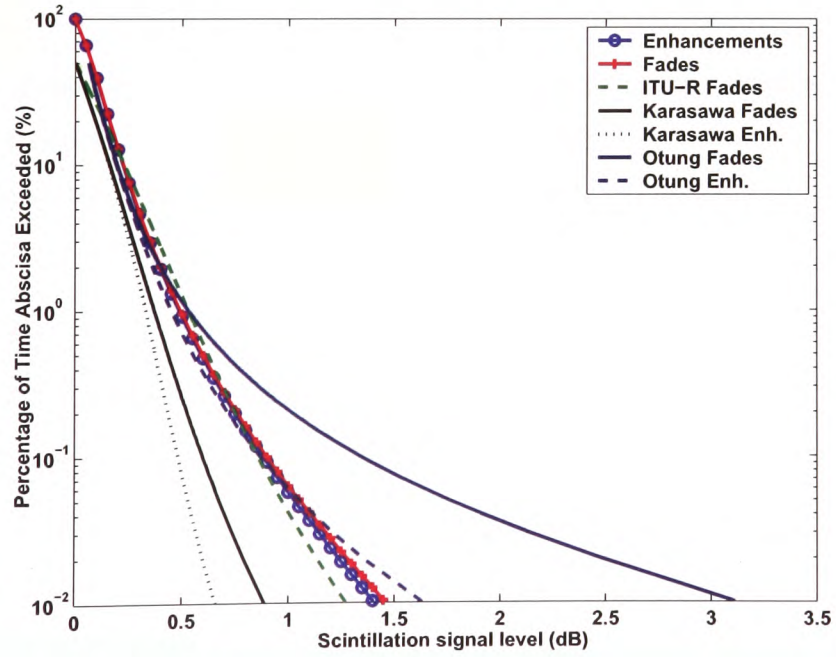

Figure 8.3. Annual cdf of scintillation signal fades and enhancements at 50GHz, and comparison with the ITU-R, Karasawa and Otung models.

8.4. Improved Prediction Model

Following the evaluation of the current prediction models, it has been concluded that their performance is not adequate and potential refinements will be examined in this section in order to improve prediction. For the development of the new model long-term measurement results from around the globe from different sites, in different climates and operating at different elevation angles and frequencies have been obtained from various publications. Only sites which reported the probability distribution and the average standard deviation measured over the same period have been selected. The main site parameters used in the analysis are summarised in Table 8.6. Some details on the data preprocessing at the different measurement sites can be found in Appendix D.

All three classical models (ITU-R, Karasawa and Otung) can be written in the following form:

$$\sigma_{pre} = (b + dN_{wet}) f^{\alpha} g(x_i)/(\sin^z \theta) \tag{8.16}$$

Where, f = frequency in GHz, θ = elevation angle (degrees), $g(x)$ = antenna aperture averaging function. The constants b, d, α and z have different values for the three models. These values are tabulated in Table 8.5 below.

Table 8.5: Parameters used in the prediction models

	ITU-R	Karasawa	Otung Model
b	3.4e-3	3.42e-3	3.4e-3
d	1e-4	1.1856e-4	1e-4
α	7/12	0.45	7/12
z	1.2	1.3	11/12

Table 8.6: Main system parameter and averaged standard deviation of the signal in the data sets analysed.

Ground Station	f (GHz)	θ (^{0})	D (m)	Temperature (^{0}C)	Humidity (%)	STD (dB)
Madrid	49.49	40	1.2	14.448	55	0.1427
Sparsholt	19.77	28.74	1.2	9.8	79.6	0.0961
Kirkkonummi	19.77, 29.66	12.7	1.8 1.8	5.5	82.6	0.165, 0.228
Sparsholt	18.69	29.9	1.22	9.9605	82.423	0.10098
Sparsholt	39.59, 49.49	29.9	0.61	10.423	79.298	0.1139 0.147
Chilbolton	11.2	7.1	3	16.5	76	0.466
Chilbolton	11.2	8.9	3	16.5	76	0.43
Chilbolton	11.8	30	3	16.5	76	0.095
Austin	11.2	5.8	2.4	20.133	71.7	0.62
Yamaguchi	11.45	6.5	7.6	15.75	76.5	0.54
Spino d'Adda 1995	18.69	37.8	3.5	11.99	79.40	0.06
Spino d'Adda 1996	18.69	37.8	3.5	11.89	80.40	0.057
Spino d'Adda 1995	39.59	37.8	3.5	11.99	79.40	0.113
Spino d'Adda 1996	39.59	37.8	3.5	11.89	80.40	0.108
Spino d'Adda 1995	49.49	37.8	3.5	11.99	79.40	0.153
Spino d'Adda 1996	49.49	37.8	3.5	11.89	80.40	0.184

Due to the different frequency and geometrical configuration of each measurement setup, it is necessary to normalise all the distributions to a reference site to be able to perform a useful comparison. In Figure 8.4, the cumulative distributions for signal fades, and in Figure 8.5, for signal enhancements, are shown for all the measurement sites. The separation into two graphs is simply for the sake of a clearer view. Note that Chilbolton signal enhancements is missing in Figure 8.5 because it was not reported in the citation.

The modelling procedure is shown in Figure 8.6, a link is a unique set of system and climatic parameters. So for example, measuring 3 beacon frequencies at a single site (as in the case of Sparsholt-Italsat link) amounts to n=3 separate links, while measuring one beacon frequency at 3 different sites also amounts to n=3 separate links. Assuming the dependence on frequency, elevation angle and antenna size as described in the models of the ITU-R, Karasawa and Otung, all distributions can be scaled to a reference link.

$$X_{nor} = \frac{g(x_i)_{ref}}{g(x_i)_{site}} \times \frac{f_{ref}}{f_{site}} \times \frac{\sin\theta_{site}}{\sin\theta_{ref}} \times \frac{Sr_{ref}}{Sr_{site}} \times CD_{site}^{(i)}(p) \tag{8.17}$$

where *ref* donates the reference link to which all other site will be normalised to, and *site* is system and meteorological parameters for each measurement site.

X_{nor} = Normalised cumulative distribution.

$g(x_i)$ = Aperture averaging function from Haddon and Vilar [2].

f = Beacon frequency (GHz).

θ = Elevation angle.

$CD_{site}^{(i)}(p)$ = Measured cumulative distribution (CD) on link i.

and $Sr = 3.6\times10^{-3} + 10^{-4} N_{wet}$, where N_{wet} is the wet-part of refractivity.

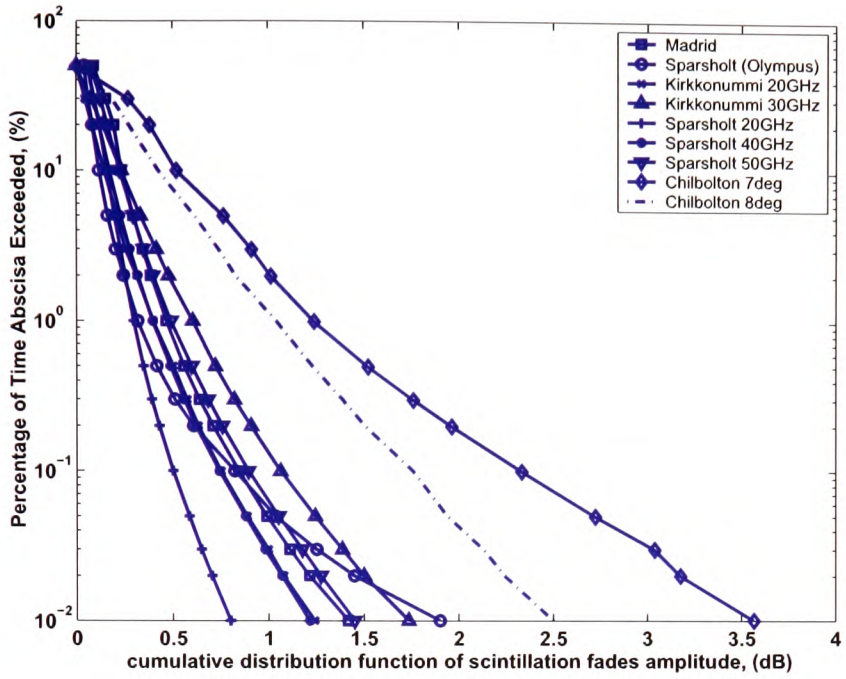

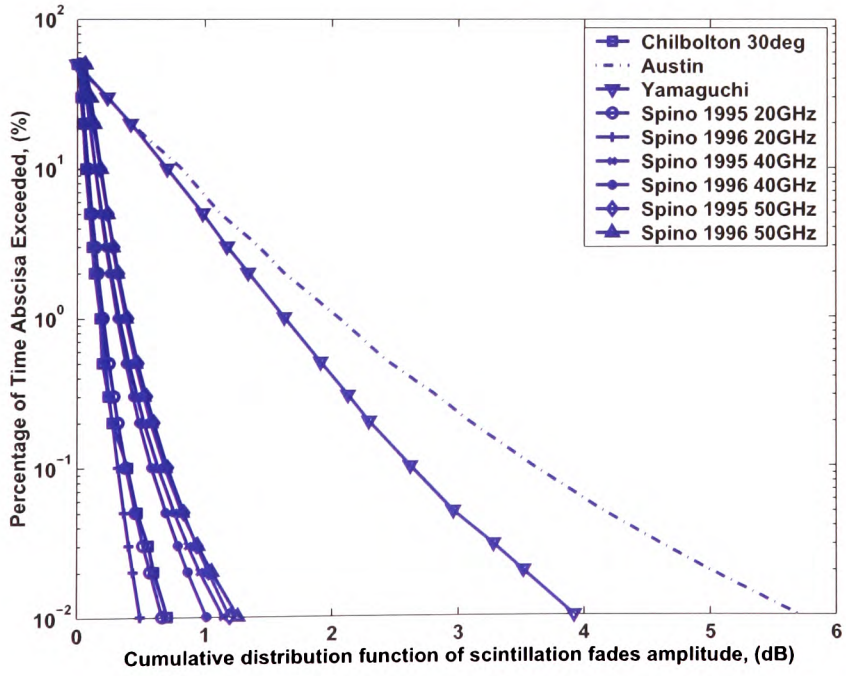

Figure 8.4. Measured cumulative distribution function of scintillation signal fades in Madrid, Sparsholt, Kirkkonummi, Chilbolton, Austin, Yamaguchi, Spino d'Adda at 20, 40 and 50 GHz for the years 1995 and 1996. The separation into two graphs is simply for the sake of a clearer view.

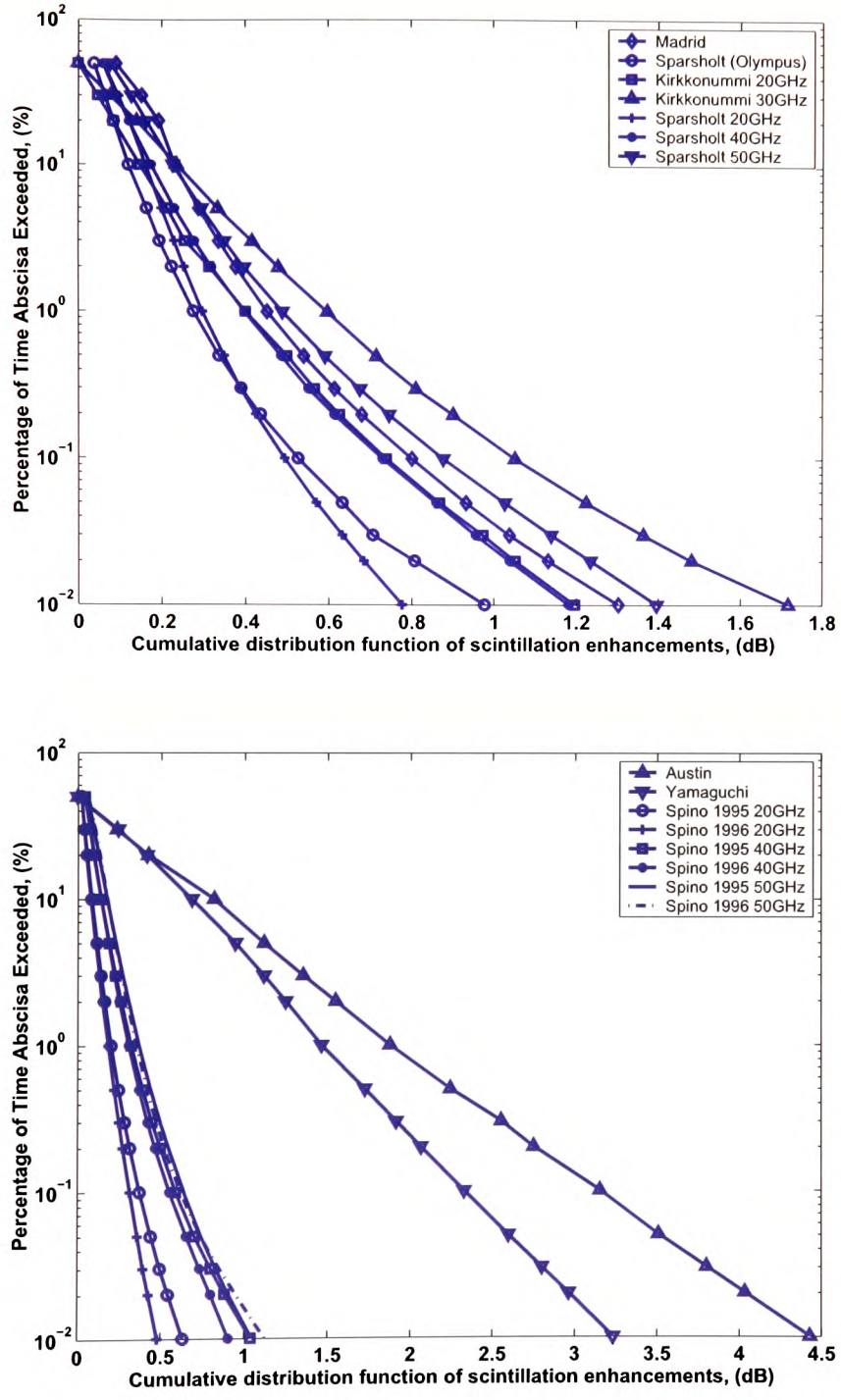

Figure 8.5. Measured cumulative distribution function of scintillation signal enhancements in Madrid, Sparsholt, Kirkkonummi, Austin, Yamaguchi, Spino d'Adda at 20, 40 and 50 GHz for the years 1995 and 1996. The separation into two graphs is simply for the sake of a clearer view.

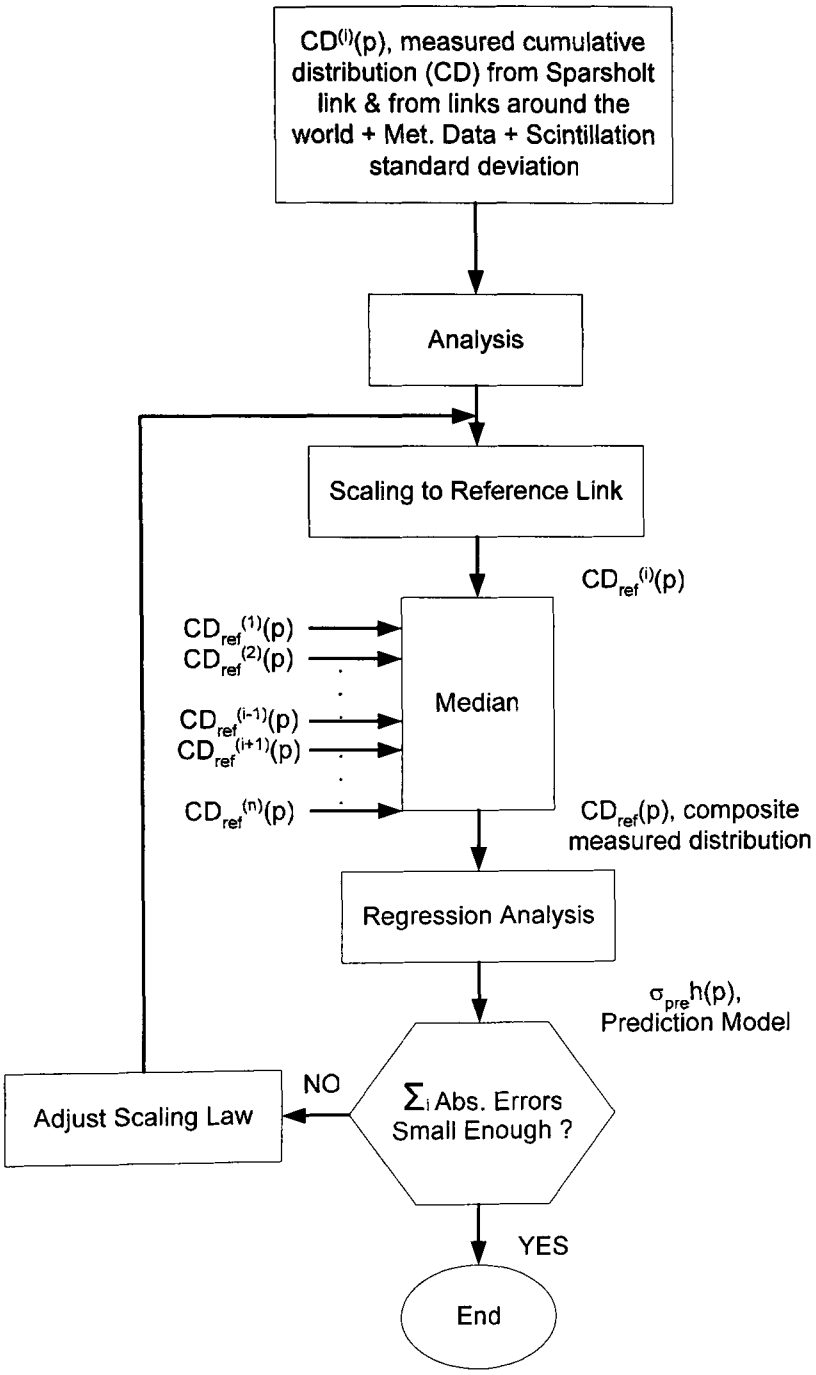

Figure 8.6. Modelling Procedure

To start with we will use the 40 GHz beacon data recorded at Sparsholt as the reference site, the normalised cumulative distributions for all the measurement sites are plotted in Figures 8.7 and 8.8. The red thick line is the composite curve obtained by taking the median value at each percent of time for all measurement sites. All distributions have been normalised therefore theoretically they should all correspond to the thick line indicated in the figures. Again the separation into two graphs is simply for the sake of a clearer view. The reader should take into account that some of the global measured data were obtained from published results. These published results are usually presented in graphs. The data have been extracted from these by enlarging the paper copies. Even though every care has been taken to get the best accuracy by using a software program and by checking the results again manually, there will always be a small margin of error. This error is typically in the order of < 1 %.

Following an extensive analysis to determine the main factors that might be responsible for the discrepancy in the scintillation standard deviation and cumulative distributions from one measurement site to another, we summarised the three main areas which we can refine to improve the accuracy of the prediction models, and develop the new improved model (see Equation (8.16)):

- Frequency power exponent.
- Elevation angle power exponent.
- The wet-part of refractivity.

Recalling from the analysis carried out in Chapter 6, a significant correlation was observed between the frequency exponent α and the elevation angle θ. It provides a good starting point for the development of the new improved prediction model. However, we have to be careful not to assume (*over-weight*) that this is the only parameter responsible for the discrepancy observed from one site to another and therefore instead of using the regression relationship obtained from Chapter 6, it was necessary to restrict the variations of α within the range 0.4 to 0.6. By applying this restriction in α and carrying-out a best-fit regression analysis to minimise the absolute errors at each site, we obtained the following expression for the frequency exponent:

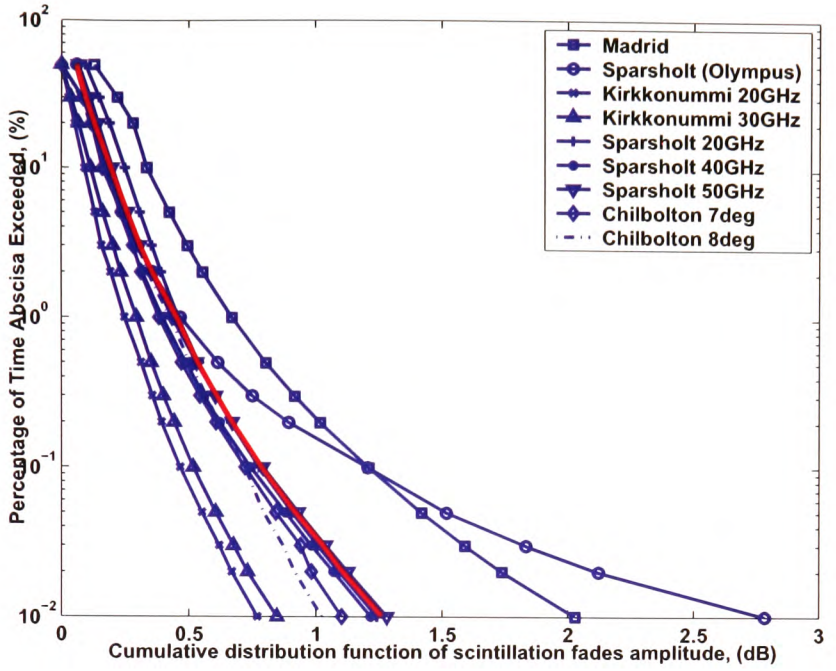

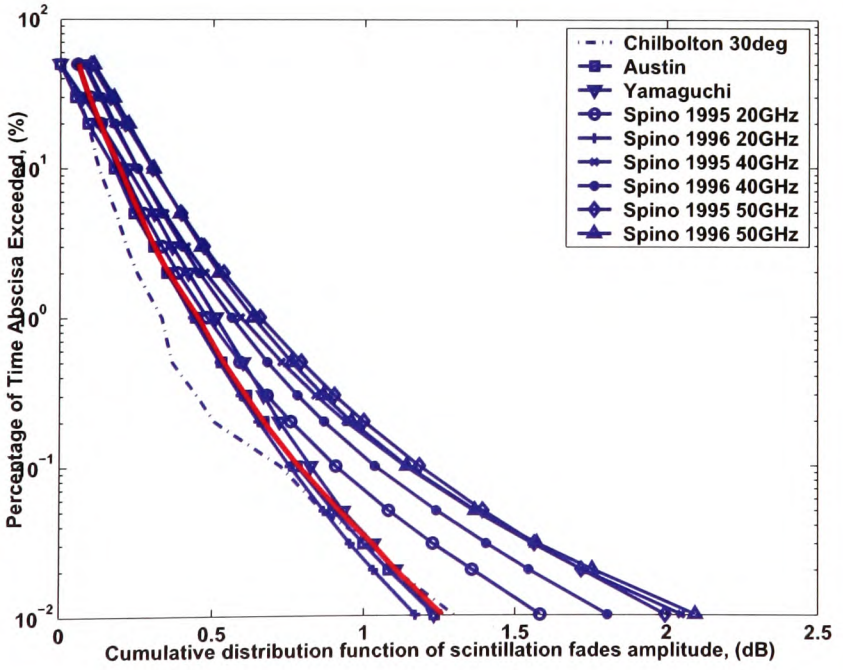

Figure 8.7. Normalised cumulative distribution function of scintillation signal fades in Madrid, Sparsholt, Kirkkonummi, Chilbolton, Austin, Yamaguchi, Spino d'Adda at 20, 40 and 50 GHz for the years 1995 and 1996. The separation into two graphs is simply for the sake of a clearer view. Red thick line is the composite curve.

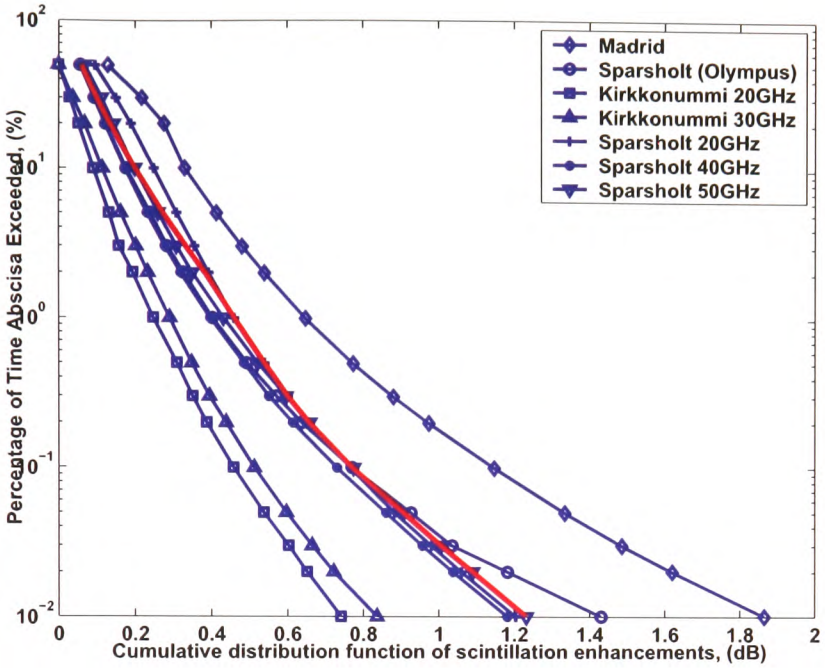

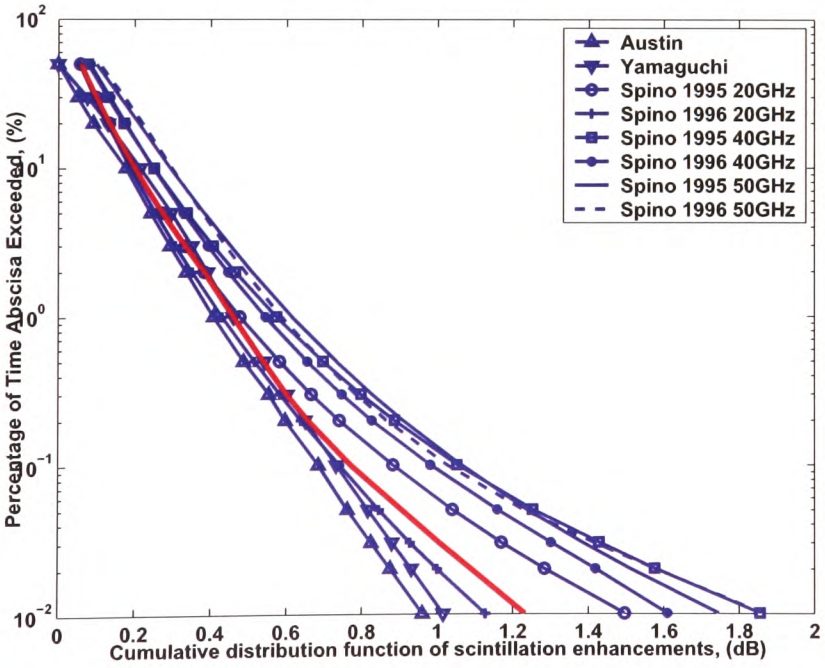

Figure 8.8. Normalised cumulative distribution function of scintillation signal enhancements in Madrid, Sparsholt, Kirkkonummi, Austin, Yamaguchi, Spino d'Adda at 20, 40 and 50 GHz for the years 1995 and 1996. The separation into two graphs is simply for the sake of a clearer view. Red thick line is the composite curve.

$$\alpha = 0.4196 \times \sin(\theta) + 0.3661 \tag{8.18}$$

The next parameter which we will attempt to optimise in order to minimise the discrepancies is the elevation angle dependence power exponent, namely the constant z in Equation 8.16. As can be seen from Table 8.5, this coefficient varies from the theoretical value of 11/12 (Otung model) to 1.3 as is the case of the Karasawa model. If we look at Table 8.7 we can see that for example in the case of very low elevation angles for example Austin or Yamaguchi employing the theoretical z=11/12 (Otung Model) yields higher absolute errors, when compared to using z=1.2 (ITU-R Model) or z=1.3 (Karasawa Model). In actual fact overall we found that when taking all measurement sites into consideration the optimum values for z is as follows:

$$\begin{aligned} z &= 1.2 \quad \textit{for } \theta > 10^0 \quad \textit{and} \\ z &= 1.3 \quad \textit{for } \theta < 10^0 \end{aligned} \tag{8.19}$$

Finally, the last parameter to consider is the wet part of refractivity, N_{wet}. In hot dry climates the use of this parameter will underestimate the impact of tropospheric scintillation. Following a thorough optimisation analysis we obtained the following relationship between averaged surface temperature and the wet-part of refractivity.

$$S_{ref} = 3.6 \times 10^{-3} + 1 \times 10^{-4} N_{wet}^{\gamma} \tag{8.20}$$

Where

$$\begin{aligned} \gamma &= 1.0 \quad \textit{if } Ave.Temperature < 15^0 C \quad \textit{and} \\ \gamma &= 1.07 \quad \textit{if } Ave.Temperature > 15^0 C \end{aligned} \tag{8.21}$$

Equations (8.18)-(8.20) together now form the new improved model for predicting the averaged scintillation intensity (standard deviation). Comparison of the performance of the ITU-R, Karasawa, Otung and the new improved model for all the measurement sites is shown in Table 8.7. When comparing the performance of the new model to

that of the ITU-R, we can see that it performs better especially for example for sites like Madrid, Kirkkonummi at 20 GHz and 30 GHz, with improvement of over 18%, 45% and 22%. These results are positive because Madrid and Kirkkonummi have very different climates. Madrid has dry and warm conditions, and the satellite is viewed from a high elevation angle, while Kirkkonummi is cold, and more humid, and the satellite is viewed from a very low elevation angle.

Another good example is Chilbolton where the data were collected at the same site using the same antenna diameter but at different elevation angles. At path elevation angle of 7.1^0 the Karasawa and Otung model underestimates the measured standard deviation by 0.3% and -43.2%, respectively. The Karasawa model is expected to perform better since it was validated at similar elevation angles and frequencies. However at the higher elevation angle of $\theta=30^0$ the errors are -24.4% and -26.3%, for the two respective models. The new model on the other hand presented errors of only 3.2% and 7%, respectively for the two path elevation angles. These findings together with the rest of the results from the other measurement sites in Table 8.7 are a good indicator that this new improved model could be globally applicable for sites in different climates and operating at different frequencies and path elevation angles.

Apart from Spino d'Adda at 20 and 50 GHz all other absolute errors for all the measurement sites are $\approx$ 10% or less. Even for Spino d'Adda at 50 GHz the model still performs $\approx$ 10% better than the ITU-R model and yields up to about $\approx$ 30% improvement over the Karasawa and Otung models. In a search for a system or meteorological parameter which might be responsible for the error, we found that assuming a height of turbulence h=2000m as in the Karasawa model reduced the errors of the new model by a further 10%. This is not surprising since in warmer climates the height of the turbulent layer is usually higher than those recorded in higher latitudes where the average temperature in much lower. Unfortunately, this did not improve the results for the other sites in similar climates and therefore it was decided to keep h=1000m, as recommended by the ITU-R.

Table 8.7: Comparison of the performance of σ_{pre} of ITU-R, Karasawa, Otung and the new improved prediction model.

Site	Measured	ITU-R Model		Karasawa Model		Otung Model		New Model	
	Std (dB)	Std (dB)	Error (%)	Std (dB)	Error (%)	Std (dB)	Error (%)	Std (dB)	Error (%)
Madrid (50GHz)	0.1427	0.1137	-20.3	0.0755	-47.1	0.1003	-29.7	0.1396	-2.2
Sparsholt (Olympus)	0.0961	0.1061	10.4	0.0823	-14.4	0.0862	-10.3	0.1013	5.4
Kirkkonummi (20GHz)	0.165	0.2408	45.9	0.1996	21.0	0.1568	-5.0	0.1658	0.5
Kirkkonummi (30GHz)	0.228	0.3061	34.3	0.2404	5.4	0.1993	-12.6	0.2004	-12.1
Sparsholt (20GHz)	0.101	0.1008	-0.2	0.0787	-22.1	0.0827	-18.1	0.0984	-2.5
Sparsholt (40GHz)	0.1139	0.156	37.0	0.11	-3.4	0.128	12.4	0.1243	9.1
Sparsholt (50GHz)	0.15	0.1767	17.8	0.121	-19.3	0.1451	-3.3	0.1712	14.2
Chilbolton (θ=7.1^0)	0.466	0.4789	2.8	0.4674	0.3	0.2648	-43.2	0.481	3.2
Chilbolton (θ=8.9^0)	0.43	0.363	-15.6	0.3464	-19.4	0.2139	-50.3	0.3679	-14.4
Chilbolton (θ=30^0)	0.095	0.0852	-10.3	0.0718	-24.4	0.07	-26.3	0.1016	7.0
Austin	0.62	0.6815	9.9	0.6835	10.2	0.356	-42.6	0.694	11.9
Yamaguchi	0.54	0.47	-13.0	0.4606	-14.7	0.2535	-53.1	0.4676	-13.4
Spino d'Adda (20GHz, 1995)	0.06	0.0682	13.6	0.0524	-12.7	0.0593	-1.1	0.0765	27.5
Spino d'Adda (20GHz, 1996)	0.057	0.0685	20.1	0.0526	-7.7	0.0595	4.5	0.0768	34.8
Spino d'Adda (40GHz, 1995)	0.113	0.0902	-20.2	0.0627	-44.5	0.0785	-30.5	0.1043	-7.7
Spino d'Adda (40GHz, 1996)	0.108	0.0906	-16.1	0.063	-41.7	0.0788	-27.0	0.1047	-3.1
Spino d'Adda (50GHz, 1995)	0.153	0.0965	-36.9	0.0651	-57.4	0.084	-45.1	0.1126	-26.4
Spino d'Adda (50GHz, 1996)	0.184	0.0969	-47.3	0.0654	-64.4	0.0843	-54.2	0.113	-38.6

8.5. Signal Level Distribution

We have demonstrated that the modifications to the current ITU-R model coefficients resulted in a new improved prediction model which gave good predictions and smaller absolute errors. In this section, we will seek to develop a distribution model of the σ_{pre} $h(p)$, where σ_{pre} is the new improved relationship and $h(p)$ gives the shape of the distribution and is obtained by careful regression analysis of the composite cumulative distribution as a function of the percent of time $p(\%)$.

Using similar nonlinear regression function of the form $h(p)=p^{z(p)}exp[y(p)]$ as in the Otung model [8]. Trial and error calculations were carried out to obtain the fit which gave the smallest absolute errors. Where p was equally spaced between 0.01% - 30%. As we mentioned previously some of the data was obtained from published graphs, the 50% value in some cases was not very accurately read because at the origin the data points were too close together to give a very accurate reading. Therefore in the modelling of the curve we decided it was best to model p between 0.01% and 30%. It is also worth mentioning that these equations may not give correct results out side the specified range of p.

The distribution models for scintillation enhancements and fades are given in Equations (8.22) and (8.23), respectively. The measured, predicted scintillation fade amplitude and the correlation coefficients with which each model fits the measurement for all the sites is given in Table 8.8. The new models have been validated for frequency range 10 to 50 GHz and for path elevation angles from 6 to 40 degrees. We repeat that σ_{pre} is the predicted standard deviation given by the new improved relationship obtained in section 8.4 of this Chapter.

Scintillation signal enhancement:

$$X_{enh} = 3.235\sigma_{pre}\exp\left\{\frac{-9.50142\times10^{-4}}{p} - [0.2317 + 0.00285p]\ln(p)\right\} \tag{8.22}$$

Scintillation signal fade

$$X_{fade} = 3.351\sigma_{pre}\exp\left\{\frac{-9.50142\times10^{-4}}{p} - \left[0.2317 + 0.00285p\right]\ln(p)\right\} \quad (8.23)$$

Comparison of the performance of equations 8.22 and 8.23 with measured distribution, ITU-R model, Karasawa model and Otung model for enhancements and fades are shown in Figure 8.9 and Figure 8.10. Note that for signal enhancements the ITU-R distribution is not included since it was not given in this model. To preserve the continuity of this section the remaining of the graphs have been placed in Appendix F.

For signal enhancements the distribution from Austin deviated slightly from that predicted by equation 8.22. The root mean square error was 19.6%, however all other distributions were very well approximated by the prediction curve. As for signal fades only significant departure from the predicted curve is for the Olympus data recorded at Sparsholt [8].

Table 8.8: Comparison of the measured distribution of scintillation fades amplitude and that predicted using equation 8.23.

Site	Corr.Coef.	Scint. Ampl., dB 10%		Scint. Ampl., dB 1%		Scint. Ampl., dB 0.1%		Scint. Ampl., dB 0.01%	
		Predict	Meas.	Predict	Meas.	Predict	Meas.	Predict	Meas.
Madrid (50GHz)	0.9988	0.257	0.235	0.467	0.468	0.790	0.845	1.237	1.418
Sparsholt (Olympus)	0.9758	0.186	0.120	0.339	0.320	0.573	0.824	0.897	1.903
Kirkkonummi (20GHz)	0.9996	0.305	0.147	0.555	0.400	0.939	0.753	1.469	1.242
Kirkkonummi (30GHz)	0.9991	0.369	0.236	0.671	0.605	1.135	1.063	1.775	1.737
Sparsholt (20GHz)	0.9999	0.181	0.161	0.330	0.297	0.557	0.502	0.872	0.802
Sparsholt (40GHz)	0.9996	0.229	0.174	0.416	0.397	0.704	0.743	1.101	1.217
Sparsholt (50GHz)	0.9998	0.315	0.227	0.573	0.492	0.970	0.896	1.517	1.452
Chilbolton (θ=7.1^0)	0.9987	0.885	0.522	1.610	1.239	2.724	2.333	4.261	3.566
Chilbolton (θ=8.9^0)	0.9931	0.677	0.428	1.232	1.044	2.083	1.761	3.259	2.503
Chilbolton (θ=30^0)	0.9928	0.187	0.069	0.340	0.182	0.576	0.396	0.900	0.711
Austin	0.9983	1.277	0.817	2.324	2.047	3.930	3.587	6.148	5.690
Yamaguchi	0.994	0.861	0.704	1.565	1.624	2.648	2.620	4.142	3.923
Spino d'Adda (20GHz, 1995)	0.9988	0.141	0.085	0.256	0.204	0.433	0.384	0.678	0.670
Spino d'Adda (20GHz, 1996)	0.9988	0.141	0.080	0.257	0.185	0.435	0.321	0.680	0.498
Spino d'Adda (40GHz, 1995)	0.9975	0.192	0.142	0.349	0.332	0.591	0.635	0.924	1.149
Spino d'Adda (40GHz, 1996)	0.9987	0.193	0.142	0.350	0.316	0.593	0.582	0.927	1.016
Spino d'Adda (50GHz, 1995)	0.9994	0.207	0.181	0.377	0.393	0.637	0.709	0.997	1.198
Spino d'Adda (50GHz, 1996)	0.9964	0.208	0.185	0.378	0.381	0.640	0.687	1.001	1.262

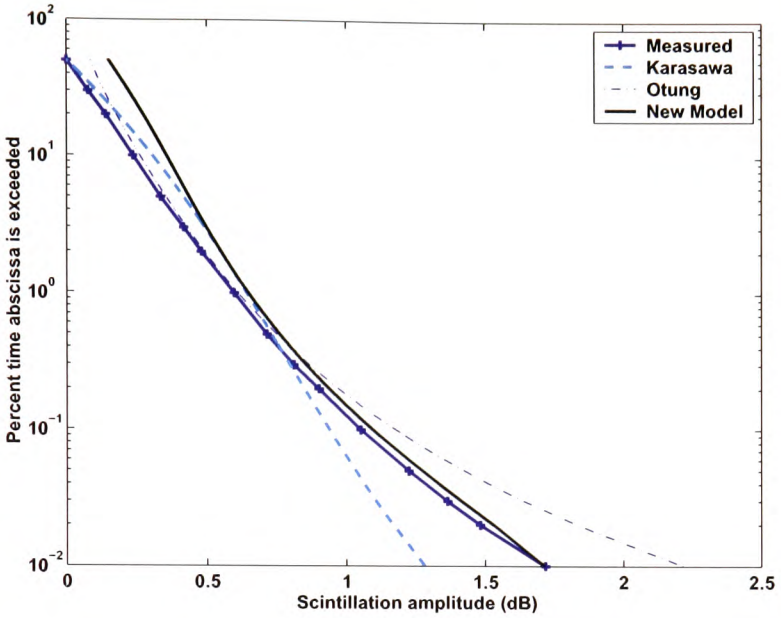

Figure 8.9. Comparison of measured distribution in Kirkkonummi at 30GHz with predicted ITU-R, Karasawa, Otung and new model distribution for scintillation signal enhancements.

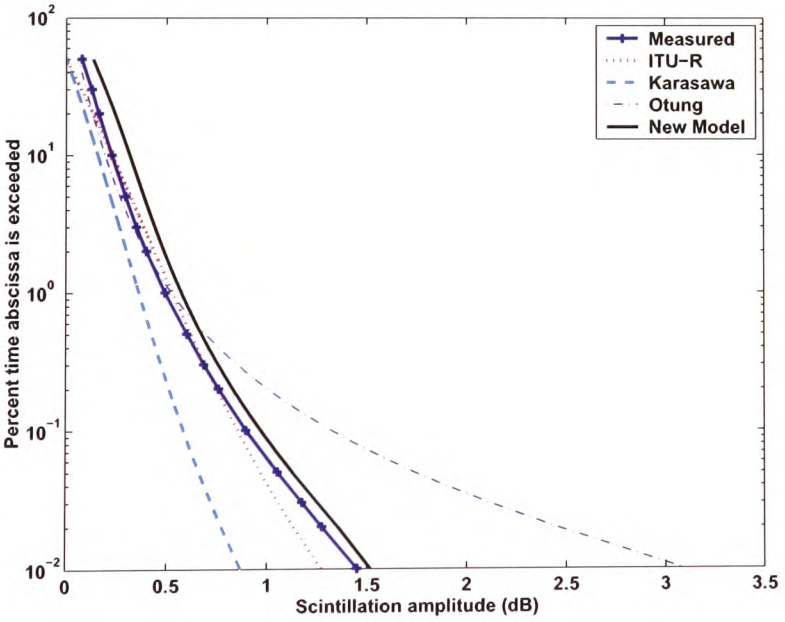

Figure 8.10. Comparison of measured distribution in Sparsholt at 50GHz with predicted ITU-R, Karasawa, Otung and new model distribution for scintillation signal fades.

8.6. Conclusions

The Chapter can be divided into three sections: the first section investigates the accuracy and performance of the current prediction model. It was necessary to carry out this task first in order to determine the shortfalls and limitations of the current prediction models. As discussed in section 8.3 there were limitations regarding the assumed frequency, elevation angle, and meteorological dependence (through the wet-part of refractivity N_{wet}).

The ITU-R and Karasawa model performs adequately well for frequencies up to about 20GHz. However, their performance degrades considerably at the higher frequencies. In search for a parameter which might be responsible for this fall in performance, we employed the elevation angle – frequency power exponent dependence found in Chapter 6 of this thesis. This improved the results but did not decrease the errors for all sites, specially those in dry climate.

As we already know in dry climates the wet part of refractivity fails to account for all the scintillation process and this results in underestimation of the scintillation levels observed. Raising the wet part of refractivity to the power γ solved this problem. Following an extensive optimisation process we concluded that γ is equal to 1 for temperatures below 15^0C, and for temperatures above 15^0C, γ=1.07.

The second part of this Chapter presents a new improved global prediction model for tropospheric scintillation. This new model utilises the frequency power exponent–elevation angle dependence, the modification to the wet part of refractivity, N_{wet} and finally a modification to elevation angle dependence. As was observed by Karasawa at lower elevation angles (e.g. Austin, Yamaguchi and Chilbolton) using $\sin^{1.3}\theta$, provided better accuracy and smaller errors. Finally the last part is the validation of the new model and obtaining the long-term time percentage dependence. The new model has been validated using long-term measurement results from around the globe

from different sites, in different climates and operating at different elevation angles and frequencies.

Long-term cumulative distributions for scintillation fades and enhancements were obtained through detailed regression analysis. Those models can be used to estimate scintillation fading and provide link budget engineers with the scintillation fade margin required on a given satellite link for frequencies above 3 GHz and path elevation angles > 6^0. Below these frequencies and elevation angles, multipath effects become important and the size of the first Fresnel zone become comparable to the outer scales of turbulence. Under these conditions the scaling factors used in this model may no longer hold.

References

[1] V. I. Tatarskii, *Wave Propagation in a Turbulent Medium*: New York, Dover, 1961.

[2] J. Haddon and E. Vilar, "Scattering induced microwave scintillations from clear air and rain on earth space paths and the influence of antenna aperture," *IEEE Transactions on Antennas and Propagation*, vol. 34, pp. 646-657, 1986.

[3] R. K. Crane, "Low elevation angle measurement limitations imposed by the troposphere: An analysis of scintillation observations made at Haystack and Millstone," MIT Lincoln Laboratory, Lexington, MA. 518, 1976.

[4] D. V. Rogers and J. E. Allnutt, "A Practical Troposheric Scintillation Model for Low Elevation Angle Satellite Systems," presented at 5th International Conference on Antennas and Propagation (ICAP87), 1987.

[5] R. K. Crane and D. W. Blood, "Handbook for the Estimation of Microwave Propagation Effects," NASA GSFC Greenbelt, MA, Technical Report No.1 NASA Contract NAS5-25341, 1979.

[6] Y. Karasawa, M. Yamada, and J. E. Allnutt, "A New Prediction Method for Tropospheric Scintillation on Earth-Space Paths," *IEEE Transactions on Antennas and Propagation*, vol. 36, pp. 1608-1614, 1988.

[7] ITU-R, "P.618-7 Propagation data and prediction methods required for the design of Earth-space telecommunication systems," Recommendations and Reports of the ITU-R 1997.

[8] I. E. Otung, "Prediction of Tropospheric Amplitude Scintillation on a Satellite Link," *IEEE Transactions on Antennas and Propagation*, vol. 44, pp. 1600-1608, 1996.

[9] J. K. Tervonen, M. M. J. L. V. d. Kamp, and E. T. Salonen, "Prediction Model for the Diurnal Behaviour of the Tropospheric Scintillation Variance," vol. 46, pp. 1372-1378, 1998.

[10] A. Savvaris, C. N. Kassianides, and I. E. Otung, "Observed Effects of Cloud and Wind on the Intensity and Spectrum of Scintillation," *IEEE Transactions on Antennas and Propagation*, vol. 52, pp. 1492-1498, 2004.

[11] E. Salonen and S. Uppala, "New Prediction Method of Cloud Attenuation," *Electronics Letters*, vol. 27, pp. 1106-1108, 1991.

[12] E. Salonen, S. Karhu, S. Uppala, and R. Hyvönen, "Study of Improved Propagation Predictions, Final Report for ESA/ESTEC," Helsinki University of Technology and Finnish Meteorological Institute, Helsinki Contract 9455/91/NL/LC(SC), 1994.

[13] M. M. J. L. V. d. Kamp, J. K. Tervonen, E. T. Salonen, and J. P. V. Baptista, "Improved Models for Long-Term Prediction of Tropospheric Scintillation on Slant Paths," *IEEE Transactions on Antennas and Propagation*, vol. 47, pp. 249-260, 1999.

CHAPTER IX

Summary and Conclusions

Summary – *This final Chapter brings together the results of previous chapters. The major contributions and conclusions of the thesis are summarised and some ideas for further research are presented.*

9.1. INTRODUCTION

Satellite communications have been in service for over 40 years now. Prior to 1970 satellite communication was operated exclusively in C-band. Satellites were small and provided a low capacity at a relatively high cost, and had a short lifespan about 1½ to 2 years only. However, since then there has been an explosive growth for telecommunication services that are either only feasible via satellite or very cost effective by that means. Today there are over 700 Ku-band satellite planned or in operation globally [1].

The need to provide new services and greater bandwidths has prompted a steady growth in the utilisation of higher frequencies in the Ku-band or above. The move to higher frequencies to introduce new services has many advantages such as smaller antennas, and smaller satellite footprints that give higher EIRP and permit frequency reuse. The main obstacle however is that they are subject to stronger propagation degradation. The small size antennas employed in VSAT and USAT systems significantly reduce the cost of earth station terminals and also eliminate tracking requirements, but they lose the mitigating effect of aperture averaging and hence experience stronger scintillation [1].

In order to provide the same performance as in the lower frequency bands, an excessively large margin would be required. Considering that this power margin is needed only occasionally, this is clearly uneconomical. At Ka-band and above atmospheric degradation becomes so severe that adaptive methods or fade countermeasures (FCMs) are required to achieve the high standards of availability [2].

Rain attenuation is the major obstacle to high-availability satellite system operating at frequencies above 10 GHz, but is of negligible importance in low-availability systems located in temperate or dry climates since the total rainy period seldom exceeds the allowed system outage. However, scintillation-induced fading is always present to varying degrees on any satellite link. Careful understanding, quantification and modelling of scintillation are imperative for the reliable design and operation of these

low-availability systems, where the effects of scintillation needs to be included to complete an accurate link budget [1].

9.2. Tropospheric Scintillation

9.2.1. Meteorological Dependence

Tropospheric scintillation was the main focus of this thesis. The raw propagation data recorded at Sparsholt at 20, 40 and 50 GHz was first preprocessed to extract scintillation and exclude all other contributions. The analysis confirmed results from previous experiments regarding the strong correlation observed between scintillation intensity (standard deviation), temperature and the wet-part of refractivity, N_{wet} [3]. Furthermore, scintillation intensity was found to exhibit diurnal and seasonal patterns of variations, which are due to the strong dependence of scintillation intensity on temperature.

In Section 4.5.1 of Chapter 4, we saw that there are two mechanisms by which atmospheric turbulence is produced, namely wind shear and buoyancy. The results show that by far the most influential factor is the temperature, and that the correlation with humidity is an indirect result of this. Furthermore, cumulus clouds are also responsible for part of the increase in the scintillation levels observed. The average diurnal variation of scintillation intensity is uncorrelated with N_{wet}, but strongly correlated with cumulus cloud cover. Scintillation intensity is larger in the day when cumulus cloud cover is also more frequent. N_{wet} on the other hand exhibits little or no diurnal variation.

9.2.2. Statistical Analysis

The extensive study of the probability density function (pdf) of scintillation amplitude and standard deviation has shown that for time intervals which are short enough for meteorological conditions to remain approximately constant, scintillation amplitude fluctuations can be assumed to follow a Gaussian distribution, whereas the long-term

amplitude fluctuations are definitely not Gaussian, the scattering process being no longer stationary.

A visual inspection of the long-term scintillation intensity distribution would suggest that it follows reasonably well a Lognormal or a Gamma distribution, however this would be wrong in light of the Chi-square goodness-of-fit test. The results suggest that the likelihood of a distribution being a Lognormal or a Gamma is very small. Another conclusion, which may be drawn based on the results obtained from the analysis is that out of the two distributions of the 1-min scintillation intensity, the Lognormal distribution gives a slightly better approximation than the Gamma distribution.

9.2.3. Frequency Scaling

Observed frequency scaling of amplitude scintillation at 20, 40 and 50 GHz was presented in Chapter 6. There was a strong correlation between scintillations at different pairs of frequencies, which means that for uplink power control applications, scintillation intensity at one frequency can be predicted with some confidence from measurements at a different but close frequency. Scintillation intensity was found to vary with frequency as f^{α}. However α was significantly variable with an average value of 0.423, which is 27% lower than the predicted theoretical value of 7/12. It was shown that the observed shortfall and diurnal variation in α could be accounted for only partly by receiver thermal noise contribution. By ascribing the minimum observed 1-minute variance in each beacon to thermal noise and excluding this contribution from the measured scintillation variance, a higher average frequency exponent $\alpha = 0.493$ was obtained, which is still 15.5% below the theoretical value.

Finally, the exponent in the power law dependence of scintillation intensity on signal frequency α, as observed from measurement results at various sites around the globe, shows remarkable differences. A significant correlation of about 0.72 was found between α and path elevation angle. Hence, a possible explanation of these results would be that the frequency exponent α can be considered dependent on the elevation angle.

9.2.4. Spectral Analysis

There was a strong correlation between transverse wind speed and estimated corner frequency, and a weaker correlation with over-all wind speed. The corner frequency shows some dependence on frequency. Furthermore, the analysis showed that the presence of cumulus clouds along the propagation path led to a drop in the observed correlation of the spectrum corner frequency with transverse wind speed. This might be due to the extra contribution to scintillation from physical processes that take place in clouds.

The shape of the power spectral density (psd) under cold and rainy weather conditions is similar to that theoretically predicted by assuming a Kolmogorov spectrum of atmospheric refractivity fluctuations, for clear sky conditions. The only difference is that the 'flat' part of the scintillation spectrum (observed during winter/summer 1997 in Sparsholt) for the summer months is higher due to stronger turbulence. In addition, the slopes of weak-to-moderate scintillation spectra revealed a weak correlation with transverse wind speed and scintillation intensity.

Finally, using measurements of amplitude scintillation for remote sensing application of transverse wind speed and turbulent parameters is feasible, however, they would not be very accurate. Over long periods meteorological conditions could not be regarded as constant, and in addition there is the practical difficulty in establishing an accurate value of the corner frequency by fitting linear regression lines to the flat and sloping portions of the spectrum.

9.3. Effects of Scintillation on Communications Systems

Statistics of observed durations of scintillation fades and enhancements of the ITALSAT satellites at 20, 40 and 50GHz were presented for various threshold signal levels, and their use in fade countermeasures was examined. The analysis showed that most signal amplitude deviations from the mean level were predominantly short lived with duration lasting less than 20 seconds and do not depend on the threshold level. Distribution of fade durations at thresholds 0.1 and 0.5dB were reasonably well approximated by the lognormal function.

Assigning a fixed fade margin at frequencies above Ka-band is not a feasible solution. At those frequencies the effects of atmospheric impairments are very severe. However, due to the considerable advantages of operating satellite communication systems in these frequency ranges, mitigating techniques have been developed to overcome the impairments associated with these frequency bands.

In Chapter 7 we examined some adaptive fade countermeasure techniques that can be applied to mitigate the severe degradation due to the atmospheric propagation fading. Depending on the priorities of the system to be designed, adaptive power control and adaptive signal processing are the prime candidates.

Up-link power control (ULPC) makes use only of transmitted Earth station power; therefore it can be implemented for any percentage of time, which makes this technique a very flexible one and can be used as a fade countermeasure (FCM) for both scintillation and rain attenuation. Most first generation fade FCM techniques for Ka-band satellite systems will use ULPC with the objective of improving system availability. In addition, the flexibility of ULPC makes it easy to combine it with another FCM such as adaptive coding or modulation to improve system performance even further.

Up-link power control combined with adaptive coding are the prime fade countermeasure candidates for mitigating against rain attenuation and scintillation effects at frequencies up to about Ka-band. The advantage of including adaptive up-link power control is that it can ensure quicker and more reliable delivery of service commands from the FCM controller (in hub), to the VSAT stations. Large central hub stations have the ability and the complexity to support up-link power control. At V-band however, which will be used for multimedia systems, adaptive modulation is more likely to be implemented because of the higher throughput. An adaptive modulation system would transmit at its most complex modulation during good propagation conditions and would reduce the complexity of the scheme (i.e. introducing fade protection margin) when fades occur.

The reader should note that in order to overcome the problem of frequent switching of modes in an adaptive system, a fixed fade margin must be introduced. For example, based on the results obtained from scintillation fade duration statistics, introducing a 0.5 dB fixed fade margin, the percentages of fades lasting one second dropped from 25% given by a threshold of 0.1 dB, to 12%, meaning that the system has to deal with fewer one-second changes.

9.4. Improved Prediction Model

In Chapter 8 we investigated the accuracy and performance of the current prediction model. It was necessary to carry out this task first in order to determine the shortfalls and limitations of the current prediction models. As discussed in section 8.3 there were limitations regarding the assumed frequency, elevation angle, and meteorological dependence (through the wet-part of refractivity N_{wet}).

Following an extensive optimisation analysis to improve the accuracy of the prediction models, the following three parameters were refined:

i) The frequency power exponent α, where α is given by Equation (8.18).

ii) Elevation angle power exponent z, where z is given by Equation (8.19) and

iii) The wet-part of refractivity N_{wet}. Power exponent γ, where γ is given by Equations 8.20 and 8.21.

The new model has been validated using long-term measurement results from around the globe from different sites, in different climates and operating at different elevation angles and frequencies. The new model performs considerably better than the current prediction models. Long-term cumulative distributions for scintillation fades and enhancements were obtained through detailed regression analysis. Those models can be used to estimate scintillation fading and provide link budget engineers with the scintillation fade margin required on a given satellite link for frequencies above 3 GHz and path elevation angles of $> 6^0$.

Below these frequencies and elevation angles, multipath effects become important and the size of the first Fresnel zone become comparable to the outer scales of turbulence. Under these conditions the scaling factors used in this model may no longer hold.

9.4. Original Aspects of the Research

In summary, the novel aspects of the research presented in this thesis are considered to be:

I. Preprocessing of RAL's Sparsholt-ITALSAT beacon measurement at 18.7, 39.6 and 49.5 GHz, which can be now submitted to the ITU-R to extend the UK scintillation database.

II. Analysis of beacon data and study of the distribution of amplitude scintillation.

III. Study of the dependence of amplitude scintillation on meteorological parameters.

IV. Study of the effects of wind and cloud presence on the intensity and power spectrum of tropospheric scintillation.

V. Analysis of instantaneous frequency scaling of scintillation and the exponent in the power law dependence of scintillation intensity on signal frequency.

VI. Study of scintillation fade and enhancement statistics and their implications on the choice and design of fade countermeasure schemes.

VII. Development of a new improved scintillation prediction model. The model was validated using data from Europe, Japan and the USA.

9.5. Recommendations for Further Work

The following are possible areas for further work.

a) In Chapter 4 of this thesis results of extensive analysis of scintillation with various meteorological parameters were presented. However, all those meteorological parameters where measured at ground level. The UK Met. Office now has height level profile of those parameters. It will be very interesting to investigate the correlation of those parameters (temperature, humidity and wind speed) at different altitudes.

b) It has been shown that the presence of Cumulus clouds along the propagation path is responsible in part for the increase in the observed

scintillation levels. Recent investigations of the effects of clouds at V-band showed that attenuation due to deep convective clouds could overtake scintillation as the second major degradation factor on Earth-Space communication links [4]. Cloud attenuation effect at Ka- and V-band frequencies therefore merits further study.

c) In this thesis we presented an improved prediction model for tropospheric scintillation. The performance of FCM systems depends crucially on the ability to estimate and predict the total attenuation suffered on any satellite link. The next logical step would be to combine the different tropospheric effects on an Earth-Satellite link and develop a total attenuation prediction model. Some work in this area is very recent and there is big scope for further research [5].

References

[1] *I. E. Otung, "Accurate prediction of scintillation degradation applicable to satellite communication system design," University of Glamorgan 1998.*

[2] *M. J. Willis and B. G. Evans, "Fade Countermeasures at Ka band for Olympus," Int. Journal of Satellite Communication, vol. 3, pp. 301-311, 1988.*

[3] *M. M. B. M. Yusoff, N. Sengupta, C. Alder, I. A. Glover, P. A. Watson, R. G. Howell, and D. L. Bryant, "Evidence for the Presence of Turbulent Attenuation on Low-Elevation Angle Earth-Space Paths - Part 1: Comparison of CCIR recommendation and Scintillation Observations on a 3.3^0 Path," IEEE Transactions on Antennas and Propagation, vol. 45, pp. 73-84, 1997.*

[4] *C. L. Wrench, P. M. Simpson, A. J. Gibson, and O. T. Davies, "Statistics of liquid water path in cloud, and slant path propagation loss in cloud at V-Band, based on measurements at Chilbolton," presented at International Conference on Antennas and Propagation (ICAP 03), UK, 2003.*

[5] *A. Dissanayake, J. Allnutt, and F. Haidara, "A prediction Model that Combines Rain Attenuation and Other Propagation Impairments Along Earth-Satellite Paths," IEEE Transactions on Antennas and Propagation, vol. 45, pp. 1546-1558, 1997.*

Appendices

Appendix A

Kolmogorov spectrum in the region between $2\pi/L_0$ and $2\pi/l_0$ (inertial subrange)

Assuming that the atmosphere is locally homogeneous, i.e. whatever condition exist at one point exist also at another point in the same region, then the structure function of a locally homogeneous field depends only on the difference of the fields at the two points. Thus the structure function is given by:

$$D_f(\vec{r}_1 - \vec{r}_2) = \overline{[f(\vec{r}_1) - f(\vec{r}_2)]^2} \tag{A.1}$$

Taking the isotropy into account, the structure function is given by:

$$D_f(\vec{r}) = \overline{[f(\vec{r} + \vec{r}_1) - f(\vec{r}_1)]^2} = D_f(r) \tag{A.2}$$

After lengthy calculations, [Tatarskii, 1961] found that the structure function is in general given by:

$$D_f(r) = C^2 r^p \qquad (0 < p < 2) \tag{A.3}$$

It can be seen that the structure function in Equation (A.3) is the same as the one in Equation (2.13) in Chapter 2, for p = 2/3. If the function f is homogeneous and isotropic, then the correlation function is measured along one line, and it is often convenient to define the spectrum as the one dimensional Fourier transform of $C(r)$ [Strohbehn, 1968]. The one dimensional spectral density corresponding to this function (A.3) is:

$$V(\kappa) = \frac{\Gamma(p+1)}{2\pi} \sin\frac{\pi p}{2} C^2 \kappa^{-(p+1)} \tag{A.4}$$

where $\Gamma(p+1)$ is the gamma function defined by:

$$\Gamma(x) = \int_0^\infty t^{x-1} e^{-t} dt, \quad x > 0 \tag{A.5}$$

The one-dimensional spectral density is related to the three-dimensional spectral density $\Phi(\kappa)$ as follows:

$$\Phi(\kappa) = -\frac{1}{2\pi\kappa}\frac{dV}{d\kappa} \tag{A.6}$$

Substituting Equation (A.4) into (A.6),

$$\Phi(\kappa) = \frac{\Gamma(p+2)}{4\pi^2}\sin\frac{\pi p}{2} C^2 \kappa^{-(p+3)} \tag{A.7}$$

For $p = 2/3$, (A.7) becomes

$$\Phi_n(\kappa) = 0.033 C_n^2 \kappa^{-11/3} \tag{A.8}$$

Equation (A.8) gives the Kolmogorov spectrum. This equation represents the spectrum in the range $2\pi/L_0 \ll \kappa \ll 2\pi/l_0$.

Appendix B

Monthly Cumulative distribution functions (cdf) at 20, 40 and 50GHz

Monthly scintillation amplitude cdf plots at 20GHz (September 99-August 00)

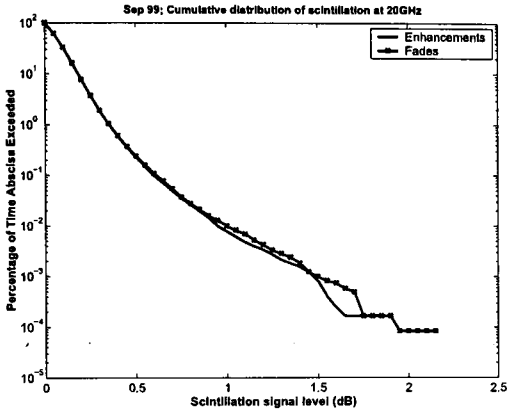

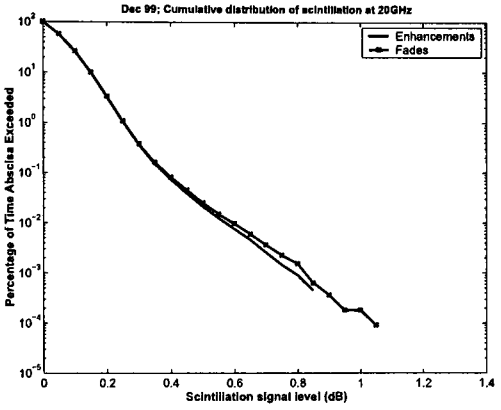

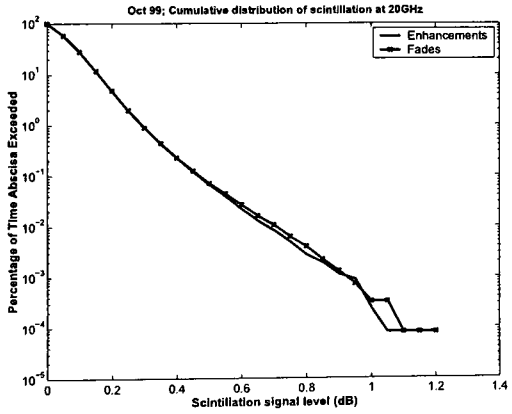

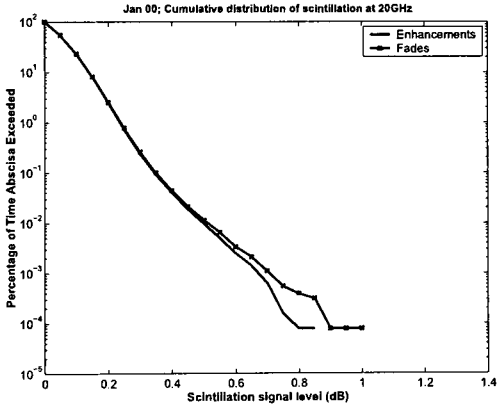

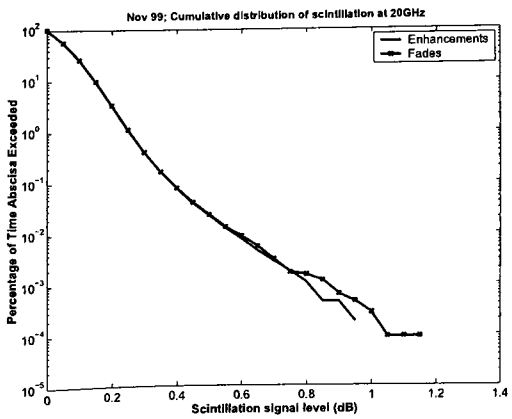

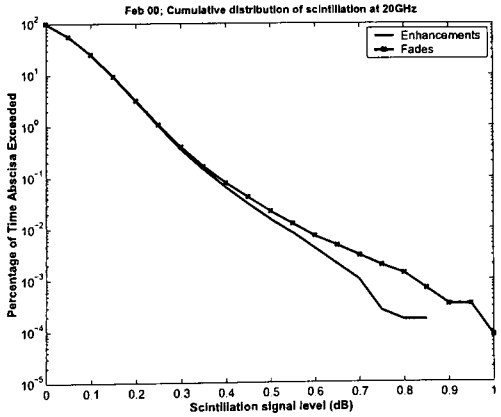

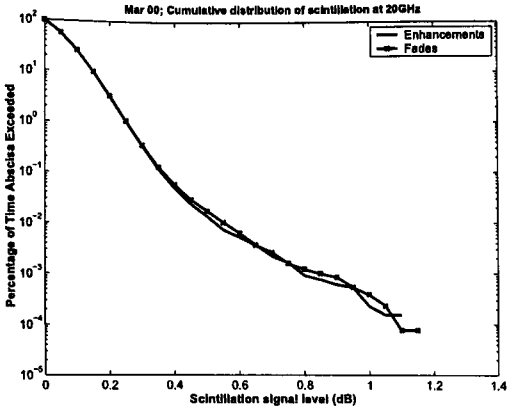
Mar 00; Cumulative distribution of scintillation at 20GHz
Enhancements
Fades
Percentage of Time Abscisa Exceeded
Scintillation signal level (dB)

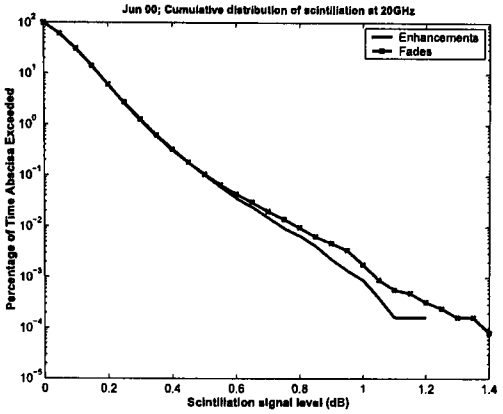
Jun 00; Cumulative distribution of scintillation at 20GHz
Enhancements
Fades
Percentage of Time Abscisa Exceeded
Scintillation signal level (dB)

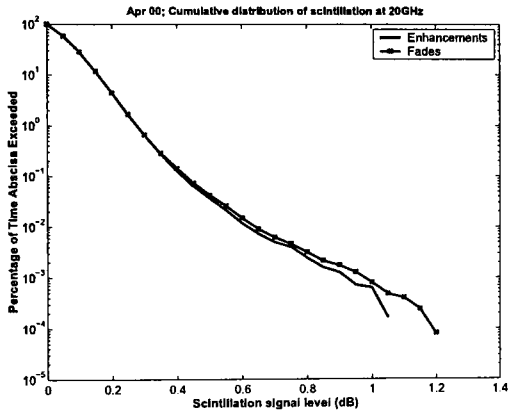
Apr 00; Cumulative distribution of scintillation at 20GHz
Enhancements
Fades
Percentage of Time Abscisa Exceeded
Scintillation signal level (dB)

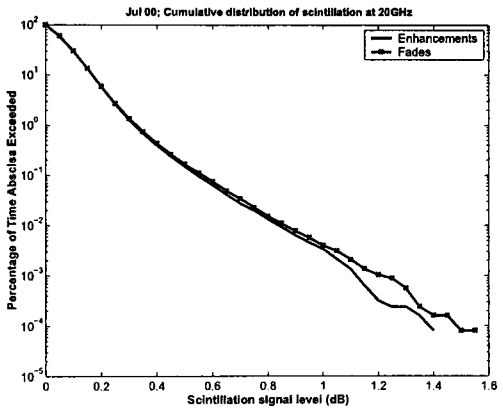
Jul 00; Cumulative distribution of scintillation at 20GHz
Enhancements
Fades
Percentage of Time Abscisa Exceeded
Scintillation signal level (dB)

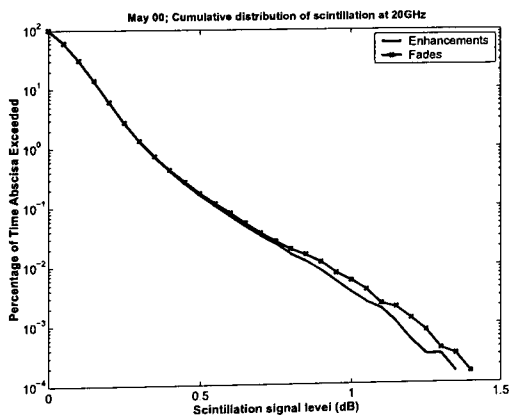
May 00; Cumulative distribution of scintillation at 20GHz
Enhancements
Fades
Percentage of Time Abscisa Exceeded
Scintillation signal level (dB)

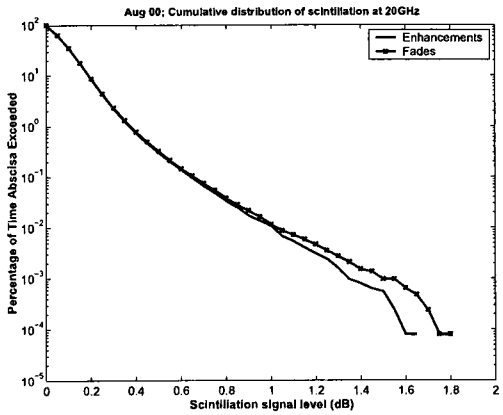
Aug 00; Cumulative distribution of scintillation at 20GHz
Enhancements
Fades
Percentage of Time Abscisa Exceeded
Scintillation signal level (dB)

Monthly scintillation amplitude cdf plots at 40GHz (July 96-August 97)

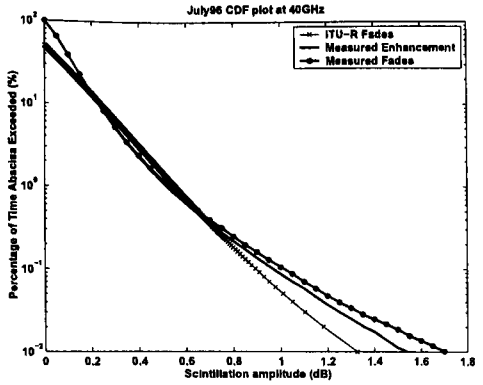

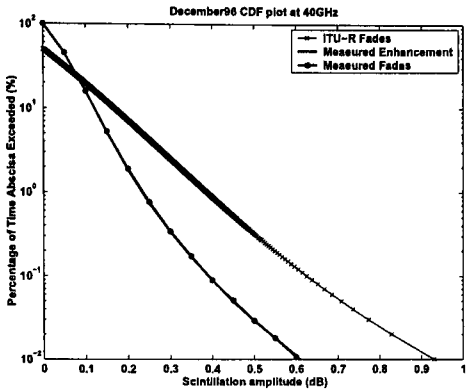

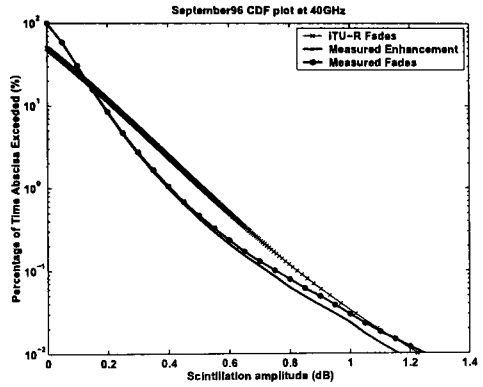

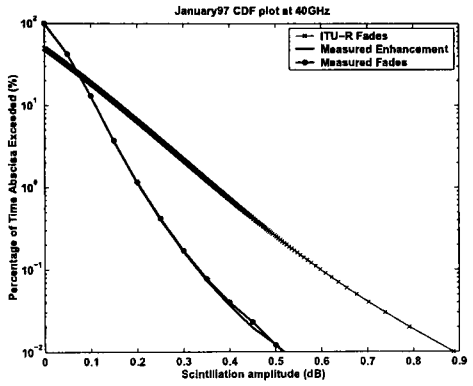

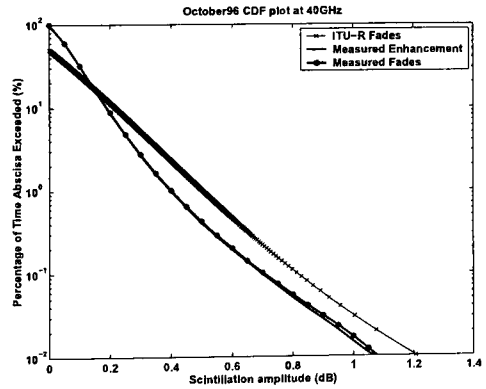

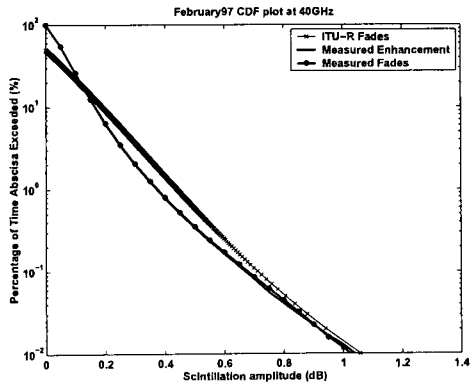

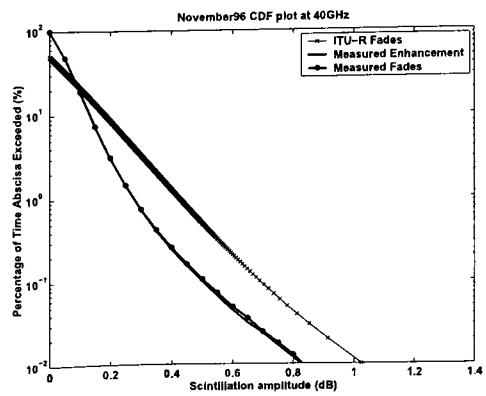

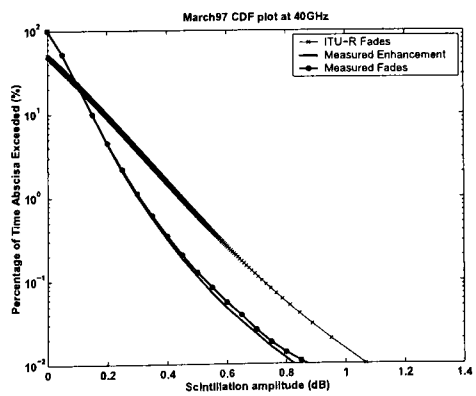

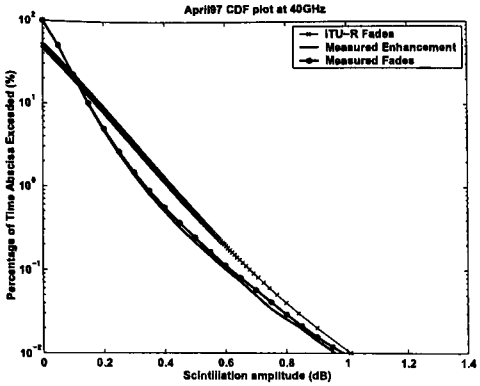
April97 CDF plot at 40GHz
ITU-R Fades
Measured Enhancement
Measured Fades
Percentage of Time Abscias Exceeded (%)
Scintillation amplitude (dB)

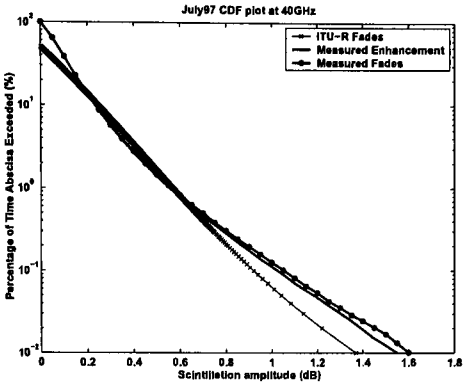
July97 CDF plot at 40GHz
ITU-R Fades
Measured Enhancement
Measured Fades
Percentage of Time Abscias Exceeded (%)
Scintillation amplitude (dB)

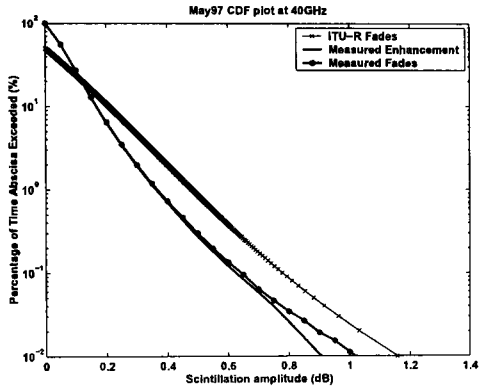
May97 CDF plot at 40GHz
ITU-R Fades
Measured Enhancement
Measured Fades
Percentage of Time Abscias Exceeded (%)
Scintillation amplitude (dB)

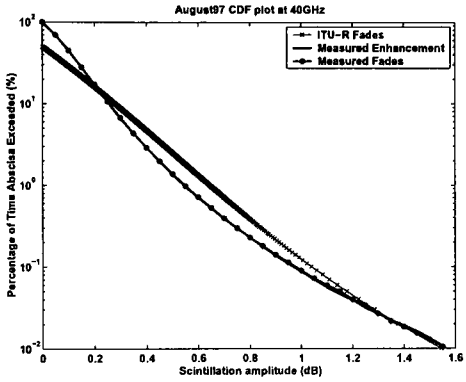
August97 CDF plot at 40GHz
ITU-R Fades
Measured Enhancement
Measured Fades
Percentage of Time Abscias Exceeded (%)
Scintillation amplitude (dB)

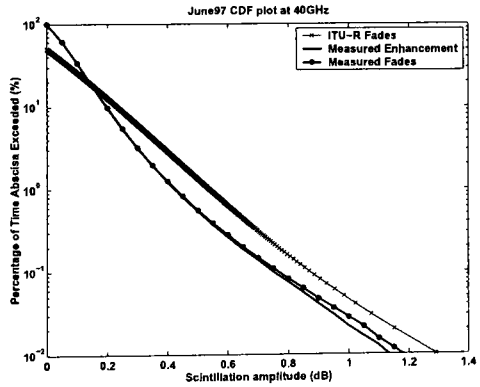
June97 CDF plot at 40GHz
ITU-R Fades
Measured Enhancement
Measured Fades
Percentage of Time Abscias Exceeded (%)
Scintillation amplitude (dB)

Monthly scintillation amplitude cdf plots at 50GHz (July 96-August 97)

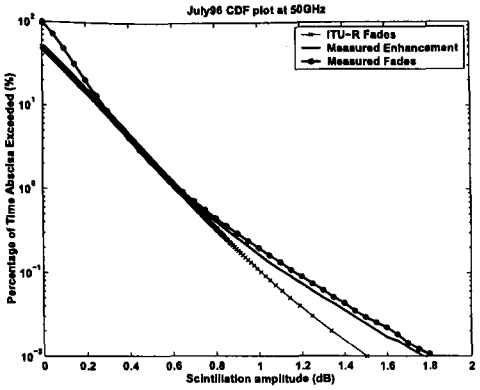

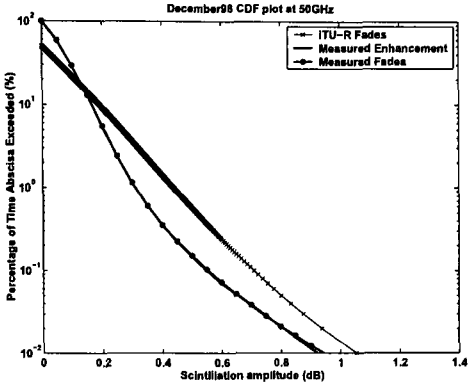

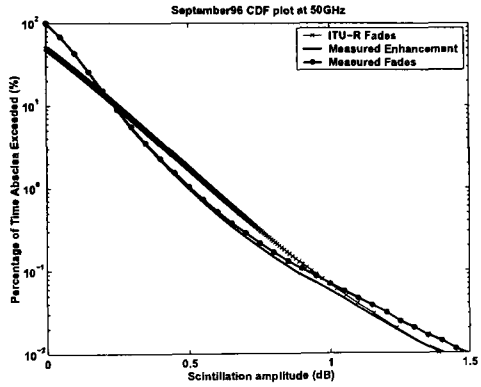

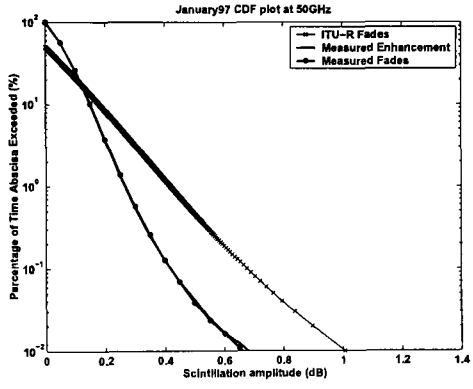

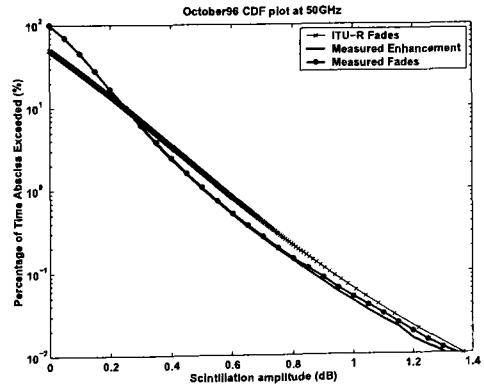

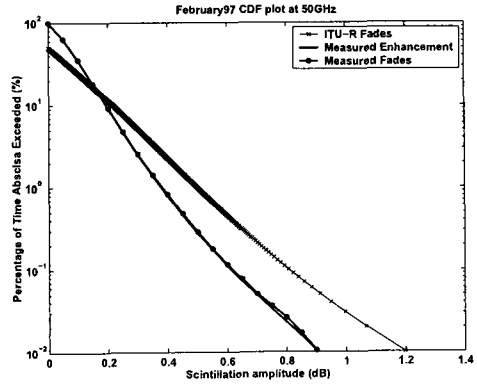

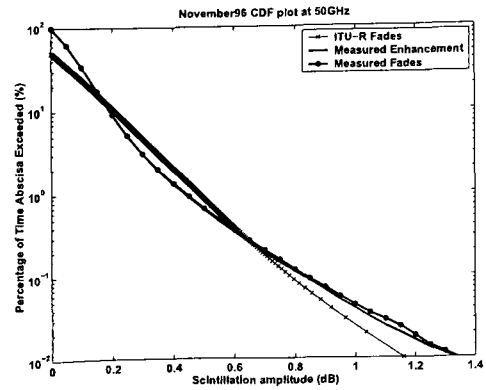

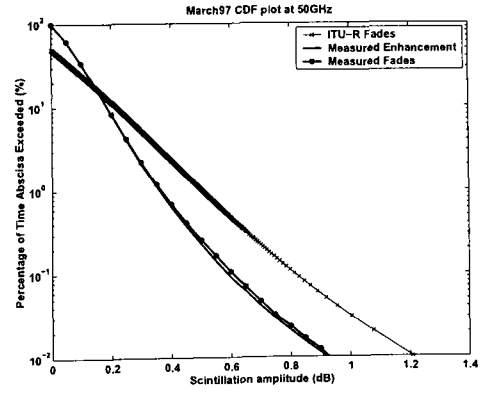

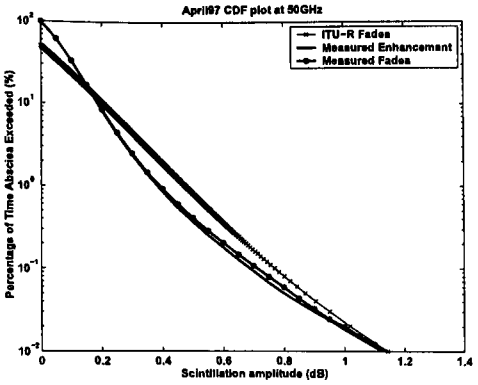
April97 CDF plot at 50GHz
ITU-R Fades
Measured Enhancement
Measured Fades
Percentage of Time Abscisa Exceeded (%)
Scintillation amplitude (dB)

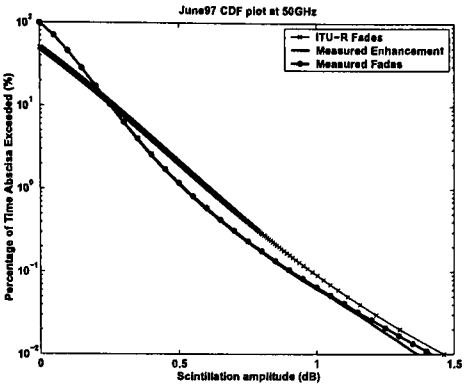
June97 CDF plot at 50GHz
ITU-R Fades
Measured Enhancement
Measured Fades
Percentage of Time Abscisa Exceeded (%)
Scintillation amplitude (dB)

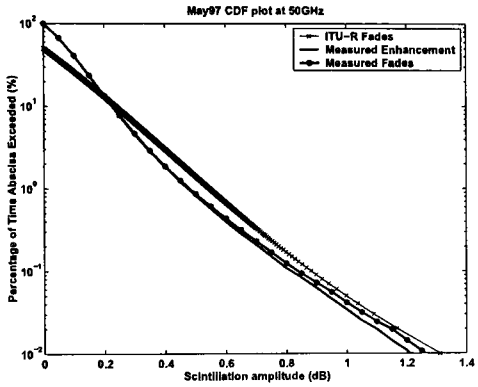
May97 CDF plot at 50GHz
ITU-R Fades
Measured Enhancement
Measured Fades
Percentage of Time Abscisa Exceeded (%)
Scintillation amplitude (dB)

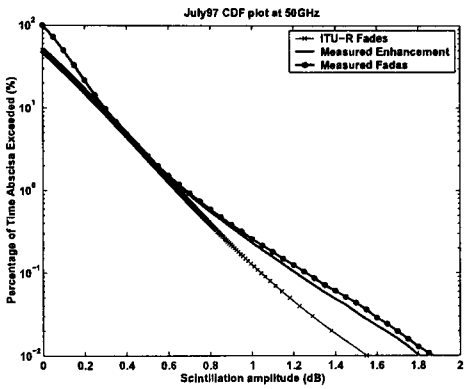
July97 CDF plot at 50GHz
ITU-R Fades
Measured Enhancement
Measured Fades
Percentage of Time Abscisa Exceeded (%)
Scintillation amplitude (dB)

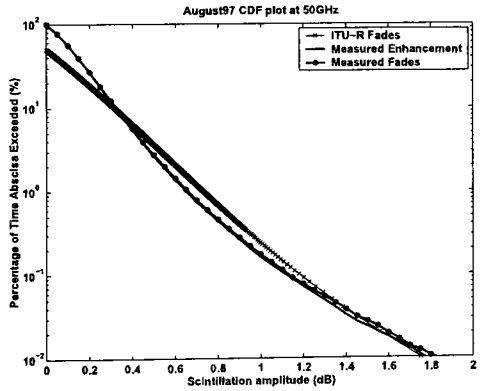
August97 CDF plot at 50GHz
ITU-R Fades
Measured Enhancement
Measured Fades
Percentage of Time Abscisa Exceeded (%)
Scintillation amplitude (dB)

Appendix C

UK Hourly Weather Observations data format

HEADER	PARAMETER	FIELDS	COLUMNS	UNITS	COMMENTS/DESCRIPTION
ID	Station Ref. Number	1	1-8	-	Station identification
IDTYPE	-	2	9-17	-	Station identification
MET_DOM	Meteorological Domain	3	18-28	-	Message types
YEAR	Year	3	29-35	-	4 characters
MON	Month	4	36-43	-	1 or 2 characters (from 1 to 12)
DAY	Day	5	44-51	-	1 or 2 characters (from 1 to 31max)
HOUR	Hour	6	52-59	-	Hour of observation from 0 to 2300
DIR	10 minutes wind direction	7	60-67	Degree true	From 0 to 360 degrees, clockwise. See Met Office documentation
SPEED	10 minutes wind speed	8	68-75	Knots	See Met Office documentation
PRST	Present weather	9	76-81	WMO Code	See Met Office documentation
PAS1	Most significant Past weather	10	82-87	WMO code	See Met Office documentation
PAS2	Least significant Past weather	11	88-93	WMO code	See Met Office documentation
TCA	Total cloud amount	12	94-98	WMO code	See Met Office documentation
LCT	Low cloud type	13	99-103	WMO Code	See Met Office documentation
MCT	Medium cloud type	14	104-108	WMO Code	See Met Office documentation
HCT	High cloud type	15	109-113	WMO Code	See Met Office documentation
CBA	Cloud base amount	16	114-118	WMO code	See Met Office documentation
CBH	Cloud base height	17	119-126	DAM	DAM = Decameters See Met Office documentation
VIS	Horizontal visibility	18	127-133	DAM	DAM = Decameters See Met Office documentation
MSLP	Mean Sea Level Pressure	19	134-146	0.1 mb	Atmospheric pressure is expressed in millibars (1 millibar = 100 pascals = 100 newtons per square metre). Precision aneroid barometers are now in general use for measuring pressure and a correction for altitude is applied to obtain the value at mean sea level (MSL).

CA1	Cloud amount - level 1	20	147-151	WMO code	-
CT1	Cloud type - level 1	21	152-156	WMO code	-
CB1	Cloud base - level 1	22	157-164	DAM	DAM = decameters
CA2	Cloud amount - level 2	23	165-169	WMO code	-
CT2	Cloud type - level 2	24	170-174	WMO code	-
CB2	Cloud base - level 2	25	175-182	DAM	DAM = Decameters
CA3	Cloud amount - level 3	26	183-187	WMO code	-
CT3	Cloud type - level 3	27	188-192	WMO code	-
CB3	Cloud base - level 3	28	193-200	DAM	DAM = Decameters
CA4	Cloud amount - level 4	29	201-205	WMO code	-
CT4	Cloud type - level 4	30	206-210	WMO code	-
CB4	Cloud base - level 4	31	211-218	DAM	DAM = Decameters
VVIS	Vertical visibility	32	219-226	DAM	DAM = Decameters See Met Office documentation
TEMP	Dry-bulb air temperature	33	227-234	0.1 Degrees Celcius	See Met Office documentation
DEW	Dew-point temperature	34	235-242	0.1 Degrees Celcius	The dew point temperature (in degrees Celcius) is the temperature to which the air must be cooled to produce saturation with respect to water at its existing atmospheric pressure and humidity.See Met Office documentation
WETB	Wet-bulb temperature	35	243-250	0.1 Degrees Celcius	The web-bulb temperature is the lowest temperature (in degrees Celcius) that can be obtained by evaporating water into the air. It measures the humidity of the air.See Met Office documentation
STNP	Station level pressure	36	251-262	0.1 mb	Atmospheric pressure (in mb) as measured at the station level. Correction for altitude is not applied.
ALTP	Altimeter pressure	37	263-270	mb	-
SOG	State of ground	38	271-275	WMO Code	-
MGS	10 minutes maximum gust speed	39	276-283	knots	See Met Office documentation

Appendix D

In this Appendix some details on the measurement systems and data preprocessing procedures from other sites around the globe will be presented. The information were taken from [1], [2] and [3]. The site parameters are summarised in Table 6.6 in Chapter 6.

Blacksburg (Virginia, USA):

In the Virginia Tech Olympus Propagation Experiment, scintillation at all three Olympus frequencies (12.50, 19.77 and 29.66GHz) was measured during several one hour clear air events in May and September 1991 [4]. The standard deviation was computed over every minute. The frequency scaling ratios were obtained as the slopes of the forced zero intercept best fit lines of the scattergrams of standard deviation for each two frequencies. Only the results from two events, on September 14 and May 10 are reported. The results from the two events are significantly different, for which two possible explanations are mentioned: a difference in average scintillation intensity between the two events, causing a different sensitivity to noise, or a difference in the turbulent layer height. In our analysis, the results from the two events have been averaged.

Darmstadt (Germany):

All three Olympus beacon signal have been received at the Research Centre of Deutsche Telekom AG with two antennas of different sizes. The receiver outputs were sampled at a rate of 80 Hz, and averaged online over every second. Slowly varying signal contributions caused by attenuation due to gases, clouds and rain were removed from the signal by a suitable hardware high-pass filter. Next, the signal variance was calculated over every minute from January 1990 to December 1992. Cumulative distributions of standard deviations over a period of one year were produced. The frequency scaling factors derived from these distributions on an equiprobability basis are reported [5].

Eindhoven (Netherlands):

The three Olympus beacons were received at Eindhoven University of Technology with one Cassegrain antenna with a frequency–dependent aperture efficiency. The signal was sampled at a rate of 3 Hz. The scintillation standard deviation was calculated over every minute for the period covering January 1991 to May 1992 (except June to August 1991). The frequency scaling factors were obtained for five 23 minutes clear-sky events, all occurring in June 1992. For each event and each frequency pair the frequency scaling factors were calculated as the ratio of these event standard deviations between the two frequencies. The resulting frequency scaling factors vary from event to event, which is stated to be mainly due to the variability of e.g. the turbulent layer height. Here, the average value of these five events for each frequency pair have been taken [6].

Kirkkonummi (Finland):

Measurements of the Olympus satellite beacon signal at 19.77 and 29.66 GHz, viewed from an elevation angle of 12.7^0 have been performed at Helsinki University of Technology. Scintillations were extracted using a digital high-pass filter with a cut-off frequency of 0.02 Hz. The variance was calculated over every 1-minute. The frequency scaling ratio was calculated from the joint distributions of the two signals, for the period covering the whole of 1990 and the period June to October 1992 [2].

Martlesham (UK):

Measurements by the British Telecom research Laboratories were performed from June 1983 to May 1987. The data were recorded at a sampling rate of 0.5 Hz. A high-pass filter algorithm was used to separate the rapidly from the more slowly varying components of the measured attenuation signal. The data were divided into rain-event data, characterised by mean fades $\geq$ 3 dB together with short pre- and post-event periods, and the remaining data. The standard deviation was calculated over every 1-min block of data. The frequency scaling ratio was obtained as the peak occurrence ratio of the 14/11 GHz standard deviation, for the dataset containing the data outside of rain events [7].

Spino d'Adday (Italy):

Measurements have been made by Politecnico di Milano of beacon signal from the satellites Olympus (at 12.50 and 19.77 GHz) and Italsat (at 18.7, 39.6 and 49.5 GHz). Scintillation measurements were recorded over a period of three months (June to August 1993) from the Italsat satellite but for the Olympus satellite it was restricted to July 1993. Cassegrain antennas of diameter D=3.5m and efficiency η=0.64 were employed. The signal was sampled at a rate of 1 Hz and slowly varying signal contributions were removed by a high-pass filtering with a cutoff frequency of 0.008 Hz. From joint distributions of 1-minute standard deviations for each frequency pair, the frequency scaling ratios were obtained as the slopes of the best fitting straight lines with forced zero offset. In addition [8], the averaged monthly standard deviation and cumulative distribution function of fades and enhancements calculated over every minute for the period covering January 1995 to December 1996 were also obtained.

Yamaguchi (Japan):

In Japan [9], long-term propagation experiments have been carried out using the INTELSAT-V satellite link during the year 1983. A satellite beacon at 11.45 GHz, right-hand circularly polarized, and a looped-back wave at 11.18 GHz, linearly polarized that was originally sent out from the ground station at 14.27 GHz (linearly polarized) were received by one Cassegrain antenna. All data were sampled at 1 Hz. A scattergram was made of the signal level variations of the two frequencies during one scintillation event on August 10, 1983, between 12:00 AM and 13:00, and another of the standard deviations of the two frequencies, calculated over every hour for the whole period of August 1983. Curve fits to both scattergrams gave the same frequency scaling ratio of scintillation.

Fairbanks (Alaska), Norman (Oklahoma), Reston (Virginia), Tampa (Florida), Vancouver (Canada), White Sands (New Mexico):

Scintillation was measured in a propagation experiment using the 20.16- and 27.51-GHz beacons received from the ACTS satellite. Beacon measurements were sampled at 20 Hz during 6–10 min of each hour for periods of 2–4 months (depending on the site) between June and September 1996. From each of these measurement intervals, power spectra were derived by fast Fourier transform (FFT). The variances were calculated from the spectra after correction for receiver noise. This noise variance was taken as the minimum observed variance value in the data for each site. Frequency scaling factors were obtained by fitting lines to scatterplots of the variances for the two frequencies. In addition, the monthly standard deviation of scintillation intensity for the period covering January 1994 to December 1998 were also obtained [3, 10].

References

[1] M. M. J. L. V. d. Kamp, J. K. Tervonen, E. T. Salonen, and K. Kalliola, "Study of Low Elevation Angle Scintillation Modelling," Helsinki University of Technology, Espoo 1997.

[2] M. M. J. L. V. d. Kamp, C. Riva, J. K. Tervonen, and E. Salonen, "Frequency Dependence of Amplitude Scintillation," *IEEE Transactions on Antennas and Propagation*, vol. 47, pp. 77-85, 1999.

[3] C. E. Mayer, B. E. Jaeger, R. K. Crane, and X. Wang, "Ka-Band Scintillations: Measurements and Model Predictions," *Proceedings of IEEE*, vol. 85, pp. 936-945, 1997.

[4] F. Haidara and C. W. Bostian, "Preliminary Results on Scintillation Intensity Frequency Scaling from the Virginia Tech Olympus Experiment," presented at IEEE International Symposium on Antennas and Propagation, Chicago, 1992.

[5] G. Ortgies, "Slant-path Frequency Scaling of Amplitude Scintillation during Clear-sky conditions and Rain," *Archiv für Elektronik und Übertrangungstechnik*, vol. 47, pp. 203-208, 1993.

[6] S. I. E. Touw and M. H. A. J. Herben, "Short-term Frequency Scaling of Clear-sky and Wet Amplitude Scintillation," *IEE Proceedings on Microwave Antennas Propagation*, vol. 143, pp. 521-526, 1996.

[7] S. M. R. Jones, I. A. Glover, P. A. Watson, and R. G. Howell, "Evidence for the Presence of Turbulent Attenuation on Low-Elevation Angle Earth-Space Paths - Part 2: Frequency Scaling of Scintillation Intensity on a 10^0 Path," *IEEE Transactions on Antennas and Propagation*, vol. 45, pp. 85-92, 1997.

[8] C. Riva. Milano, 2004.

[9] Y. Karasawa, K. Yasukawa, and M. Yamada, "Tropospheric Scintillation in the 14/11-GHz Bands on Earth-Space Paths with Low Elevation Angles," *IEEE Transactions on Antennas and Propagation*, vol. 36, pp. 563-569, 1988.

[10] C. E. Mayer, 2003.

Appendix E

Publication List
2000-2004

Publications (2000-2004)

1. A. Savvaris, and I. E. Otung, "Preliminary Preprocessing of ITALSAT Data at 20, 40 and 50 GHz", National URSI Symposium, Abingdon, UK, 3-4 July 2000.

2. A. Savvaris, and I. E. Otung, "Probability Distribution of Tropospheric Scintillation and the Diurnal and Seasonal Behaviour", Post Graduate Research in Electronics, Photonics, Communications and Software (PREP 2001), University of Keele, UK, 9-11 April 2001.

3. A. Savvaris, C. N. Kassianides, and I. E. Otung, "Observed Effects of Wind on the Intensity and Spectrum of Scintillation", 11th International Conference on Antennas and Propagation (ICAP 2001), Manchester, UK, 17-20 April 2001.

4. A. Savvaris, and I. E. Otung, "Frequency Scaling of Clear-Sky Amplitude Scintillation", National URSI Symposium, Malvern, UK, 11-12 December 2001.

5. A. Savvaris, and I. E. Otung, "Spectral Analysis of Amplitude Scintillation on a V-band Satellite Link", Post Graduate Research in Electronics, Photonics, Communications and Software (PREP 2002), Nottingham, UK, 17-19 April 2002.

6. A. Savvaris, C. N. Kassianides, and I. E. Otung, "Scintillation Fade and Enhancements Duration Statistics at 20, 40 and 50 GHz", 20th International Communications Satellite Systems Conference & Exhibition (AIAA 2002)", Montreal, Canada, 12-15 May 2002.

7. A. Savvaris, and I. E. Otung, "Effects of Meteorological Parameters and the Averaging Period on the Intensity of Tropospheric Scintillation", 3rd International Research and Educational Colloquium on Electronics (IRCE 2002), University of Glamorgan, UK, July 2002.

8. A. Savvaris, and I. E. Otung, "Observed Correlation Between Frequency Exponent and Elevation Angle of Tropospheric Scintillation", 12th International Conference on Antennas and Propagation (ICAP 2003), Exeter, UK, 31st March – 3rd April 2003.

9. A. Savvaris, and I. E. Otung, "Effects of Meteorological Parameters and the Averaging Period on the Intensity of Tropospheric Scintillation", 12th International Conference on Antennas and Propagation (ICAP 2003), Exeter, UK, 31st March – 3rd April 2003.

10. I. E. Otung and A. Savvaris, "Observed Frequency Scaling of Amplitude Scintillation at 20, 40 and 50GHz", IEEE Transactions on Antennas and Propagation, Vol. 51, No.12, Dec. 2003, pp. 3259-3267.

11. A. Savvaris, C. N. Kassianides, and I. E. Otung, "Observed Effects of Cloud and Wind on the Intensity and Spectrum of Scintillation", IEEE Transactions on Antennas and Propagation, Vol. 52, No.6, June 2004, pp. 1492-1498.

12. A. Savvaris, and I. E. Otung, "The Effect of Atmospheric Refractivity on Observed Scintillations Levels on Earth-Space Communication Links", 4th International Research and Educational Colloquium on Electronics (IRCE 2003), University of Glamorgan, UK, July 2003.

13. A. Savvaris, A. P. Chambers, and I. E. Otung, "Fade Mitigation Techniques for Earth-Space Satellite Communication Systems Operating at V-band", Post Graduate Research in Electronics, Photonics, Communications and Software (PREP 2004), University of Hertfordshire, UK, April 2004.

14. A. Savvaris, and I. E. Otung, "Observation of Scintillation Degradation on Satellite Links in Southern England", 22nd International Communications Satellite Systems Conference & Exhibition (AIAA 2004)", Monterey, USA, 6-9 May 2004.

Appendix F

Comparison of the performance of the new distribution models with measured distribution, ITU-R model, Karasawa model and Otung model for scintillation signal enhancements and fades

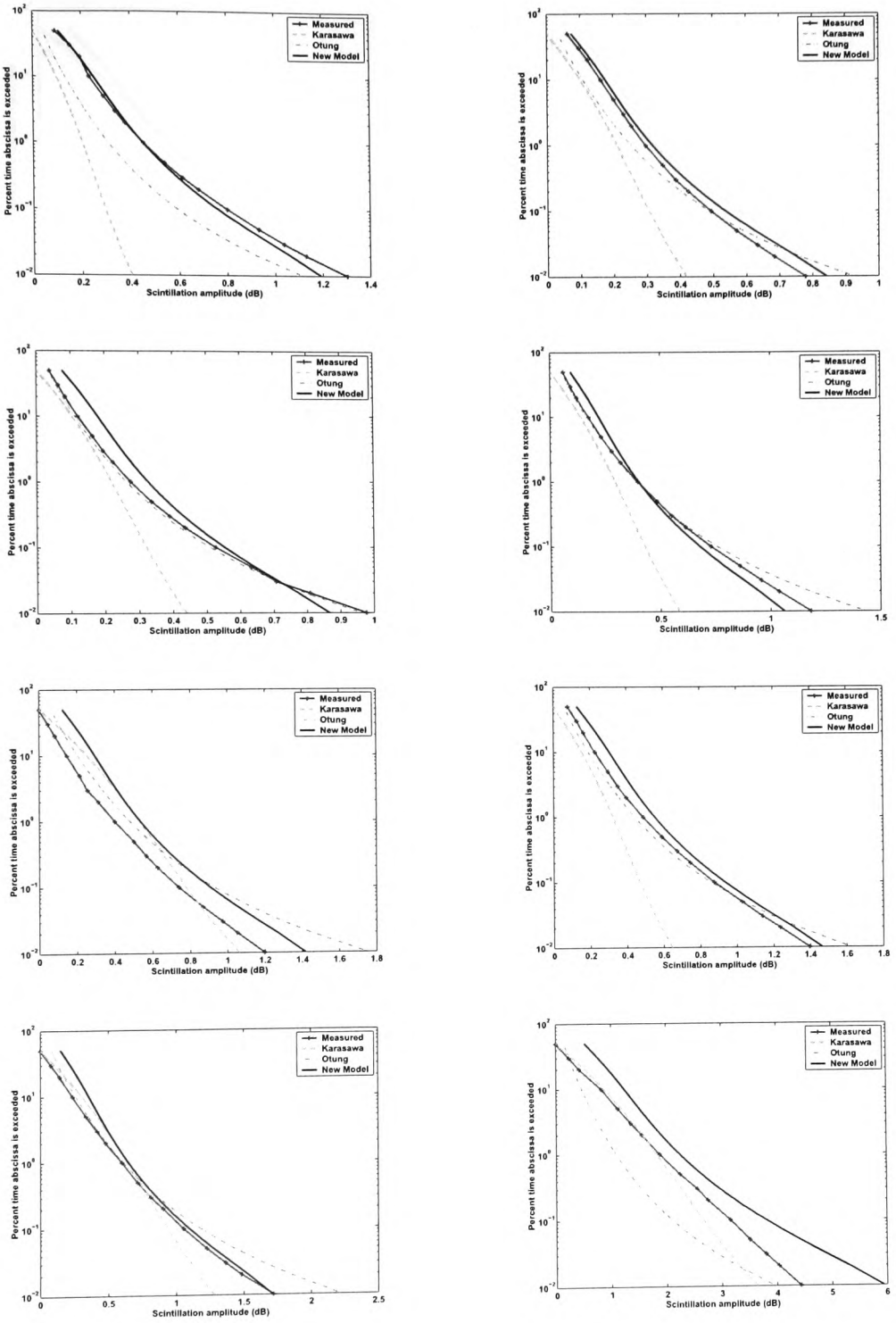

Figure F.1. Comparison of measured distribution with predicted ITU-R, Karasawa, Otung and new model distribution for scintillation signal enhancements.

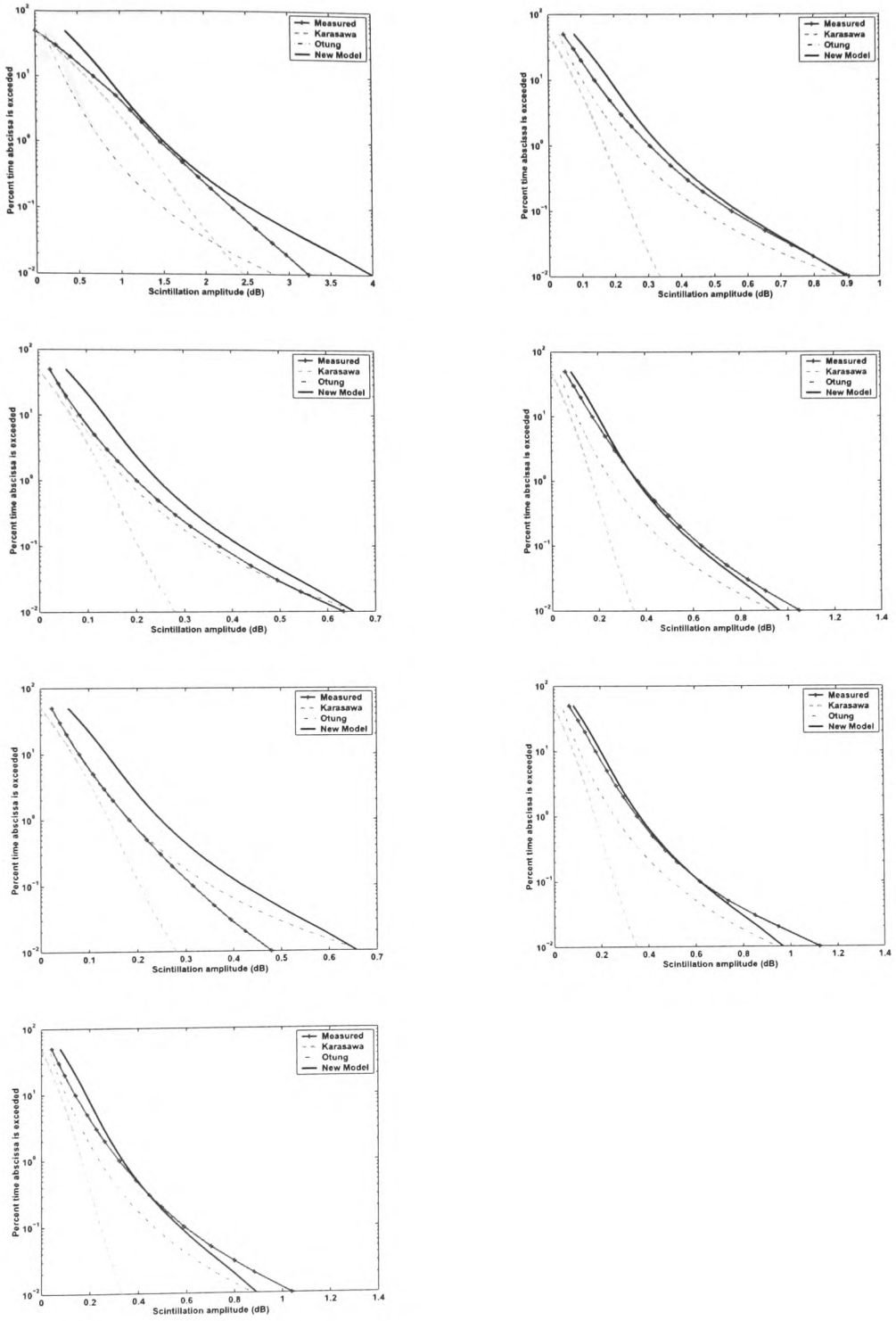

Figure F.2. Comparison of measured distribution with predicted ITU-R, Karasawa, Otung and new model distribution for scintillation signal enhancements.

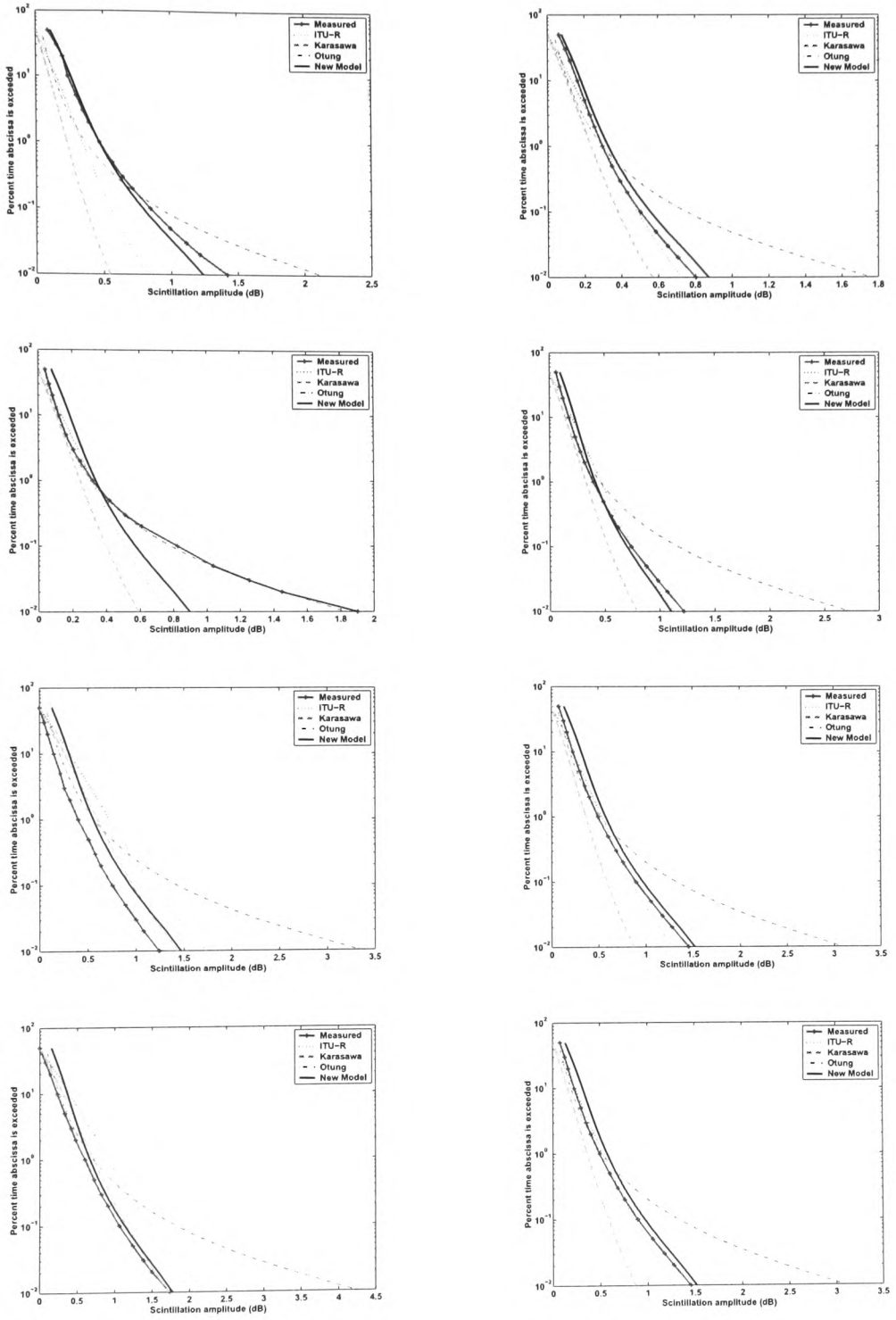

Figure F.3. Comparison of measured distribution with predicted ITU-R, Karasawa, Otung and new model distribution for scintillation signal fades.

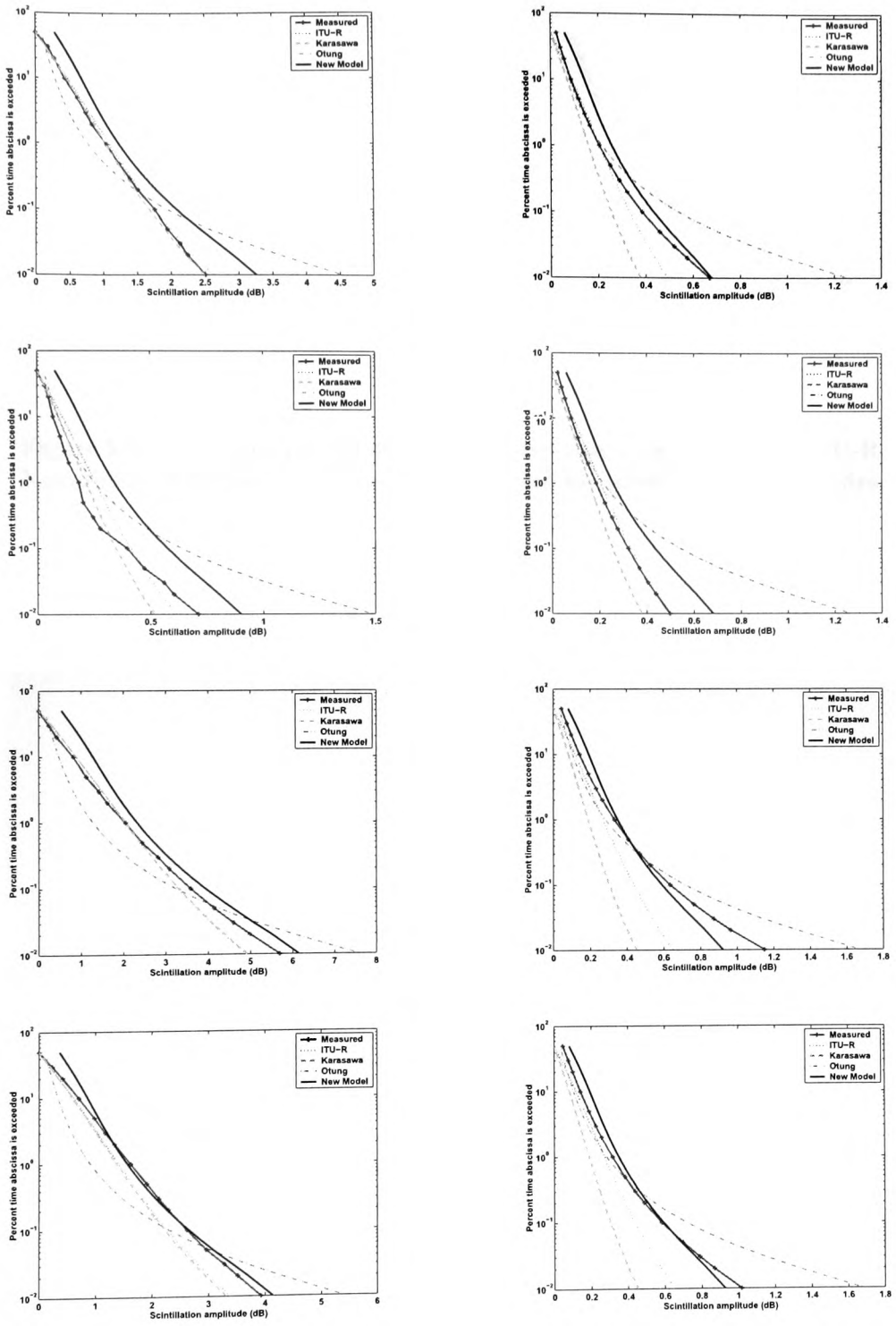

Figure F.4. Comparison of measured distribution with predicted ITU-R, Karasawa, Otung and new model distribution for scintillation signal fades.

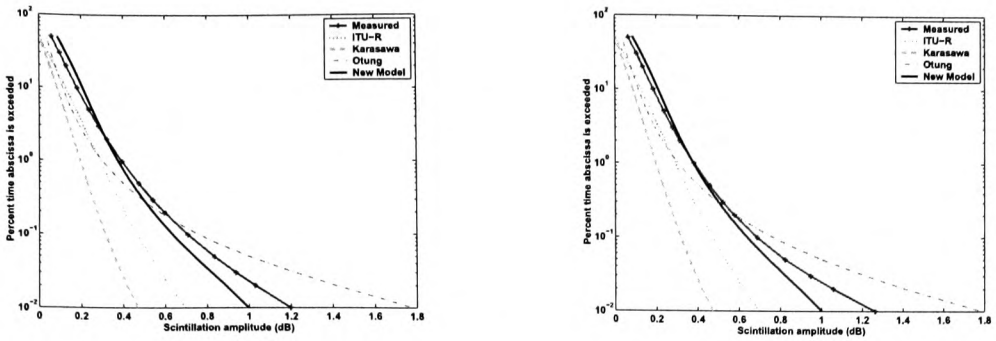

Figure F.5. Comparison of measured distribution with predicted ITU-R, Karasawa, Otung and new model distribution for scintillation signal fades.